THE LOCAL UNIVERSE AS SEEN BY THE MILLENNIUM GALAXY CATALOGUE

David John Lemon

A Thesis Submitted for the Degree of PhD
at the
University of St Andrews

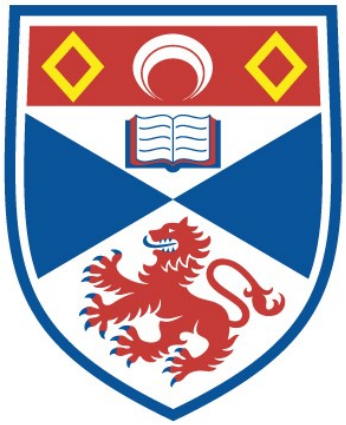

2003

THE UNIVERSITY OF ST ANDREWS

The Local Universe as seen by the Millennium Galaxy Catalogue

D.J. Lemon

Submitted for the degree of Ph.D.

July 2003

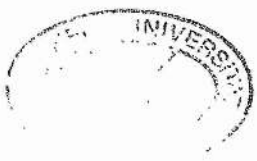

I, David John Lemon, hereby certify that this thesis, which is approximately 50000 words in length, has been written by me, that it is the record of work carried out by me and that it has not been submitted in any previous application for a higher degree.

July 2003

I was admitted as a research student in October 1999 and as a candidate for the degree of Ph.D.in October 1999; the higher study for which this is a record was carried out at the University of St. Andrews between 1999 and 2003.

July 2003

In submitting this thesis to the University of St. Andrews I understand that I am giving permission for it to be made available for use in accordance with the regulations of the University Library for the time being in force, subject to any copyright vested in the work not being affected thereby. I also understand that the title and abstract will be published, and that a copy of the work may be made and supplied to any *bona fide* library or research worker.

July 2003

I hereby certify that the candidate has fulfilled the conditions of the Resolution and Regulations appropriate for the degree of Ph.D. in the University of St. Andrews and that the candidate is qualified to submit this thesis in application for that degree.

July 2003

I dedicate this thesis to me. Without whom, none of this would have been possible.

Acknowledgments

"There's two types of people. Good people and bastards, nothin' else comes into it."

Lemmy (Motorhead)

To begin with I need to thank my supervisor, Dr Simon Driver for giving me a chance at a PhD and helping me thorough it at every stage of the way. I also thank Dr Joe Liske for his tireless work on the MGC photometry, without which it would not be the the pristine data set it is. I thank Dr Nick Cross for all his work on combining the MGC to the 2dFGRS and SDSS-EDR (not to mention sharing and office with me for two years). I thank the Research School of Astronomy & Astrophysics of the Australian National University for there hospitality during my visit. I would also like to thank Dr Rosemary Wyse for all her help and guidance on the star counts chapter. I must also thank Dr Tim Lister and Rodger Stapleton for putting up with my endless supply of daft computer related questions.

I can not go on with out thanking my family and friends, though if truth be told I've never really seen the difference. First, my dad for his love and support over the years and for giving me the freedom to grow up (or not) in my own way. I thank my brother for just being there should I ever need him and for making my childhood and even funner place. I must also thank my new family: Jan, Rose and Felix for welcoming me into there home and lives.

Those I met on the way: Saun, Neil, Martin, Sarah, Phiona, Danni, Keith, Ed, Richard and the Optics lads. Those LJMU days seem so long ago, but I still remember them with a smile. Its a pity all that pesky science stuff kept getting in the way. Kroina, Eleni and Rayn, for making the QMW and the East End a home away from home. I still can't think of London with out thinking of the Drapers Arms and singing "Pretty fly, for a white guy". (Dr) Sandra Jeffers, (Dr) Paul Clark and Dr Heidi Rowe, you managed to keep me sane in St-Andrews with plenty of BBQs, drinking and dancing.

And now for the ones who where always there: Bakewell, Frank, Lou, Kato, Jen, Claire, Bean-flicker, Cod & Caz, Monster & Emma, Boogie, The Gwar, Ralph, Sly and Big-Chief Minging-Hair...Wallasey Funky Squad for life! There are tooooo many memories here so I'll just thank you all for letting me be a part of your lives.

"Theirs so much I don't know about Astrophysics. I wish I'd read that book by that wheel-chair guy."
Homer Simpson

Abstract

In this thesis we construct a B-band catalogue of the local universe which we call the Millennium Galaxy Catalogue (MGC). The MGC is photometrically and astrometrically accurate to ± 0.03 mags and $\pm 0.08''$ respectively and covers an area of$\sim$ 36 sq deg in the NGP. Colour and redshift information are available from overlapping regions of the two-degree Field Galaxy Redshift Survey (2dFGRS) and the Sloan Digital Sky Survey Early Data Release (SDSS-EDR). With an exposure time of 750s and an isophotal surface brightness limit of 26 mags/sq arcsecs, the MGC is the largest and deepest photometric survey of the local universe to-date.

As well as containing photometric information, by making use of a newly developed software package- Galaxy Image 2D (GIM2D), and assuming a standard de Vaucouleurs and exponential galaxy profile, the MGC also contains structural parameters (half light radius and (B/T) etc) to all galaxies in the magnitude range $16 < B_{\rm MGC} < 20$.

By making use of the information in the MGC we are able to classify our galaxies into three morphological types (E/S0, Sabc and Sd/Irr) using (B/T) cuts. In doing this we find that 30.52% of the galaxies form a "new" galaxy population identified by having a (B/T) of *exactly* 0. After visual inspection this population is found to be a mixture of early and late type star-forming Spirals and Irregular galaxies, all of which have a disk component that is flatter than an exponential. After visually redistributing these galaxies we find that the local galaxy population consists of 28.1% E/S0, 39.64% Sabc and 31.37% Sd/Irr.

From the redshift information contained within the MGC we are able to look at the galaxy distribution in terms of physical parameters. We find that the galaxies are distributed in absolute magnitude, surface brightness and half light radii in a manner that is consistent with the hierarchical formation scenario.

We derive total and morphological galaxy number counts and, after combining them via a step wise maximum likelihood (SWML) technique, we arrive at morphological LFs. From examining the galaxy counts we find that there is no steep rise in the bright end, eradicating the need for strong local evolution. Also one does not need to renormalise the morphological or total galaxy counts in order for them to be consistent with faitner counts. The Sabc and Sd/Irr LFs are surprisingly similar with both showing a mild faint end slope.

We look at the properties of bulges and disks of galaxies. We find that as galaxies become more diskey there bulges move away from the Kormendy law for Elliptical galaxies.

Due to the similarity of the Spiral and Irregular population LFs, as well as apparent and intrinsic parameter distributions, we are forced to conclude that one can only reliably distinguish between the Ellipticals and the general galaxy population, and that investigating the bulge and disk components of a galaxy may be more useful than Hubble types.

CONTENTS

LIST OF FIGURES

LIST OF TABLES

CHAPTER 1

Introduction

1.1 Background

In the years 1925 to 1929 Hubble demonstrated that many of the nebulae found in the surveys of the time were galaxies, external and at some distance from the the Milky Way, Hubble (1925), Hubble (1926a), Hubble (1926b) & Hubble (1929), (see Sandage 1998 for a review). In the second 1926 paper Hubble used data later published in the Mount Wilson Catalogue (Seares & Kapteyn 1930) to show that the logaritham of the number of galaxies, log N(m), is proportional to 0.6×mag to a limiting magnitude of m=16.7, which is the relation required by a non-evolving Euclidean universe. It is these two discoveries which lay the foundation of modern observational cosmology. However, the data used by Hubble in 1926 was patchy and had poorly calibrated zero points, and hence magnitudes. To try to improve the quality of these results, Hubble, starting in 1927, undertook what was to be the first proper galaxy survey. It was completed in 1934. The Hubble (1934) survey contained 44000 galaxies in an area of 650 sq degrees covering both Galactic hemispheres. In his 1934 paper Hubble not only confirmed the number-magnitude relation, but also showed that, for absorption, there is a strong latitude effect and gave the first indication that galaxies were clustered. Hubble also mapped the "zone of avoidance" in much greater detail than had previously been done. Later, Hubble (1936b), attempted to extend the counts to fainter magnitudes. However, photometric errors, an incorrect K term and a misunderstanding of the proper distance redshift relation all led Hubble (1936a) to the conclusions that the observed redshifts are not velocity shifts and that "...if redshifts are not primarily due to velocity shifts...The velocity-redshift distribution is linear; the distribution of nebulae [galaxies] is uniform; there is no evidence of expansion, no trace of curvature, no restriction of the time scale." Hubble (1936b), page 553. We can probably forgive Hubble for using the wrong proper distance redshift relation, since it was not until 1958 that Mattig published his revolutionary paper in which was the first full derivation of proper distance as a function of redshift. In 1949 Hubble began a program to repeat his ground breaking survey by using the then newly commissioned 48 inch Palomar Schmidt telescope. This would allow Hubble to extend his number counts down to fainter magnitudes. This project was never completed as it was realised that for any new number count studies the magnitudes of each individual galaxy should be measured instead of just counting galaxies to the plate limit. At the time the technology to do this was not available. Also the process of aperture corrections, to obtain total magnitudes, had not and still hasn't been completley solved (see Cross 2002). It is here that observational cosmology came to a bit of a stand still until the late 1970s when the required technologies and techniques became available. When these technologies arrived it became apparent that at faint B-band magnitudes (B_J>20) the counts did not match the no-evolution predictions. This was discovered by Kron (1980) and became known as the faint-blue galaxy problem. Although, especially with the advent of the Hubble Space Telescope (HST), we have been able to probe even deeper magnitudes, there is still an unsolved problem as to how this blue excess came about. The obvious explanation is that some evolutionary process has occurred. Indeed this seems to be supported by the

excessively high number of faint (high z) irregular galaxies, 50%, when compared to the local sample where there are only 5% irregulars, Sandage (1998). However, due to the large angular area required to get a complete sample of the local universe and the relative small angular size of CCDs, the morphological mix of the local group is far from being firmly established. This is one of the prime goals of the Millennium Galaxy Catalogue (MGC).

1.2 The MGC

The motivation for this survey is essentially the same as Hubble's was all those years ago, that of the lack of detailed knowledge of the local galaxy population over a large angular scale. As we have seen this makes it very difficult to get an accurate description of the number of different types of galaxies in the local universe and therefore even more difficult to imply anything about the high redshift universe. Up until the Millennium Galaxy Catalogue (MGC), all previous large galaxy catalogues such as the Catalogue of Galaxies and Clusters of Galaxies (Zwicky et al. 1961 to 1968), the Morphological Catalogue of Galaxies (Vorontsov-Vel'Yaminov & Arkhipova 1962 to 1974), the Uppsala General Catalogue of Galaxies (Nilson 1973), the ESO/Uppsala Catalogue (Lauberts 1982, Lauberts & Valentijn 1989), the Southern Galaxy Catalogue (Corwin, de Vaucouleurs & de Vaucouleurs 1985), the Catalogue of Principal Galaxies (Paturel et al. 1989), the Edinburgh/Durham Southern Galaxy Catalogue (Heydon-Dumbleton, Collins & MacGillivary 1989), the APM catalogue (Maddox et al. 1990), the Third Reference Catalogue of Bright Galaxies (de Vaucouleurs et al. 1991) and the SuperCOSMOS Sky Survey (Hambly, Irwin & MacGillivray 2001) were based on photographic plates. While these catalogues have provided invaluable information and insight, uncertainty remains as to their completeness, particularly for low surface brightness and compact galaxies (Disney 1976; Sprayberry et al. 1997; Impey & Bothun 1997; Drinkwater et al. 1999). In addition there are concerns as to the photometric accuracy (e.g. Metcalfe, Fong & Shanks 1995), the susceptibility to scale errors (Bertin & Dennefield 1997), plate-to-plate variations (Cross et al. 2003) and the dynamic range. These photographic based catalogues have been the starting point for numerous spectroscopic surveys aimed at measuring the local space density of galaxies (the local galaxy luminosity function). The space density of galaxies is our fundamental tool for describing the local galaxy population and therefore a crucial constraint for models of galaxy formation (e.g. White & Frenk 1991; Cole et al. 2000; Pearce et al. 2001). If the imaging catalogues are incomplete and/or photometrically inaccurate then regardless of the completeness of the spectroscopic surveys themselves our insight into the galaxy population will be incomplete and most likely biased against specific (typically intrinsically faint and/or low surface brightness) galaxy types.

1.3 The Luminosity function

One of the most frequent uses of any galaxy survey, of cluster or field galaxies, is to be able to extract a galaxy luminosity function (hereafter LF). An accurate calculation of the galaxy LF provides a statistical description of the space density of galaxies as a function of absolute magnitude. It should be noted that there is no general LF that can describe the entire galaxy population. This is because galaxy statistics are heavily dependent on environment and so different LF's are needed for both the cluster and field galaxy environments. These may still not be suitable and are often broken down into morphology dependent LF's. It is further argued that another break down of the LF into high and low redshift LF's is required. The best analytic description of the field and cluster LF's takes the same form, that of the Schechter (1976) function:

$$\Phi(L)dL = \phi^*(L/L_*)^\alpha exp(-L/L_*)dL \tag{1.1}$$

where the parameters, α, ϕ^* and L_* are environment and redshift dependent. $\Phi(L)dL$ gives the number of galaxies per unit volume in the luminosity interval L to L+dL, α controls the slope at the faint end, L_* is a characteristic luminosity giving the turn-over point between the exponential bright end and the power law faint end and ϕ^* (the normalisation parameter) gives the number of galaxies per unit volume. From this the local luminosity and space density of galaxies can be derived. The Schechter function is shown in its more useful magnitude form in Appendix B.1. From the LF we are able to model galaxy number counts which can help to understand galaxy evolution. However, this is more difficult to get at as cosmology will affect the LF, sometimes in the same way as evolution, therefore appearing to overstate the amount of evolution that has taken place and sometimes in the opposite direction as evolution, resulting in an underestimate of the amount of evolution. It is therefore vital that as accurate as possible an LF is found.

Over the past two decades there have been numerous estimates of the local galaxy luminosity function (e.g. Efstathiou, Ellis & Peterson 1988, Mt Stromlo/APM, Loveday et al. 1992, SSRS2, Marzke et al. 1998, ESP, Zucca et al. 1997, Autofib, Ellis et al. 1996, Durham/UKST, Ratcliffe et al. 1998, SDSS-EDR, Blanton et al. 2001 and 2dFGRS, Norberg et al. 2002) and consequently of the three parameter Schechter function used to represent it, see Eqn. 1.1. Typically the surveys agree broadly on the faint end slope (α, $\Delta\alpha \approx \pm 0.15$) but show a marked variation in the characteristic luminosity (L^*, $\Delta L^* \approx 40$ %) and normalisation (ϕ^*, $\Delta\phi^* \approx 50$ %). The uncertainties in the Schechter parameters result in an uncertainty of a factor of 3 (see Cross et al. 2001) in the local luminosity density, j, $j = L^*\phi^*\Gamma(\alpha+2)$. The uncertainty in ϕ^* is known as the normalisation problem and has been somewhat overshadowed by the better known faint blue galaxy problem (Koo 1986 and Ellis et al. 1996). Possible solutions to the normalisation problem are that it is a result of strong evolution in the local giant population, though this is ruled out from HST observations (Driver & Phillipps 1996), a large local underdensity, or photometric errors and/or surface brightness selection effects in the local (mostly photographic) samples.

The faint blue galaxy problem describes the inability of basic galaxy number count models to predict the numbers of galaxies seen at faint magnitudes in the deep pencil beam CCD based surveys (e.g. Tyson 1988, Metcalfe, Fong & Shanks 1995 and Metcalfe et al. 2001). Essentially, the models underpredict the number of galaxies observed at $B > 19$ mags. It is incorrect to interpret this as an indication that one is observing the epoch of galaxy formation. The predicted counts start to fail at around z=1 due to the effects of spacial curvature and k-corrections whereas galaxies are formed at around z=6 – 8, (Peacock 1999), cosmology depending. The faint blue galaxy problem is described in detail in Koo & Kron (1992).

As the normalisation problem describes the inability of number count models to explain the galaxy counts even at bright magnitudes ($18 < B < 20$ mag) by as much as a factor of 2 (see discussions in Shanks et al. 1984, Driver, Windhorst & Griffiths 1995, Marzke et al. 1998 and Cohen et al. 2002), it is this that is the more fundamental problem. Whilst luminosity evolution, cosmology and/or dwarf galaxies can and have been, invoked in varying mixtures to explain the faint blue galaxy problem (e.g. Broadhurst, Ellis & Shanks 1988, Babul & Rees 1992, Phillips & Driver 1995 and Ferguson & Babul 1998), none of these can be used to resolve the normalisation problem.

In the past the problem was essentially ignored by renormalising the number count models to the range $18 < B < 20$ mag (e.g. Metcalfe, Fong & Shanks 1995, Metcalfe et al. 2001, Driver et al. 1994, Driver, Windhorst & Griffiths 1995, Driver et al. 1994 and Marzke et al. 1998). The justification was that the bright galaxy catalogues, on which the luminosity function measurements are based, are shallow and as such susceptible to local clustering. However the crucial normalisation range typically occurs at the faint limit of the photographic surveys (where the photometry and completeness are more likely to be a problem) and at the bright end of the pencil beam CCD surveys (where statistics are poor). This clustering explanation overlooks two more fundamental problems: gross

photometric errors and gross incompleteness in the local catalogues. If either of these two latter explanations play a part this will have important consequences for the new-generation spectroscopic surveys, namely the 2dFGRS (Colless et al. 2001) and the SDSS, (York et al. 2000). The input catalogue of the 2dFGRS is an extensively revised version of the photographic APM survey (which is known to show a peculiar steepening in its galaxy counts at bright magnitudes, Maddox et al. (1990b)), with zero point and scale-error corrections from a variety of sources including the 2MASS K-band survey, and the data presented in this thesis, (Norberg et al. 2002). In the case of the SDSS – which leaps forward in terms of dynamic range, uniformity and wavelength coverage – the effective exposure time is relatively short (54 s) and the isophotal detection limit is comparable to that of the photographic surveys. Hence, while issues of photometric accuracy should be resolved the question mark of completeness will remain.

1.3.1 The morphological and colour LF

The local morphological populations can be statistically represented by looking at the LF of different Hubble types. Loveday et al. (1992), Marzke et al. (1994), Marzke et al. (1998) and Madgwick et al. (2002) have all published morphological LFs. Fig. 1.1 shows schematic examples of LFs for 3 broad Hubble types. There is a broad consensus that the faint, α dominated, end of the LF is most affected by morphological type. The E/S0 galaxies have a flat (or even turned over, Loveday et al. 1992) faint end slope which then rises as one moves to later type galaxies. This indicates that it is the Irregular galaxies that overwhelmingly dominate the faint end and therefore α. It is vital then, that the fraction of Irregular galaxies and their associated redshift distribution is well understood, as they will contribute significantly to the faint end galaxy counts which are heavily influenced by galactic evolution and cosmology, see Chapter 4, § 4.1.

Marzke & Da Costa (1997), Lilly et al. (1995) and Blanton et al. (2001) have all looked at LFs and their dependency on colour. Fig. 1.2 shows the LFs for both red and blue galaxies taken from Lilly et al. (1995). They show that it is the blue galaxies which dominate α and that the red galaxies have a much flatter faint end slope. Given what we have previously said about the morphological LF and its dependency on α this is hardly surprising, as it is the Sd/Irr galaxies which will dominate the blue end and the E/S0 population that reside in the red end. Fig. 1.2 does illustrate that by moving to redder bands one does not need to worry so much about the effects of evolution on the galaxy number counts. However, if derived from a survey/catalogue comprised from observations in the redder regions of the optical window, the relative numbers of galaxy types (specifically the Sd/Irr) will be dramatically underestimated. Thus, the description of the local galaxy population will be woefully incomplete.

1.4 Galaxy Morphologies

It is one thing to be able to statistically represent the local galaxy population, it is another to actually decipher it. This is the problem of obtaining galaxy morphologies. In other words we want to be able to individually classify each galaxy into a family of objects. This cannot be done by the LF as it only describes the populations as a whole and any information regarding the individual galaxies is lost. Also, as the LF is only a 1-dimensional statistical tool it is difficult to reliably extract any physical description of the galaxy population. Attempts to expand the LF and to get at the physics behind the galaxy population(s) have been made and has resulted in the rise of a Bivariaite Brightness Distribution (BBD, see § 1.4.4). It is here that we now review the most widely used methods for classifying galaxies and understanding the physics behind the various galaxy populations.

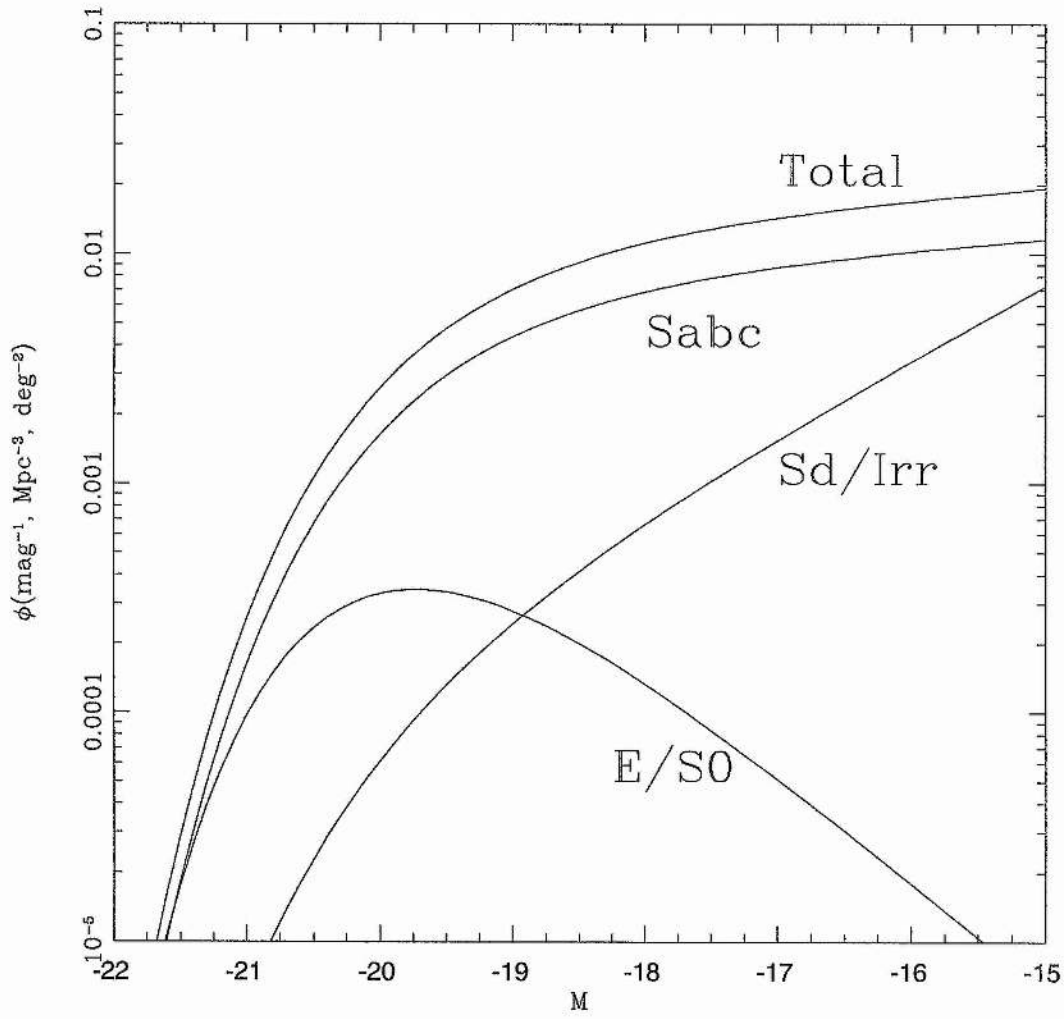

Figure 1.1: A schematic of the LF for different Hubble types.

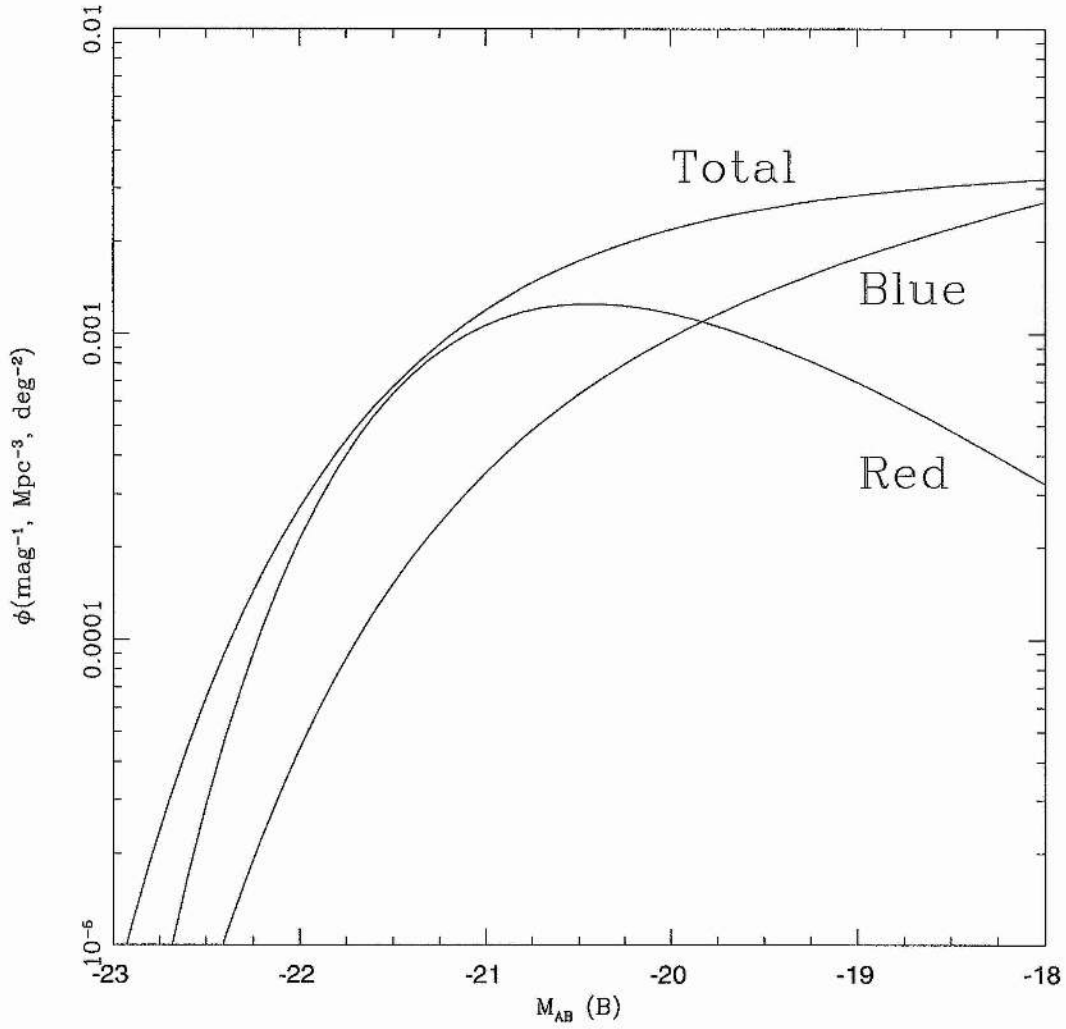

Figure 1.2: The LF for both red and blue galaxies. The Schechter function parameters for each LF where taken from Lilly et al. (1995).

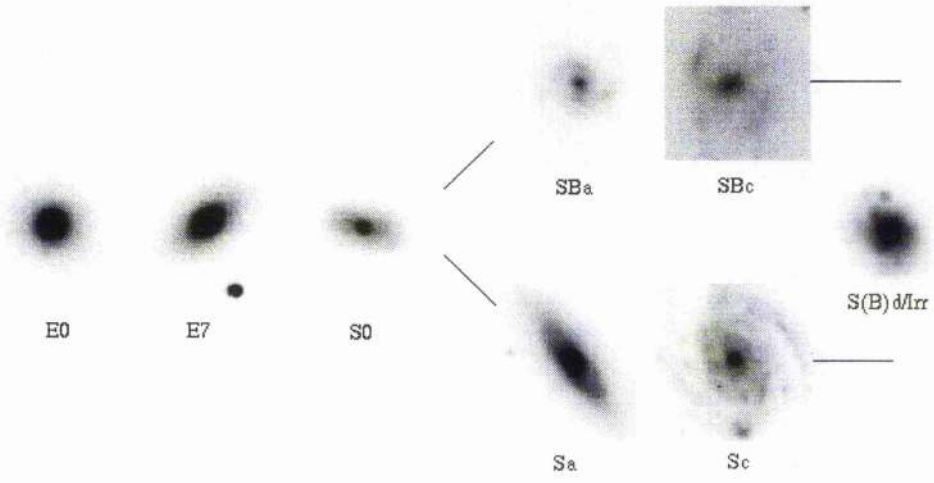

Figure 1.3: The Hubble tuning-fork diagram. The various Hubble types are illustrated using MGC galaxies.

1.4.1 The Hubble tuning-fork

Traditionally the classification of galaxies has been performed using the qualitative based Hubble tuning-fork scheme (Hubble 1939). In this method the observer assigns a galaxy a class, known as a Hubble type, depending upon where it lies on the tuning-fork, see Fig 1.3. Its position on this diagram is determined by the absence or presence (and strength), of observed physical properties. Since the initial conception of the Hubble diagram there have been many modifications to it (Sandage 1961, de Vaucouleurs 1959 & van den Bergh 1976) in an attempt to try to include new galaxy classes, however its basic shape remains the same.

To the left of the tuning-fork are the smooth featureless Elliptical galaxies. These are tri-axial spheroids of varying ellipticity consisting of gravitationally bound stars embedded in dark matter halos and mostly devoid of gas, Phillipps et al. (1996). The ellipticity is classified by assigning each galaxy a number, n, where $n=10 \times (1 - b/a)$, where a and b are the projected major and minor axis of the galaxy. It is found that elliptical galaxies lie somewhere between E0 and E7, where E0 galaxies are spherical with an axial ratio of (b/a)=1 and E7 are highly ellipsoidal, (b/a)=0.3.

To the right of the tuning-fork are the spiral and barred spiral galaxies. Spiral galaxies (barred and unbarred) have the same basic shape, that of a central spherical bulge embedded within a disk of stars containing spiral arms. The difference between barred and unbarred spirals is the existence of a "rigid" bar of stars in the disk connecting the bulge to the spiral arms. Both types of spirals are classed into 4 sub groups: Sa, Sb, Sc

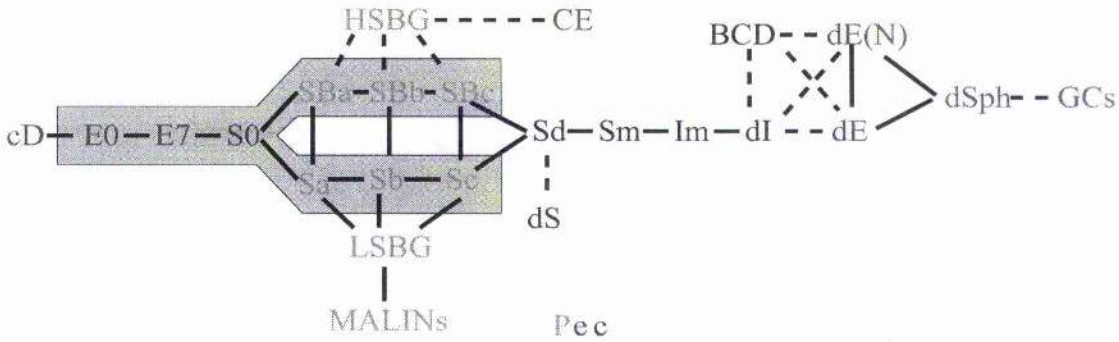

Figure 1.4: The "revised" Hubble tuning-fork. This figure is taken from Driver & Cross (2000).

Table 1.1: T-types in the Hubble Revised System.

cE	E0	E^+	$S0^-$	$S0^0$	$S0^+$	S0/a	Sa	Sab	Sb	Sbc	Sc	Scd	Sd	Sdm	Sm	Im	cI
-6	-5	-4	-3	-2	-1	0	1	2	3	4	5	6	7	8	9	10	11

and Sd/Irr (SBa, SBb, SBc & SBd/Irr for barred spirals) [1]. The classification of galaxies into these subgroups is based on the observed relative size of the bulge to the disk, how tightly wound the spiral arms are and the ease with which the spiral arms are resolved. Sa/SBa have large bulges and tightly wound smooth arms and Sc/SBc have small bulges with loosely wound easily resolvable arms.

Sandwiched between the Ellipticals and the Spirals are the Lenticular/S0 galaxies. These galaxies consist of an elliptical smooth concentration of stars surrounded by a structureless extended stellar envelope.

One problem with the Hubble tuning-fork is that it is incomplete. As not all galaxy types where known in Hubble's time they were never included in the tuning-fork. Since then the initial picture has been somewhat revised to incorporate all the know galaxy types, however, its main advantage, its simplicity, has clearly been lost, see Fig. 1.4. To try to recapture some of the initial simplicity of the tuning-fork, as well as to make it easier for computers to handle morphological information, each Hubble type can be assigned a numerical value known as a T-type, see Table 1.1 and de Vaucouleurs, de Vaucouleurs & Corwin (1976).

The main problem with the Hubble tuning-fork, as with any other observer based classification system, is that, as it depends upon an observer's interpretation of an image, it is a highly subjective process. This often results in confusion with observers giving the same object different Hubble types. In Naim et al. (1995a) a group of 6 experts are used to classify a selection of 832 APM galaxies. They find an overall rms dispersion of 1.8 T-types on the revised Hubble system. Also as galaxies are classified solely on their appearance there is no information available as to how or why they look the way the do. Other problems with this and other visual inspection techniques, are that it becomes very difficult to classify galaxies as their inclination increases and that with the sizes of todays photometric catalogues, notably the SDSS (York et al. 2000), it is rapidly becoming an impractical method. It is with these problems in mind that alternative automated classification routines have been devised.

[1] Although irregular (Irr) galaxies are a class in there own-right, Sd/SBd and Irr galaxies are often indistinguishable and so the two classes are usually merged

1.4.2 Neural Network Classifications

Artificial Neural Networks (hereafter ANN) have been successfully used in star-galaxy classification (Bertin & Arnouts 1996, Odewahn et al. 1992 and Odewahn et al. 1995). As this is a simplified version of the galaxy morphology question it is only natural that ANNs should be applied to galaxy morphologies. Looking at Fig. 1.5 we get an idea of how an ANN works. Essentially a set of input parameters (for example magnitude, surface brightness, ellipticity and colour) are fed into the ANN's input nodes (each parameter goes into a different node). For each input node there is a function which translates the parameter into a normalised value between some predefined range (essentially a probability), ie. 0 to 1. Every input node is linked to every hidden layer of nodes via a different, and initially random, multiplicative factor. The normalised and factorised input nodes are collected and summed in each hidden node. These hidden nodes are then linked to either another set of hidden nodes or the output nodes by a different, and again initially random, factor. There is no limit, other than perhaps computational time, to the number of hidden nodes one can use. At the output node or nodes the values of the previous layer of hidden nodes are collected and summed to give a final numerical value. In our case the value at the output node will be a galaxy type. As the multiplicative factors are initally random numbers the initial value at the output node is meaningless and needs to be "calibrated". To do this the ANN is "trained" on a smaller ($\sim$100 galaxies) well understood and preclassified data set. This data set is then passed through the ANN and the multiplying factors are tweaked until the a sensible result is achieved. One draw back to the ANN is that, although accurate human-like morphologies are achieved, it is essentially an empirical process and as such no information as to the physics of galaxy morphologies is resolved. The ANN we use is that developed in Odewahn et al. (1992) and Odewahn et al. (1995) to produce galaxy types on the system defined in Odewahn et al. (1992). This ANN has been successfully used to consistently and accurately classify galaxy types from *HST* data (Odewahn et al. 1996).

A big advantage of ANNs is that they can consistently and accurately replicate human classifications of a small training set for a much larger data set *that covers the same parameter space.* Naim et al. (1995b) use the galaxy sample from Naim et al. (1995a) to train an ANN to recognise different galaxies. The ANN assigns each galaxy a T-type, see Table 1.1. They find that the ANN is able to achieve a T-type scatter that is similar to the observer T-type scatter found in Naim et al. (1995a). Whilst the advantage of a ANN is that they are able to "quickly" classify a large sample of galaxies, they are essentially flawed in that they do not improve upon but only replicate the human eye, which is known to be inaccurate. An ANN is only as good as its "trainer"; if there is an error in the training set it will be reproduced in the larger data set.

1.4.3 Concentration-Asymmetry System

In the C-A system, developed in Abraham et al. (1994), morphologies are achieved by comparing a galaxies concentration index (C), a measure of how compact the galaxy light is and the asymmetry parameter (A), which indicates how evenly the light is distributed over the galaxy. C is essentially the ratio of the intensities within some inner and outer radii and is formally defined in Abraham et al. (1994) to be:

$$C = \frac{\sum_i \sum_{j \in E(\alpha)} I_{ij}}{\sum_i \sum_{j \in E(1)} I_{ij}} \tag{1.2}$$

where I_{ij} is the intensity in pixel (i, j). E is an elliptical aperture whose radius is normalized to 1 when the aperture encloses the area covered by the 2σ isophote. Abraham et al. (1994) find an inner isophotal radius of α=0.3 gives the best results. A is measured by rotating the galaxy image 180^o and subtracting it from itself and is calculated by:

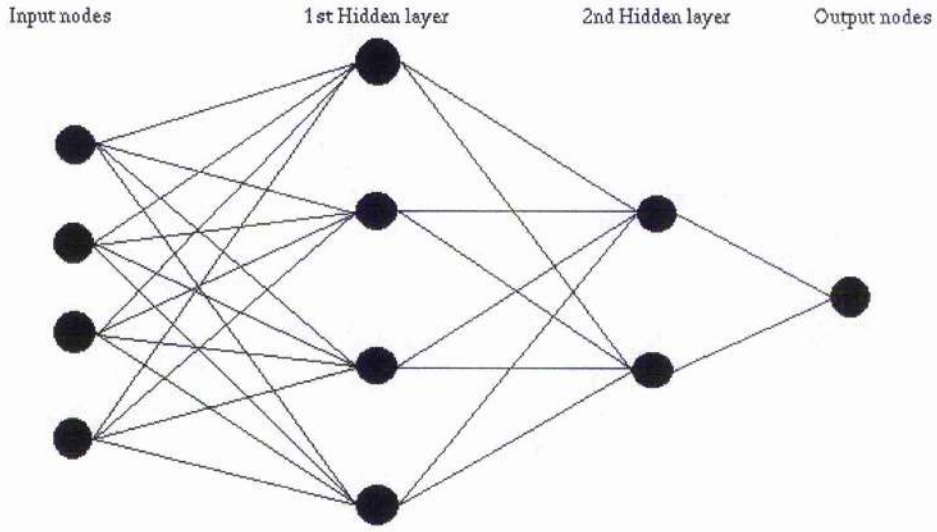

Figure 1.5: A schematic of an artificial neural network.

$$A = \frac{\sum_{i,j} \frac{1}{2}|R_{ij} - R_{ij}^{180}|}{\sum_{ij} I_{ij}} - \frac{\sum_{i,j} \frac{1}{2}|B_{ij} - B_{ij}^{180}|}{\sum_{ij} I_{ij}} \tag{1.3}$$

here R_{ij} is the intensity in of pixel (i,j) in the residual image and $R_{i,j}^{180}$ is the intensity of pixel (i,j) in the residual image rotated by 180^o. $B_{i,j}$ is the background intensity in pixel (i,j) of the residual image and $B_{i,j}^{180}$ is the background intensity of pixel (i,j) in the residual image rotated by 180^o. The asymmetry parameter is calculated over the area covered by the 2σ isophote. Fig 1.6 is a schematic showing the locations of the 3 main Hubble types in the C-A system. Fig. 1 of Abraham et al. (1996) shows a C-A plot for HDF I-band data. Although there is some substantial overlap, most notably by Irregulars falling into the Spiral region, overall the Irr and E/S0 galaxies appear well separated.

Whilst the C-A system has the advantage that it removes the subjectivity of any observer based system (and to some extent the ANNs). It does rely on the C and A parameters being accurately measured, as any error could cause a galaxy to be scattered across the imposed boundaries. As noted above there is also a significant scatter along the Irr/Sabc boundaries which is in-addition to any photometric errors. It is also assumed that the location classification boundaries are redshift independent, though until now (see § C.1) there has been no evidence to either confirm or refute this.

1.4.4 Bivariate Brightness Distribution Classifications

As was first noted by Binggeli (1993) galaxy morphologies may be mapped in a similar fashion as to the C-A system onto a Bivariate Brightness Distribution (BBD). In this case the galaxy parameters plotted are absolute magnitude versus absolute (central or effective) surface brightness. These parameters provide a more physical description of the galaxy population as absolute magnitude and absolute effective surface brightness are believed to be linked to mass and angular momentum respectively (see de Jong & Lacey 2000). The mass-luminosity relation comes from assuming a disk-mass power law relation, $M_D \propto L^\gamma$, with gamma expected to be close to 1. The surface brightness-luminosity comes from the dimensionless spin parameter, λ, defined by Peebles (1969) to be

$$\lambda = J|E|^{1/2} M_{tot}^{-5/2} G^{-1} \tag{1.4}$$

were J is the total angular momentum, E the total energy, M_{tot} the total mass of the system and G is the gravitational constant. All of these parameters are dominated by the galaxies dark matter halo. de Jong & Lacey (2000) then make several more assumptions. The first is that the halo can be modeled by an isothermal sphere with circular velocity V_c, mass M_{tot} and a density profile that scales as $\rho \propto \frac{1}{r}$. From this assumption, along with the virial theorem, $2KE + PE = 0$ which gives $|E| = |KE|$, we get

$$E \propto M_{tot} V_c^2 \tag{1.5}$$

The next assumption is that the disk is a pure exponential with mass M_D, effective radius r_e and that its circular velocity is equal to that of the halos. We then have that the disk angular momentum scale as

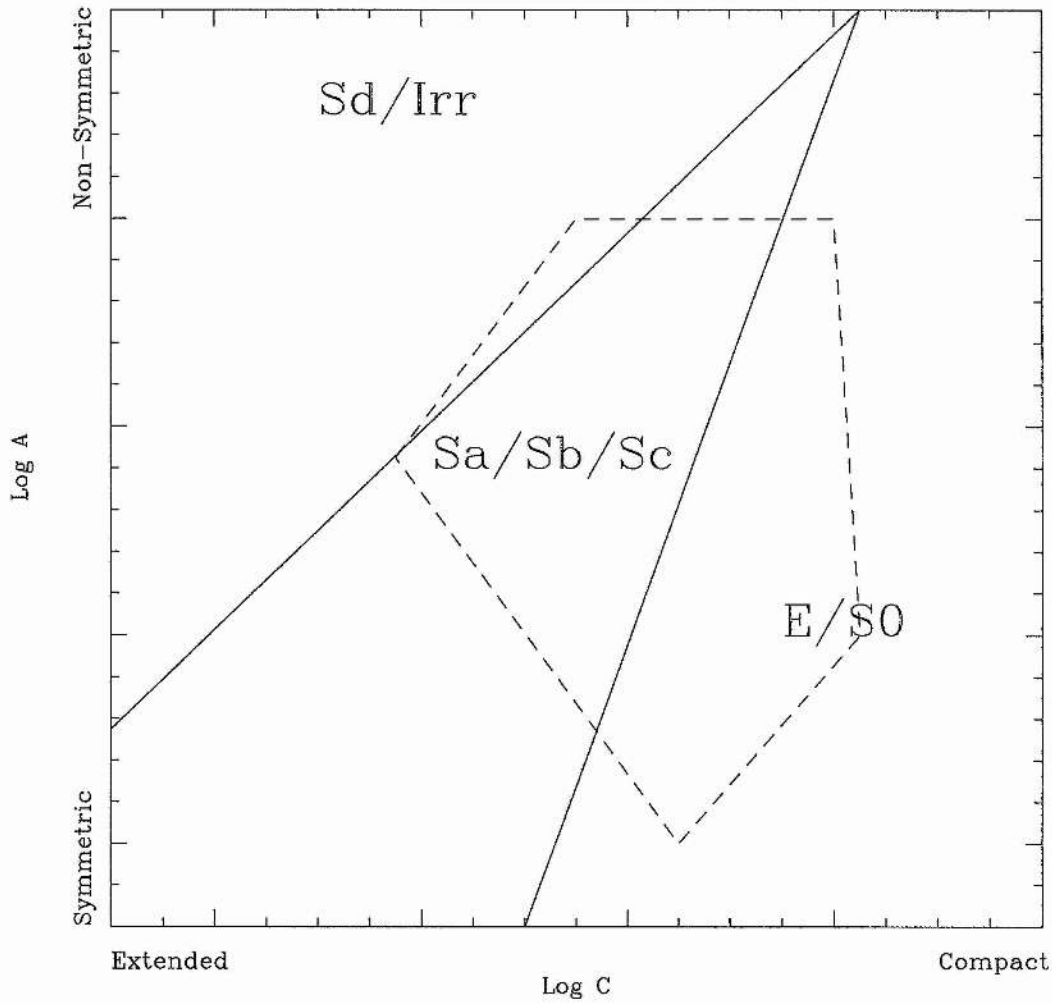

Figure 1.6: A schematic of the C-A system with the locations occupied by the main Hubble types. The dashed line marks out the so-called galaxy hull, which theoretically encloses the parameter space occupied by non-evolving galaxies with T-types -5 to 6, Abraham et al. (1996).

$$J \propto M_D r_e V_c. \tag{1.6}$$

The third assumption is that the disk and halo specific angular momentum are proportional to each other, i.e. $\frac{J_D}{M_D} \propto \frac{J_{tot}}{M_{tot}}$. From this follows the next assumption, that the ratio of baryonic to dark matter is constant and the fraction of baryonic matter that ends up in the disk is universal, so that $M_D \propto M_{tot}$. These assumptions combine with Eqn. 1.4 to give

$$\lambda \propto \frac{V_c^2 r_e}{M_D}. \tag{1.7}$$

Using this with the previously mentioned mass-luminosity power law and the observed Tully-Fisher relation, $L \propto V_c^{\epsilon}$ (Tully & Fisher 1977, where $\epsilon \sim 3.$), we get the spin parameter, and therefore angular momentum, as a function r_e and L, which relate to surface brightness

$$\lambda \propto r_e L^{(2/\epsilon)-\gamma}. \tag{1.8}$$

Eqn. 1.8 simply states that for two galaxies with the same luminosity (and therefore mass) but different angular momentum, the galaxy with the higher angular momentum the light is distributed over a larger radius and so its surface brightness decreases.

Fig. 1.7 shows a schematic of a BBD with the locations occupied by the various Hubble types and Fig. 1.8 shows a composite BBD comprised of real B-band data. Fig. 2.21 showes a BBD for the full MGC-BRIGHT data set. Cross (2002) showed that, while the BBD is a theoretically useful tool for understanding galaxy evolution, it is of the upmost importance that they are properly corrected for surface brightness selection effects. They also show that low surface brightness galaxies are few in number and do not substantially contribute to the luminosity density of the universe. See Cross (2002), Cross et al. (2001) and Cross & Driver (2002) for a detailed discussion on BBDs. Again, as with the C-A system, the BBD classifications remove any subjectivity. However, whilst the BBD may constrain the galaxy population as a whole, it usefulness as a morphological tool is in doubt. Cross (2002) find that while "Elliptical galaxies do not have a strong correlation, but have a sharp edge at the bright, high surface brightness end." and that "...spiral galaxies have a strong correlation between M and μ_e..." but that "This does not change significantly from early type spirals to late type spirals." This suggests that the BBD may not be able to accurately distinguish between the Irregular and Spiral galaxy populations. This scatter between the Sabc and Sd/Irr class boundaries may be reduced by adding a third axis to the BBD and forming a Trivariate Brightness Distribution or TBD, see § C.2.

1.4.5 Light Profiles

This will be discussed in more detail below, see § 5.1.3. Essentially there is a generic formula, the Sersic profile, that can be used to describe the light profile of any galaxy type:

$$I(r) = I_0 exp\left(-\left(\frac{r}{r_0}\right)^{1/\beta}\right) \tag{1.9}$$

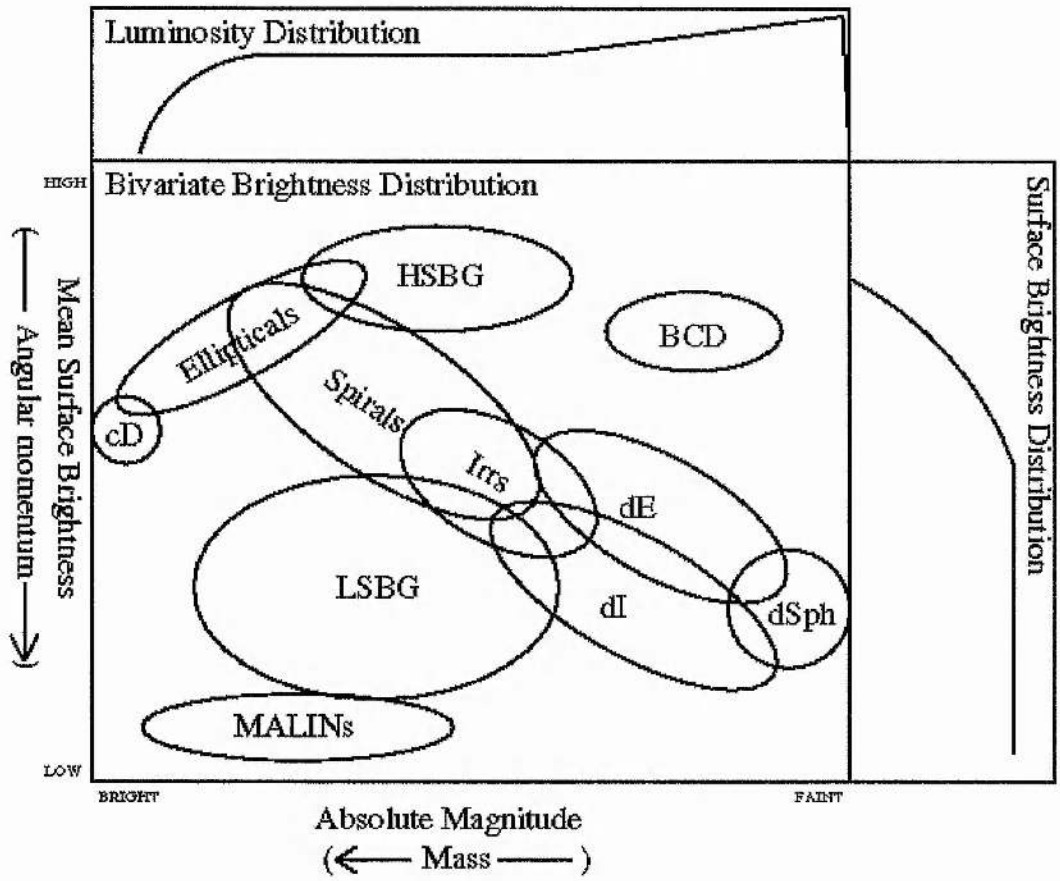

Figure 1.7: A schematic of a BBD with the locations occupied by the various Hubble types. This figure is taken from Driver & Cross (2000).

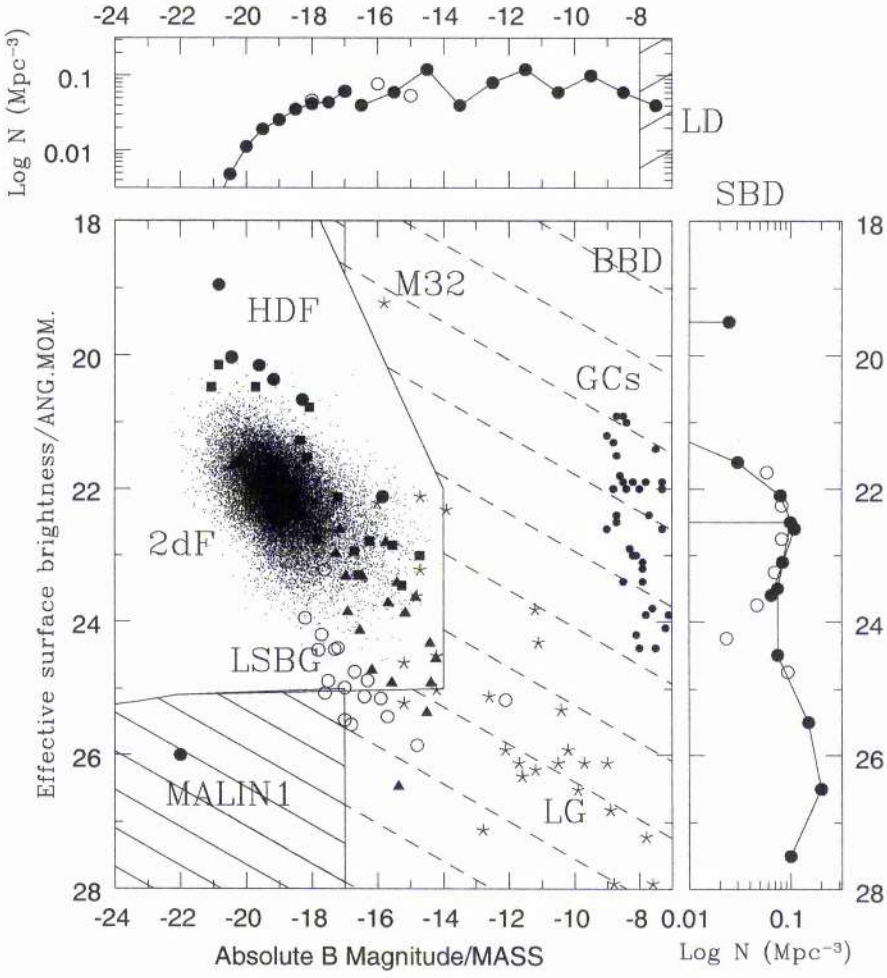

Figure 1.8: A B-band BBD containing data from various sources, most notably the Two-degree Field Galaxy Redshift Survey (2dFGRS, Cross et al. 2001), the Hubble Deep Field (HDF, Driver 1999) and the Local Group (LG, Mateo 1998). This figure is taken from Driver & Cross (2000).

Here I(r) is the intensity at radius r, I_0 is the central intensity, and r_0 is the scale length. The parameter β controls the curvature of the profile. Traditionally it is found that for a pure disk system a flat (β=1, Freeman 1970) profile provides the best description, where as for an Elliptical a negative curvature (or convex) (β=4, de Vaucouleurs 1959) profile best fits the light distribution. One can then assign a morphology to a galaxy based on the curvature parameter, β, of its light profile.

For the MGC we will be using a package called Galaxy IMage-2D (GIM2D). This uses a Metropolis algorithm to fit a an exponential disk and a de Vaucoulers profile to each galaxy (Marleau & Simard 1998). GIM2D is described in detail in Chapter 5. The galaxies morphology is in theory determined by applying cuts in the bulge-to-total light ratio which is known to be correlated with Hubble type, Kent (1985). The advantage of this method is that it goes some way to remove the subjectivity of classification. However, there may still be some disagreement between authors on the exact placement of the class boundaries.

In profiling we have a classification that is not subjective and if combined with redshift information, like the BBD, tells us something about the physical properties of the galaxies. However, profiling is a delicate business and is not only dependent on the getting an accurate model of the PSF for each observation but also requires accurate background measurements if the outer disk is to be well profiled. Depending on the algorithms involved used to derive the profile, this can be time consuming process in *some* cases. The main question over the profiling technique is, as is assumed, are *all* the galaxies profiles well modeled by a pure exponential plus $\beta > 1$ Sersic combination? This is addressed in Chapter 5.

1.5 Summary

In this thesis we investigate the problems of galaxy classification within a single, well-defined data set that is reasonably deep and yet has a large enough solid angle to provide accurate and statistically significant galaxy counts over the crucial normalisation range. Fig. 1.9 shows a number of imaging surveys in terms of their sky coverage and magnitude range. Dashed and solid lines indicate photographic and CCD based surveys respectively. Typically the faint surveys are CCD based while the local surveys are photographic (with the notable and recent exception of the SDSS-EDR, Stoughton et al. 2002). While the CCDs surveys make significant improvements in surface brightness and magnitude limits their sky coverage is small. It is only very recently that large CCD mosaics such as the Wide Field Camera (WFC, Irwin & Lewis 2001) and the SDSS instrument (Gunn et al. 1998) have been constructed that now allow a large area of sky to be surveyed within a realistic time frame.

The lay out of this thesis is a follows: In Chapter 2 we provide a detailed description of the data set. We describe how the data was collected and reduced as well as detailing the photometric and astrometric accuracies of the MGC and star-galaxy separation. We put the data to its first use in Chapter 3 by using star counts to derive structural properties of the Galaxy, namely the Galactic halo axial ratio, and discuss the clustering of stars in the Galaxy. In Chapter 4 we obtain galaxy number counts and use them to constrain the general Schechter function parameters. Chapter 5 discusses in detail how we obtain galaxy profiles, and hence morphologies, using GIM2D. In Chapter 6 we look at the physical properties of galaxies and discuss the morphological LFs. Our conclusions are given in Chapter 7.

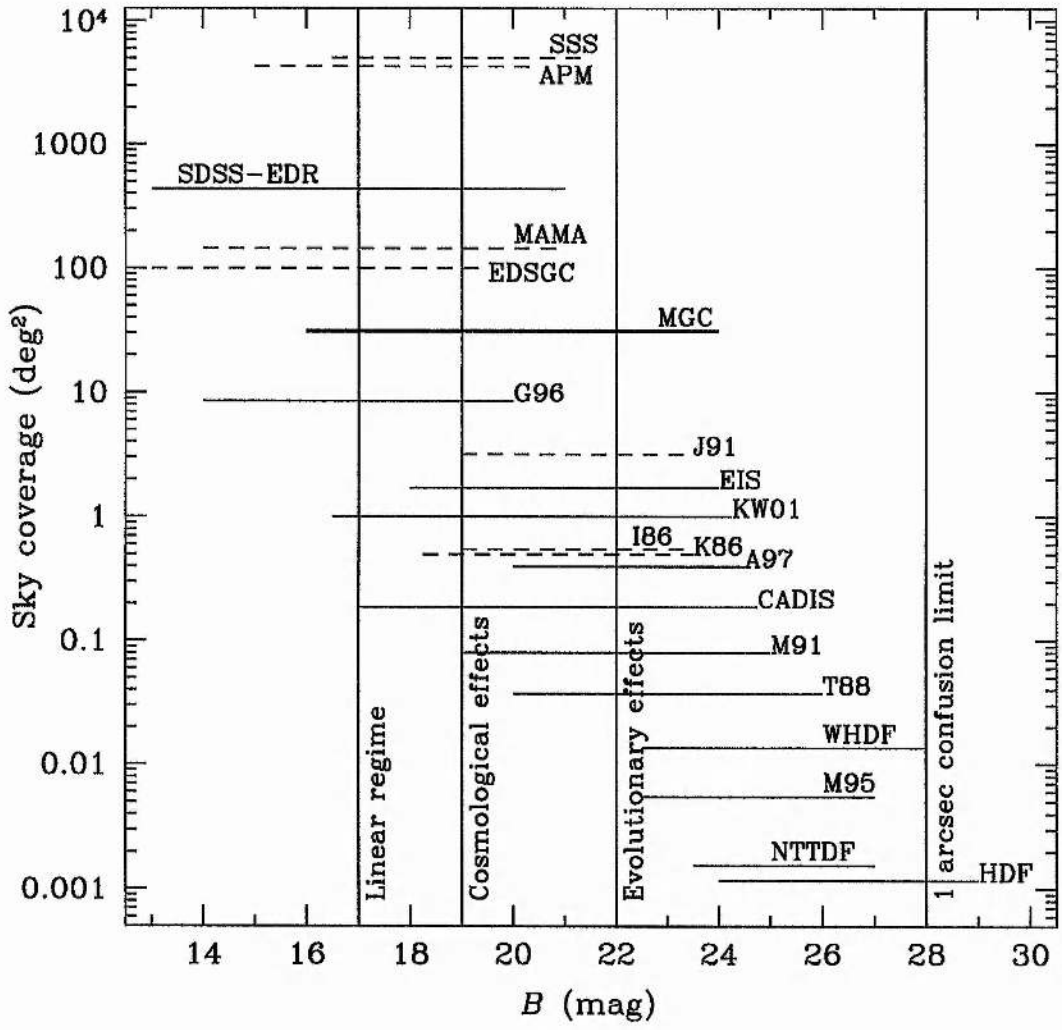

Figure 1.9: The magnitude ranges and survey areas spanned by some previous number count publications. Surveys based on photographic material are shown with a dashed line. The vertical lines show various transition regions where various effects start to dominate the galaxy counts. Key: SSS (Hambly, Irwin & MacGillivray 2001), APM (Maddox et al. 1990), SDSS-EDR (Yasuda et al. 2001), MAMA (Bertin & Dennefield 1997), EDSGC (Heydon-Dumbleton, Collins & MacGillivary 1989), MGC (this work), G96 (Gardner et al. 1996), J91 (Jones et al. 1991), EIS (Paradoni et al. 1999), KW01 (Kummel & Wagner 2001), I86 (Infante, Pritchet & Quintana 1986), K86 (Koo 1986), A97 (Arnouts et al. 1997), CADIS (Huang et al. 2001), M91 (Metcalfe et al. 1991), WHDF (Metcalfe et al. 2001), T88 (Tyson 1988), NTTDF (Arnouts et al. 1999), M95 (Metcalfe et al. 1995), HDF (Williams et al. 1996).

CHAPTER 2

The Millennium Galaxy Catalogue

Here we describe the data set, known as The Millennium Galaxy Catalogue (MGC), that will be used through out this thesis.

We describe what instruments and filters were used to make the observations as well as fundamental data properties such as the exposure time, seeing and the RA and DEC range of the observations. The photometric and astrometric properties of the MGC are discussed with particular emphasis on gaining accurate zero points for each observation.

We detail how the MGC was generated and its division into two sub-catalogues, MGC-BRIGHT and MGC-FAINT. The detection of objects using SEXTRACTOR and their classification into, amongst other things, stars and galaxies.

The work in this chapter was performed jointly with Dr Jo Liske for presentation in a forthcoming paper, Liske et al. (2003).

2.1 The Data

2.1.1 The Wide Field Camera

All data frames were taken using the Wide Field Camera (WFC). The WFC is mounted at prime focus on the 2.5m Isaac Newton Telescope (INT) situated at La Palma. The WFC is a mosaic of four 4k×2k thinned EEV CCDs with a smaller 2k×2k Loral CCD which is used for auto-guiding. Each of the science CCDs measures 2048×4100 pixels with a pixel scale of 0.333 arcsec/pixel – this gives a total sky coverage of 0.29 deg^2 per pointing. The four science chips are arranged as shown in Fig. 2.1. Full details of the WFC are provided at http://www.ast.cam.ac.uk/~wfcsur/technical.html (see also Irwin & Lewis 1999).

2.1.2 The observations

The data, constituting the Millennium Galaxy Catalogue (MGC), comprises 144 overlapping pointings forming an equatorial strip from $10^{\rm h}00^{\rm m}$ to $14^{\rm h}48^{\rm m}$ (J2000). The observations were taken during 4 observing runs, 15–16 March 1999, 16–17 April 1999, 6–13 June 1999 and 26 March – 4 April 2000. Each pointing was observed for a single 750 s exposure through a Kitt Peak National Observatory B filter ($B_{\rm KPNO}$). Pointing 1 (Field 1) is centered on RA = $10^{\rm h}00^{\rm m}00^{\rm s}$, DEC = $00^o00'00''$ (J2000) and pointing 144 (field 144) is centered on RA = $14^{\rm h}46^{\rm m}00^{\rm s}$, DEC = $00^o00'00''$ (J2000). Hence each pointing is offset

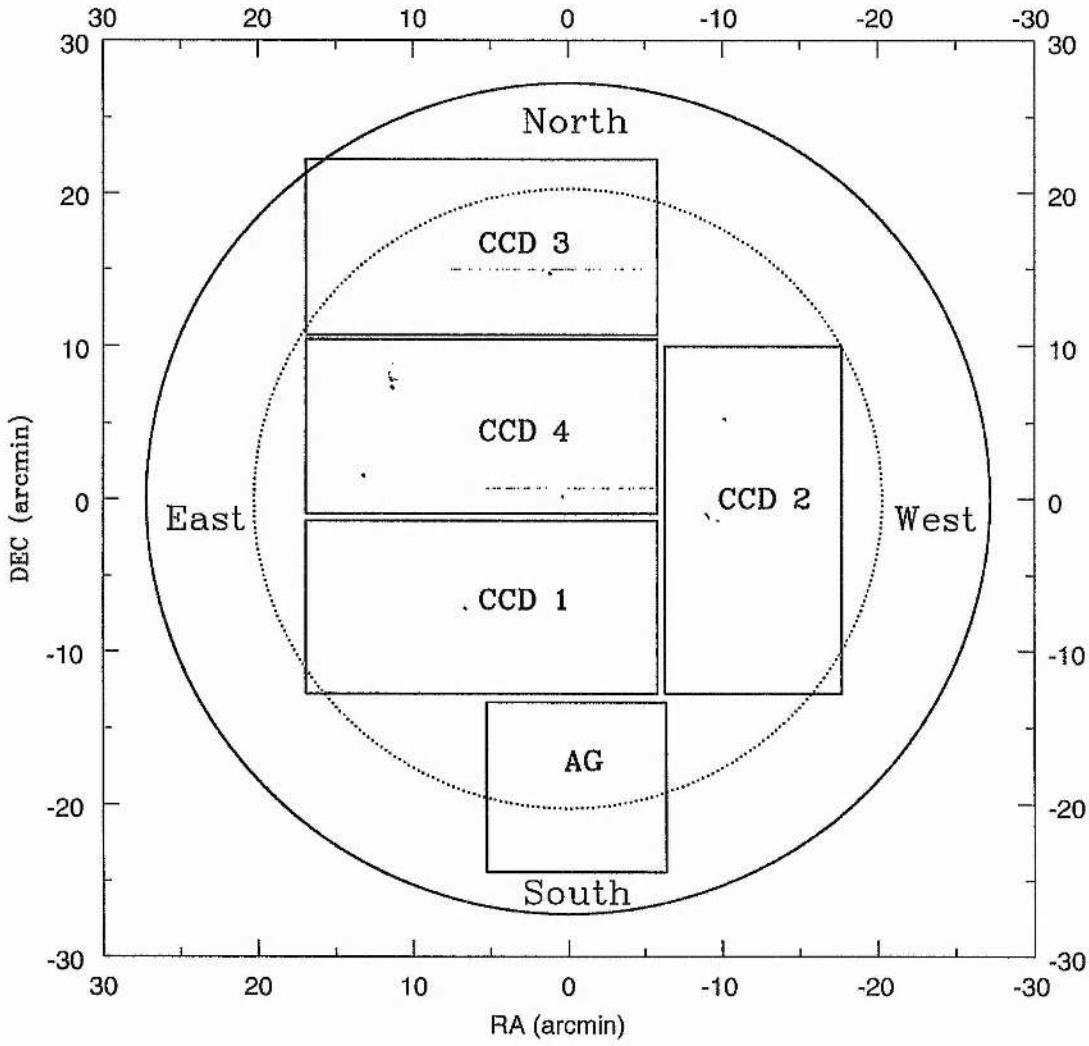

Figure 2.1: A schematic diagram of the wide field camera. The inner and outer circles denote the onset of vignetting and complete vignetting respectively. Also shown are the CCD defects.

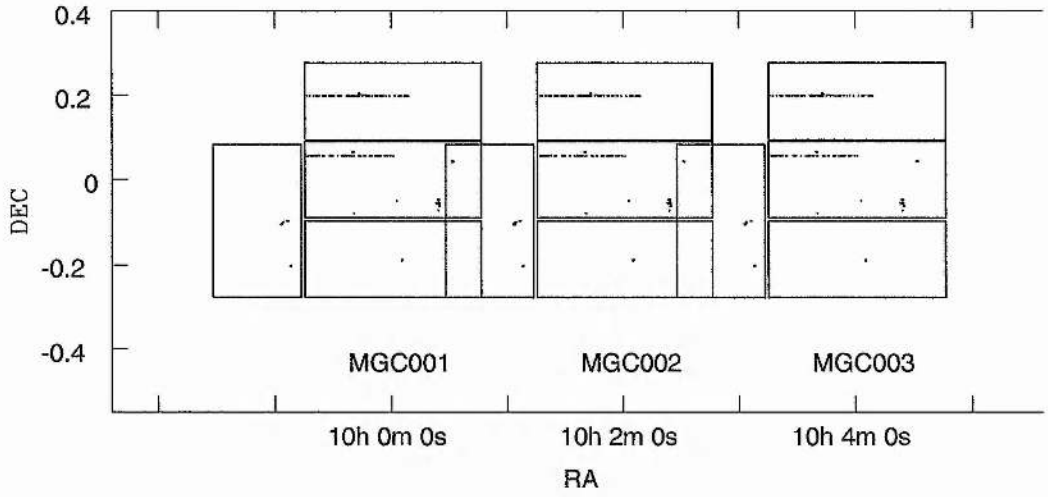

Figure 2.2: A schematic diagram of the pointing for MGC fields MGC001, MGC002 and MGC003. The dots indicate the positions of known CCD defects.

from the previous by 30 arcmin along the equatorial great circle. Fig. 2.2 shows the survey footprint for the first three pointings.

The survey region was chosen because it overlaps with both the Sloan Digital Sky Survey Early Data Release region (SDSS-EDR, York et al. 2000) and the Two Degree Field Galaxy Redshift Survey (2dFGRS, Colless et al. 2001) thus providing redshifts for the brighter galaxies ($B_{\rm MGC} \leq 19.1$) and colours for $B_{\rm MGC} \leq 20$. All observations were taken during dark or grey time through variable conditions. The seeing ranged from 0.9 arcsec to 2.0 arcsec with the median seeing at 1.3 arcsec. The air-masses range from 1.141 to 1.671. Fig. 2.3 shows a graphical summary of the general observing conditions across the survey.

As much of the data was collected during clear but non-photometric nights it was necessary to dedicate a single pristine photometric night (30 March 2000) to obtain suitable calibration data at various stages along the strip. In total 20 MGC fields were observed during the photometric night. Of these 6 were 100 s exposures since they had been observed previously. These observations were interspersed with 10 s observations of standard stars spanning a wide range in airmass. The standard stars where taken from the Landolt (1992) standard areas SA98, SA101, SA104 and SA107.

Retrospectively some science frames were later found to be of too poor a quality to be useful and these were re-observed. Each of the first eight fields was replaced with the mean of two 400 s exposures. Field 111 is a single 900 s exposure.

2.1.3 Data reduction and astrometry

All the preliminary data reduction – flat fielding, bias correction and astrometric calibration – was done by the Cambridge Astronomy Survey Unit (CASU) and full details of this process are provided in Irwin & Lewis (2001). Briefly, a number of bias frames are collected each night and the median is subtracted from the data. All data (including flat-fields) are corrected for a known non-linearity. A twilight flat-field is taken during evening and morning twilight (when possible) and a median flat-field derived for that particular run is divided into each data frame. After this process an initial astrometric

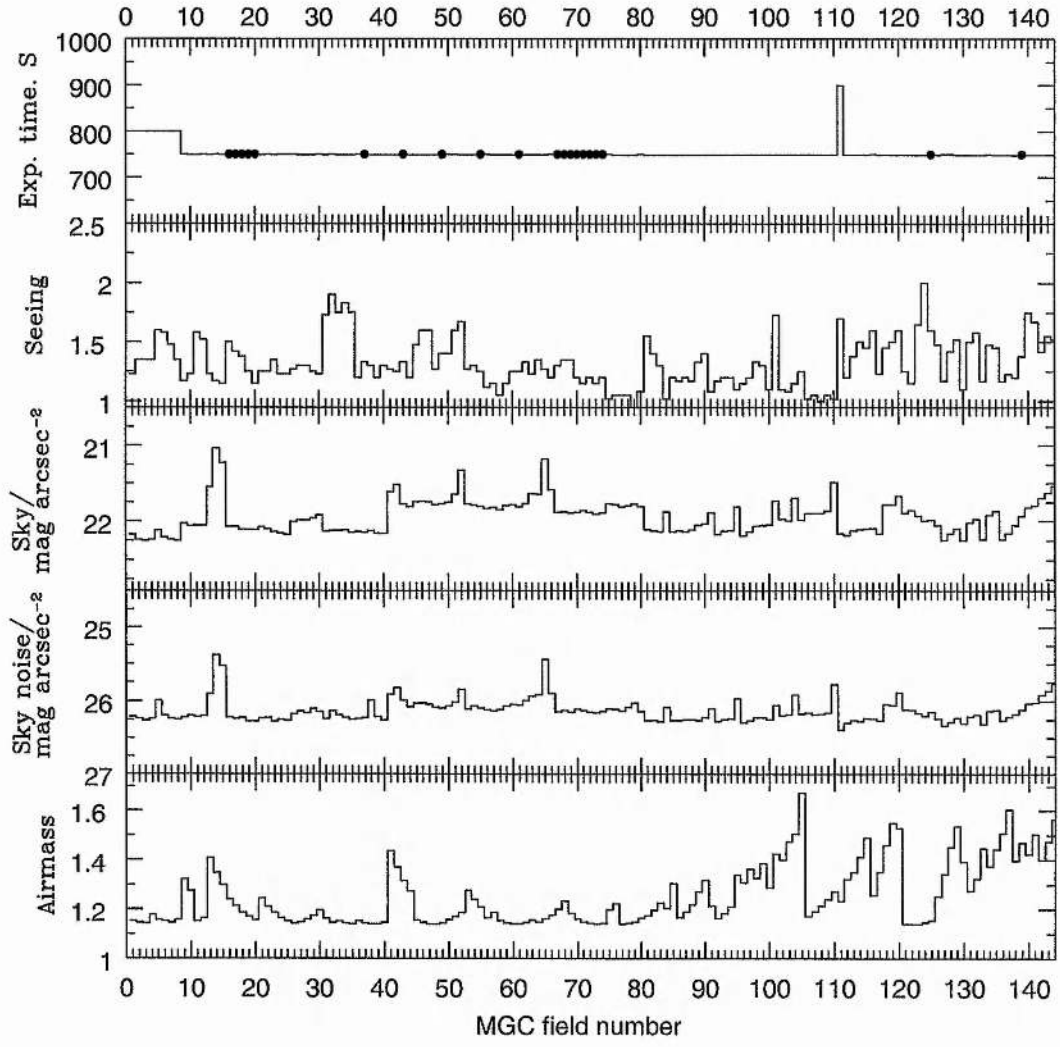

Figure 2.3: A pictorial summary of the data quality across the MGC survey strip. The dots indicate the location of the calibration fields.

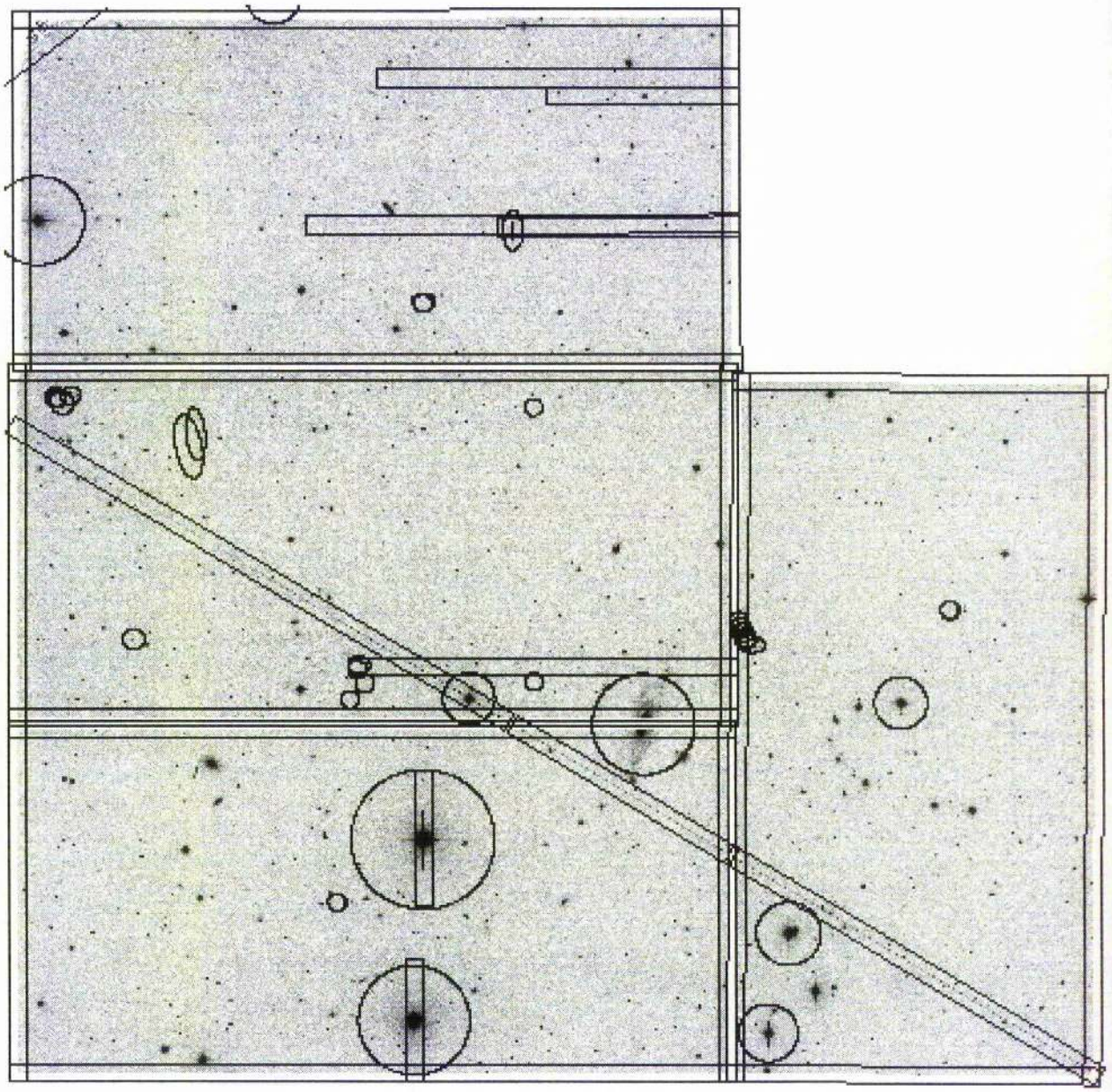

Figure 2.4: Field MGC036.

calibration is made to the HST Guide Star Catalogue. Finally the frames are matched to the Automated Plate Measuring Machine catalogue (i.e. the UK Schmidt Survey) which itself is calibrated onto the Tycho-2 astrometric system. Fig. 2.4 shows the final reduced image for one of our pointings, MGC036. This field was chosen as it illustrates problems with satellite trails and the CCD gaps.

To assess the final astrometric accuracy we examined objects in the overlap regions and compared their derived RAs and DECs. The overlap regions are of size ~ 0.03 deg^2 and contain ~ 1000 objects each. Fig. 2.5 shows the median positional differences for these objects for each overlap region. From Fig. 2.5 we find that the astrometry is accurate to $\pm$ 0.08 arcsec in both RA and DEC.

2.2 Calibration

As mentioned previously, four Landolt standard star fields were observed at a range of airmasses throughout the course of the photometric night. For each observation of each standard star we computed a zero point

$$ZP_{\rm std} = m_B + 2.5 \log f, \tag{2.1}$$

where m_B was taken from Landolt (1992) and f is the flux of the star as measured from the data. We then fitted these zero points with a double linear function in airmass (sec Z), and colour:

$$ZP_{\rm std} = a + a_{\rm am}\, {\rm sec}Z + a_{B-V}(B-V). \tag{2.2}$$

In Fig. 2.6 we show the data and the fit. The residuals have an rms of 0.02 mag and show no obvious trend with airmass, colour, m_B or date of observations.

For each MGC field we then computed a theoretical zero point $ZP_{\rm th} = a + a_{\rm am}\,{\rm sec}Z$, which is expected to be correct only for those fields observed during the photometric night. We extracted objects as described in §2.3 and identified duplicate detections in regions where any two images overlapped. Using only objects with $17 < m < 21$ and, STELLARICITY > 0.5 we computed for each overlap region, the median of the magnitude differences of the double detections, $\langle \Delta m \rangle$, as well as an error on the median, $\sigma_{\langle \Delta m \rangle}$. In Fig. 2.7(a) we show $\langle \Delta m \rangle$ for all the overlap regions using the initial, theoretical zero points.

A linear least-squares routine was then used to adjust the zero points of the non-photometric fields in order to minimize the quantity

$$\chi^2 = \sum \left(\frac{\langle \Delta m \rangle}{\sigma_{\langle \Delta m \rangle}} \right)^2 \tag{2.3}$$

where the sum goes over all overlap regions. The process of object extraction, matching and zero point adjustment was then repeated until a stable solution was reached (four iterations).

Since the zero points of the photometric fields are held fixed at their theoretical values, the above procedure assumes that the observing conditions were perfectly stable throughout the photometric night. One can derive an estimate of the real-life error on the photometric zero points, $\sigma_{\rm ZP}$, by comparing the scatter of $\langle \Delta m \rangle$ with $\sigma_{\langle \Delta m \rangle}$ for those

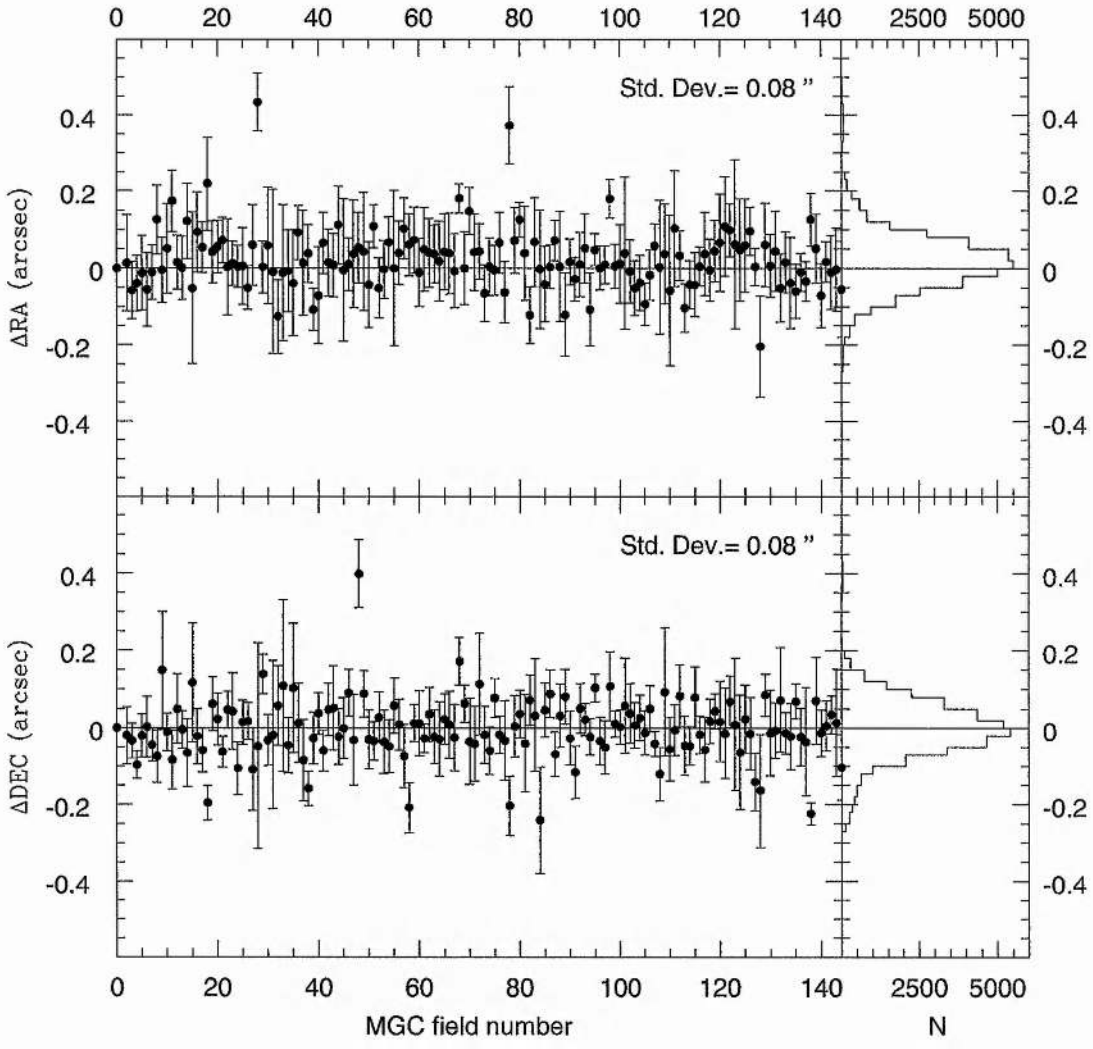

Figure 2.5: Upper panel: Median RA differences for each MGC overlap region. Lower panel: median DEC differences. The errors are the half-width half-maximum seeing for the overlap divided by the square root of the number of objects.

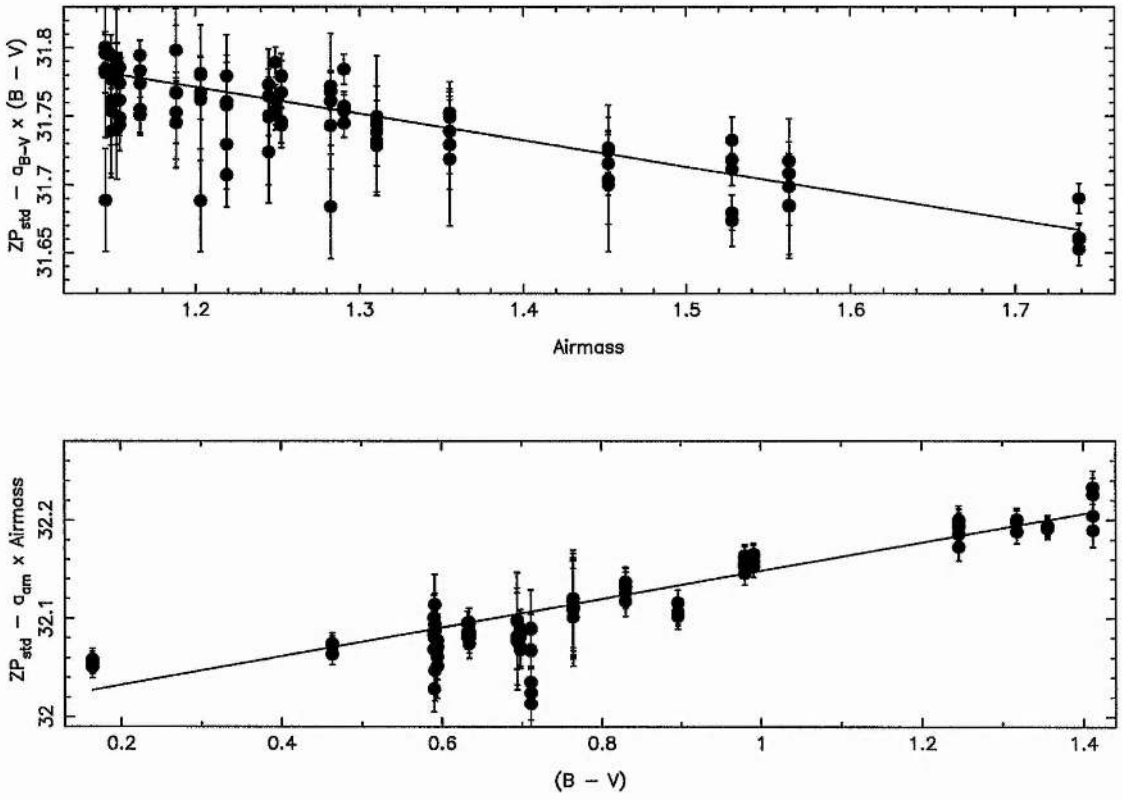

Figure 2.6: Upper panel: Colour corrected zero points versus airmass. Lower panel: Airmass corrected zero points versus colour. The solid lines show the best fit (cf. equation 2.2). The error bars include contributions from photon counting, sky subtraction, read-out noise and the uncertainty in m_B. A further systematic error of 0.01 mag (added in quadrature) was needed to achieve an acceptable fit.

overlap regions that only involve photometric fields. We found $\sigma_{\rm ZP} = 0.005$. Thus we modified the above calibration procedure by including the zero points of the photometric fields in the parameters to be fit and adding the additional constraints that they must lie 'close' to their theoretical values. In other words we now minimize the quantity

$$\chi^2 = \sum_{\rm all} \left(\frac{\langle \Delta m \rangle}{\sigma_{\langle \Delta m \rangle}} \right)^2 + \sum_{\rm phot} \left(\frac{ZP - ZP_{\rm th}}{\sigma_{ZP}} \right)^2, \tag{2.4}$$

where the first sum again runs over all overlap regions and the second sum runs over all photometric fields. In Fig. 2.7(c) we show $\langle \Delta m \rangle$ for all the overlap regions using the final zero points. Fig. 2.7(d) shows the histogram of the individual Δm values. The width of this distribution indicates an internal photometric accuracy of < 0.03 mag. The noticeable dip at around field MGC080 in Fig. 2.7 c is due to a lack of calibration fields beyond this point, see Fig. 2.3.

Given the above calibration process the relationship between an object's magnitude as given in the MGC and its Landolt $m_{\rm B}$ magnitude is given by:

$$B_{\rm MGC} = m_{\rm B} - 0.1447(B - V). \tag{2.5}$$

2.3 Object detection and photometry

Object detection was performed using **Extractor**, which is the STARLINK adapted[1] version of SEXTRACTOR developed by Bertin & Arnouts (1996) & Bertin (2002).

2.3.1 Background estimation

The SEXTRACTOR code initially derives a background map. This is achieved by first defining a grid over each CCD and then passing a median filter (set to a size of 7×7) over each pixel within the grid-box. The local sky within this region is then taken as the median of these points. Finally a background map is constructed via a bi-cubic spline interpolation over these points. The size of the mesh and other controlling parameters are determined by values stored in a default file. Here we opted for the largest possible mesh size (256×256) to minimise the smoothing out of any extended low surface brightness features.

2.3.2 Object detection and deblending

SEXTRACTOR uses a multi-thresholding algorithm for the detection and deblending of objects. The SEXTRACTOR code identifies regions with some minimum number of connected pixels (10 in the case of th MGC) that are above a user determined brightness threshold

[1]Note that the STARLINK version has additional data handling routines, the STARLINK World Coordinate system software and a graphical interface. In all other aspects the code is identical to that developed and described in Bertin & Arnouts (1996), thus henceforth we refer to SEXTRACTOR in the text.

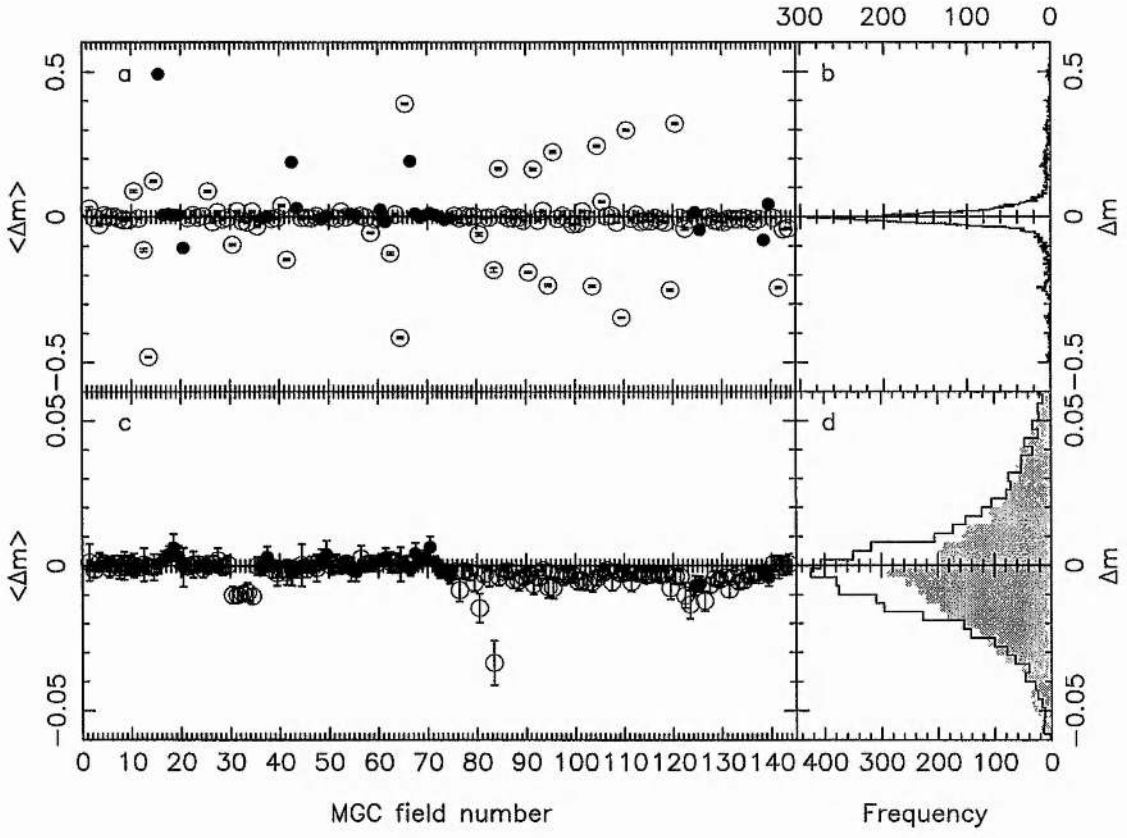

Figure 2.7: (a) Median magnitude differences of doubly detected objects in overlap regions, using initial zero points given by equation (2.2). Solid points indicate overlap regions involving at least one photometric observation. The error bars are 68 per cent ranges divided by the square root of the number of objects (on average 35). (b) Frequency distribution of all of the individual Δm values. (c) Same as (a) using the final zero points. Note that the scale of the $\langle \Delta m \rangle$-axis is expanded by a factor of 10 compared with (a). (d) The solid line shows the frequency distribution of the individual Δm values using the final zero points. This distribution has a mean of -6.4×10^{-5} and an rms of 0.023. For comparison, the shaded histogram is the same as that shown in (b).

($\mu_{lim} = 26$ mag/arcsec^2). Once an object has been detected it is then re-thresholded at n (30 here) levels, exponentially spaced between the peak value and the detection threshold. SEXTRACTOR then starts at the top and works its way down at each level deciding whether it should pull out two or more objects. SEXTRACTOR makes this decision based on two criteria: i) Is the integrated pixel intensity greater than a certain fraction of the whole object's total intensity and ii) can this first condition be repeated for one or more parts of the object at the same level. Only if these two criteria are confirmed will the object be split up. This multi-thresholding is ideally suited for galaxy extraction as at no point has any assumption about the object's shape been made (Bertin & Arnouts 1996).

2.3.3 Photometry

The photometry was performed using SEXTRACTOR with a constant limiting analysis isophote of 26 mag/arcsec^2 to provide a uniformly processed catalogue. Among the object parameters, given by SEXTRACTOR, are four different types of magnitude: an adaptive aperture magnitude (KRON); an isophotal magnitude (ISO); a corrected isophotal magnitude (ISOCOR) and a best magnitude (BEST). KRON magnitudes (i.e., elliptical apertures of 2.5 Kron Radii, see Kron 1980) are known to underestimate the fluxes in perfect exponential profiles by 0.04 mag and in de Vaucouleur profiles by 0.10 mag, nevertheless they have been shown to be the most robust to variations in redshift, bulge-to-disk ratio, the isophotal limit and the seeing (see Cross 2002). The ISOCOR magnitude is calculated by assuming the profiles of faint objects are Gaussian. The fraction of the flux within a particular isophote to the total flux is calculated and converted to a magnitude, this is then added to the normal isophotal magnitude to give a corrected isophotal magnitude, see Bertin & Arnouts (1996) and references therein for details. The BEST magnitude is taken to be the KRON magnitude except in crowded regions where the ISOCOR magnitude is used (the criterion hardwired into SEXTRACTOR is if an object's neighbour is calculated to bias the KRON magnitude by more than 0.1 mag). All objects are individually corrected for Galactic extinction using the dust extinction maps provided by Schlegel & Finkbeiner (1998) and adopting $A_{B_{\rm KPNO}} = 4.23$:

$$m_{\rm DC} = m_{\rm BEST/ISO/ISOCOR/KRON} - A_{\rm B_{KPNO}} E(B-V). \tag{2.6}$$

where E(B – V) is derived from the Schlegel & Finkbeiner (1998) maps and $m_{\rm DC}$ is the dust corrected magnitude. Figs. 2.8 to 2.16 show a random selection of galaxies with apparent (dust corrected) BEST magnitudes in the range $16.0 < B_{\rm MGC} < 20.0$ in 0.5 mag intervals. Each galaxy is labeled with its MGC catalogue number (top), magnitude (top-left) and surface brightness (top-right). In each figure the galaxies are arranged in order of decreasing surface brightness and are displayed between sky-1.5σ and 21.0 mags/sq arcsec. The postage stamps are 100×100 pixels (33.3×33.3 arcsec) with the galaxies centered at pixel coordinates (50,50).

2.3.4 Overlap regions

Due to the substantial overlap regions the catalogue contains many duplicate objects (c.f. Fig. 2.2). These were used in the previous section to bootstrap the photometry. For any pair of duplicate detections of the same object we now remove the detection closest to a CCD edge – in effect splitting the overlap regions in two and throwing away the outer most superfluous regions.

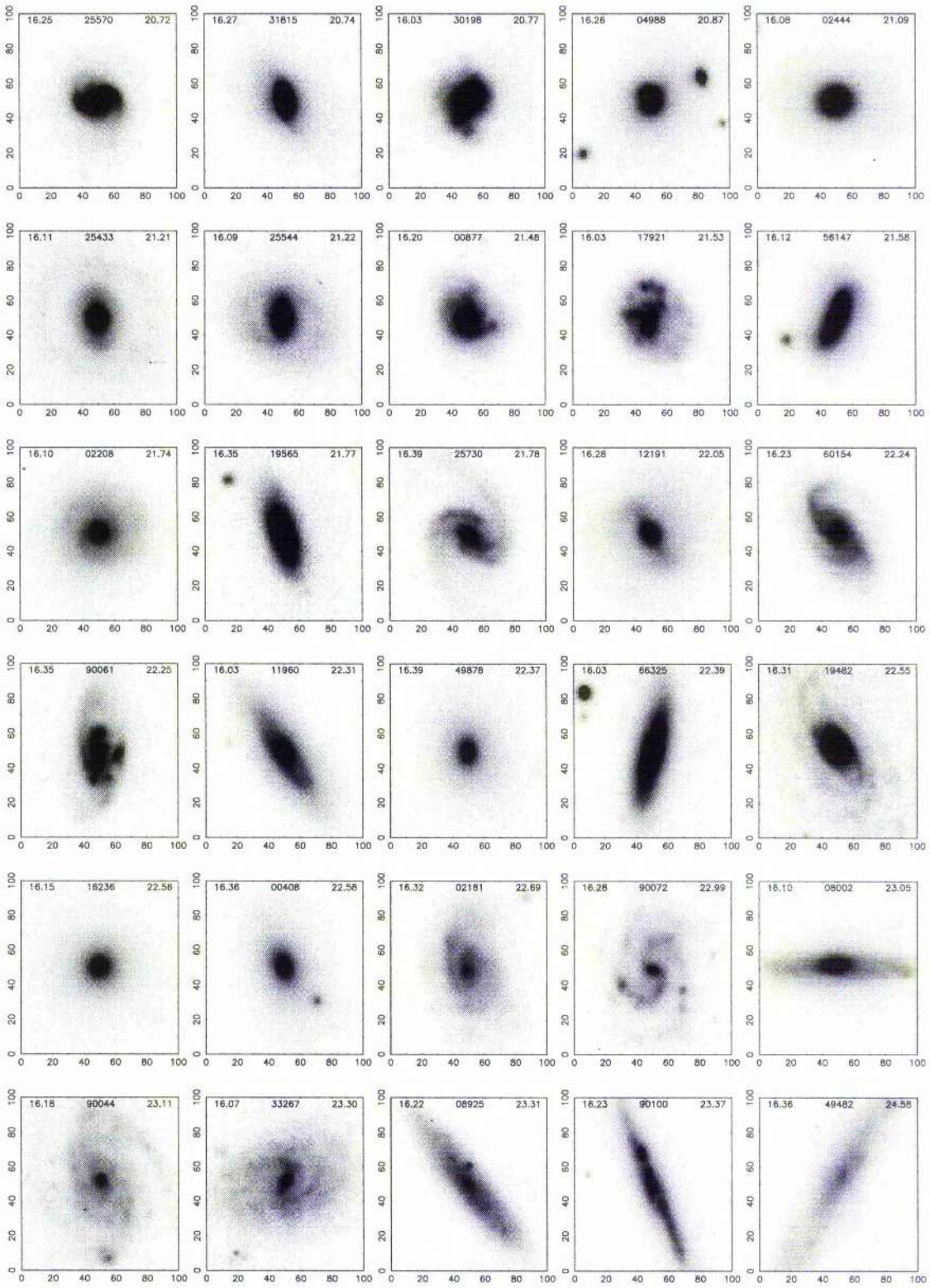

Figure 2.8: The galaxy population at $B_{\rm MGC} = 16.0$ mag.

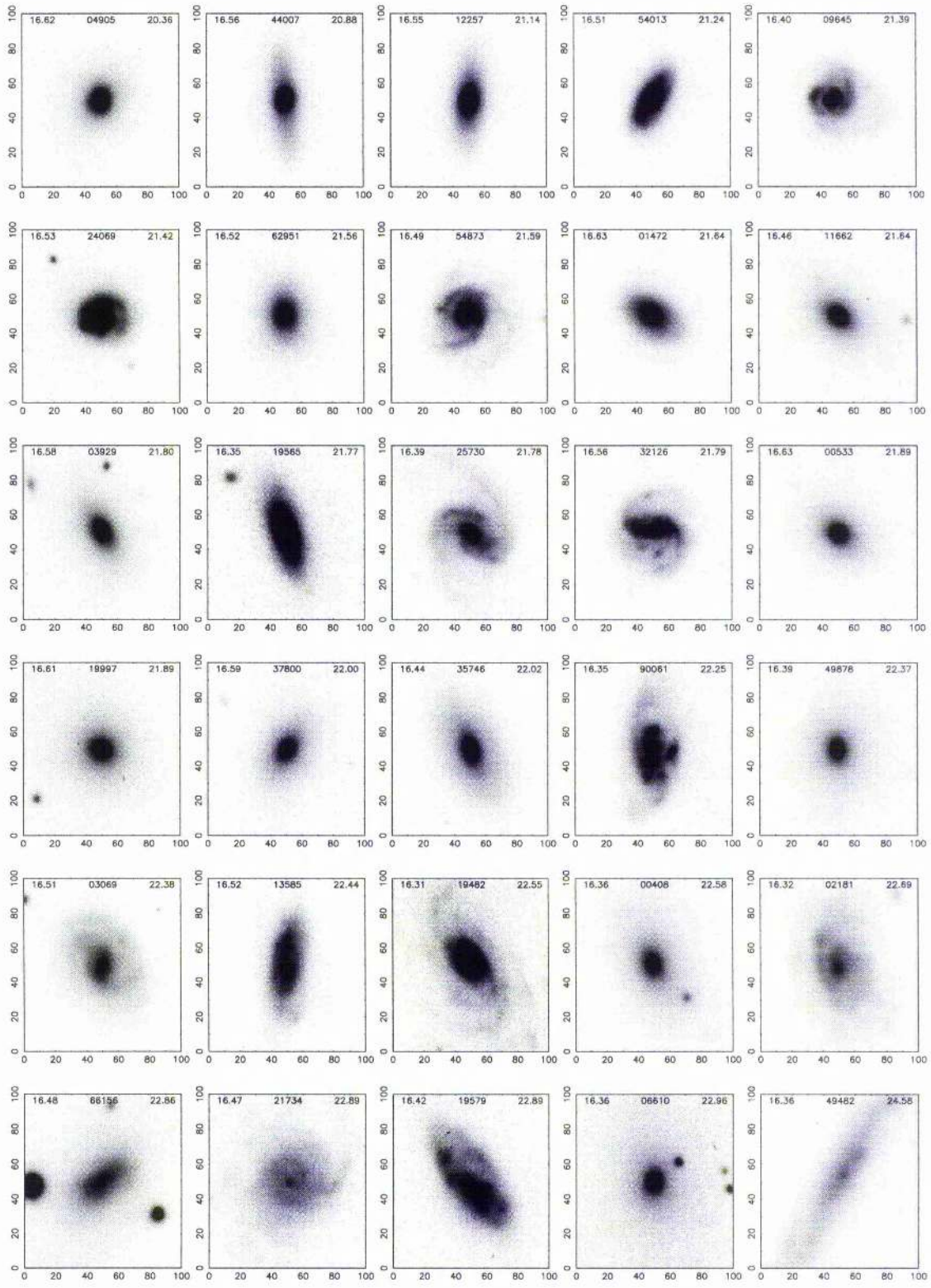

Figure 2.9: The galaxy population at $B_{\rm MGC} = 16.5$ mag.

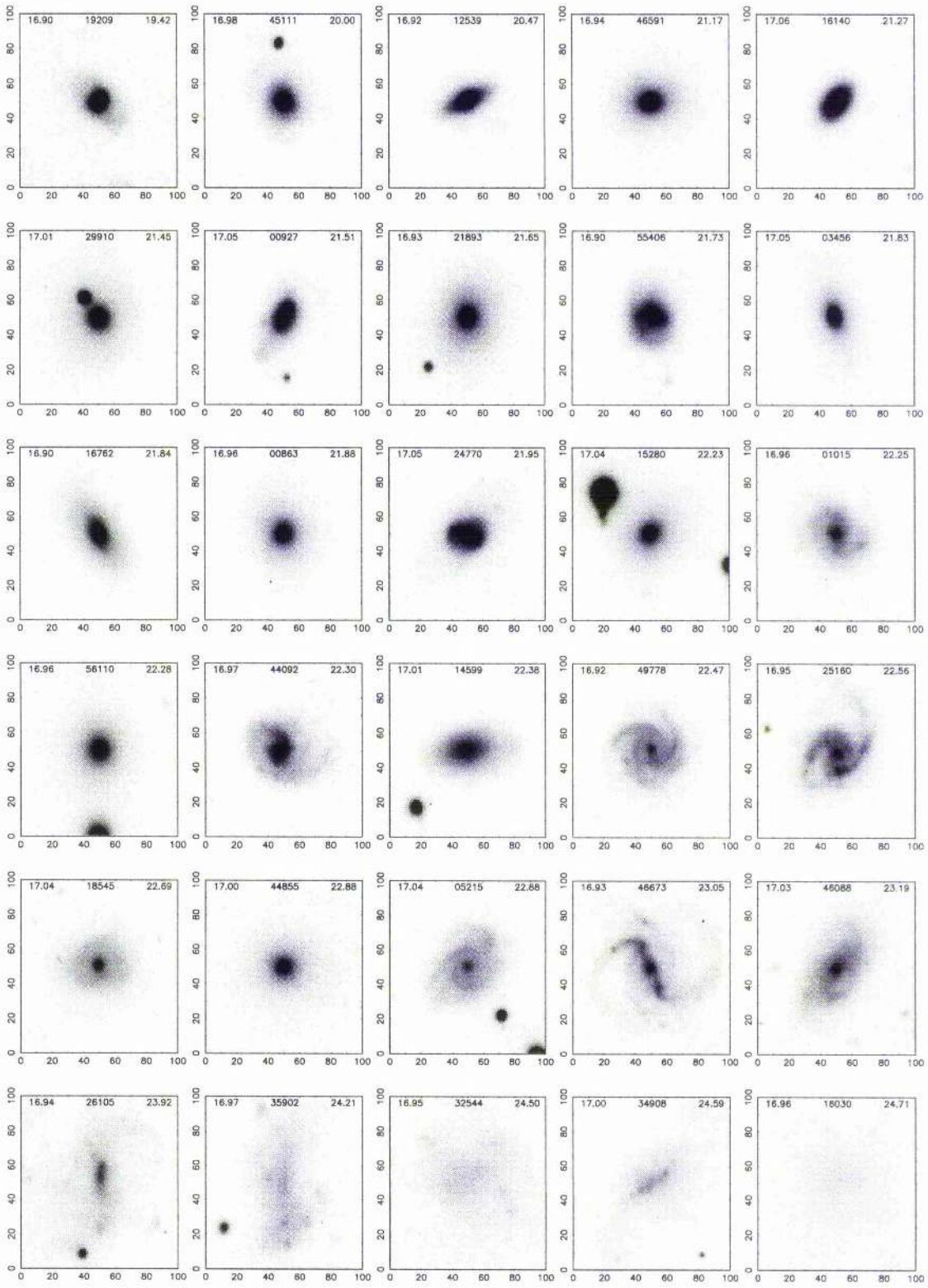

Figure 2.10: The galaxy population at $B_{\rm MGC} = 17.0$ mag.

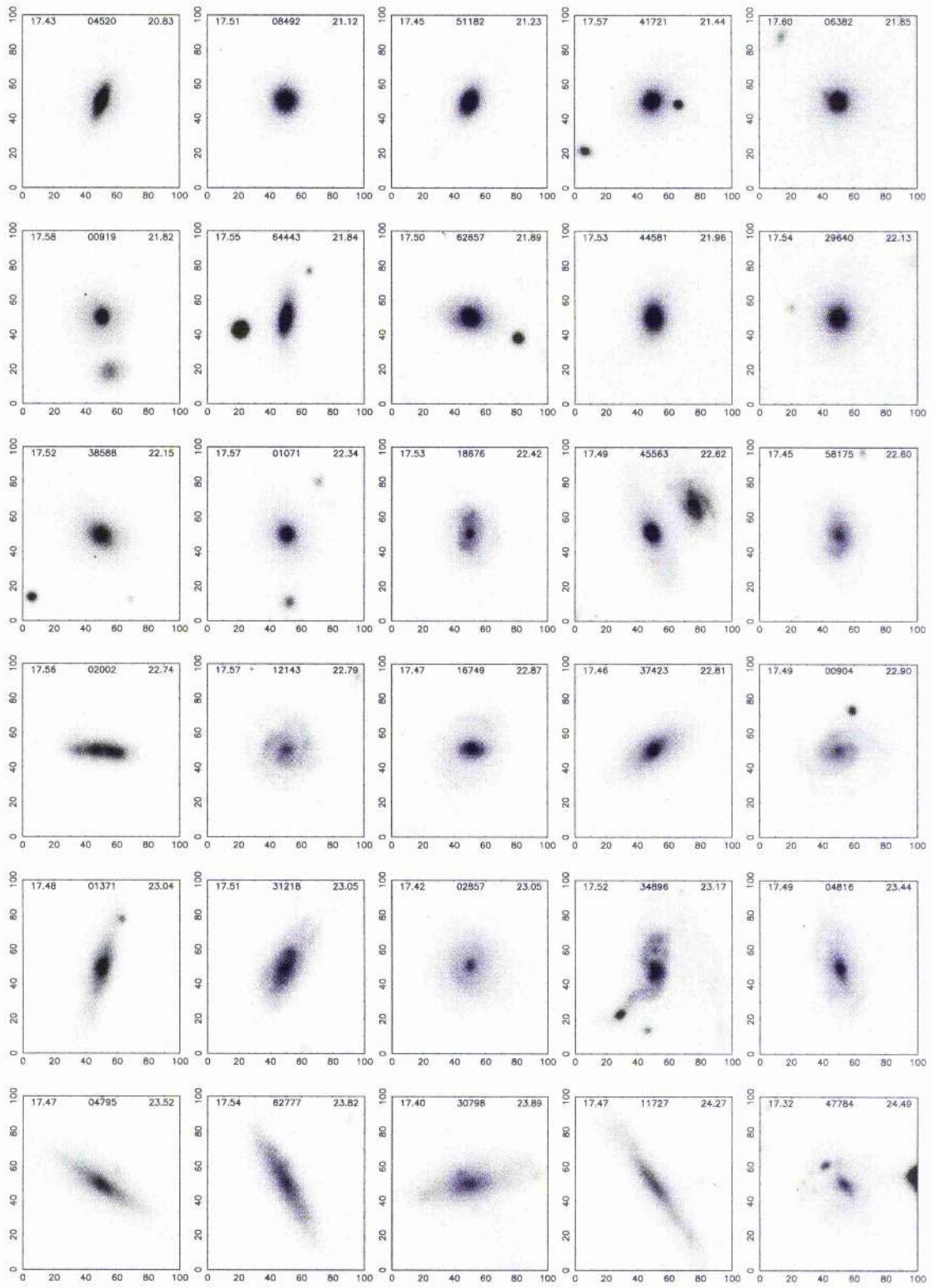

Figure 2.11: The galaxy population at $B_{\rm MGC} = 17.5$ mag.

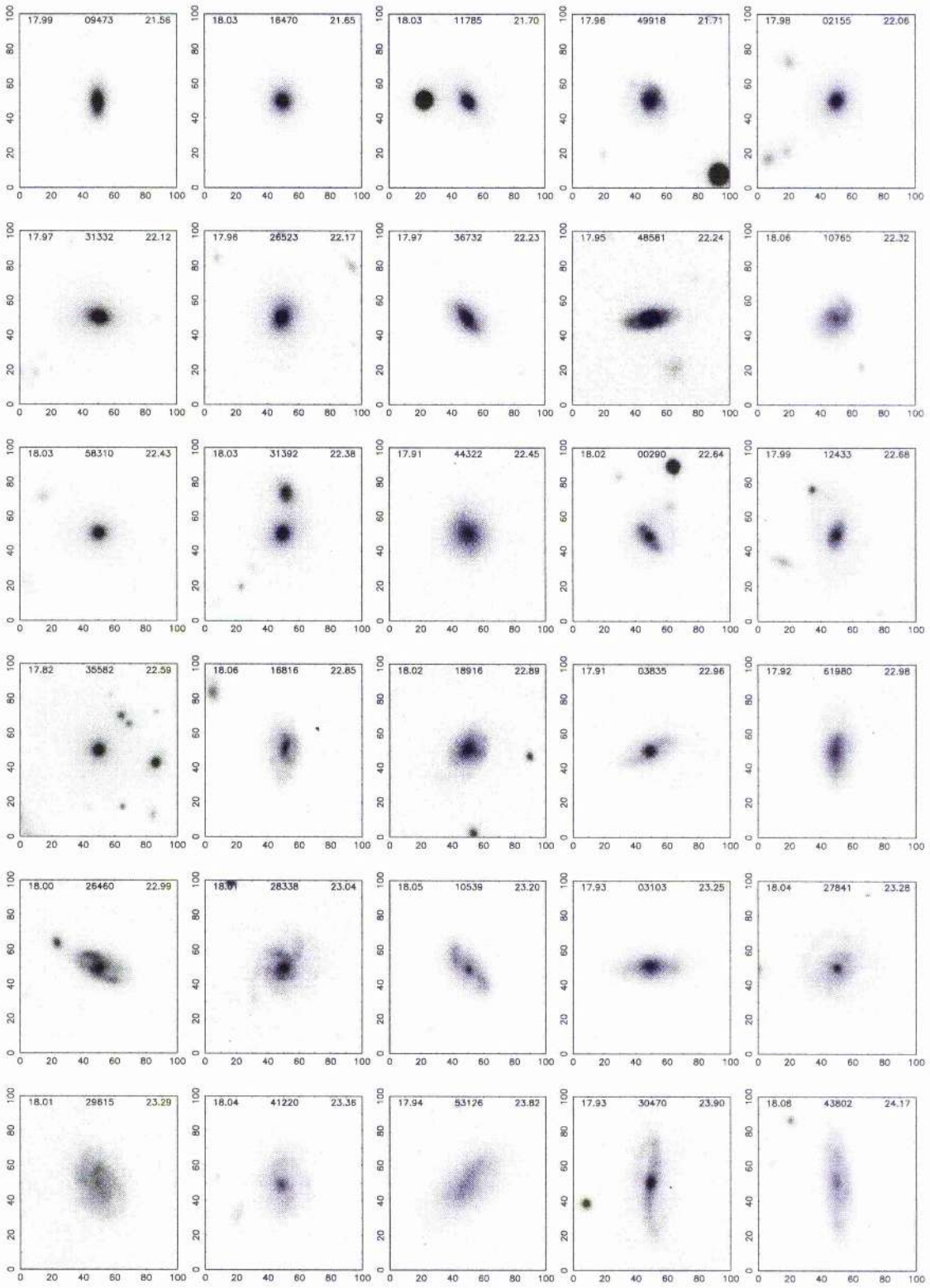

Figure 2.12: The galaxy population at $B_{\mathrm{MGC}} = 18.0$ mag.

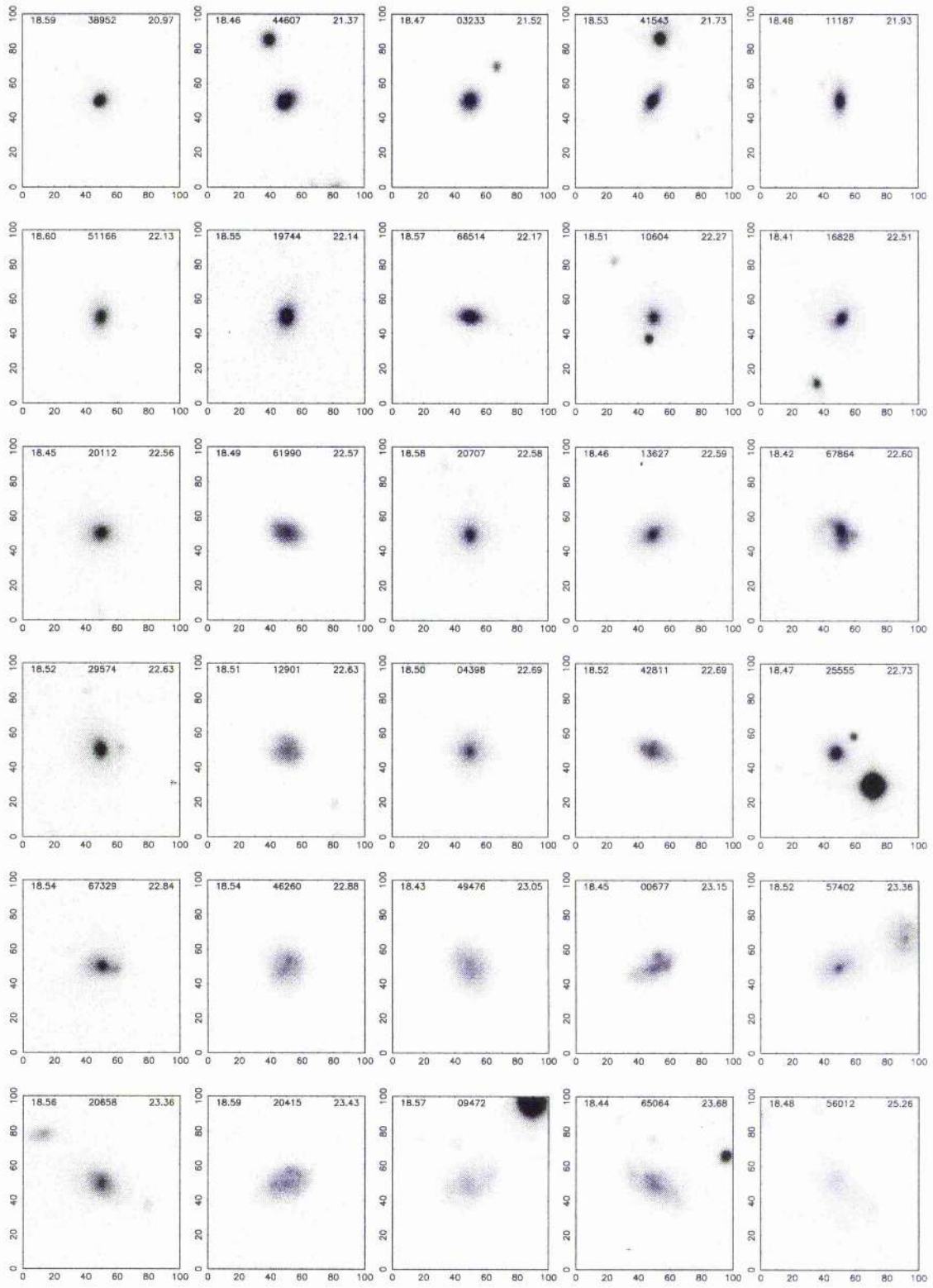

Figure 2.13: The galaxy population at $B_{\rm MGC} = 18.5$ mag.

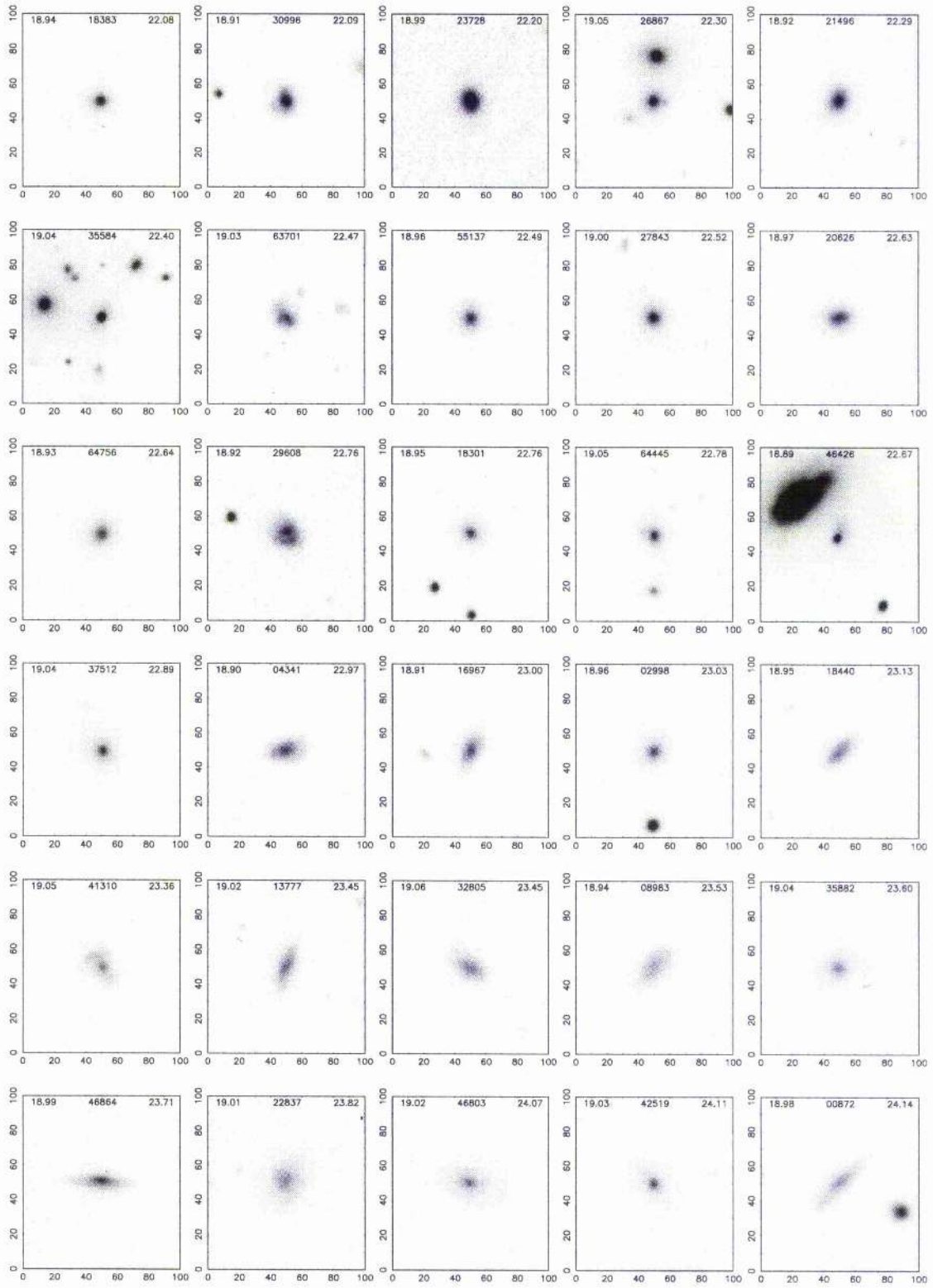

Figure 2.14: The galaxy population at $B_{\rm MGC} = 19.0$ mag.

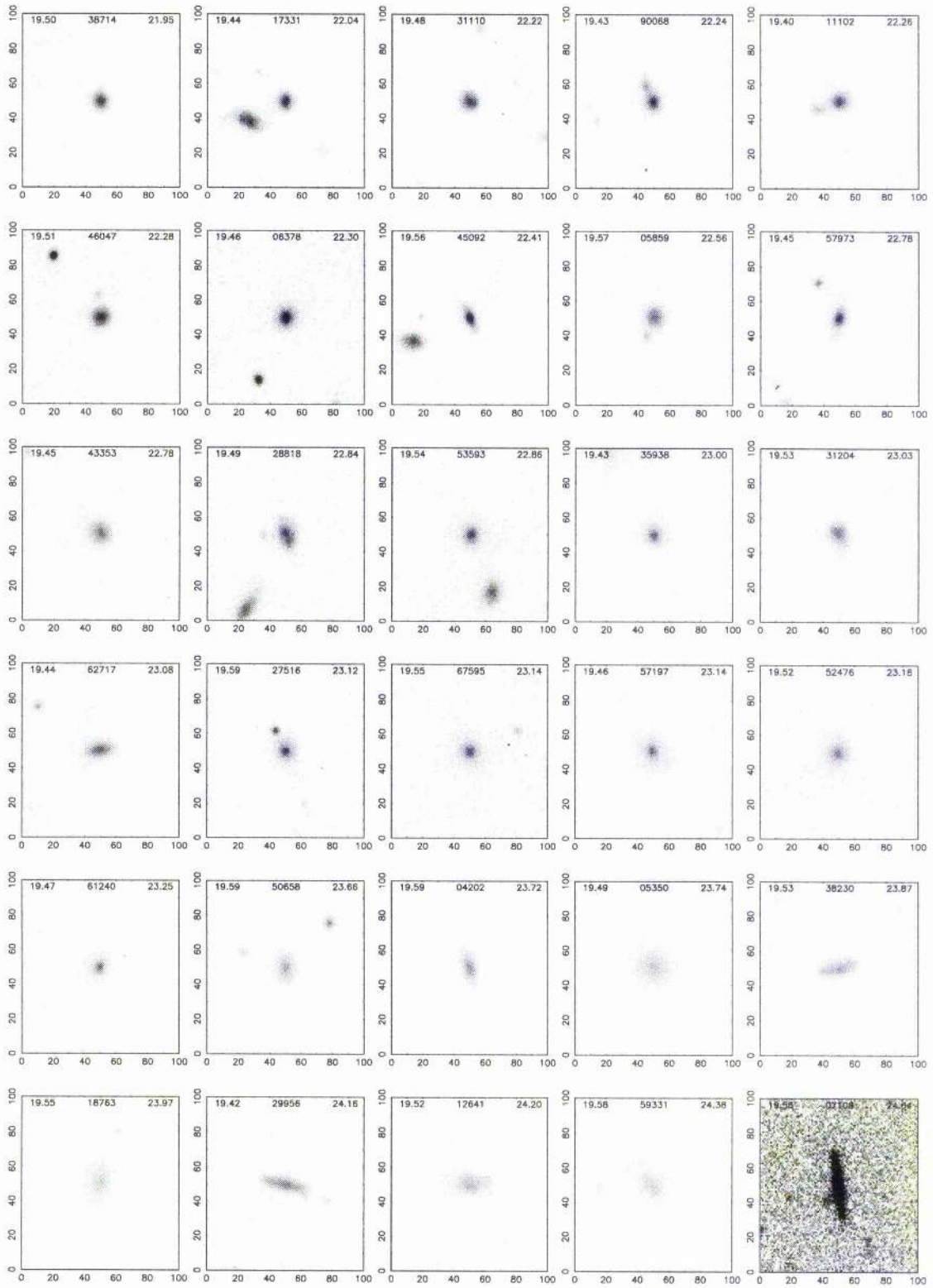

Figure 2.15: The galaxy population at $B_{\rm MGC} = 19.5$ mag.

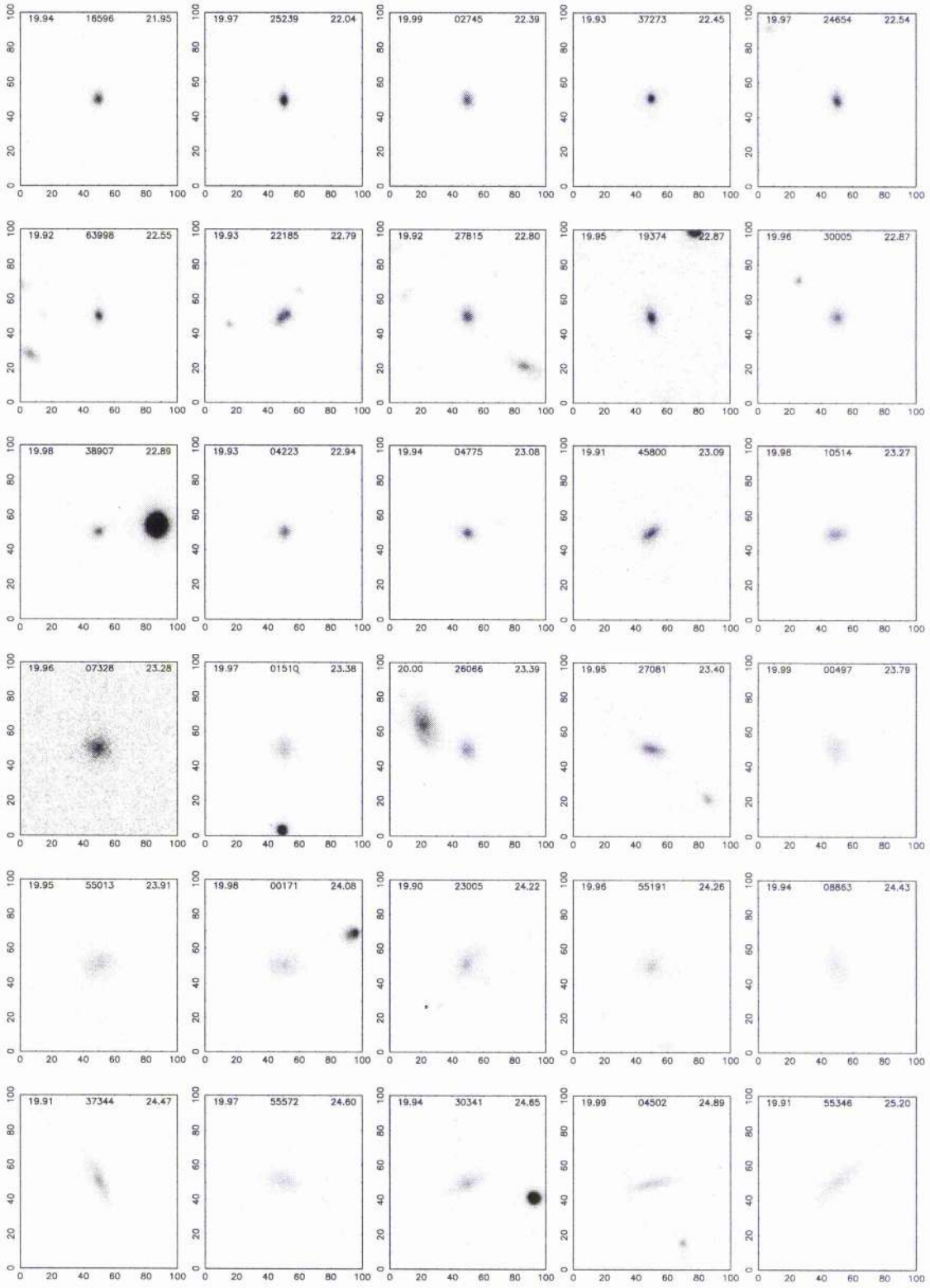

Figure 2.16: The galaxy population at $B_{\rm MGC} = 20.0$ mag.

2.3.5 Classification and cleaning

At this stage the catalogue contains a total of 1,448,212 objects to $B_{\rm MGC} = 24$ mag with a constant detection and analysis isophote of 26 mag/arcsec^2. The catalogue comprises galaxies, stars and various artifacts such as satellite trails, CCD defects, cosmic rays, diffraction spikes, asteroids and spurious noise detections. The next stage was to classify each object into one of these categories. As a starting point we used the STELLARICITY parameter produced by the SEXTRACTOR software. This was determined for each object using an artificial neural network (ANN) that had been extensively trained to differentiate between stars and galaxies, see Bertin & Arnouts (1996) for details. The ANN uses nine object parameters, 8 isophotal areas, the peak intensity and the seeing. Using these input parameters the ANN produces a quantity called STELLARICITY, which takes a value of 1 for stars, 0 for galaxies and intermediate values for more dubious objects. Fig. 2.17 shows the distribution of the STELLARICITY parameter as a function of apparent magnitude. At $B_{\rm MGC} < 20$ mag the distribution is bimodal, Fig. 2.18, with most values at the extremes. Hence star-galaxy separation is relatively trivial (see Fig. 2.17). At fainter magnitudes the star-galaxy separation degenerates into an intractable problem. We now define two catalogues: i) MGC-BRIGHT, dealing with all objects with $B_{\rm MGC} \leq 20$ and ii) MGC-FAINT,dealing with objects in the range $20 < B_{\rm MGC} < 24$.

2.3.6 MGC-BRIGHT: $B_{\rm MGC} \leq 20$

For our MGC bright catalogue ($B_{\rm MGC} \leq 20$ mag) we adopt the following classification strategy. Brighter than $B_{\rm MGC} = 15$ mag we classify all objects with a STELLARICITY of greater than 0.65 as stars. This low stellar cut was used to ensure that the galaxy catalogue was not contaminated by flooded stars. In the range $15 < B_{\rm MGC} \leq 20$ mag we classify all objects with a STELLARICITY of greater than 0.9 as stars. All objects classified as non-stellar were inspected visually and classified into one of the following categories: star, galaxy, galaxy with compromised photometry, galaxies incorrectly deblended, asteroid, satellite trail, cosmic ray, CCD defect, diffraction spike or noise detection. Incorrectly debelended objects where fixed by hand but their original catalogue entries were kept and reclassed as obsolete. In addition we also looked at all objects with FWHM or major or minor axis less than the seeing (these turned out to be primarily cosmic rays and CCD defects). The breakdown of the final MGC Bright catalogue is shown in Table 2.1 and is a good indication of the level of contamination in purely automated galaxy catalogues. As well as the MGC Class there is also a quality flag, Q: 0 = unknown, 1 = good, 2 = compromised, 3 = poor. At this stage MGC-BRIGHT contains 11,775 galaxies covering 36 deg^2. Table A.1 describes the object parameters in MGC-BRIGHT and MGC-FAINT.

2.3.7 MGC-FAINT: $B_{\rm MGC} > 20$

For fainter magnitudes, $B_{\rm MGC} > 20$, star-galaxy separation becomes intractable and we make the classification in a pseudo-statistical way (e.g. Kummel & Wagner 2001). Kummel & Wagner show that for stars the slope dlogN/dm is constant for magnitudes fainter than $B_{\rm MGC} = 18$. Following their lead we used our accurate star counts from brighter magnitudes, $B_{\rm MGC} \geq 17$ to $B_{\rm MGC} < 20$, to define the gradient of the stellar counts which are then extrapolated to fainter magnitudes. However, as the STELLARICITY parameter is dependent on seeing we split our fields in to 4 seeing bins, less than 1.15 (seeing class 1), 1.15 to 1.25, 1.25 to 1.42 and greater than 1.42 (seeing class 4) arcsecs. The seeing bins where defined such that each bin contain more-or-less the equal numbers of fields. In each seeing bin at every subsequent magnitude a STELLARICITY cut was chosen that would give a star count value closest to the extrapolated bright star counts. This resulted in a decreasing STELLARICITY cut towards fainter magnitudes. Fig. 2.17 shows how the STELLARICITY cut varied with magnitude, the solid lines indicate the STELLARICITY cuts used in each magnitude bin. To the right of the dashed line the uppermost solid line

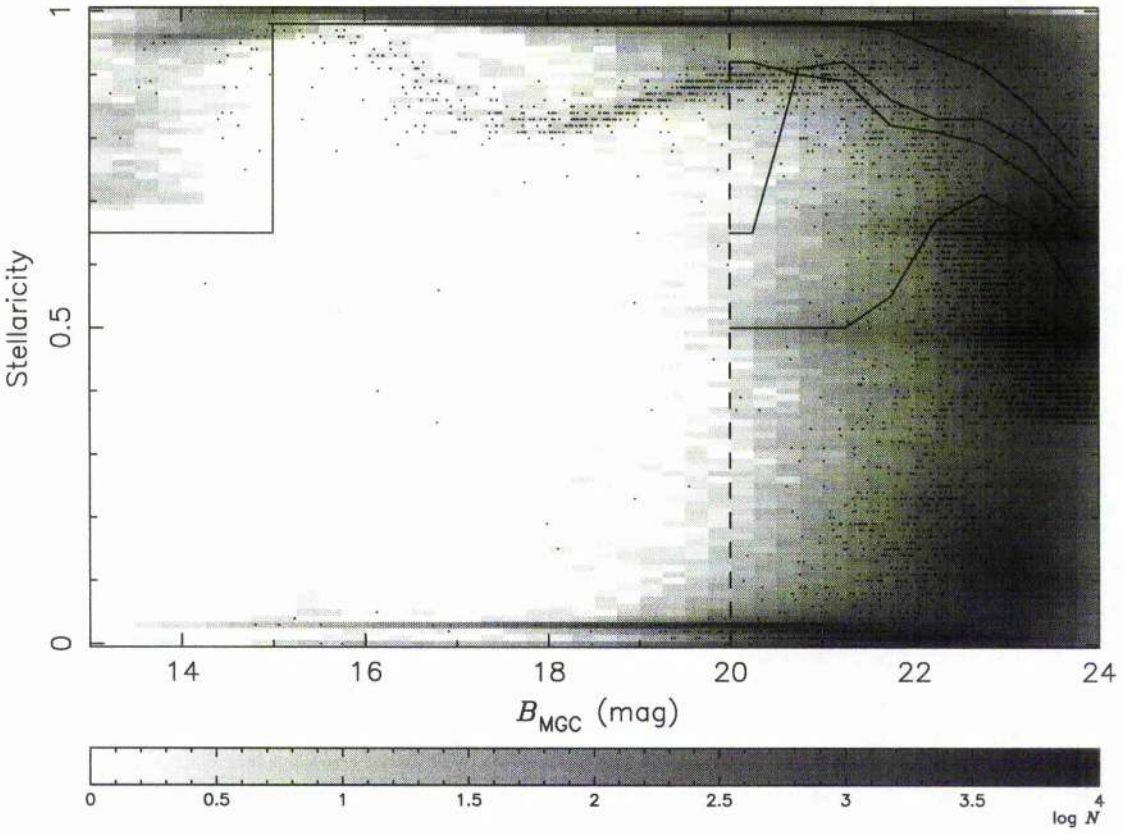

Figure 2.17: A grey scaleplot of STELLARICITY versus apparent magnitude. Crosses indicate the positions of objects from the field with the very worst seeing (1.95 arcsecs), field 124. The solid lines indicate the STELLARICITY cut used at each magnitude in each seein class (see text). The division between MGC-BRIGHT and MGC-FAINT is marked by a vertical dashed line. Objects below the solid line and to the left of the dashed line where classified by eye.

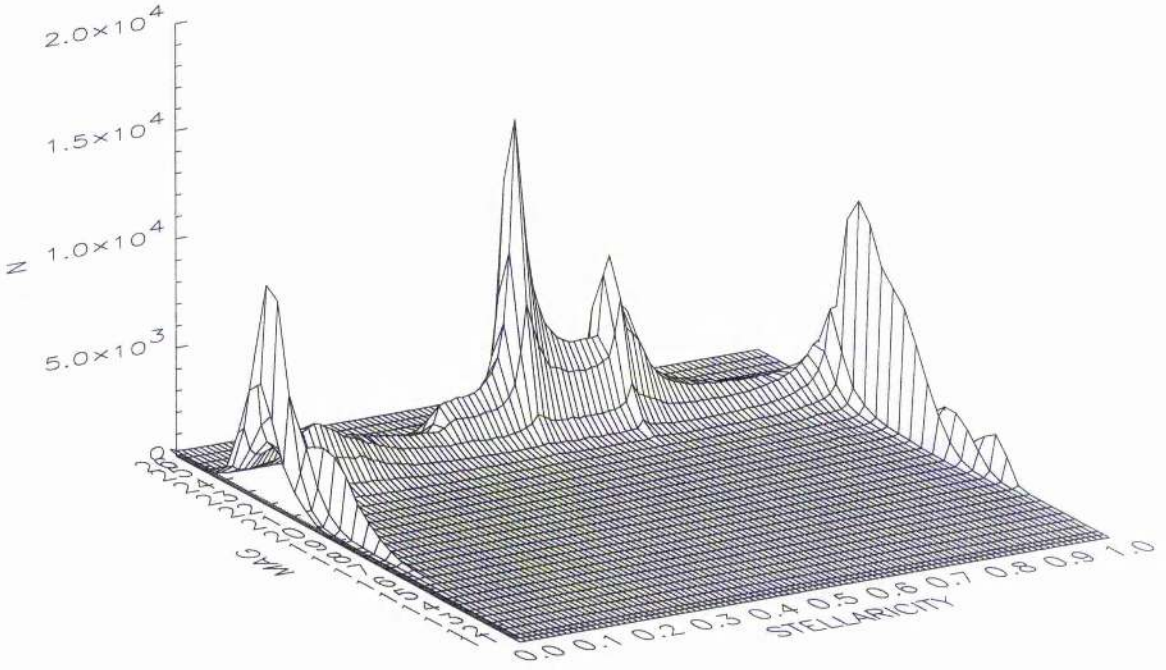

Figure 2.18: A STELLARICITY-magnitude surface plot.

Table 2.1: A breakdown of the 68851 objects detected brighter than $B_{\mathrm{MGC}} = 20$ mag.

MGC Class	Description	Number	After cleaning
1	Galaxy	11808	9863
8	Star	51213	42344
9	Asteroid	148	126
10	Satellite Trails	162	0
11	Cosmic ray	113	62
12	CCD defect	3027	0
13	Diffraction spike	263	0
14	Noise detections	2023	13
15	Obsolete	140	116
Total		68897	52524

indicates the STELLARICITY cuts used for seeing class 1 objects and the lowest solid line seeing class 4.

All object from fields 5, 13, 14, 15, 41, 42, 52, 63, 64, 65, 66, 104, 110, 120, 142, 143, 144 have been removed from MGC-FAINT because the sky noise of these fields is significantly less than our 26 mag/arcsec^2 detection limit, see Fig. 2.3. This results in spurious object detections at faint magnitudes $\sim$23 $B_{\rm MGC}$. At this stage MGC-FAINT contains 1.3 million objects covering an area of $\sim$32 deg^2, =36-$\left(36 \times \left(\frac{17}{144}\right)\right)$.

There still exists a source of contamination in MGC-FAINT, that of cosmic rays. As there are too many objects in MGC-FAINT to visually inspect and at the very faint limit cosmic rays become indistinguishable from real objects an automated procedure of cosmic ray identification had to be devised. At $B_{\rm MGC}$ <22.5 all objects with a semi-minor axis range of 0.7$\leq$b$\leq$1 pixel where assumed to be cosmic rays. Fig 2.19 shows how this cosmic ray population is clearly distinct from the stars & galaxies. At fainter than $B_{\rm MGC}$ =22.5 the cosmic rays merge with the star-galaxy population and this method fails. For objects fainter than $B_{\rm MGC}$ =22.5 we use the FWHM parameter of each object calculated by SEXTRACTOR, which assumes a Gaussian profile, to remove cosmic rays. Specifically, any object with a FWHM $\leq$ 0.9 $\times$ *seeing* was flagged as a cosmic ray. However, this final cut fails for those cosmic rays which leave a trail (have a high angle of incidence) and are therefore indistinguishable from real objects. Thus, at $B_{\rm MGC}\geq$22.5 there will still be some contamination from cosmic rays.

2.3.8 Exclusion regions

Finally due to the density of bright stars, satellite trails and other artifacts (e.g. diffraction spikes, ghosting etc), it is necessary to define exclusion regions where the photometry is likely to be inaccurate or erroneous and detections unreliable. We define exclusion regions as follows:

(i) CCD defects: Visually allocated circular, rectangular or elliptical apertures closely cropped to the defects.

(ii) Satellite trails: Visually allocated rectangles with position angles as calculated by SEXTRACTOR extending across the pointing. The width of the rectangle is set to the minor axis of the trail as defined by SEXTRACTOR.

(iii) Bright stars: Automatically allocate circular apertures extending from the star to the radius of the 2$\times$ the nearest detection.

(iv) Bright galaxies: Automatically allocate elliptical apertures extending from the galaxy to the 3$\times$ the nearest detection.

The bright stars/galaxies where identified by pulling out all objects at $B_{\rm MGC}$ <12.5 that lay within the MGC area in the SuperCOSMOS Sky Survey (SSS, Hambly, Irwin & MacGillivray 2001). The SSS was used to generate a bright object list as the MGC doesn't detect these very bright objects, or if it does their magnitudes and positions are inaccurate. This list was then checked and any bright objects missing where added by hand. The size of the exclusion region around the object was taken to be the larger of 2.5 times the distance, d, to the objects nearest neighbour or 2.5 times a theoretical distance derived by fitting a polynomial to d vs $B_{\rm MGC}$. It was not only bright objects in the MGC that needed to be excluded but also any very bright objects near the survey area, as these are likely to spill over and contaminate the catalogue. These objects where also identified using the SSS and an exclusion area of 2.5 times the theoretical distance was placed around them. All the exclusion regions where then visually checked and any fixes necessary where made by hand.

Fig. 2.4 shows the exclusion regions for field MGC036. The area covered by this pointing is 0.29 deg^2 of which 0.07 deg^2 is contained within the exclusion regions.

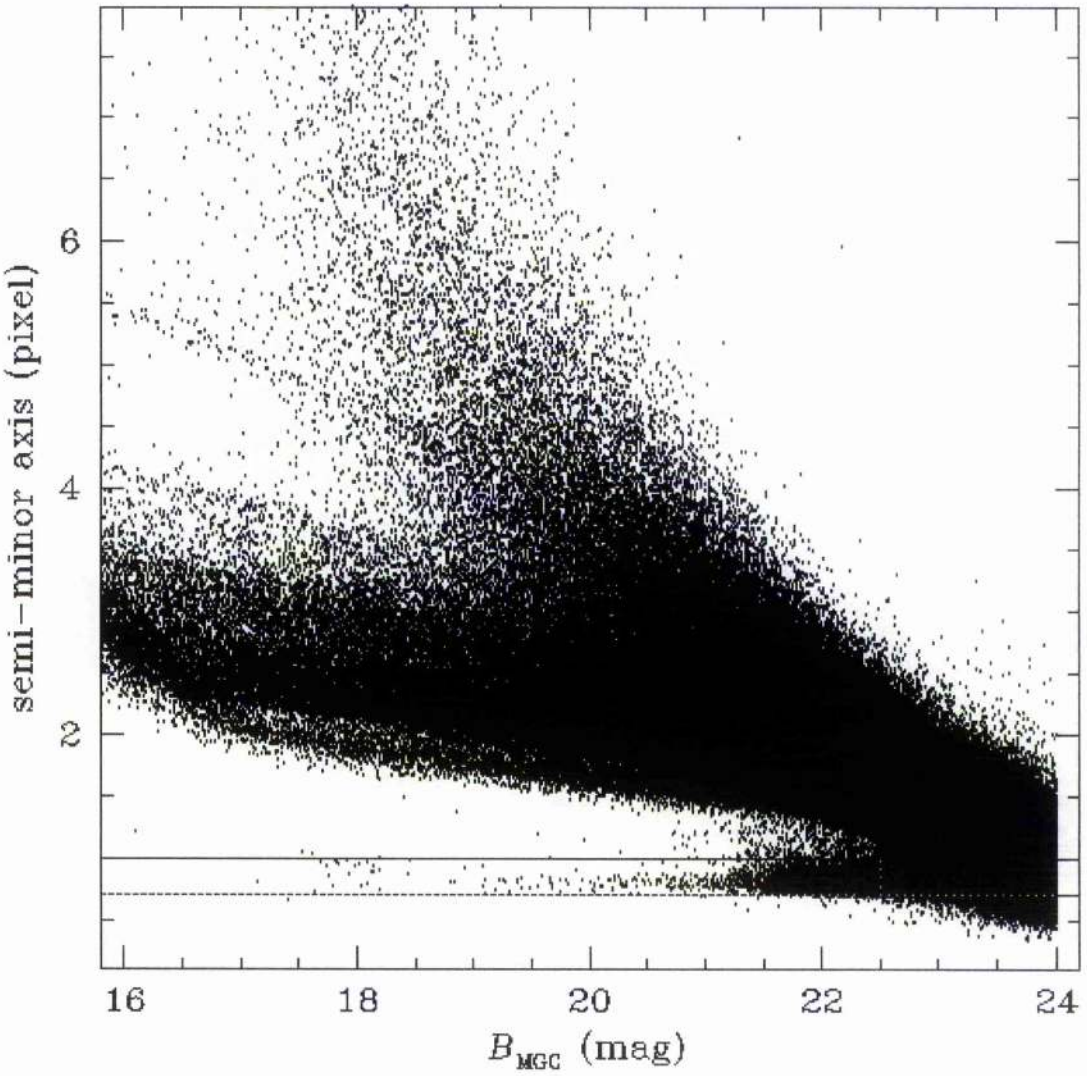

Figure 2.19: Flux rms along the minor axis versus $B_{\rm MGC}$ for all objects from the cleaned versions of MGC-BRIGHT and MGC-FAINT. Almost all cosmic rays lie in the band delineated by the two solid lines. For $B_{\rm MGC} < 22.5$ mag the band is well separated from the general population and hence reliable and complete cosmic ray identification is possible using a minor axis cut alone. At $B_{\rm MGC} \geq 22.5$ mag we apply the additional cut of FWHM $< 0.9 \times$ SEEING to identify cosmic rays but the selection is now incomplete.

The exclusion regions reduce the coverage from 36 to 31.391 deg^2 for MGC-BRIGHT and from 32 to 27.697 deg^2 for MGC-FAINT resulting in final galaxy catalogues of 10,097 and 769,965 galaxies respectively.

2.3.9 Object distribution

Figure 2.20 shows how the MGC-BRIGHT (upper) and MGC-FAINT (lower) galaxies are distributed along the MGC strip. The vertical dashed lines in the lower panel indicate the position of known $z < 1$ galaxy clusters, it is encouraging to note that on the whole they coincide with peaks in the galaxy numbers. The horizontal solid line indicates the mean number of galaxies per field.

We also show how the numbers of bright stars vary across the survey and how they compare to predictions using the Bachall & Soneria model, Bachall & Soneira (1981) and Bahcall (1986). The basic shape of the counts and model agree, in that there is a steep rise as you approach the galactic bulge. However, there appears to be significant discrepancies towards the Galactic Bulge between the predicted and the actual counts. The star counts are discussed in detail in Chapter 3.

2.4 Completeness and selection limits

One of the primary aims of the MGC is to create a sample of galaxies with well defined selection criterion, hence the use of a constant detection isophote. Fig. 2.21 shows the distribution of galaxies in the apparent magnitude versus apparent effective surface brightness plane for MGC-BRIGHT along with the three principle selection boundaries: a median seeing limit of 1.3 arcsec; a central surface brightness isophotal detection limit of $\mu_{\rm lim}$=26 mag/arcsec^2 (by combining Eqn. B.85 with Eqn. 2.7 and assuming an exponential profile, we find this is equivalent to an effective SB limit of 27.12 mag/arcsec^2); and the imposed pseudo-total magnitude cut of 20.0 mag. Note that this latest cut is an arbitrary choice and is set by the magnitude at which the seeing and isophotal limits begin to impinge upon the galaxy population. The apparent effective surface brightness is simply calculated as:

$$\mu_{eff} = m + 2.5 \times log_{10}(2\pi r_{0.5}^2) \tag{2.7}$$

where, $r_{0.5}$ is the half-light radius as measured along the major axis.

Within the shaded region galaxies cannot, theoretically, be detected although noise may scatter a few objects across these boundaries. Inside the shaded region galaxies with these apparent properties should be detectable. The galaxy population is NOT randomly distributed within this region indicating that galaxies come with a restricted range of intrinsic properties. The clear space between the galaxy population and the isophotal detection limit shows that the sample is complete within the selection boundaries and for example bright luminous low surface brightness galaxies are indeed rare as claimed by Cross et al. (2001) and Blanton et al. (2001). One possible caveat to this is the impact of the background estimation discussed earlier (see §1.3.1). SEXTRACTOR uses a background mesh of 256 by 256 pixels (85.2 by 85.2 arcsec) which implies that any structures covering a substantial fraction of this grid will produce an erroneously high background measurement. We estimate that objects must extend over an isophotal area of $\sim$ 25% of the 256 by 256 mesh to produce such an effect. This represents an upper size limit in terms of half-light radii of 64 by 64 pixels (21.3 by 21.3 arcsec) assuming $r_{iso} \sim 2r_e$. This line is shown as the lower dotted line on Fig. 2.21.

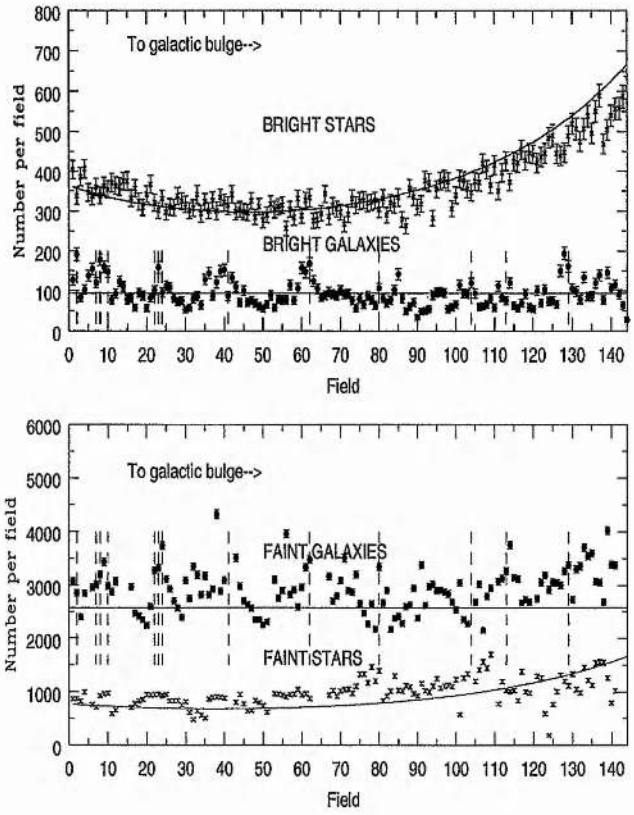

Figure 2.20: The distribution of bright galaxies, faint galaxies, bright stars and faint stars across the survey strip. The dashed vertical lines indicate the positions of galaxy clusters, with z<1, found using the NASA Extragalactic Database (NED, nedwww.ipac.caltec.edu) in the MGC strip. The galaxy distribution shows a uniform distribution whereas the stars show the latitude dependency expected. The solid horizontal lines indicate the mean number of bright and faint stars per field. The curved solid line is the model star counts generated by the Bachall & Soneria model, Bachall & Soneira (1981) & Bahcall (1986). Note that all the values of N shown here have been scaled for a constant area of 0.29 deg^2 per field.

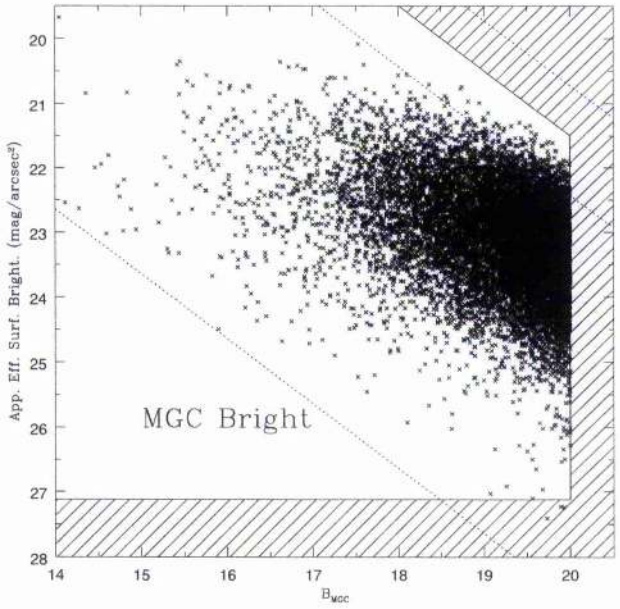

Figure 2.21: The Apparent Bivariate Brightness Distribution along with the selection boundaries determined by the median seeing (solid diagonal line), the isophotal detection limit (horizontal solid line) and the magnitude limit (vertical solid line). The two upper dotted lines are the selection limits for the fields with the worst (upper-lower) and the best (upper-upper) seeing. The lowest dotted line is the maximum size selection limit for reliable detection, see text.

2.5 Summary

In this chapter we have described the collection and analysis of a data set and the construction of a photometric catalogue called The Millennium Galaxy Catalogue (MGC).

The images where observed at the INT using the WFC with the Kitt Peak National Observatory B filter. Analysis of the overlap between consecutive pointings indicates that the data is astrometrically accurate to ± 0.08" in both RA and DEC and is internally photometrically consistent to < 0.03 magnitudes.

Object detection was performed to a limiting isophote of 26mags/arcsec^2 using the SEXTRACTOR package developed by Bertin & Arnouts (1996). At $B_{\rm MGC} < 20$ star galaxy separation was performed by using a combination STELLARICITY cuts and observer classification. At $B_{\rm MGC} > 20$ a pseudo-statistical approach was used to choose a STELLARICITY cut appropriate for each 0.5 magnitude bin. The value of each STELLARITICTY cut was chosen in order to keep the faint star counts following a constant gradient derived from the bright star counts. Following this the MGC was split in to two catalogues, MGC-BRIGHT which contains all objects at $B_{\rm MGC} < 20$ mags and MGC-FAINT which includes all other objects.

In Chapter 3 we use MGC-BRIGHT to derive star counts as a function of galactic longitude and discuss their implications for the structure of The Galaxy.

CHAPTER 3

Star Counts

In this chapter we derive a star catalogue generated from the Millennium Galaxy Catalogue (MGC), see Chapter 2. From this catalogue, and in conjunction with colours gained from the Sloan Digital Sky Survey Early Data Release (SDSS-EDR; Stoughton et al. 2002), we obtain reliable star counts, to a limiting magnitude of $B_{\rm MGC}$ <20, as a function of Galactic longitude. We investigate the structure of the Galactic halo, with an emphasis on the flattening and the quantification of the statistical significance of (or lack of) substructure.

3.1 The Galactic structure

The basic stellar components of the Milky Way are the thin disk, thick disk, stellar halo and central bulge, albeit that the inter-relationships and distinction amongst different components remains subject to some debate (e.g. Norris & Ryan 1991). Quantifying the properties of the stellar components of the Milky Way Galaxy is of wide importance, since the multi-variate stellar distribution function is a product of Galaxy formation and evolution and in turn constrains those processes that are important during and after the formation of the stars. The thick disk was introduced by Gilmore & Reid (1983) based on their deep star counts towards the South Galactic Pole, as a component with a scale-height some 3–4 times that of the old thin disk. That the stellar population of the thick disk is distinct from that of the halo is seen clearly in colour magnitude diagrams derived from star count surveys (e.g. Fig. 2 of Gilmore, Wyse & Kuijken 1989; Chen et al. 2001; Fig. 4 here), and many derivations of the field kinematics and metallicity distributions have established its existence definitively.

However, even the structural parameters of these major stellar components of the Galaxy are less well-established, and deep wide-area star counts are important in their determination. The flattening of the stellar halo, when combined with metallicity and kinematic information, can distinguish between models in which the halo formed with a little, or with a lot, of gaseous dissipation, and constrains the flattening of the dark matter halo (e.g. White 1985). Substructure in phase space is expected in hierarchical clustering theories of Galaxy formation, and while the signature in kinematics may be more obvious and long-lived (e.g. Helmi & White 1999; Helmi et al. 1999), late accretion and merging may produce observable over-densities in coordinate space (e.g. Johnston, Hernquist & Bolte 1996; Zhang et al. 2002). The streams from the Sagittarius dwarf spheroidal galaxy are extreme examples (e.g. Yanny et al. 2000; Ibata et al. 2001; Vivas et al. 2001; Ibata, Irwin & Cambresy 2002). Placing constraints on the level of clustering in coordinate space, for the bulk of the stellar halo, is obviously important to constrain recent tidal disruption of, and accretion of stars from, satellite stellar systems.

Most previous investigations have utilised small area star counts in a few selected lines-of-sight (e.g. Gilmore & Reid 1983; Bachall & Soneira 1984; Wyse & Gilmore 1989; Reid & Majewski 1993). Investigations into large-scale Galactic structure, and to quantify

the global importance of potentially rare effects – such as substructure – obviously benefit from large-area surveys. While combination of the data-sets from several independent smaller surveys is possible (cf. Reyle & Robin 2001), the advantages of uniformity of photometry, star-galaxy classification etc. all argue for the superiority of one survey across a wide range of Galactic coordinates. This has recently become possible through the advent of wide-field CCD mosaic cameras on medium-sized telescopes, such as that built for the Sloan Digital Sky Survey (York et al. 2000) and the Wide Field Camera (WFC) on the Isaac Newton 2.5m Telescope (INT).

3.2 Star count model

The star count model we use is that developed by Gilmore (1984) (see also Gilmore, Reid & Hewett 1985 and Gilmore & Wyse 1985) and includes a double-exponential thin disk, a double-exponential thick disk, and a de Vaucouleurs stellar halo. The thin disk and halo luminosity functions are based on those of Wielen (1974). For the thick disk the Wielen LF applies only for $M_V > 4.5$ – for $M_V < 4.5$ the luminosity function of the thick disk follows that of 47 Tuc, the globular cluster with metallicity and age similar to that of a typical thick disk star (cf. Gilmore, Wyse & Jones 1995). Indeed the colour-magnitude relation of 47 Tuc is adopted for the thick disk. The colour-magnitude relation of the metal-poor globular cluster M5 is adopted for the stellar halo. The Gilmore model code was provided by Prof. R. Wyse (priv. comm).

To facilitate our determination of the flattening of the stellar halo we held all the structural parameters of this model fixed, with the exception of the stellar halo axial ratio. We adopted a solar Galactocentric distance of 8 kpc, an old thin disk scale-height of 325 pc, a thin (and thick) disk scale length of 3.5 kpc, a thick disk scale-height of 1300 pc and thick-disk normalisation in the mid-plane, relative to the thin disk, of 2 per cent. The major-axis de Vaucouleurs radius for the stellar halo was fixed at 2700 pc. We made predictions for models with oblate stellar halos, with axial ratio (c/a) in the range 0.45 - 0.80, at a resolution of 0.01, and all with a local normalisation of the stellar halo relative to the thin disk of 0.125 per cent (cf. Morrison 1993).

With these parameter values, the stellar halo does not contribute significantly to the star counts until $B \geq 17.5$ (shown graphically in Fig. 3.3 below). Given our intended aim here is to investigate the structure of the halo, we will only compare with data fainter than this limit.

3.3 The Observed Star Counts

3.3.1 Constraints from B-magnitudes Alone

Fig. 3.1 shows how the observed faint star counts, taken from the MGC-BRIGHT catalogue, vary with Galactic longitude and magnitude. Also shown are the predicted counts from the model with a range of flattening of the stellar halo (the value of the axial ratio, (c/a), is given in parentheses in the Figures). We quantified the fits of the models to the data as given in Table 3.1 and Fig 3.2, assuming that the errors on the counts are Poisson errors plus a maximum 3 per cent systematic error to be added in quadrature, derived from our estimates (see section 4 below) of the reliability of our stellar classification. In the range $17.0 < B_{\rm MGC} < 19$ there is a consistent signal of a flattened halo, with axial ratio (c/a)$\sim$ 0.5, with the best fit giving an axial ratio of (c/a)=0.54$\pm$0.03. In all cases the error given for the ratio (c/a) is the $\chi^2 + 1$ error. The rise for brighter magnitudes, where there are only $\sim$ 30 stars in each field, is significant at only the $\sim 2\sigma$ level. The rise at fainter

Table 3.1: The best fit model in each magnitude bin using all the data.

$B_{\rm MGC}$	(c/a)	χ^2
$18.0 < B_{\rm MGC} < 18.5$	0.55 ± 0.06	1.62
$18.5 < B_{\rm MGC} < 19.0$	0.49 ± 0.04	1.30
$19.0 < B_{\rm MGC} < 19.5$	0.54 ± 0.03	1.27
$19.5 < B_{\rm MGC} < 20.0$	0.65 ± 0.03	1.42

magnitudes may reflect real changes in the axial ratio with increasing Galactocentric radius (cf. Hartwick 1987) although the signal would have to be produced by intrinsically bright (and hence distant) tracers. Additionally, the presence of halo substructure could bias the result.

3.3.2 The Colour-Magnitude Diagram

Colour data for our star catalogue would allow us to identify particular spectral types of stars. The main sequence turn-off of the stellar halo is in the F-star region, and isolation of these stars maximizes the signal from the stellar halo, allowing a more sensitive testing of the flattening of the halo. Further, we can derive statistical measures of substructure in the stellar halo from analysis of the F-star distribution.

As noted above, the area covered by the MGC overlaps with part of the SDSS-EDR, specifically the SDSS run 756, stripe 10. We identified all the objects in the SDSS-EDR stellar database that lay within the MGC strip. Each object that was classified as a star in the MGC was then matched to the SDSS-EDR catalogue using a positional tolerance of $\Delta\theta$=$\pm$1 arcsec (equivalent to $\sim$3 pixels on the WFC camera). Of the 42413 MGC stars, 96.7 per cent had SDSS-EDR counterparts, and there was no case where an MGC star was matched to more than one SDSS-EDR star. Of the 1396 unmatched MGC stars, 49.79 per cent had $B_{\rm MGC} < 15$, all of which fell in the "flooded stars region" of the $B_{\rm MGC}$-Stellaricity plot (see Fig. 10 of Liske et al. 2003). This leaves a total of 41718 MGC-stars at $B_{\rm MGC} > 16$ of which only 701 (2 per cent) have no SDSS-EDR counter-part. From these 701 unmatched objects, 115 were classified based on visual inspection by Liske, Lemon & Driver, and nearly all have $B_{\rm MGC} > 19$. Of the remaining 586 stars, 151 fall into the known holes in the SDSS-EDR at $\sim 215.50° <$ RA $< 215.95°$ and DEC $< -0.21°$ and $0° <$ DEC $< 0.21°$. A further 24 are clumped in a strip at $\sim 193.0° <$ RA $< 195.0°$ and $0° <$ DEC $< 0.21°$. The rest of the unmatched stars are evenly distributed across the MGC strip.

The SDSS-EDR magnitudes used in this paper are SDSS PSF magnitudes (see Lupton et al. 2002). Using the 41017 matched MGC-SDSS-EDR stars we are able to plot a colour-magnitude diagram (hereafter CMD; Fig. 3.3), and colour-colour diagram (Fig. 3.4), for MGC stars in the range $16 < B_{\rm MGC} < 20$. The $(B - V)$ colours are gained via the colour transformation found in Fukugita et al. (1996):

$$(g^* - r^*) = 1.05(B - V) - 0.23 \tag{3.1}$$

Three distinct concentrations of stars are obvious in the CMD of faint stars in high-latitude fields, representing the stellar halo, the thick disk and the thin disk, as shown in Fig. 3 of Gilmore & Wyse (1985) and in Fig. 2 of Gilmore, Wyse & Kuijken (1989). The

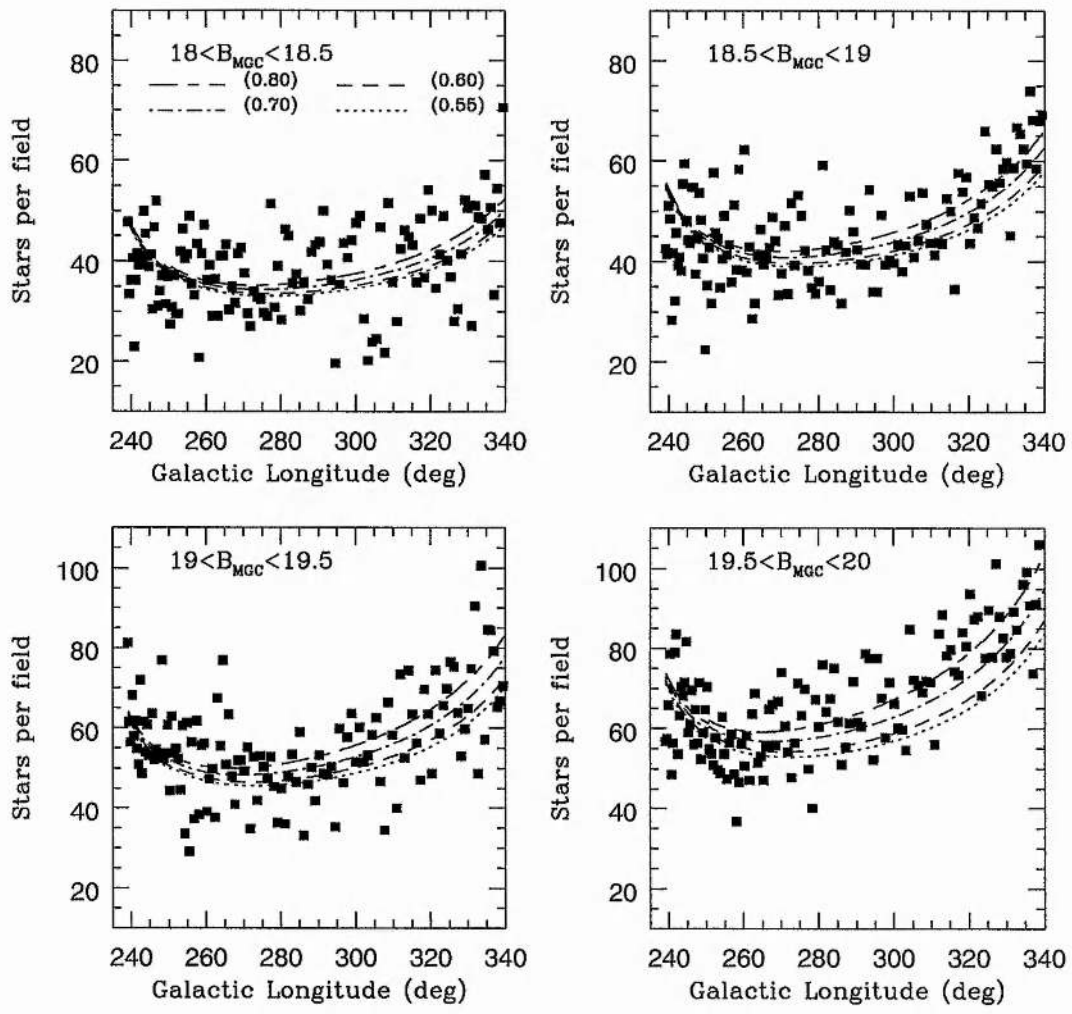

Figure 3.1: The MGC star counts as a function of Galactic longitude, in bins of apparent magnitude $B_{\rm MGC}$, for $B_{\rm MGC} > 18$, compared to the predictions of star count models with a range of flattenings of the stellar halo. The axial ratio of the stellar halo is given in parentheses. Note here we have scaled the counts so that each field covers and area of 0.29 deg^2.

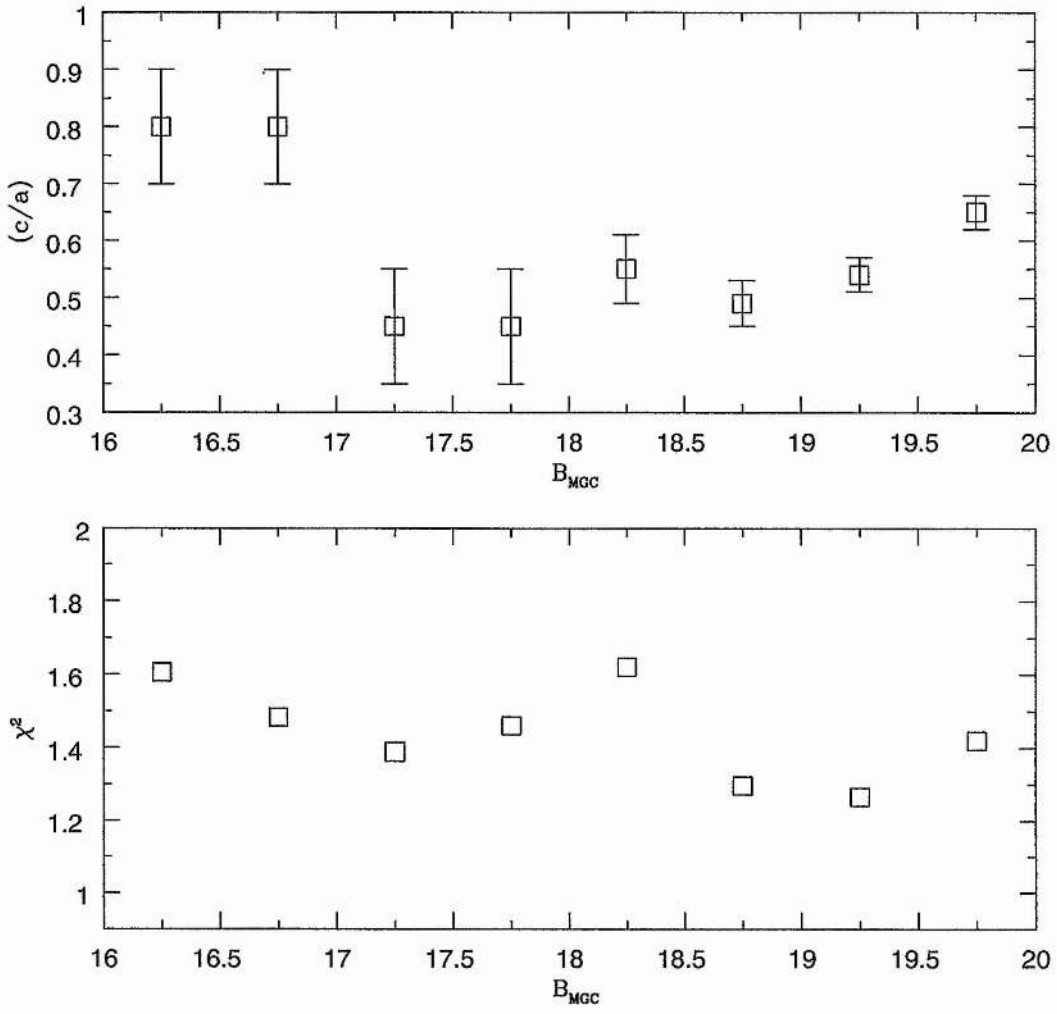

Figure 3.2: The quality of fit and axial ratio (c/a) of the best-fit star-count model in each magnitude bin from $16 < B_{\rm MGC} < 20$. Here and through out χ^2 refers to the minimum reduced χ^2 value. Also, unless otherwise indicated in the figure (through cuts in l and b),for each minimum χ^2 estimate there are 144 fields and hence 144 data points (see Fig.3.1) and only one free parameter (the axial ratio of the stellar halo).

first, seen here in Fig. 3.3 at $(B-V)\sim0.45$, $B_{\rm MGC} > 18$, reflects the main-sequence turnoff colour of metal-poor, old stars, and contains stars that are members of the stellar halo. The well-defined blue limit suggests a uniform old age for stars in the halo, with no significant intermediate-age population (see Unavane, Wyse & Gilmore 1996 for quantification of this point, and discussion of the implications for late accretion into the halo). The second concentration, at $(B-V)\sim0.65$ and $B_{\rm MGC} < 18$, marks the main-sequence turnoff of more metal-rich old stars, which reside in the thick disk (cf. Gilmore, Reid & Hewett 1985). The final concentration, at $(B-V) > 1.5$, is due to thin disk stars, and reflects the insensitivity of the B and V bands to cool stars on the main sequence (see Gilmore & Wyse 1985 for a comparison of the CMD in different band-passes). The CMD for the full SDSS-EDR data, in the SDSS band-passes, was presented by Chen et al. (2001).

It is clear from the morphology of the CMD that one cannot neglect the thick disk. It is also clear that the contribution of the stellar halo to our star counts is maximised by considering only F-stars, $B - V \leq 0.6$, and restricting the analysis to stars fainter than $B_{\rm MGC} = 18$.

The colour-colour diagram of the MGC stars, using the SDSS photometry, is shown in Fig. 3.4 and provides a basis for spectral-type selection. Our chosen boundaries for various spectral classes of stars are as indicated. In principle F-stars cover a wide range in $(g^* - r^*)$ and $(u^* - g^*)$, but after taking into consideration the sharp halo turn-off at $(B - V)$=0.45 (see Fig. 3.3 above), we adopted the more conservative limits $0.1 < (g^* - r^*) < 0.3$ and $0.7 < (u^* - g^*) < 1.0$ (see also Yanny et al. (2000) and Newberg et al. (2002) for similar selection criteria). The objects making up the fuzzy patch in the top left are likely to be quasars and contribute 2.5 per cent to the total MGC-SDSS matched sample. These should be distributed isotropically across the sky and so while increasing the background somewhat, should not contribute a false clustering or flattening signal.

3.3.3 Substructure in the Halo Star Counts

Hierarchical clustering scenarios of galaxy formation, such as in a Cold-Dark-Matter-dominated Universe, predict that the Milky Way formed from the merging of many smaller progenitors (see e.g. reviews of Silk & Wyse 1993 and White 1996). The satellite galaxies of the Milky Way may be surviving examples of the earlier systems. It has been suggested that a significant part of the *outer* halo could be the result of accretion and merging of substructure (cf. Searl & Zinn 1978), with this process on-going, as evidenced by the Sagittarius dwarf spheroidal (Ibata, Gilmore & Irwin 1994; Ibata et al. 1997). The kinematic signature of 'moving groups' is long-lived, producing observable effects at the solar Galactocentric distance and beyond, even after $\sim$ 10 Gyr (Helmi & White 1999; Johnston et al. 1999; Helmi et al. 1999; Gilmore, Wyse & Norris 2002). The signature of clustering in coordinate space is less robust and decays faster in time with orbit wrapping, but has clearly been detected for the tidal streams from the Sagittarius dwarf spheroidal galaxy (Yanny et al. 2000; Vivas et al. 2001; Ibata et al. 2001, Ibata, Irwin & Cambresy 2002). Newberg et al. (2002) identified several over-dense regions in their wide-area faint F-star sample using SDSS imaging data, several most likely to be associated with streams from the Sagittarius dwarf, but others that may be independent structures in the outer halo. These identified over-densities in the SDSS data are at faint magnitudes, $g^* \sim V > 19.4$, corresponding to $B_{\rm MGC} \geq 20$, or heliocentric distances of $\geq$ 10kpc for metal-poor F-stars. Most of the mass of the stellar halo lies interior to these distances and is sampled by the brighter stars. Quantification of the level of substructure in these brighter stars has heretofore been lacking in analyses of star counts.

Our present sample is ideal to quantify the clustering in the bulk of the halo; this has two applications, the first to constrain recent accretion, the second to estimate the possible effect of small-scale non-uniformities on our derivation of the large-scale structure of the stellar halo. Simulations (e.g. Johnston, Hernquist & Bolte 1996) have shown that over-densities in coordinate space can survive for several orbital periods, albeit the alignment is dependent on the shape of the Galactic potential (longest for spherical potentials) and on the time dependence of the potential (e.g. Zhao et al. 1999). The present analysis may be expected to constrain accretion into the bulk of the halo over the last few Gyr, being

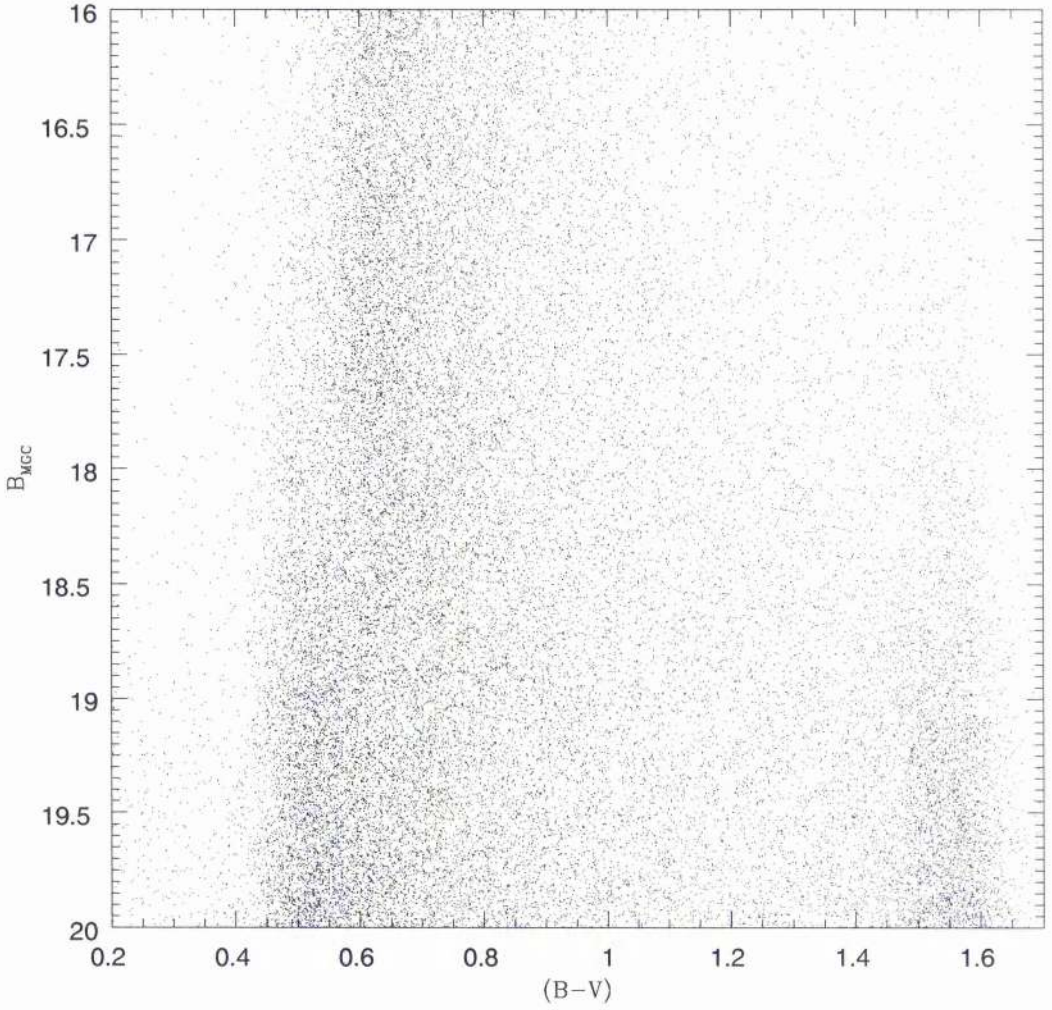

Figure 3.3: A CMD plot for the MGC stars in the range $16 < B_{\mathrm{MGC}} < 20$.

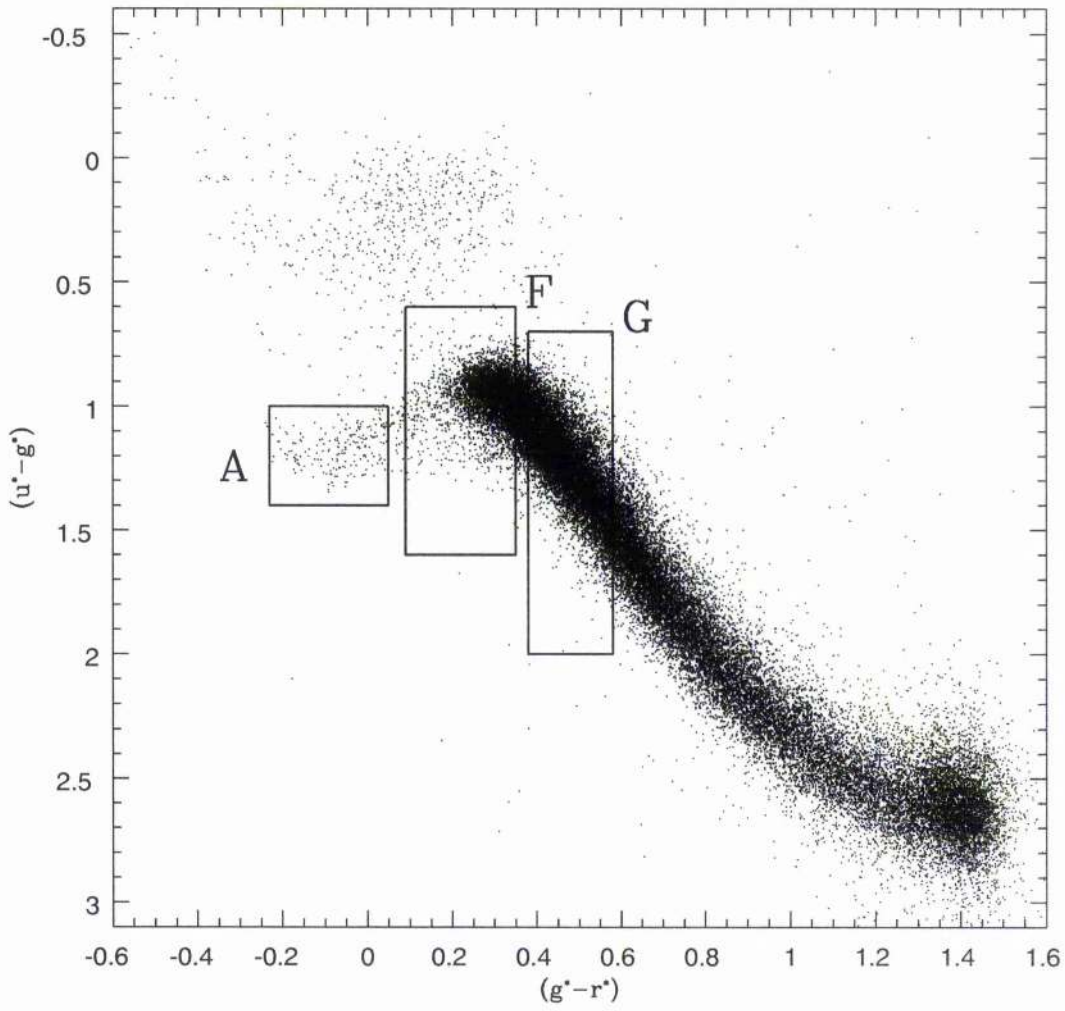

Figure 3.4: A colour-colour plot for the MGC stars in the range $16 < B_{\mathrm{MGC}} < 20$. The boxes indicate the selection boundaries for A, F & G stars. Objects making up the fuzzy patch to the top left are most likely quasars.

several orbital periods within several kpc of the Sun's location. While the uniform old age of the bulk of the halo, seen again here in the location of the well-defined main sequence turn-off in Fig. 3.3, argues against the accretion of systems containing intermediate-age populations, such as the typical satellite galaxies, in the last $\sim$ 10 Gyr being important in general (Unavane, Wyse & Gilmore 1996), the accretion of systems with stellar populations similar to the old, metal-poor halo is better constrained by signatures in kinematics and coordinate space.

3.3.3.1 Counts-in-Cells

A first impression of the clustering of the stars can be seen by a simple analysis of counts-in-cells. The contour and surface plots that results from counts in cells of size 0.1 degree in DEC and 5 degree in RA of the full stellar distribution (irrespective of colour, and with limiting magnitude $B_{MGC} = 20$) is shown in Fig. 3.5 (note that there are around 10^3 stars per square degree at these magnitudes, with fields at high latitude and intermediate longitude, corresponding to the counts per cell here being around 500, and increasing towards the Galactic Center). The large scale gradient in the stellar distribution towards the direction of the Galactic Center is clearly seen. We removed this gradient by fitting a smooth quadratic to the stellar distribution in RA for each DEC bin, and then dividing the actual number of stars in each cell by the "model" number of stars for that cell. In this way the large scale stellar distribution is taken out and only fluctuations due to random noise and/or stellar clustering are left, as shown in Fig. 3.6. Some fluctuations are seen in this plot, but all are at less than 1σ (σ =0.058) away from the mean $\left(\overline{\frac{N}{N_{\rm model}}} = 1\right)$.

Isolating just the selected F-stars provides the contour and surface plots shown in Fig. 3.7; note that by restricting the colour range the number of stars per field has reduced to several tens rather than the several hundreds for all stars. Again fluctuations are seen, superimposed on the large scale gradient, but again at only low level of significance, at typical level of 1.27σ away from the mean.

The colour selection to narrow the spectral type also allows us to use apparent magnitude as an approximate distance modulus, since the selected F-stars should have a fairly narrow range in absolute magnitude. One can then look for clustering along the line-of-sight. The 'pie-diagram' plot of RA versus apparent magnitude (remember the survey is a narrow strip with little range in DEC) is shown in Fig. 3.8, with Fig. 3.9 showing the contour and surface plots in this RA-$B_{\rm MGC}$ plane. The rise in Fig. 3.9 shows the combination of the large scale stellar gradient and the stellar number count gradient, more stars exist at fainter apparent magnitudes.

The strongest signal seen in our sample is again at the faintest magnitudes, $B_{\rm MGC} \geq 19$, and at larger RA$\geq 210°$. As we will also see below, this is close to the coordinates and apparent magnitude range of the detection of the tidal arm from the Sagittarius dwarf spheroidal galaxy in A-stars, at distances of $\sim$ 40 kpc; this structure was identified in F-stars by Newberg et al. (2002), at apparent magnitudes of $g^* \sim 22.5$. No plausible dynamical model for the orbit of the Sagittarius dwarf and its debris would put debris in this direction at the heliocentric distance of $\sim$ 10 kpc implied by our F-star data. We have either identified a new structure, or A-stars have contaminated our F-star sample at the faintest limits. While it is almost inevitable that there will be some contamination of the F-star data by stars of other spectral types, this should be relatively small since our colour cuts were conservatively chosen to minimise any contamination, and thus only random errors in colour should contribute.

Fig. 3.10 compares the projected spatial distributions of the F-stars and the full stellar samples, by taking the ratio of the star counts. Towards the end of the MGC strip there are bins in which the F-stars are more clustered. In other words, the surface plot in the lower panel of Fig 3.10 is not flat, which is what one might have expected if the F-stars were distributed in the same manner as the total stellar population. We now investigate other ways of confirming and quantifying this implied F-star clustering.

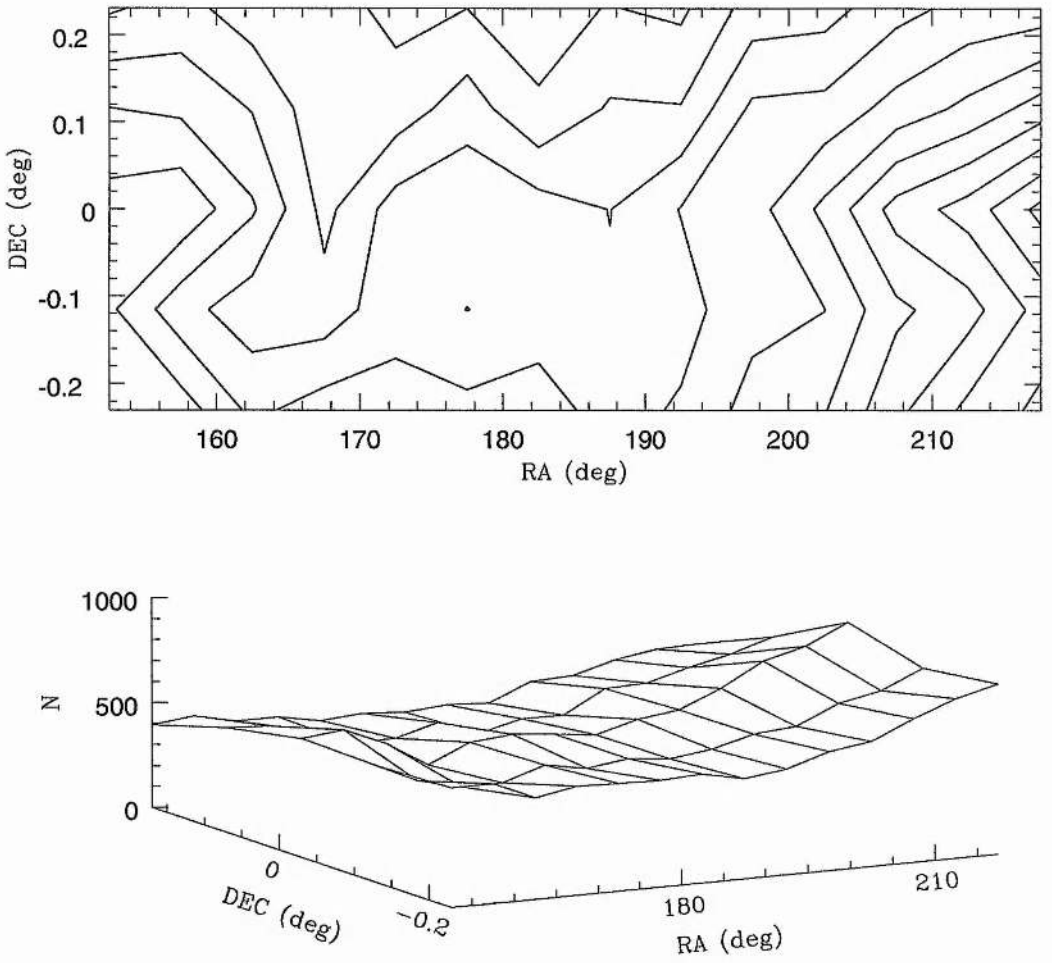

Figure 3.5: A contour (upper) and surface (lower) plot of the full stellar distribution. The large scale (galactic) stellar distribution is clearly visible. The contours are evenly spaced at intervals of ΔN=50 between N=300 and N=900.

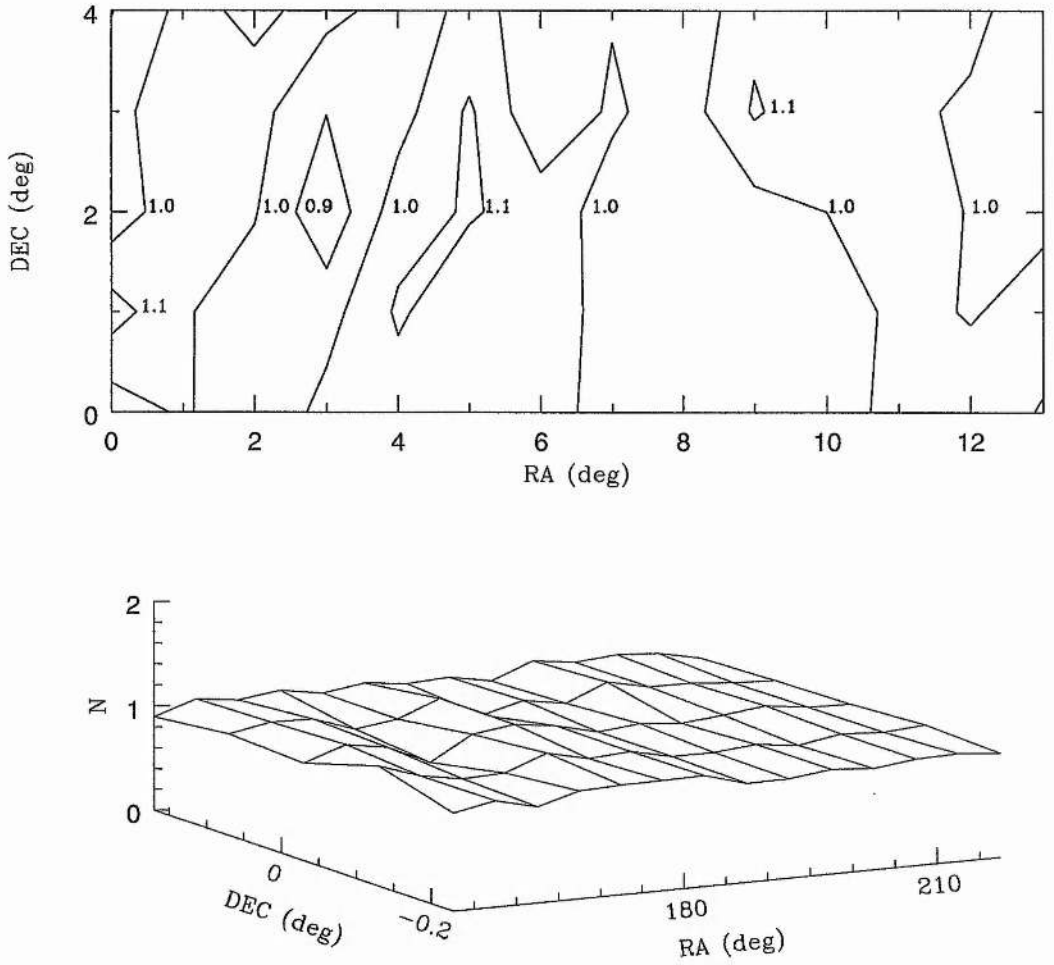

Figure 3.6: A contour (upper) and surface (lower) plot of the full "flat-fielded" stellar distribution with the large scale stellar distribution removed. The contours are evenly spaced at the levels of $\frac{N}{N_{\text{model}}}$=0.9, 1.0 and 1.1

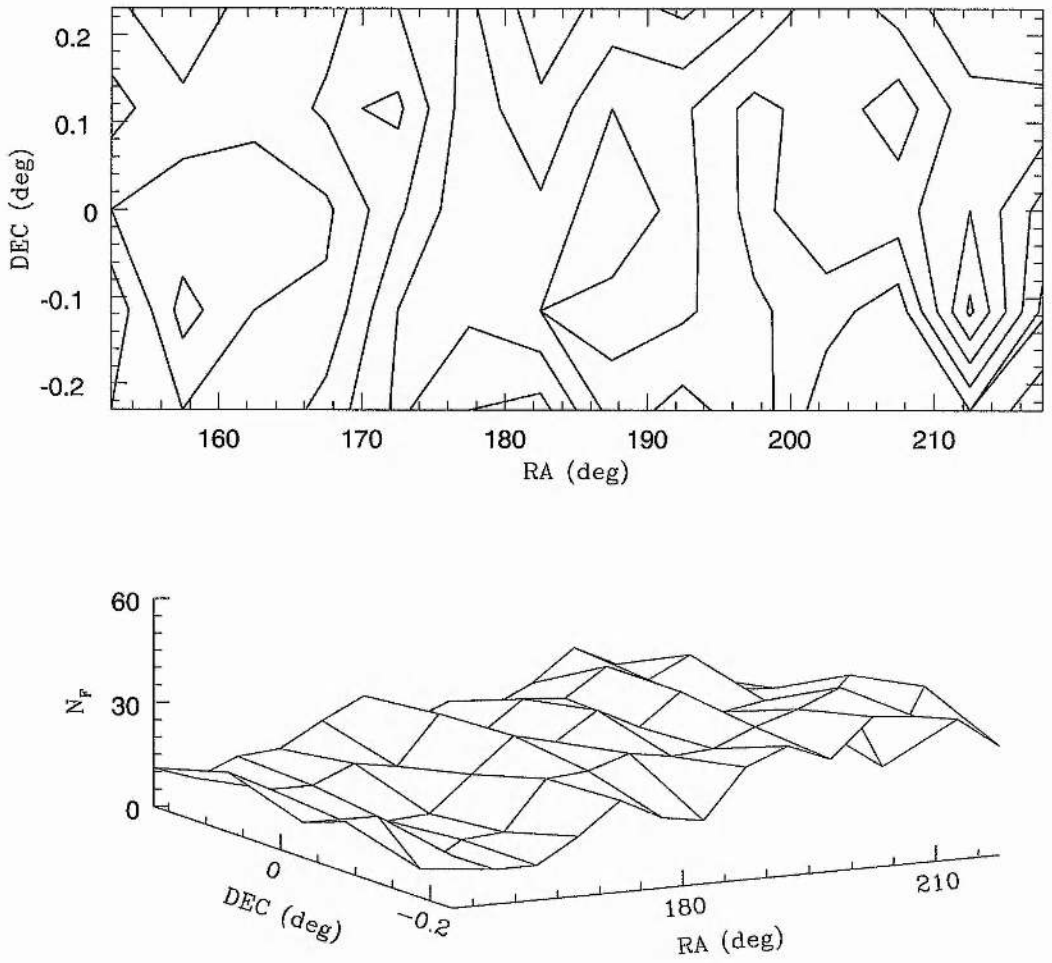

Figure 3.7: A contour (upper) and surface (lower) plot of the F-star distribution. The large scale (galactic) stellar distribution is clearly visible. The contours are evenly spaced at intervals of ΔN_F=5 between N_F=10 and N_F=60.

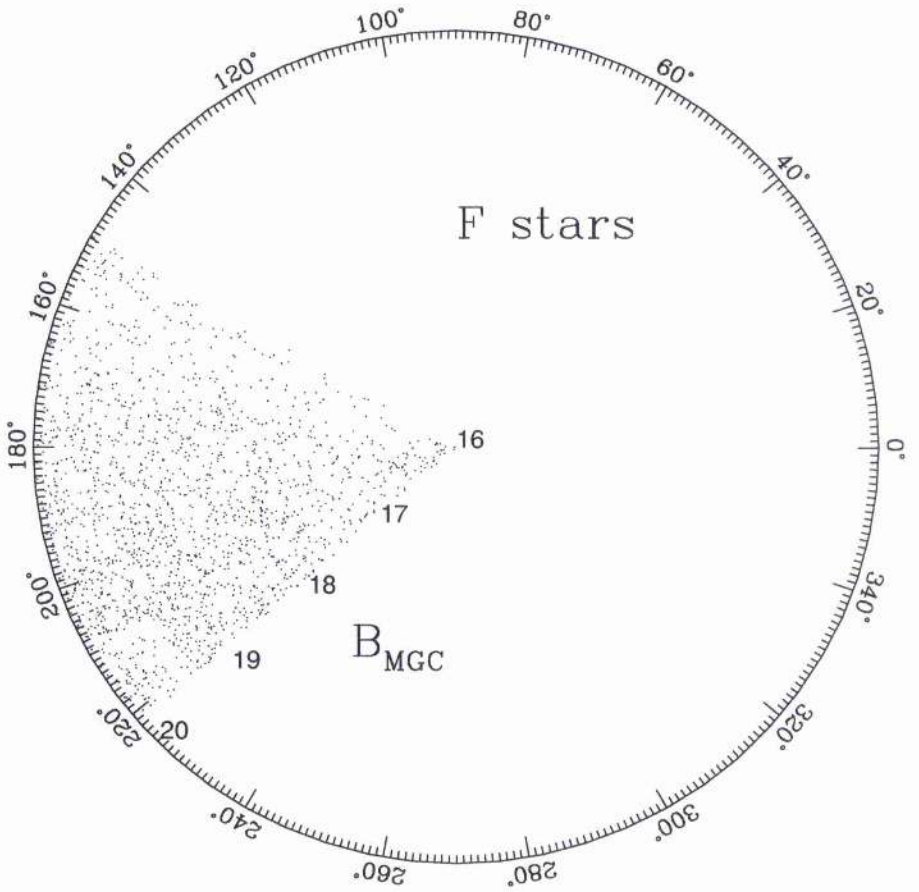

Figure 3.8: A 'pie-diagram' plot of RA and B_{MGC} for the F-star sample contained within the whole MGC b & l range.

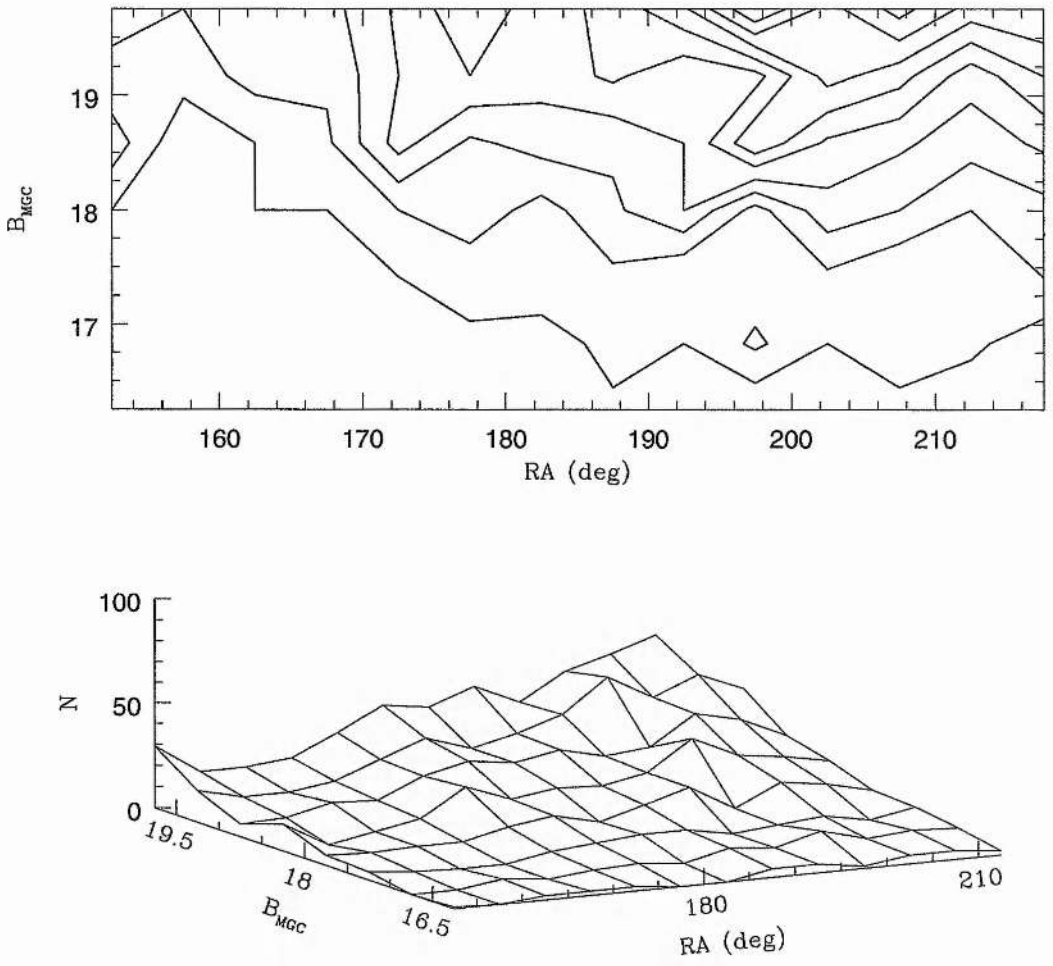

Figure 3.9: A contour and surface plot of the F-stars in RA-magnitude space. The contours are evenly spaced at intervals of ΔN=5 between N=10 and N=60.

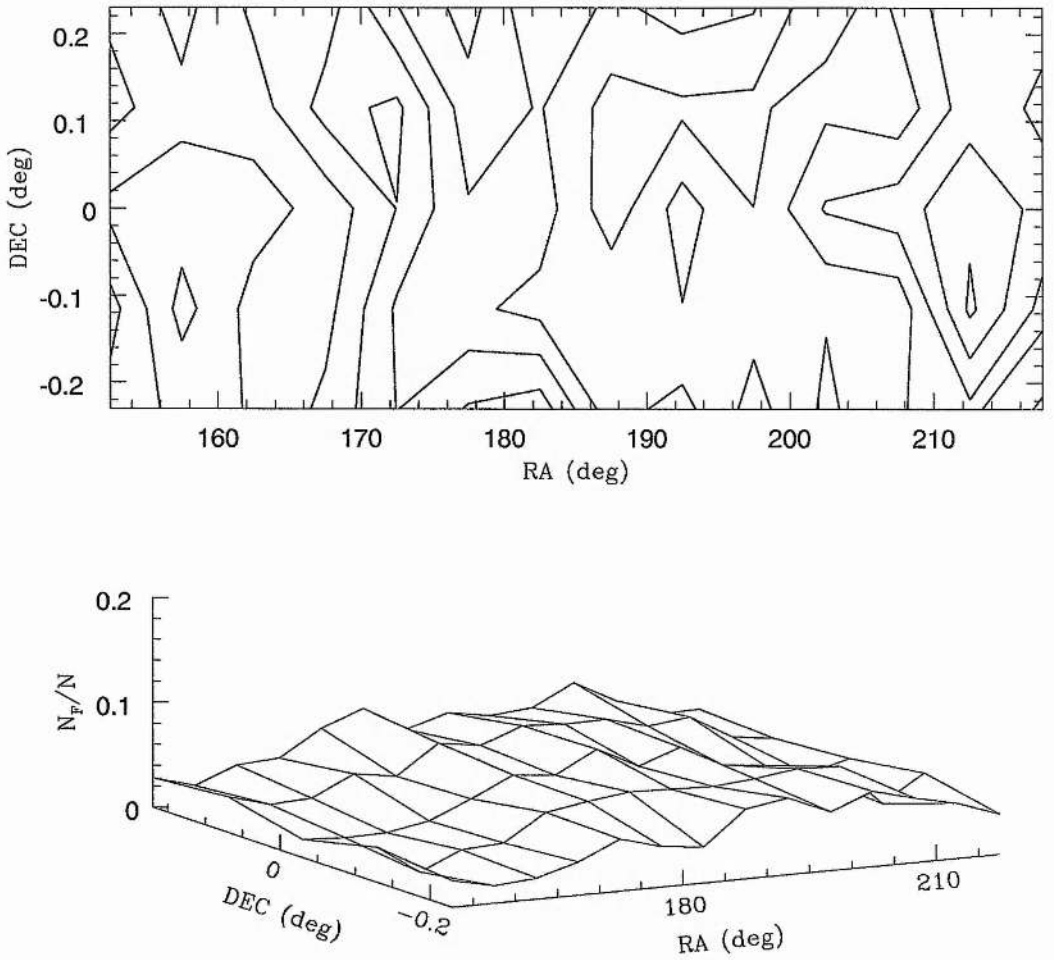

Figure 3.10: A contour (upper) and surface (lower) plots showing how the F-star distribution ($N_{\rm F}$) compares to the full stellar distribution (N). The contours are evenly spaced at $\Delta\frac{N_F}{N}$=0.01 intervals between $\frac{N_F}{N}$=0.01 and $\frac{N_F}{N}$=0.15.

3.3.3.2 Angular correlation function

An alternative means of quantifying clustering on the sky is through the well-known angular correlation function, $\omega(\theta)$. This approach has been used widely to analyse the clustering properties of galaxies (e.g. Groth & Peebles 1977; Shanks et al. 1980; Maddox, Efstathiou & Sutherland 1996; Collins, Heydon-Dumbelton & MacGillivray 1989, Cabanac, de Lapparent & Hickson 200, Kummel & Wagner 2000 and Couch, Jurcevic & Boyle 1993). Applications of the angular correlation function to samples of faint stars have been limited. Gilmore, Reid & Hewett (1985) derived the two-point correlation function of their large sample of faint, $B_J < 19.5$, Galactic stars, derived from photographic plates covering ≤ 30 square degrees at high Galactic latitude, and showed that it was flat, consistent with a 'complete absence of clustering'. These authors used this to argue that their star-galaxy separation was robust, and that patchy reddening was not important. They did not quantify what 'complete absence' meant in terms of limiting the existence of substructure. Doinidis & Beers (1989) analysed the angular correlation function of 4400 candidate field horizontal branch stars over 2300 square degrees, finding evidence for clustering on angular scales of $\leq 10''$, or physical scales of ≤ 25 pc for the characteristic magnitude of the sample. They did not consider the clustering properties of more general field stars.

Here we want to quantify the (absence of?) features seen in the stellar angular correlation function. Of the different methods devised for measuring $\omega(\theta)$ we adopt the method used in Shanks et al. (1980) and Collins, Heydon-Dumbelton & MacGillivray (1989):

$$\omega(\theta) = \frac{N_{ss}}{N_{rr}} - 1 \tag{3.2}$$

Here N_{ss} is the number of star-star pairs with separation θ and N_{rr} is the number of simulated random-random pairs, again with separation θ. In practice we follow the same methodology as Doinidis & Beers (1989). In what follows, $\omega(\theta)$ will be derived from the mean random number of pairs calculated from 200 simulations. The simulations take into account the Galactic large scale stellar gradients and contain the same number of simulated stars as found in each sample. We calculate $\omega(\theta)$ for the range $0 < \theta < 5$ deg with $\Delta\theta$=0.1°. Figs. 3.11, 3.12 & 3.13 display $\omega(\theta)$ as a function of θ for a bright F-star sample (limited brighter than $B_{\rm MGC} = 19$), the full F-star sample, and the total SDSS matched stellar distributions respectively.[1]

The angular correlation functions are essentially flat, with zero mean angular correlation function, fully consistent with a random distribution and no excess clustering at greater than the 3-σ level of significance. In Fig 3.12 $\omega(\theta)$ has both a mean and standard deviation of less than 0.005. The fluctuations detected may reflect simply statistics, as indicated by the variation seen in simulated random distributions, or may be in part attributable to patchy reddening/extinction (see Hewett (1983)). To illustrate, the spatial distribution of stellar colour in bins of size 0.2° by 0.1° is shown in Fig. 3.14 (limited to the first three degrees of the survey); although there is a mean of only 10 stars in each RA-DEC bin, the standard deviation in colour ($\sigma_{\overline{(u^*-g^*)}}$=0.2) is significantly smaller than the mean standard deviation of colour across all bins ($\overline{\sigma}$=0.6). This uniformity of the colour indicates that the observed fluctuations are not due to random errors alone but that patchy reddening may contribute to the fluctuations on scales less than a degree.

[1] In order to save on computational time, for the total stellar distribution only 50 random simulations were used.

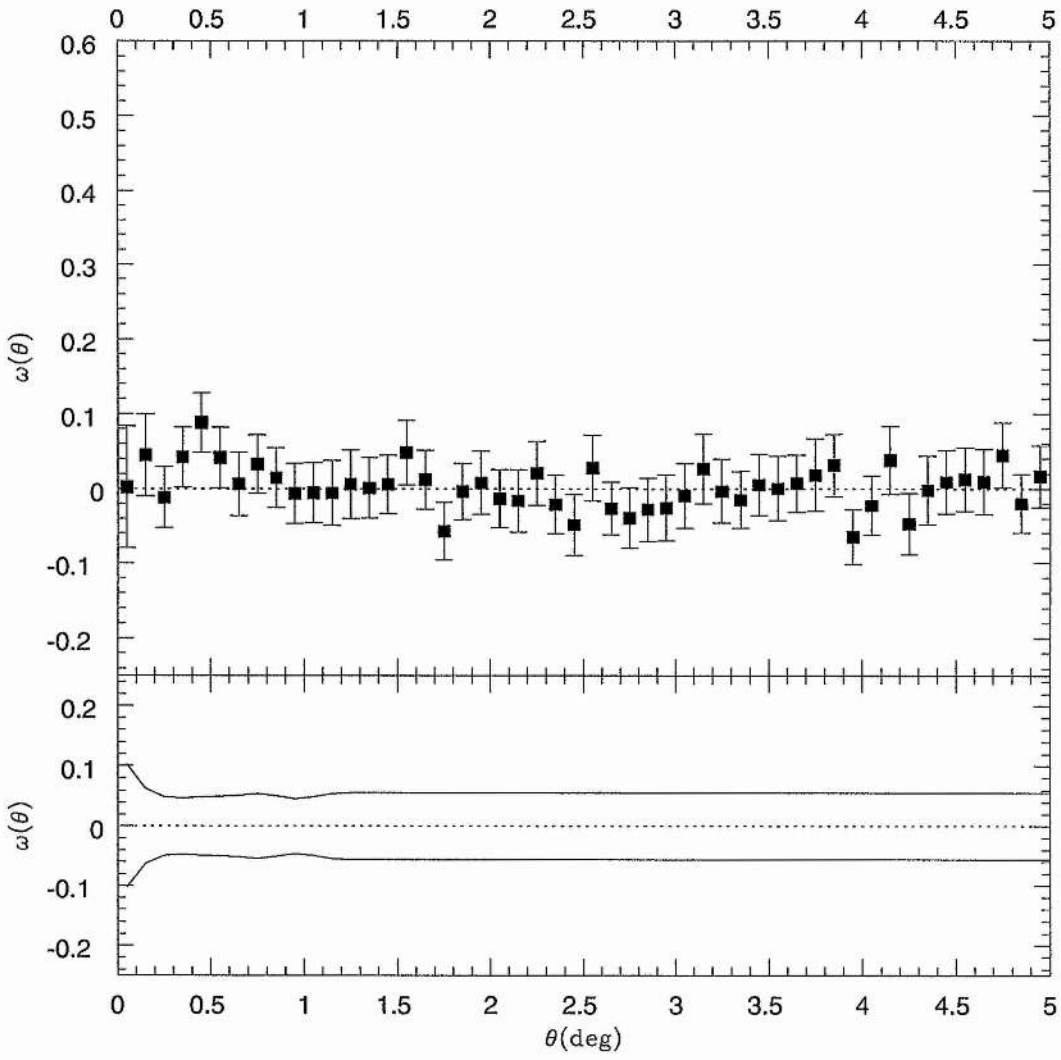

Figure 3.11: The upper panel shows the angular correlation function, $\omega(\theta)$, for the bright, $B_{\rm MGC} < 19$, F-stars, as a function of angular separation, θ. The mean correlation function is shown by the dotted line and is flat and essentially zero. The errors shown are $\pm 1\sigma$ limits about the mean of each bin. No point is more than 3σ deviant. The lower panel shows the correlation functions of 200 random simulations, taking account of the overall gradient in stellar number density of the sample. The solid lines indicate the 1σ range of the simulations correlated about themselves; the fluctuations in the measured data correlation function are again seen to be at most about 3σ away from random.

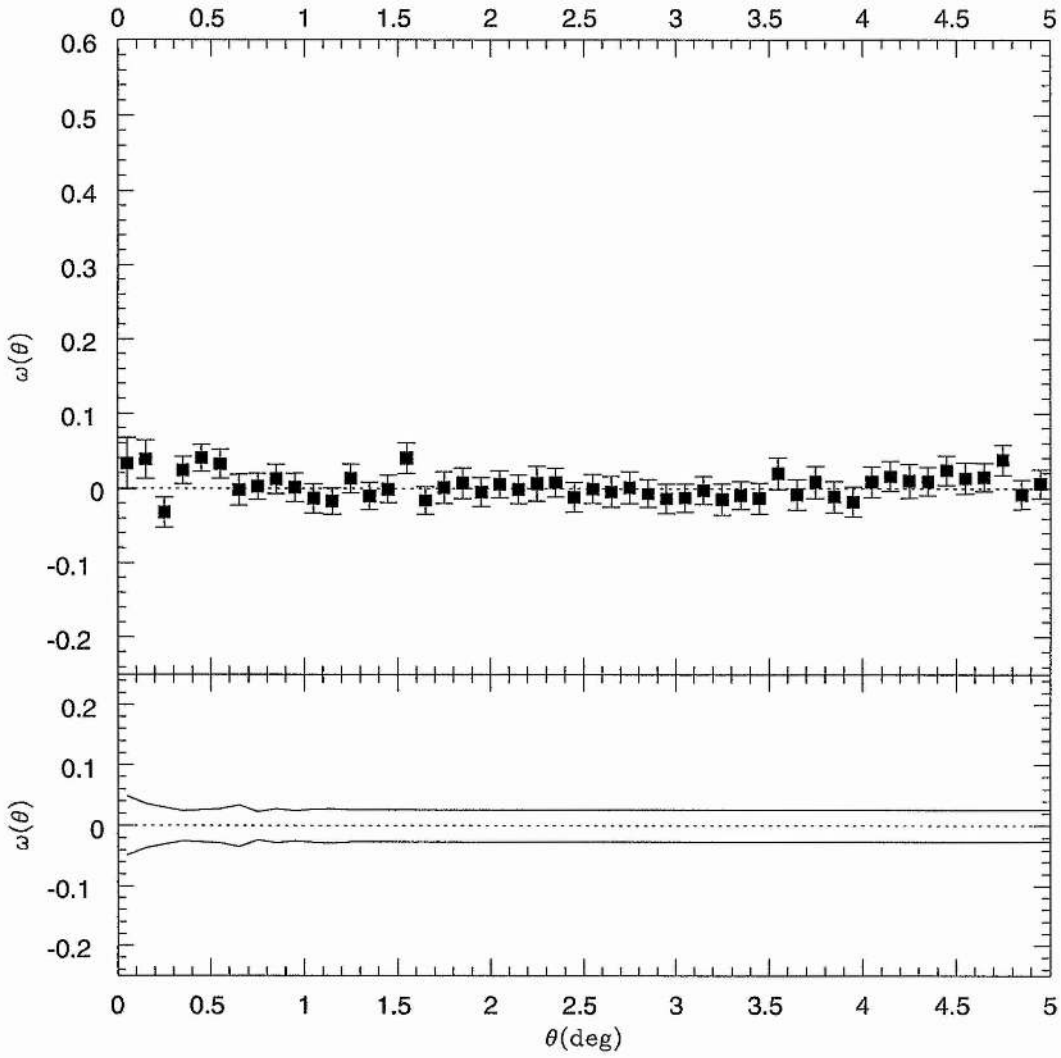

Figure 3.12: As Figure 3.11, but for all the F-stars, with no magnitude cut. Again the upper panel is the measured angular correlation function and the lower panel the results of random simulations. Again no deviations more significant than 3σ are seen.

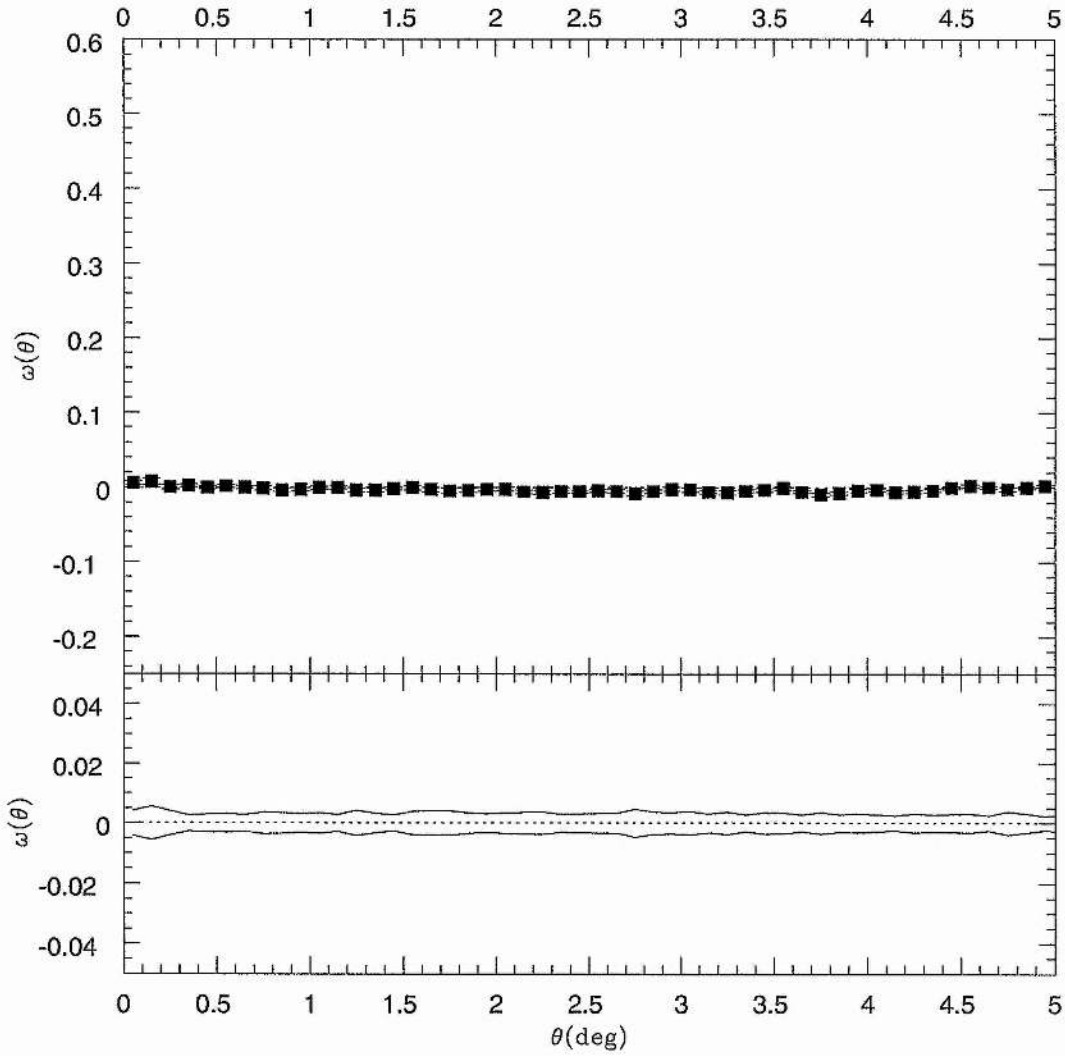

Figure 3.13: As Figure 3.11, but for the full SDSS-matched stellar sample. Again the upper panel is the measured angular correlation function and the lower panel the results of random simulations. Again no deviations more than 3σ significant are seen.

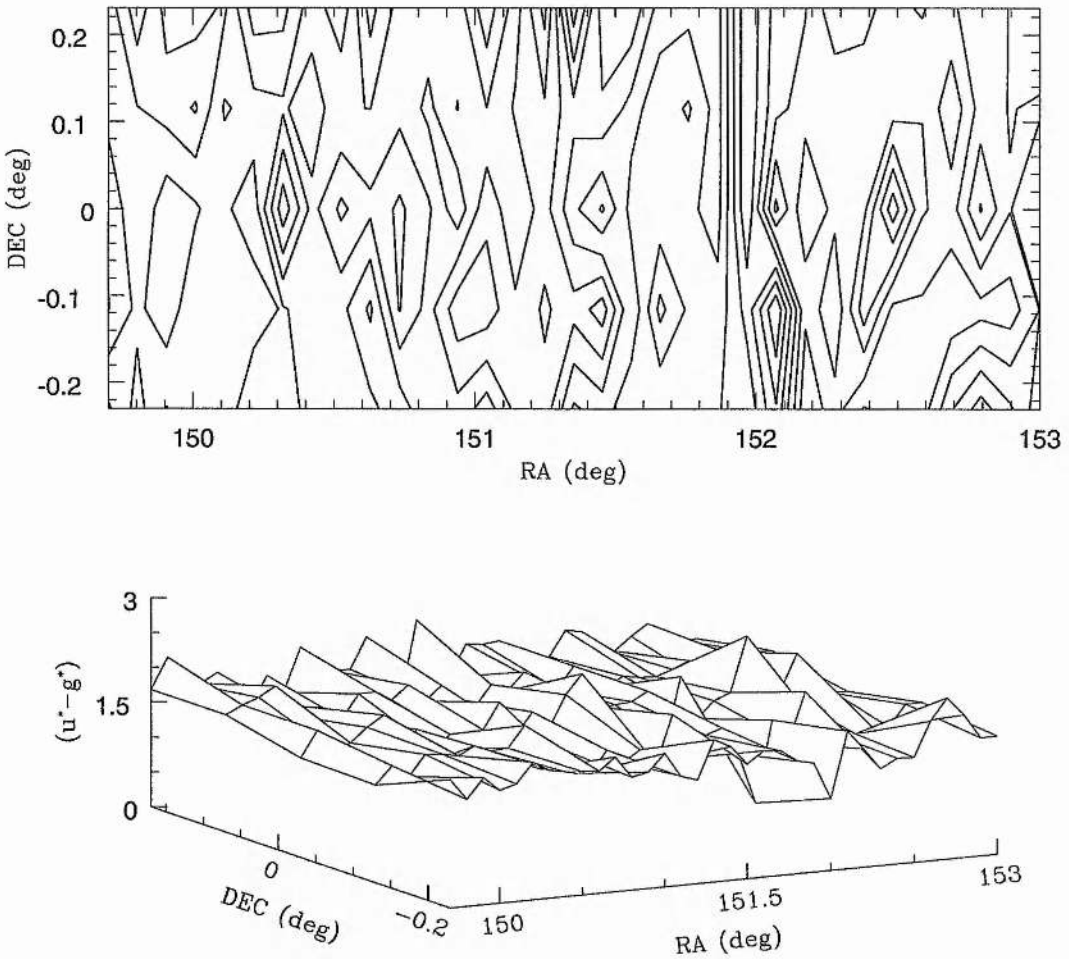

Figure 3.14: A contour (upper) and surface (lower) plot of the colour distribution in the first 3 degrees of the MGC strip. The contours mark the colour range $0.2 < (u^* - g^*) < 3$ in 0.2 intervals. The observed fluctuations have narrow colour ranges are not thus probably not due to random effects alone (see text). This may reflect reddening that is patchy on scales of $\sim 1°$.

3.3.3.3 The Lee 2d statistic

The angular correlation function contains only low-level suggestion of any clustering, indeed limiting substructure to very low amplitude. The counts-in-cells did hint at substructure, but again at low significance. When examining just the F-stars and the F-star-all star ratio (see Figs 3.7 & 3.9 and 3.10) we have found that there are some small overdensities of faint stars towards the end of the MGC strip. We now turn to more innovative tests for clustering, to see if they can either place more stringent limitations, or indeed reveal low-level clustering with more significance.

The Lee 2d statistic (Lee 1979) has been used previously mostly in studies of substructure in clusters of galaxies, and indeed has been found to be the more sensitive test to the presence of structure (Rhee, van Haarlem & Katgert 1991) when compared to the angular separation test of West, Oemler Jr & Dekel (1998) (formally similar to the angular correlation function). A detailed discussion of the Lee statistic can be found in Fitchett (1988). The Lee 2d statistic is essentially a likelihood ratio, with the statistical analysis analogous to looking for the maximum likelihood split of a two-dimensional data set into two similar clumps.

The Lee statistic is calculated by projecting the data perpendicularly on to a line. At each point along this line a measure of the clumpiness of the data is found and a maximum determined, $\mathrm{L}(\theta)$. The clumpiness is determined at each point/partition along the line by measuring the deviation away from the mean (or Gaussian distribution) of all the points to the left and right of the partition. This is then compared to the deviation away from the mean of the total data set. In this way any underling large-scale structure gradient is "flat fielded" out. The line is then rotated by some small amount, $\Delta\ \theta$, and the process is repeated. From this we can plot $\mathrm{L}(\theta)$ against θ, the maximum of which, $\mathrm{L}(\theta)_{\mathrm{max}}$, indicates the position angle of a line partitioning the data into two clumps. The Lee 2d statistic has been used to look for substructure within galaxies, clusters of galaxies (Fitchett & Webster 1987; Rhee, van Haarlem & Katgert 1991) and in simulations of clusters (Crone, Evrard & Richstone 1996). We now apply it to our high-latitude stellar data set.

We first apply this test to the (projected) angular distribution on the sky of the entire SDSS matched stellar data set. The data are shown in the lower panel of Fig. 3.15 and the values of the Lee statistic $\mathrm{L}(\theta)$ for this sample are shown in the upper panel. The position angle, θ_{max}, of the maximum of the Lee statistic is indicated in the lower panel.

The $\mathrm{L}(\theta)$ curve shows a rather broad peak, indicating only a low-significance detection of an over-density; a stronger detection would result in a more obvious peak. The value of the angle at which the Lee statistic has its maximum, $\theta_{\mathrm{max}} = 92.1$, indicates that the overdensity is located towards the top right of the lower plot, again at high values of RA (as in the earlier statistical tests). The significance of this detection can be quantified by the analysis of randomly distributed data-sets. Thus we fill the MGC survey area with the same number of stars as found in the high latitude sample, but randomly distributed (remember that any large-scale gradient is removed by the analysis technique). Fig. 3.16 shows the simulated data-set, as well as the corresponding $\mathrm{L}(\theta)$ plot. The angle at which $\mathrm{L}(\theta)_{\mathrm{max}}$ occurs is now 90.7°, the slight offset from the perpendicular being understandable as due to the uneven distribution of MGC exclusion regions.

We note that for the simulated data the L_{rat} statistic is higher, indicating a more significant detection (of the MGC holes), than in the real data. This can be explained by noting that in the simulations there was no minimum star-star separation used. Therefore the simulated stellar distribution will be slightly smoother than the real data, making the effects of the MGC holes more apparent in the simulation. This implies that any result from the Lee 2d test will provide only a rough estimate on the size of the clustering signal. The lack of a minimum star-star separation in the simulated data should not have affected the $\omega(\theta)$ test as it is only dependent on the number of stars at a given radius and not their distribution about a partition.

Taking the ratio of $\mathrm{L}(\theta)_{rat}$ $\left(= \frac{L(\theta_{\mathrm{max}})}{L(\theta_{\mathrm{min}})}\right)$ for the simulated and real data we find that

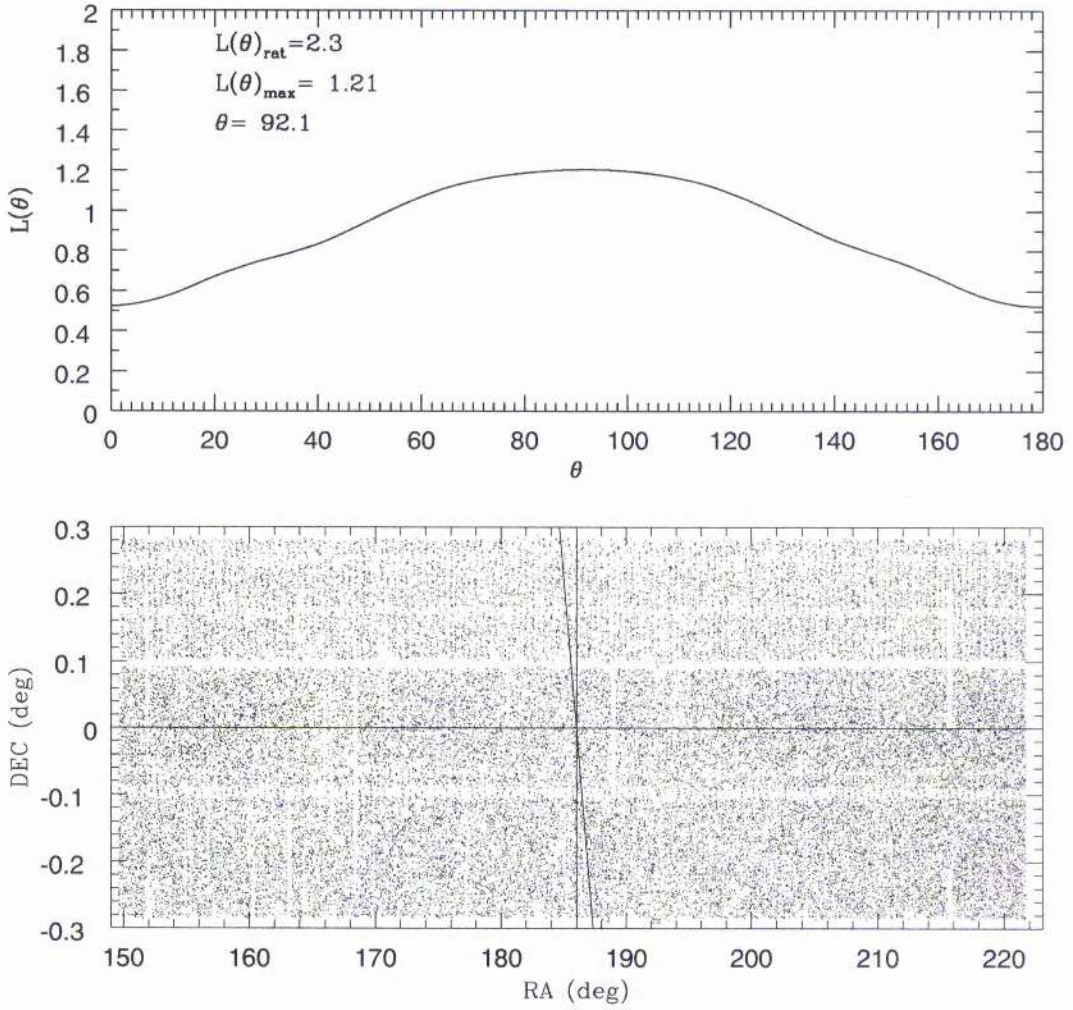

Figure 3.15: Upper: A plot of $L(\theta)_{max}$ for the high latitude stellar sample. Lower: The full MGC-SDSS stellar sample on the sky.

Table 3.2: The best fit model in each magnitude bin using all data at $b > 45°$.

$B_{\rm MGC}$	(c/a)	χ^2
$18.0 < B_{\rm MGC} < 18.5$	0.57 ± 0.06	1.45
$18.5 < B_{\rm MGC} < 19.0$	0.52 ± 0.05	1.17
$19.0 < B_{\rm MGC} < 19.5$	0.54 ± 0.04	1.44
$19.5 < B_{\rm MGC} < 20.0$	0.65 ± 0.04	1.45

the over-density seen in the MGC region is detected at 8% $\left(= 100 \times \mathrm{mod}\left(1 - \frac{L(\theta)_{rat_{MGC}}}{L(\theta)_{rat_{MGC-sim}}}\right)\right)$ above a smooth stellar distribution.

To summarise the Lee 2d scheme, an angle *theta* defines a line, and every star is projected onto that line, defining a partition point for each star. The clumpiness/asymmetry parameter L(θ) is then calculated for all stars/partitions along the line and the largest value of L(θ) is found for that line/angle. The MGC RA and DEC coordinates of the star whose partition gave that value of L(θ) is then used as the coordinates of the over-density. By doing this we find the structure to be placed at RA=216.5° and DEC=0° which is consistent with visual inspection of the distribution of the stars. This coincides with the detection of the Sagittarius dwarf tidal stream found by Yanny et al. (2000), Vivas et al. (2001) and Ibata et al. (2001). As above, this likely is due to the A-stars in the sample, which, being some four magnitudes intrinsically more luminous than are F-stars, would be at the appropriate distance at these magnitudes.

Having shown that the Lee 2d statistic is sensitive to substructure, we now investigate the signal for the bulk of the halo by using only the brighter F-stars, in the magnitude range $17.5 < B_{\rm MGC} < 19$. Figs. 3.17 and 3.18 show the results of the Lee 2d test for the real and simulated (random distribution) F-star population. We find a deviation away from a random distribution of 12.6 per cent with the structure now placed at RA=205° and DEC=0°. Again this places it within the 2-D coordinate space covered by Sagittarius dwarf tidal stream. However, as this tidal stream is found by Yanny et al. (2000) to be at distances greater than can been seen to using this F-star sample the small overdensity we are detecting could be the result of A-star contamination in the sample. We find no other evidence of clustering.

3.3.4 Halo Flattening Revisited

Although there is no strong detection of structure within the Galactic halo we decided, to be conservative, to re-fit the star-count models to a restricted sub-sample. We now fit to star count data at $b > 45°$ and for data in the range $b > 45°$ and $l < 340°$ (see Tables 3.2 & 3.3). This was done to minimize the contributions from the thin/thick disks and the thin/thick disks and bulge respectively. Note that this longitude cut also serves to remove any effects of the Sagittarius Dwarf tidal stream. Fig. 3.19 shows the effect of removing the low latitude and high longitude fields from the χ^2 fitting; a stellar halo with an axial ratio of (c/a)=0.52±0.05 now provides the best fit to the data.

A further refined sample contains only MGC-SDSS matched stars with $(u^* - g^*) > 0.6$. Although there are 2418 fewer stars in this sub-sample than in the full stellar sample 1021 of the rejected stars having $(u^* - g^*) < 0.6$, this sub-sample should now be free from any spurious effect that may have been induced by the possible inclusion of QSOs (previously identified as the fuzzy patch in Fig. 3.4).

Table 3.4 shows the best fit halo axial ratio in each magnitude bin for the sample with

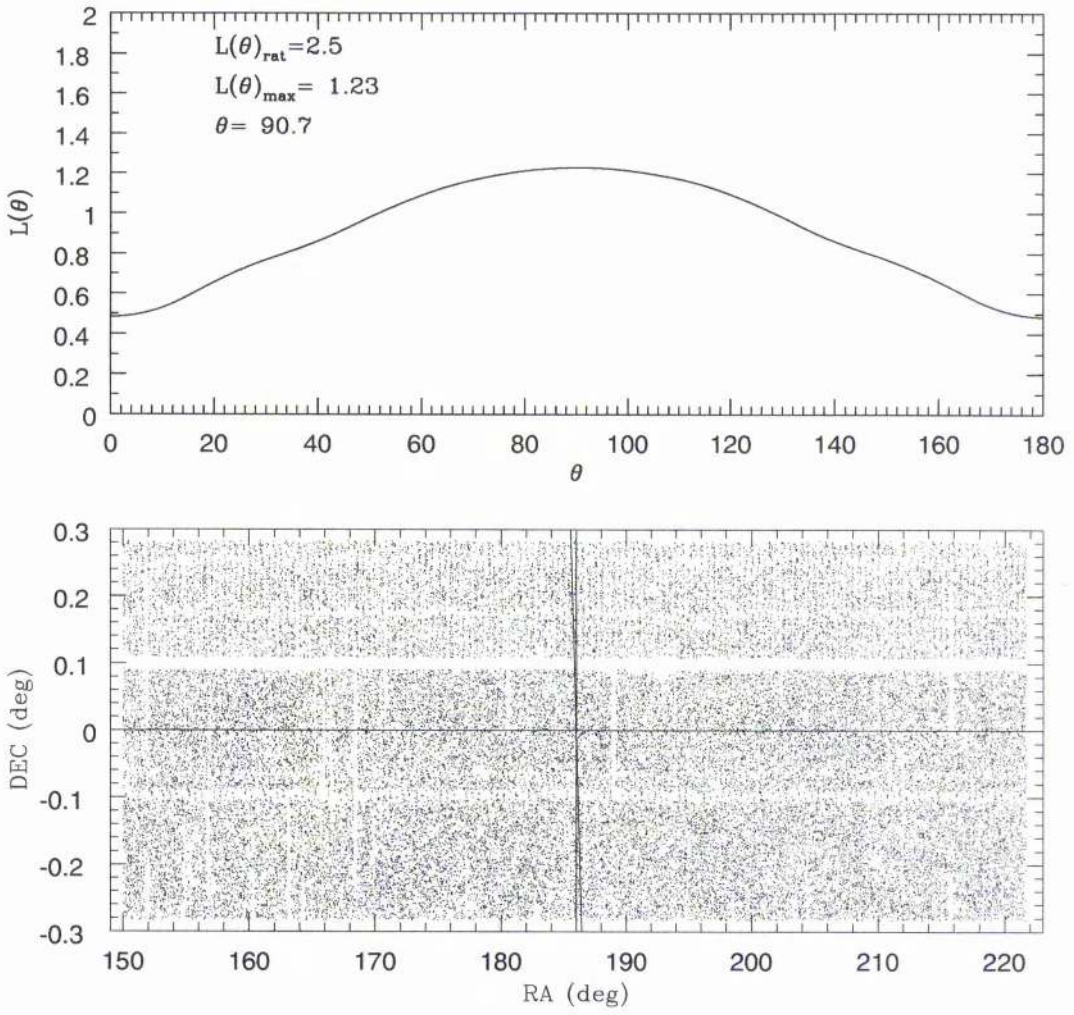

Figure 3.16: Upper: A plot of $L(\theta)_{max}$ for the simulated high latitude stellar sample. Lower: The full simulated stellar sample.

Table 3.3: The best model in each magnitude bin in using all data at $b > 45°$ & l <340°.

B_{MGC}	(c/a)	χ^2
$18.0 < B_{MGC} < 18.5$	0.49 ± 0.08	1.49
$18.5 < B_{MGC} < 19.0$	0.53 ± 0.06	1.18
$19.0 < B_{MGC} < 19.5$	0.59 ± 0.04	1.44
$19.5 < B_{MGC} < 20.0$	0.70 ± 0.03	1.45

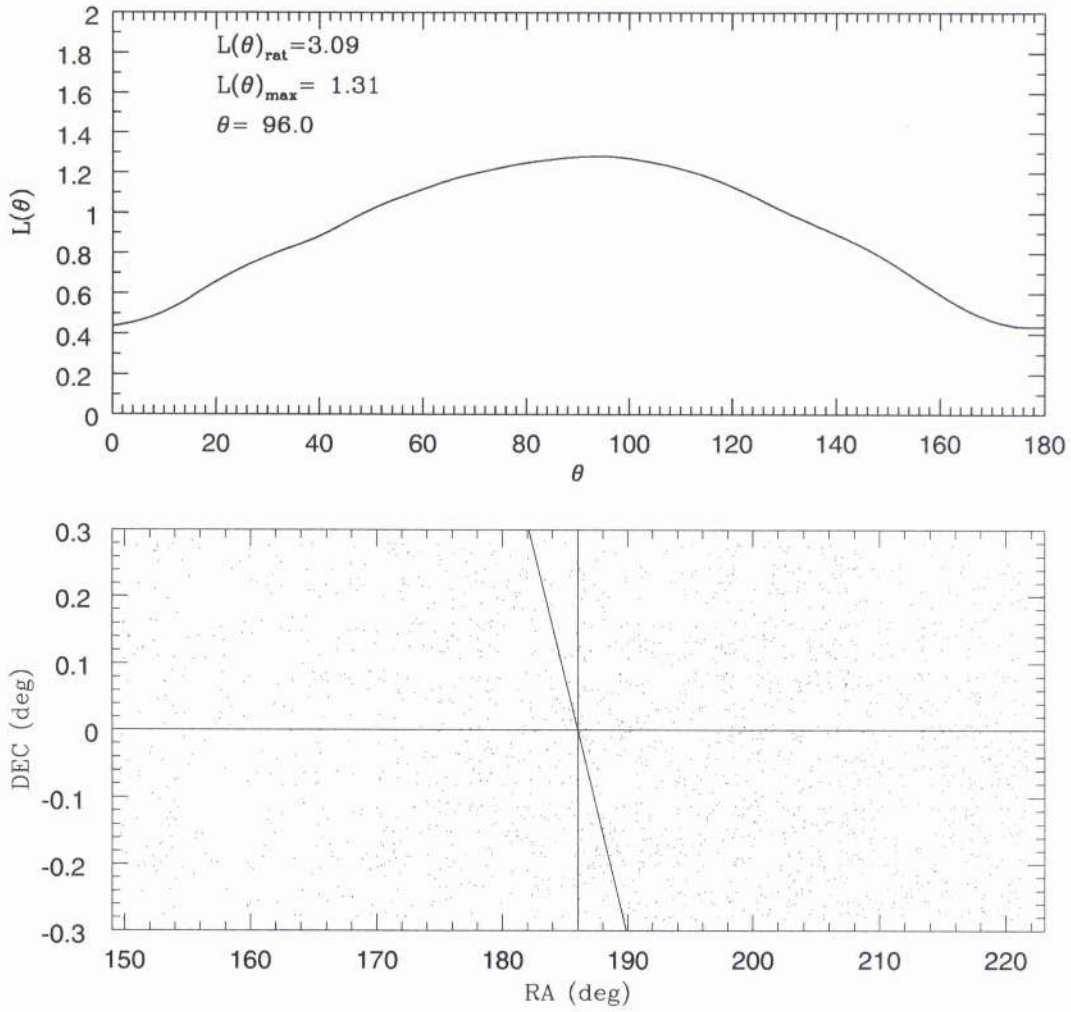

Figure 3.17: The Lee 2d test for the F-star sample. The upper and lower panels are the same as in Fig. 3.15.

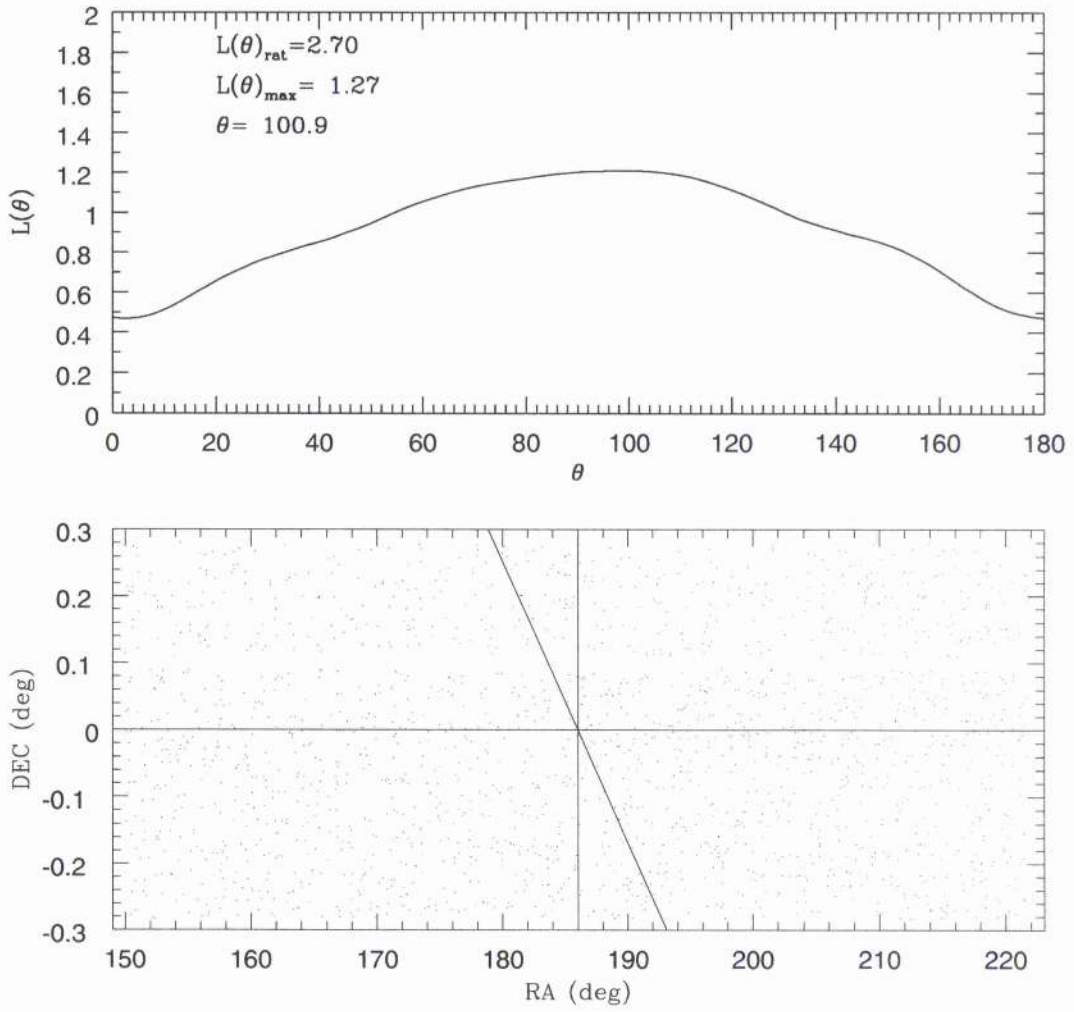

Figure 3.18: The Lee 2d test for the simulated F-star sample. The upper and lower panels are the same as in Fig. 3.16.

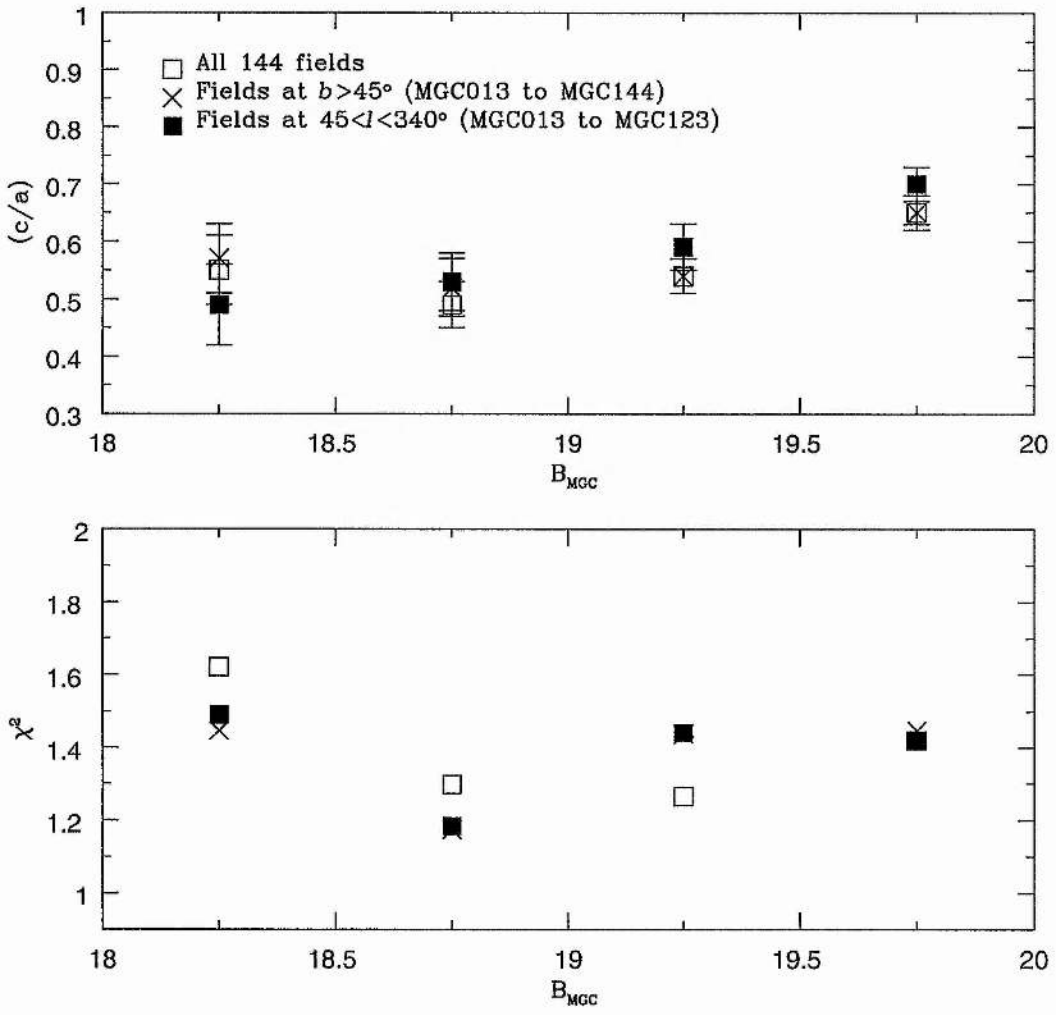

Figure 3.19: Here we show the effect on the favored axial ratio of the stellar halo of removing the low ($b < 45°$) Galactic latitude and high ($l > 340°$) Galactic longitude fields from the χ^2 fitting.

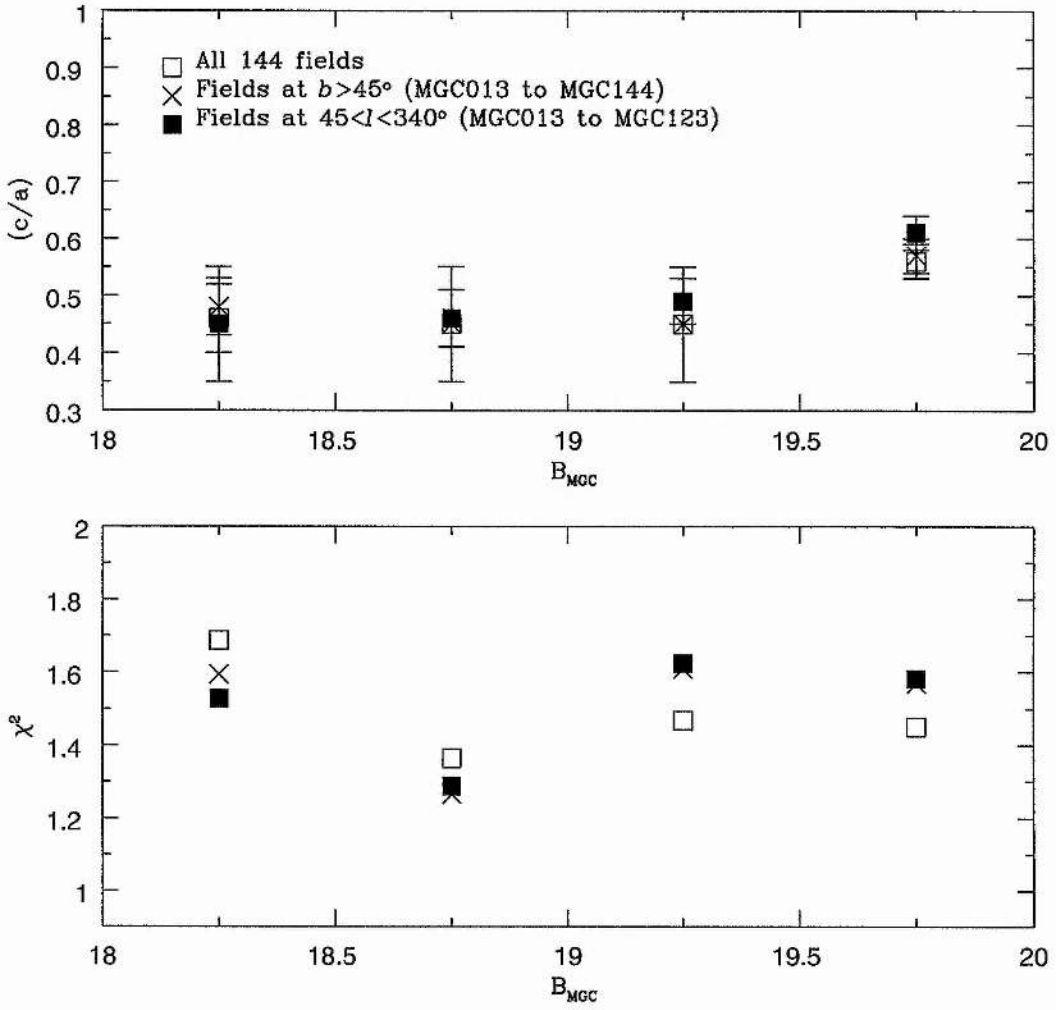

Figure 3.20: Here we show the effects of using a potentially cleaner sample, one consisting of only MGC-SDSS matched stars with $(u^* - g^*) > 0.6$.

Table 3.4: The best model in each magnitude bin using colour selected stars, with $(u^* - g^*) > 0.6$, at $b > 45°$ & $l < 340°$.

$B_{\rm MGC}$	(c/a)	χ^2
$18.0 < B_{\rm MGC} < 18.5$	0.45 ± 0.10	1.53
$18.5 < B_{\rm MGC} < 19.0$	0.46 ± 0.10	1.28
$19.0 < B_{\rm MGC} < 19.5$	0.49 ± 0.06	1.62
$19.5 < B_{\rm MGC} < 20.0$	0.61 ± 0.04	1.58

Galactic latitude and longitude cuts, and Fig. 3.20 compares the results from this reduced sample to the original one. In fact the χ^2 values and overall shape of the "axial-profile" remain more or less the same. It is only the value of the halo axial-ratio that has changed, with the reduced sample preferring a slightly more flattened halo, with $(c/a) = 0.45 \pm 0.1$. Note that as the models are only generated within the range $0.45 \leq (c/a) \leq 0.8$, any 'best-fit' model with an axial ratio less than 0.45 is spurious and simply represents a lack of stars within the magnitude bin and b and l range being tested.

The star-count models are then fitted to the full MGC stellar sample, to the MGC-SDSS sample and to the F-star sample in the magnitude range $18 < B_{\rm MGC} < 19$, both with and without the b and l cuts. In doing this we find that the best fit comes from the full MGC stellar sample with both the b and l cuts and gives an axial ratio of (c/a)=0.61 $\pm$0.02. However, the axial ratio with the smallest error is given by the F-star sample, again with both the b and l cuts, (c/a)=0.56$\pm$0.01.

3.4 Summary

We have used a sample of 42457 stars from the MGC-Bright photometric catalogue, most of which ($\sim$ 97 per cent) have SDSS-EDR counterparts, to investigate the structure of the stellar halo of the Milky Way. The MGC-SDSS matched objects were used to define colour selection limits allowing us to isolate a sample of F-stars.

After an initial estimate of the best-fit value of the axial ratio of an oblate stellar halo, we employed a variety of statistical tests to quantify the level of substructure in both the full stellar sample and a restricted F-star sample. For the F-stars, we also looked at substructure as a function of apparent magnitude.

We conclude that the stellar halo of the Milky Way is significantly flattened, with an axial ratio of (c/a)=0.56$\pm$0.01. While this result is in line with previous determinations, it is more robust, having been derived from samples cleaned of substructure and with contamination from quasars and other stellar components minimised.

We find only some weak evidence for substructure beyond the known Sagittarius streams at these relatively bright magnitudes, with F-stars probing distances typically $\leq$ 10 kpc from the Sun. This essentially null result implies that recent accretion of stellar systems is not important in the bulk of the stellar halo. Quantification of limits on the disruption rate of putative satellites needs to be investigated, but is beyond the scope of the present paper. However these firm limits of observable clustering need to be included in future hierarchical clustering models.

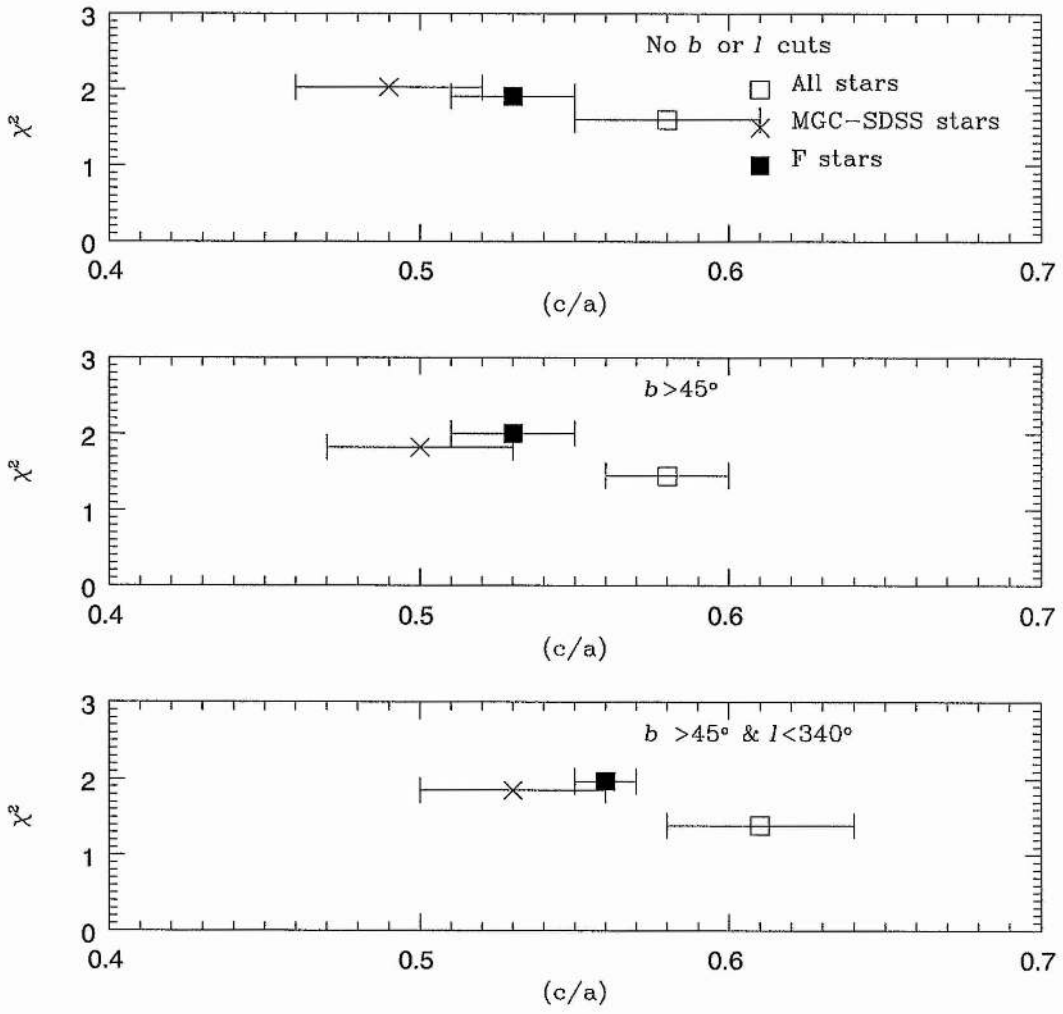

Figure 3.21: A graphical summary of all the best fit star-count models for each stellar sample.

CHAPTER 4

Galaxy Number Count Modeling

In this chapter we derive the galaxy counts from the MGC-BRIGHT and MGC-FAINT catalogues. The MGC-BRIGHT galaxy counts we use to constrain the Schechter function parameters. The work in this chapter was performed using code supplied by Dr's Jo Liske and Simon Driver.

4.1 Cosmology, evolution, the LF and number counts

In Chapter 1 we saw that it was first argued in Hubble (1926b) that by plotting the number of galaxies (N) in each apparent magnitude bin (m) one can discriminate between different cosmologies and/or evolutionary models. In a Euclidean universe the relation $\log N \; \alpha \; 0.6m$ should hold true, see Appendix B.3. As can be seen in Fig. 4.6 this is clearly not the case and so a Euclidian universe is ruled out. However, things get more complicated as the LF parameters, cosmology and galaxy evolution all influence the number counts [1].

Fig. 4.1, top left, shows how the matter density parameter, Ω_m, affects the B-band galaxy number counts. Note how faint (and hence how far) one needs to observe in order to see the effects of Ω_m. In an open universe (low Ω_m) the volume over which galaxies are observed increases which in turn increases the galaxy number counts. For a closed universe (high Ω_m) the volume over which galaxies are observed decreases which in turn decreases the galaxy number counts. The inclusion of Λ acts in the same way as reducing Ω_m, increasing the observed volume and galaxy number counts.

Galaxy evolution, broadly speaking, comes in two types: luminosity evolution and number evolution, see Fig. 4.1, top right. The former is due to passive stellar evolution i.e the stars in a galaxy getting older, redder and fainter. This causes the volume over which the galaxies are seen to increase, and hence, increase number of galaxies at the faint end of the number counts (a horizontal shift in the LF). PLE takes the form $B_{\rm MGC}$=$B_{\rm MGC}$+2.5log $((1+z)^m)$ (Bruzual & Charlot 1993). Number evolution arises from galaxies merging with each other. Specifically, dwarf galaxies being "swallowed up" by the larger E/S0 and S galaxies. This results in a dip in ϕ at each redshift bin (a vertical downward shift in the LF) and hence a drop in the overall number of galaxies in each absolute magnitude bin. However, as dwarf galaxies being the most numerous, are also the most faint the most significant effect of number evolution is seen at the faint end of the galaxy number counts. PNE takes the form $\phi = \frac{\phi}{(1+z)^n}$. Note how evolution can have a similar effect on the faint number counts as changing the density parameter, Ω_m.

We now look at how changing the luminosity function parameters, ϕ_*, M_* and α

[1] It should be mentioned that they do not alter the predicted counts enough to make a Euclidean universe a viable model.

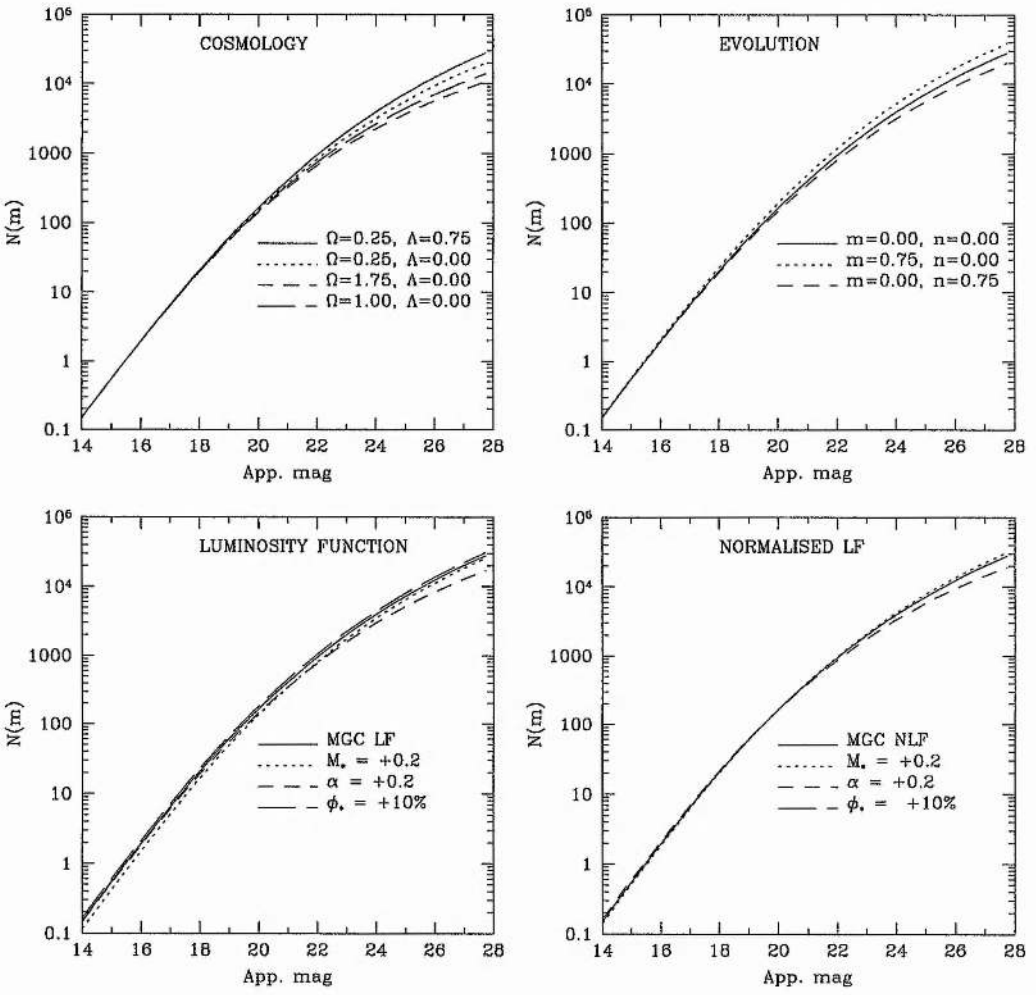

Figure 4.1: The effects of cosmology, evolution and the LF parameters on the galaxy number counts.

(see Eqn. 1.1), can affect the number counts, see Fig. 4.1, bottom left. A change in either ϕ_* or M_* simply results in the number counts being offset in N or m respectively. However, a change in α effects both N and m. The affect of lowering $|\alpha|$ is to reduce the number of dwarf galaxies in each absolute magnitude bin. And so, in the same way as number evolution, the dominant effect is only seen in the faint end of the galaxy number counts. Fig. 4.1, bottom right, shows how the uncertainties in the LF parameters affect the number count produced from the normalised MGC LF. Fig. 4.2 re-displays the effects of cosmology, evolution and LF parameters on the galaxy number counts but with the concordance model counts subtracted in order to highlight the effects of their various influences. From this we can see, bottom left, that the effects of the LF parameter ϕ_* are constant across the magnitude range. However, the effects of M_* are strongest at the bright end ($B_{\rm MGG}$ <20). For this reason we use only the counts derived from MGC-BRIGHT to constrain the LF parameters.

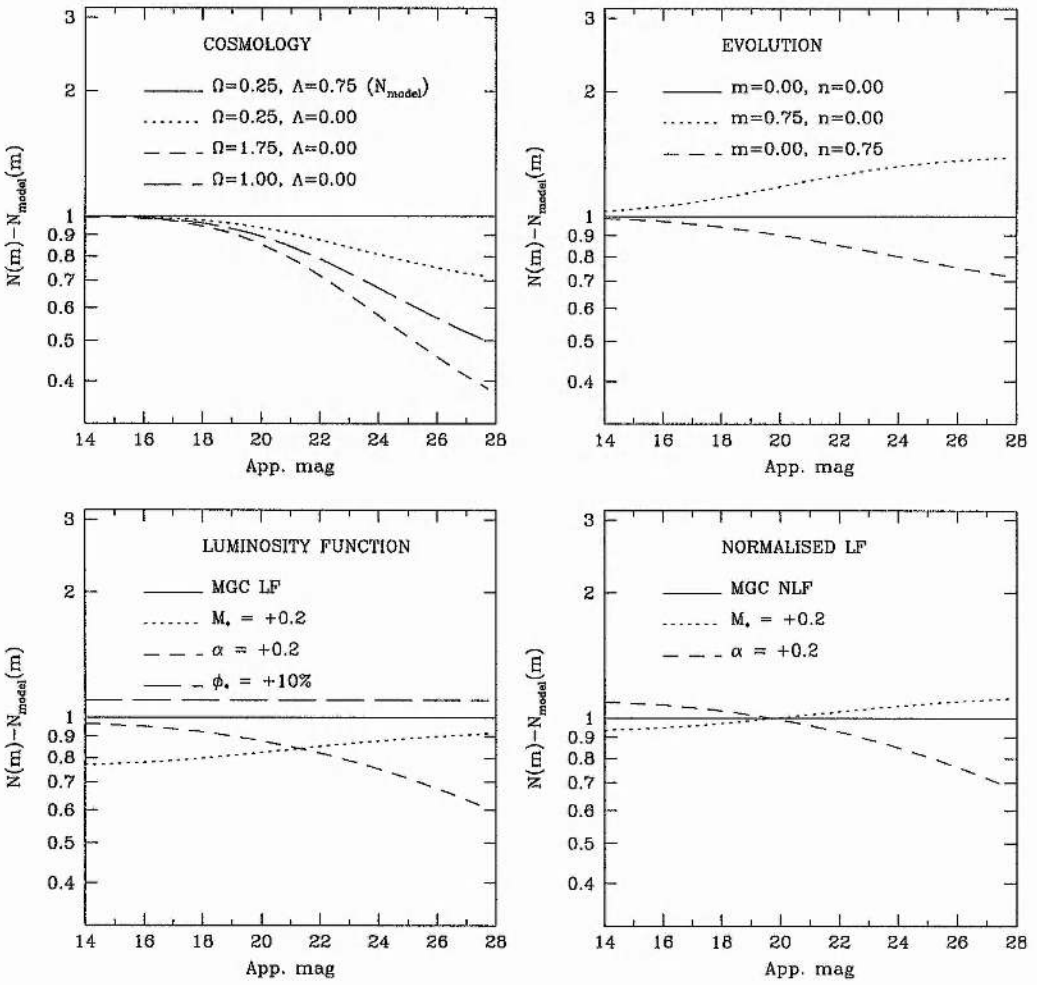

Figure 4.2: As Fig. 4.1 but with the concordance model counts subtracted.

4.2 Correcting for large scale structure

Before we can derive the galaxy counts we need to make a correction for any effect of large scale structure (LSS) present in the MGC. The correction is made because any clustering will artificially boost the number density of *field* galaxies. If the MGC where substantially bigger then the clustering correction would, theoretically, not be needed as the larger surveyed volume should render any such effects negligible. However, even the larger surveys find that some correction is still necessary. Indeed, Norberg et al. (2002) find that for $b_J < 19.2$ mag the 2dFGRS North Galactic Pole (NGP) region is over-dense by about 7% when compared to the 2dFGRS South Galactic Pole (SGP) region. As the MGC is contained within the NGP region of the 2dFGRS this implies that our data will require an LSS correction.

To correct our counts for LSS we have identified those galaxies in the 2dFGRS imaging catalogue (2dFGRS-IC[2]) that lie within the MGC survey area, excluding objects in exclusion regions. We converted the 2dFGRS-IC magnitudes to the $B_{\rm MGC}$ filter system using $B_{\rm MGC} = b_J + 0.13$ (see Eqn. 4.1). We then derived galaxy counts for the magnitude range $16 \leq B_{\rm MGC} < 19.5$ mag for both the entire 2dFGRS-IC and the 2dFGRS-IC-MGC sub-sample. These are shown in the upper panel of Fig. 4.3. Not surprisingly the counts for the full area are smoother and show that the MGC region is slightly over-dense as compared to the full survey. The middle panel of Fig. 4.3 shows the ratio of the full 2dFGRS-IC counts over the counts from the MGC region. In each magnitude bin in the range $16 \leq B_{\rm MGC} < 19.5$ mag we multiply the MGC-BRIGHT counts by these values in order to correct for LSS. The result is shown in the lower panel of Fig. 4.3. This procedure is valid regardless of any concerns over completeness and photometric accuracy of the 2dFGRS-IC. All we are assuming is that these issues affect the 2dFGRS-IC in the MGC region in the same way as in the rest of the survey.

We can not correct the counts at $B_{\rm MGC} \geq 19.5$ mag due to the magnitude limit of the 2dFGRS-IC of $b_J = 19.6$ Colless et al. (2001). In any case the LSS correction decreases with magnitude and the required correction for the last bin is already within the Poisson error. Hence it appears that at $B_{\rm MGC} \geq 19$ mag the total volume surveyed is large enough so that the counts are robust with respect to clustering. So for $B_{\rm MGC} \geq 19$ mag no LSS correction is applied to the MGC galaxy counts. Both the original and corrected counts are shown in Fig. 4.5 and tabulated in Table 4.1.

4.3 Correcting for cosmic ray incompleteness

In Section 2.3.7 we noted that the identification of cosmic rays is incomplete for $B_{\rm MGC} \geq 22.5$ mag. We now estimate the size of the incompleteness and attempt to correct the galaxy number counts.

In the upper panel of Fig. 4.4 we show as filled circles the number counts of all objects with semi-minor axis $\leq$ 1pixel, see Fig. 2.19. For $B_{\rm MGC} > 22.5$ mag the counts are a mixture of cosmic rays and real objects. At $21 \leq B_{\rm MGC} < 22$ mag the cosmic ray counts are very steep and would exceed the galaxy counts by $B_{\rm MGC} \approx 23$ mag if they did not flatten out.

The filled squares show the number counts of objects that lie in the cosmic ray band and have FWHM $< 0.9 \times$ SEEING. From taking the ratio of the two sets of counts we find that for $B_{\rm MGC} < 22.5$ mag 81.3% of all objects within the cosmic ray band also have FWHM $< 0.9 \times$ SEEING and that this ratio remains constant to within the errors, see Fig. 4.4 (lower panel). We now make the assumption that this ratio remains constant to $B_{\rm MGC} = 24$ mag . We correct the cosmic ray number counts in the range

[2]The 2dFGRS-IC should not to be confused with the 2dFGRS target list which applies a variable magnitude limit and explicitly excludes galaxies whose images are merged with other objects.

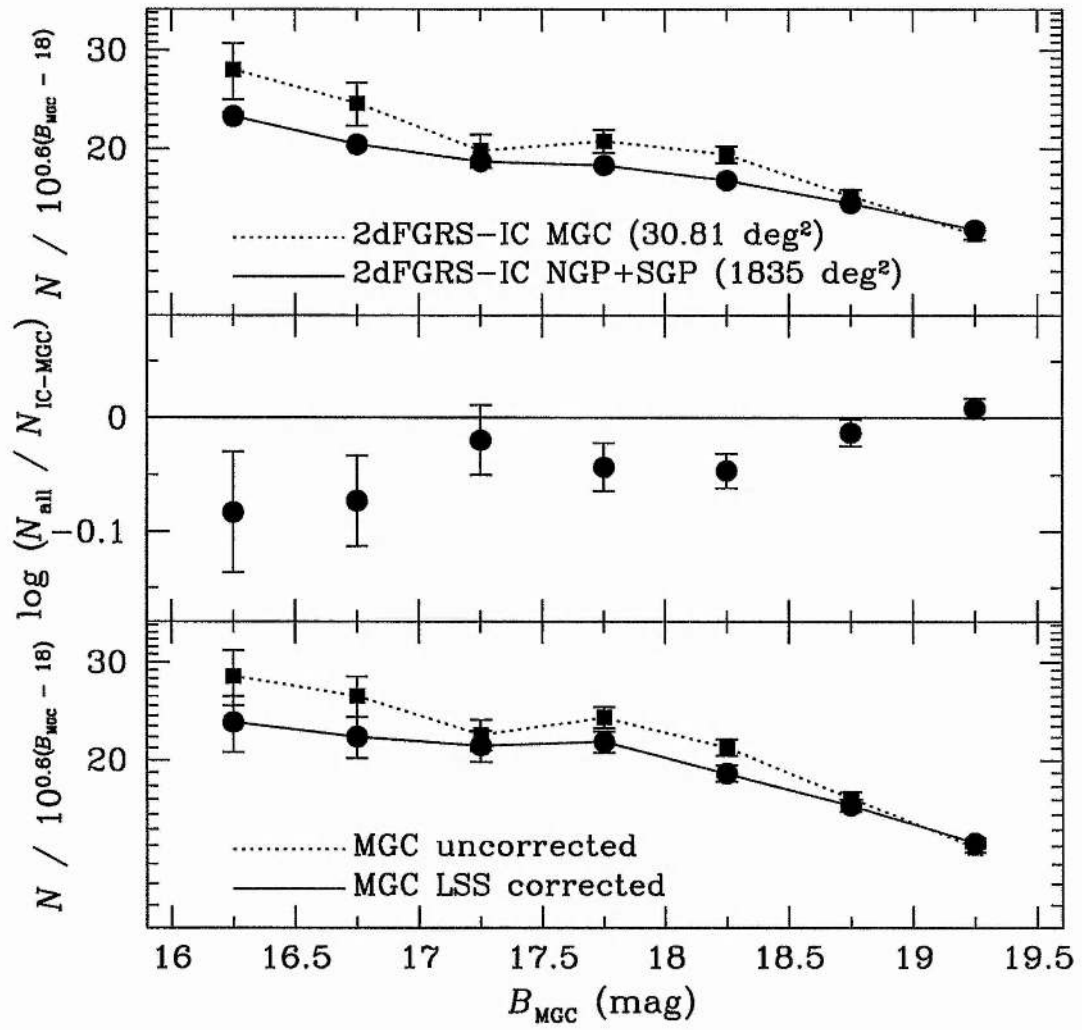

Figure 4.3: The top panel shows the 2dFGRS-IC counts within the MGC region (dotted line) and the 2dFGRS-IC counts for the full 2dFGRS area (solid line). The middle panel shows the ratio of these and this reflects the impact of large scale structure on our survey for each magnitude bin. The bottom panel shows our bright MGC raw counts (dotted line) and those corrected for large scale structure (solid line). Both sets of counts are tabulated in Table 4.1.

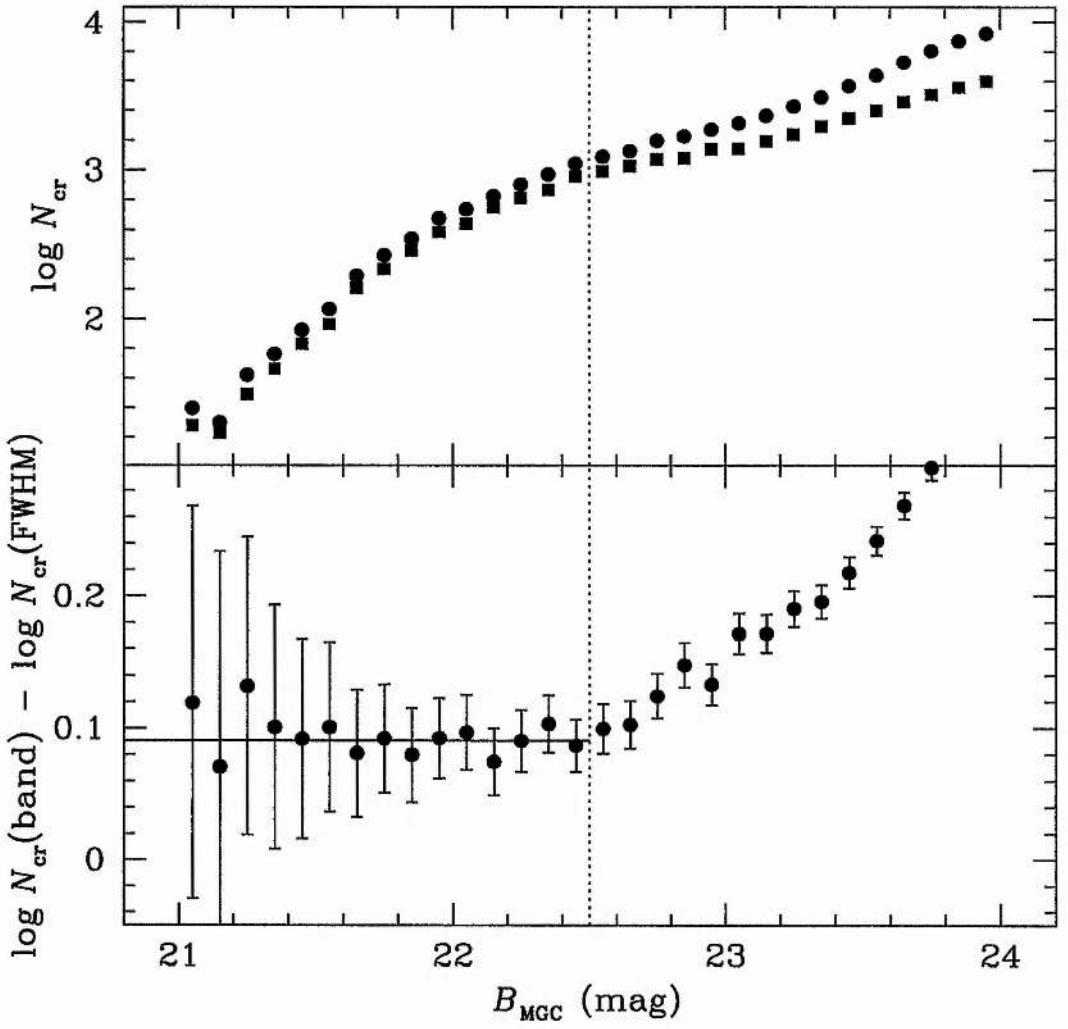

Figure 4.4: Upper panel: the dots show the number counts of all objects in the cosmic ray band delineated by the two solid lines in Fig. 2.19. The squares show the number counts of objects selected by applying the additional cut FWHM $< 0.9 \times$ SEEING. Lower panel: the ratio of the above counts appears to remain constant to $B_{\rm MGC} = 22.5$ mag (dotted line), where real objects begin to contaminate the counts from the cosmic ray band. The incompleteness of cosmic rays selected by the additional FWHM cut is found to be 18.8% and is indicated by the solid horizontal line.

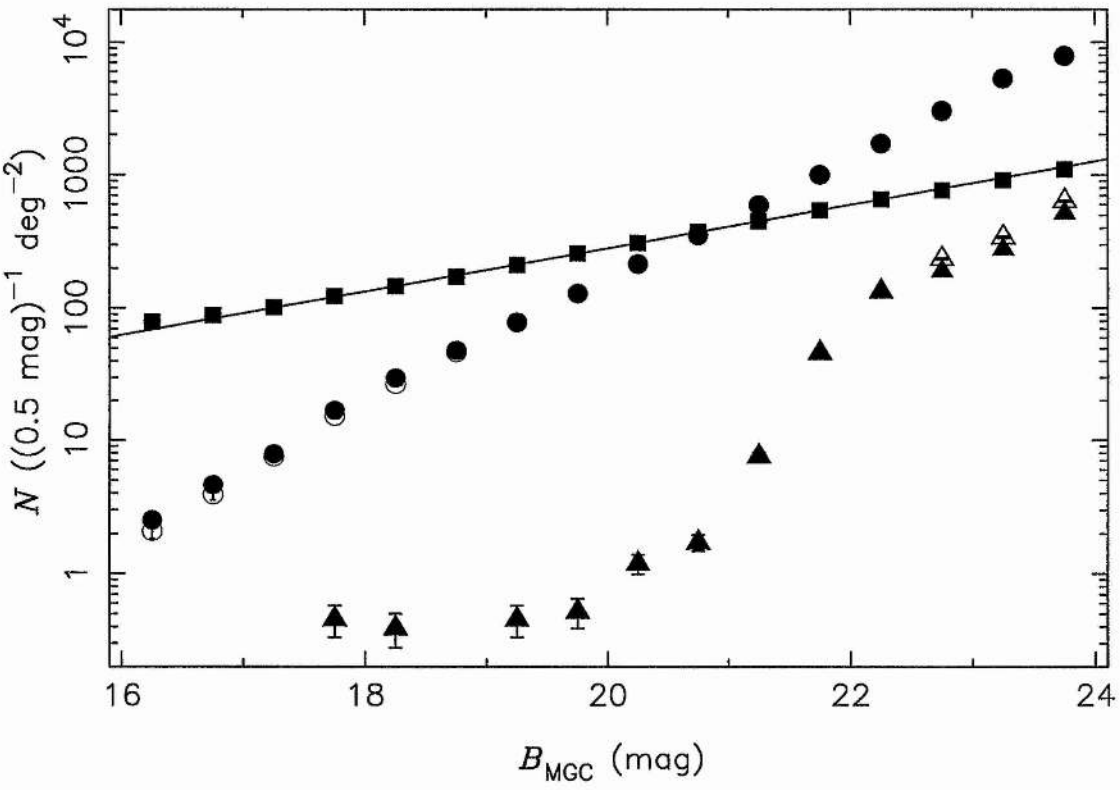

Figure 4.5: MGC number counts. Squares: stars. The line is a fit to the stellar counts in the range $17 \leq B_{MGC} < 20$ mag. The classification procedure described in Section 2.3.7 was designed to reproduce the extrapolated bright star counts at $B_{MGC} \geq 20$ mag. Solid triangles: cosmic ray counts. Open triangles: cosmic ray counts corrected for incompleteness at $B_{MGC} \geq 22.5$ mag. Solid circles: galaxy counts. Open circles: galaxy counts corrected for LSS ($B_{MGC} < 19$ mag) and cosmic ray incompleteness ($B_{MGC} \geq 22.5$ mag, barely visible).

$22.5 \leq B_{MGC} < 24$ mag by multiplying the FWHM<0.9×SEEING counts by a factor of 1.23. The difference between the corrected and uncorrected cosmic ray counts is then subtracted from the galaxy counts. Both the original and corrected galaxy number counts are shown in Fig. 4.5 and tabulated in Table 4.1.

4.4 Star and galaxy counts

Fig. 4.5 and Table 4.1 show the galaxy number counts, the error bars shown assume Poisson statistics. Objects in seeing class 4 (>1.42 arcsec) were not included in the last three bins and only objects in seeing class 1 (<1.15) were used in the last two bins. The solid line in Fig. 4.5 represents the best fit to the observed bright star counts down to $B_{MGC} = 20$ mag. At fainter magnitudes the counts continue to agree with the fit only because the star-galaxy separation was designed to ensure this, see § 2.3.7.

Note that the correction for LSS (which affects the counts only in the range $16 \leq$

Table 4.1: MGC galaxy number counts.

$B_{\rm MGC}$ (mag)	N^a	Area ($\deg^2$)	N^b	ΔN	$N^c_{\rm cor}$
16.25	78	30.90	2.52	0.29	2.08
16.75	143	30.90	4.63	0.39	3.91
17.25	243	30.90	7.87	0.50	7.52
17.75	521	30.90	16.86	0.74	15.26
18.25	920	30.90	29.78	0.98	26.76
18.75	1489	30.90	48.2	1.3	46.8
19.25	2419	30.90	78.3	1.6	78.3
19.75	3994	30.90	129.3	2.1	129.3
20.25	6537	30.31	215.7	2.7	215.7
20.75	10712	30.31	353.5	3.4	353.5
21.25	17981	30.31	593.3	4.4	593.3
21.75	30304	30.31	999.9	5.7	999.9
22.25	51917	30.31	1713.0	7.5	1713.0
22.75	69317	22.80	3040	12	2996
23.25	37839	7.09	5334	27	5270
23.75	56375	7.09	7947	33	7827

[a]Number of galaxies in the MGC in units of $(0.5\ \mathrm{mag})^{-1}$.

[b]Number counts in units of $(0.5\ \mathrm{mag})^{-1}\ \deg^{-2}$.

[c]Number counts corrected for LSS ($16 \leq B_{\rm MGC} < 19$ mag) and cosmic ray incompleteness ($22.5 \leq B_{\rm MGC} < 24$ mag).

$B_{\rm MGC} < 19$ mag) is significant at the brightest end (17%) but relatively minor (3 to 10%) at fainter magnitudes. At 1 to 2% the cosmic ray incompleteness correction (which affects the counts only in the range $22.5 \leq B_{\rm MGC} < 24$ mag) is smaller still.

Fig. 4.6 compares the MGC galaxy number counts to those of previous surveys. The various counts were converted onto the $B_{\rm MGC}$ system assuming $\overline{(B-V)} = 0.94$ Norberg et al. (2002).

In the range $16 \leq B_{\rm MGC} < 24$ mag our counts lie among those of previous publications and provide a fully consistent, uniform, well-selected and complete sample spanning eight magnitudes. The data thus represent a significant connection between the local photographic based surveys ($B < 20$ mag) and the deep pencil beam surveys ($B > 22$ mag). At bright magnitudes our counts are consistently higher than the original APM counts Maddox et al. (1990b) indicating that the steep rise of the APM counts is an artifact and that there is no more need for strong local evolution of the luminous galaxy population originally put forward by Maddox et al. (1990b). The 2dFGRS-IC is a substantially revised version of the APM catalogue and also shows a less pronounced rise, although some local effect is still evident.

Fig. 4.7 shows a close-up comparison of the MGC-BRIGHT, 2dFGRS-IC, SDSS-EDR and Gardner et al. (1996) counts, here we have normalised the counts by a linear model in order to make any differences more easily discernible. We assume only Poisson errors. We have used the SDSS-EDR g^* counts of the Northern stripe of Yasuda et al. (2001) and converted to $B_{\rm MGC}$ using the transformation listed in equation (4.1). We could have used the SDSS-EDR B counts which were derived using individual galaxy colours rather than a mean global colour. However, the colour equation used by Yasuda et al. (2001) is inconsistent with that of Fukugita et al. (1996). We prefer the Fukugita et al. (1996) transformation as Cross et al. (2003) have used it in a direct comparison of SDSS-EDR and MGC magnitudes which showed only a small difference of Δm(MGC$-$SDSS-EDR) $= (-0.009 \pm 0.001)$ mag. It was also used in the Norberg et al. (2002) comparison of the 2dFGRS and SDSS-EDR photometry which again shows only a small difference of Δm(2dFGRS$-$SDSS-EDR) $= 0.058$ mag.

The MGC and SDSS-EDR appear similar in shape. In particular they both show a characteristic change of slope near $B_{\rm MGC} = 18$ mag. However, the SDSS-EDR counts are consistently and significantly higher than the MGC counts.

To explain the discrepancy photometrically would require a shift of at least $\Delta m \approx +0.08$ mag which is an order of magnitude higher than, and in the opposite direction of the difference found by Cross et al. (2003) mentioned above. The only caveat here is our use of a mean galaxy colour of $\overline{(B-V)} = 0.94$. The colour equation (Eqn. 4.1) implies that a colour term of $(B-V) = 1.2$ is required to achieve a shift of $\Delta m \approx 0.08$ mag $(= (1.2 - 0.94) \times 0.3)$. While this is reasonable at $B_{\rm MGC} > 20$ mag it cannot explain the discrepancy at brighter magnitudes.

The fact that the SDSS-EDR counts agree better with the uncorrected MGC counts (open circles) implies that LSS might be the source of the discrepancy. However, as the SDSS-EDR is substantially bigger than the MGC region it should require a much smaller LSS correction. While LSS may plausibly explain some part of the observed differences at $B_{\rm MGC} < 19$ mag, it will not account for the differences out to $B_{\rm MGC} \approx 21$ mag.

In order to assess the performance of their automated object classification Yasuda et al. (2001) visually inspected all objects to $r^* < 16$ mag. They found that the machine classifier typically over-predicted the galaxy counts by $\sim$3%. This and other tests led them to conclude that mis-classification was not a serious problem at $r^* < 21$ mag.

Star-galaxy separation in the SDSS-EDR is performed by looking at the differences of an object's magnitude derived from fitting a PSF ($m_{\rm PSF}$) and a galaxy profile ($m_{\rm model}$, exponential or de Vaucouleurs, whichever fits best). SDSS-EDR classify an object as a galaxy if it satisfies the condition $c = m_{\rm PSF} - m_{\rm model} > 0.145$ (Stoughton et al. 2002). However, Yasuda et al. (2001) use a stricter classifying criteria in that they require $c > 0.145$ in two of the three bands g^*, r^* and i^*. Blanton et al. (2001) use a cut-off

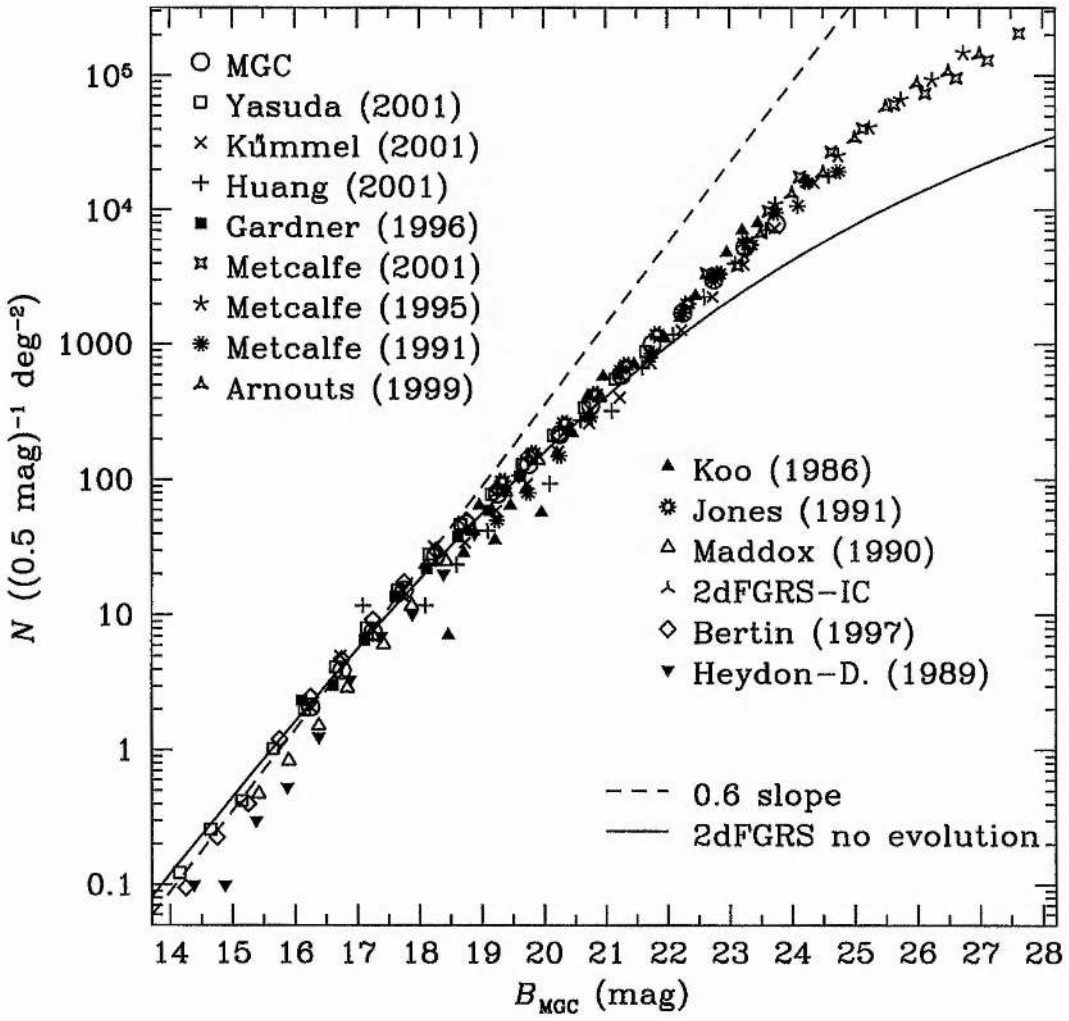

Figure 4.6: The galaxy number counts derived from the MGC as compared to the number counts of various other authors. The 2dFGRS no evolution model counts are calculated from the luminosity function parameters given in Table 4.2. Also shown is the 0.6 'Euclidean' slope.

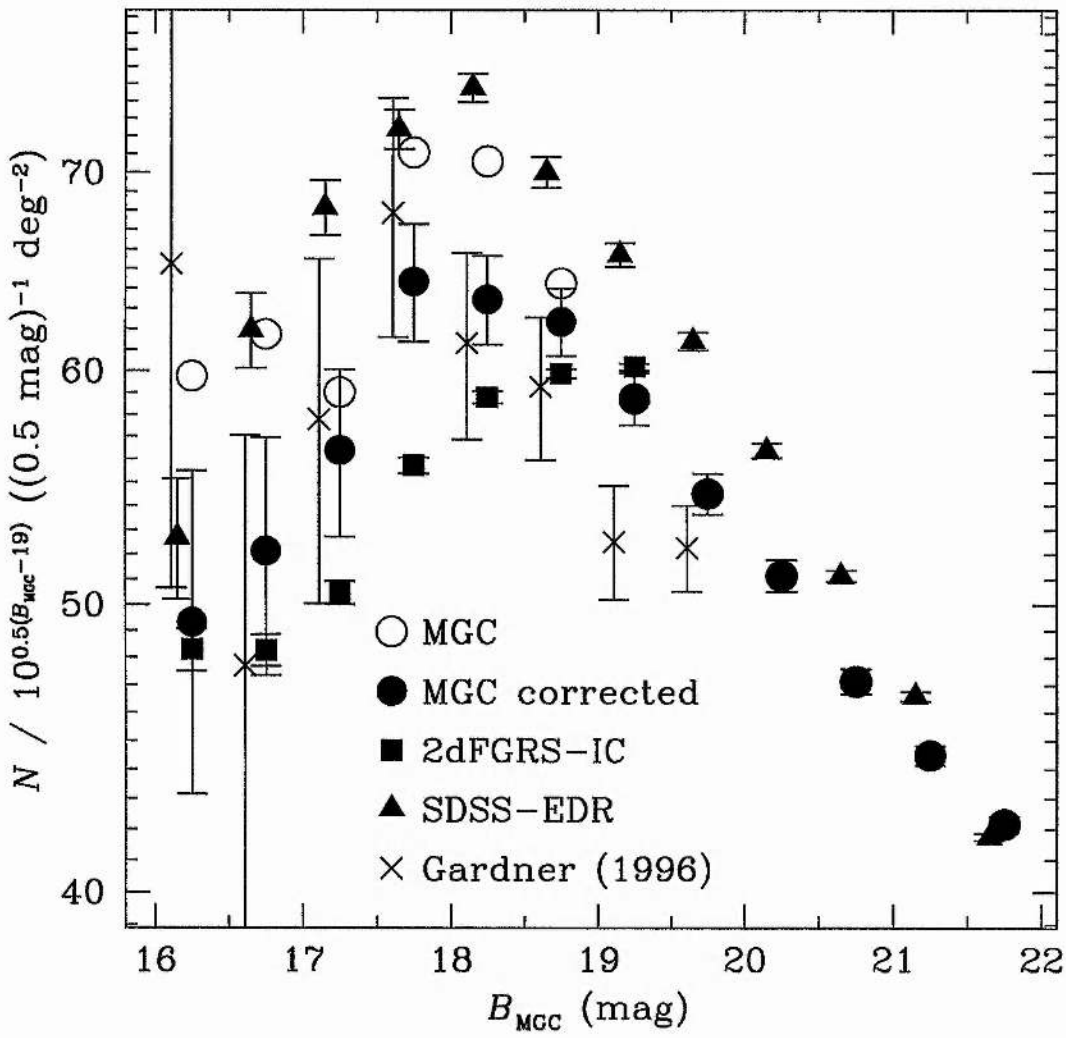

Figure 4.7: A close-up comparison over the important normalisation range $16 \leq B_{\rm MGC} < 20$ mag of the MGC number counts with three other datasets as indicated. Errors are purely Poissonian and do not contain any LSS component.

value of 0.242 in the r^* band. Strauss et al. (2002) even use a value of 0.3 in the SDSS spectroscopic target selection in addition to a surface brightness cut and further selection based on photometric flags. They find that at the bright magnitudes of the spectroscopic sample ($r^* < 17.8$ mag) only 10% of all objects with $0.15 < c < 0.3$ are actually galaxies (see also their figure 7).

It seems that contamination by mis-classified objects may at least in part be responsible for the observed excess of the SDSS-EDR counts. In contrast to these uncertainties, all MGC-BRIGHT galaxies have been visually inspected and hence there is *no* contamination. The complete explanation of the SDSS-EDR excess will be provided by a direct the comparison of the MGC and SDSS-EDR classifications on an object-by-object basis (see Cross et al. 2003).

The 2dFGRS-IC counts disagree with both the MGC and the SDSS-EDR as there is no turnover in the counts. At $B_{\rm MGC} < 19$ mag they are also significantly lower than the MGC counts. It is known that the 2dF target list (and hence the IC) is known to be contaminated by stars by around ~5% level (Pimbblet et al. 2001 & Norberg et al. 2002) and therefore underestimates the galaxies by the same amount.

As we used the 2dFGRS-IC counts to correct our counts for LSS, any discrepancy cannot be due to LSS and must be due to some photometric error and/or incompleteness in the 2dFGRS-IC.

We note that in the transformation from b_J to $B_{\rm MGC}$ magnitudes we have used the Blair & Gilmore (1982) colour term of 0.28 (see Eqn 4.1). Using instead a value of 0.35, as used in Metcalfe, Fong & Shanks (1995), only increases the difference.

During the final 2dFGRS photometry recalibration procedure the MGC was used to establish a relationship between the non-linearity coefficient and the offset between b_J and 2MASS J magnitudes Norberg et al. (2002). This relationship was then used to predict the coefficient for each Schmidt plate from the plate's mean 2MASS offset. For those 15 plates in the NGP covered by the MGC the measured coefficient is used, and not the predicted one. However, if one uses the predicted value instead then a meaningful comparison between the MGC and 2dFGRS photometry can be made, Cross et al. (2003) found Δm(MGC−2dFGRS) = −0.078 mag. Alternatively we can combine the same authors' Δm(MGC−SDSS-EDR) = −0.009 mag with the Norberg et al. (2002) Δm(2dFGRS−SDSS-EDR) = 0.058 mag to derive Δm(MGC−2dFGRS) = −0.067 mag. This −0.07 mag offset is large enough to move the 2dFGRS-IC points in Fig. 4.7 onto the MGC points at $B_{\rm MGC} < 19$ mag. This suggests that the 2dFGRS-IC incompleteness is of similar size to its stellar contamination. This result is in good agreement with the results of Pimbblet et al. (2001), Norberg et al. (2002) and Cross et al. (2003) who also found an incompleteness of ~10% of the 2dFGRS target list. Both Pimbblet et al. (2001) and Cross et al. (2003) found that roughly half of this incompleteness was due to badly blended galaxies which are explicitly excluded from the 2dFGRS-IC in the construction of the target list, leaving the 2dFGRS-IC with an incompleteness of ~5%.

4.5 Refining the field galaxy luminosity function

The field galaxy luminosity function (LF) has been measured many times by many different surveys but, as pointed out by Cross et al. (2001), their results and most notably their derived normalisations are inconsistent with each other. The predicted galaxy counts of all the LFs, even locally, are significantly different. We now use the local galaxy counts derived here to assess which LFs predict counts consistent with the data and to constrain the LF normalisation parameter, ϕ_*.

Table 4.2: Parameters of published luminosity functions. For each LF we also list the probability that its number count predictions fit the data (8 degrees of freedom).

LF	Filter conversion $B_{\rm MGC} =$	$M^*_{B_{\rm MGC}} - 5\log h$ (mag)	α	ϕ_* (h^3 Mpc^{-3})	$P(\geq \chi^2_{\rm min})$
2dFGRS	$b_j + 0.13$	-19.53	-1.21	0.0161	9.1×10^{-6}
SDSS-EDR	$g^* + 0.40$	-19.64	-1.26	0.0206	0
SSRS2	$b_{\rm SSRS2} - 0.16$	-19.59	-1.12	0.0128	0
Durham/UKST	$b_j + 0.13$	-19.55	-1.04	0.0170	1.2×10^{-6}
ESP	$b_j + 0.13$	-19.48	-1.22	0.0200	1.2×10^{-26}
Stromlo/APM	$b_j + 0.13$	-19.37	-0.97	0.0140	0
Autofib	$b_j + 0.13$	-19.07	-1.09	0.0260	7.3×10^{-29}
CS	$V_{\rm CS} + 0.77$	-19.53	-1.09	0.0187	1.5×10^{-2}
NOG	$B_{\rm RC3} + 0.26$	-19.79	-1.10	0.0140	3.0×10^{-2}

Table 4.3: Revised normalisations and luminosity densities. For each LF we also list the probability that its number count predictions fit the data after the adjustment of ϕ_* (7 degrees of freedom, 8 data points and 1 free parameter ϕ_*).

LF	$\phi^{*a}_{\rm MGC}$ (h^3 Mpc^{-3})	$P(\geq \chi^2_{\rm min})$	j_{b_J} ($10^8 h L_\odot$ Mpc^{-3})
2dFGRS	0.0171	0.36	1.93
SDSS-EDR	0.0147	0.35	1.94
SSRS2	0.0168	0.29	1.85
Durham/UKST	0.0181	0.23	1.82
ESP	0.0179	0.34	1.95
Stromlo/APM	0.0223	0.34	1.82
Autofib	0.0296	0.16	1.98
CS	0.0181	0.31	1.85
NOG	0.0137	0.065	1.79

[a] The typical 1σ error on $\phi_{*_{\rm MGC}}$ is 2×10^{-4} h^3 Mpc^{-3}.

4.5.1 Modeling the number counts

In Table 4.2 we list the LF parameters from the 2dFGRS (Norberg et al. 2002), SDSS-EDR (Blanton et al. 2001), SSRS2 (Marzke et al. 1998), Durham/UKST (Ratcliffe et al. 1998), ESP (Zucca et al. 1997), Mt Stromlo/APM (Loveday et al. 1992), Autofib (Ellis et al. 1996), CS (Brown et al. 2001) and NOG (Marinoni et al. 1999) surveys. Where available we have used the parameters for an $(\Omega_{\rm m}, \Omega_\Lambda) = (0.3, 0.7)$ cosmology (2dFGRS, SDSS-EDR and CS; all other surveys used a $(1, 0)$ cosmology except for the SSRS2 which used $(0.4, 0)$). All M^* values have been converted to the $B_{\rm MGC}$ system using Eqns. 4.1 below.

$$\begin{aligned} B_{\rm MGC} &= b_J + 0.14(B-V) \\ B_{\rm MGC} &= g^* + 0.12 + 0.30(B-V) \\ B_{\rm MGC} &= b_{\rm SSRS2} - 0.02 - 0.1447(B-V) \\ B_{\rm MGC} &= V_{\rm CS} - 0.072(V-R) + 0.8553(B-V) \\ B_{\rm MGC} &= B_{\rm RC3} + 0.74 - 0.51(B-V) \end{aligned} \tag{4.1}$$

These were derived from Eqn. 2.5 and the colour equations of Blair & Gilmore (1982), Fukugita et al. (1996) (SDSS-EDR), Alonso et al. (1994) (SSRS2), Brown et al. (2001) (CS), Kirshner, Oemler & Schechter (1978) and Peterson et al. (1986) (NOG). We assume $\overline{(B-V)} = 0.94$ from Norberg et al. (2002) and $\overline{(V-R)} = 0.53$ from Brown et al. (2001). Fig. 4.8(a) shows these LFs in the $B_{\rm MGC}$ band.

To model the counts we need to calculate the differential

$$\frac{dN}{dm} = \int_{M_1}^{M_2} \left(\Phi(M) \times \int_{z_1}^{z_2} \frac{dV}{dz} \right), \tag{4.2}$$

for each apparent magnitude bin, dm. Here $\Phi(M)$ is the space density of galaxies, given by the LF, with absolute magnitude, M, occupying a volume, V, out to redshift z. The co-moving volume element is given by Peacock (1999) as

$$dV = 4\pi d_p^2 R_0 dr \tag{4.3}$$

where d_p is the proper distance and R_0 is the scale factor at t_0. d_p and Eqn. 4.3, in terms of redshift, are derived in Appendix B.4 and B.5 respectively for an Einstein de Sitter universe (Eds). Here we use the currently favored cosmology $(\Omega_{\rm m}, \Omega_\Lambda) = (0.3, 0.7)$. The absolute magnitude, M, is given by the distance modulus equation which is derived in Appendix B.2 to be:

$$m - M = 5 \log d_l + 25 + k + e, \tag{4.4}$$

were d_l is the luminosity distance, in Mpc, which is related to the proper distance, d_p, by

$$d_l = d_p \times (1 + \mathrm{z}). \tag{4.5}$$

The band-pass reddening, k, correction accounts for the shift in wavelength, due to cosmology, of emitted galaxy light. If one is to observe the emitted light of a high redshift galaxy using, say a blue filter, then by the time the emitted blue light reaches the observer a significant fraction of the blue light will have been redshifted out of the filters range, thus artificially dimming the galaxies B-band magnitude. The evolutionary, e, correction corrects a galaxies observed light for any evolutionary (i.e. rapid star formation) events which can dramatically alter a galaxies magnitude. The k and e corrections are taken to be

$$\mathrm{k} = 2.5\mathrm{z}, \tag{4.6}$$

and

$$\mathrm{e} = 2.5\log((1+\mathrm{z})^{-0.75}). \tag{4.7}$$

which, assuming pure luminosity evolution, will correct a galaxies observed magnitude to a z =0 magnitude and are not dependent on cosmology. At z <0.4 this combination matches well the k+e-correction given by Norberg et al. (2002) which was derived using Bruzual & Charlot (1993) models to match the colour-redshift trend seen in the SDSS-EDR. Fig. 4.8(b) shows how the predicted counts compare with the MGC-BRIGHT counts.

Clearly the data prefer some models over others. We have performed a goodness-of-fit test for the predicted counts in the range $16 \leq B_{\rm MGC} < 20$ mag and list the resulting probabilities in column 6 of Table 4.2. The model counts based on the 2dFGRS, Durham/UKST, CS and NOG LFs provide reasonable fits.

From Fig. 4.8(b) it is clear that the main difference between the various predicted counts and the MGC measured counts lies in their normalisation and not their shape. This scatter is known as the "normalisation problem".

4.5.2 The normalisation problem

The three possible reasons for the normalisation problem are photometric error, incompleteness and clustering. We now discuss each on in turn.

Cross & Driver (2002) showed that the derived LF parameters depend on the limiting isophote and the photometric method (e.g. isophotal, corrected, total, etc.). They concluded that when using isophotal magnitudes for a limiting isophote of 25 mag/sq arcsec one might expect errors in M^* of up to $\pm$0.4 mag, in ϕ_* of up to $\pm$10% and in α of up to $\pm$0.01. Therefore photometric errors may well be the cause for the variation of M^* seen in Table 4.2.

Although the underestimation of the magnitudes due to the limiting isophote will cause some galaxies to fall below a surveys limiting magnitude, it also causes the volume over which such galaxies can be seen to be *underestimated*, if m_{lim} decreases then so does M_{lim} and hence z, V and N (see Eqns. 4.2 and 4.3). Fig. 2.21 indicates that at $B_{\rm MGC} < 19$ mag no significant galaxy population below 25 mags/sq arcsec exists. In other words at these surface brightness limits it is typically a case of missing light from the outer isophotes rather than missing galaxies. This is in line with Pimbblet et al. (2001) and Cross et al. (2003) who found only a few percent of galaxies missing from the 2dFGRS due to their low surface brightness. Incompleteness does not appear to play a significant role.

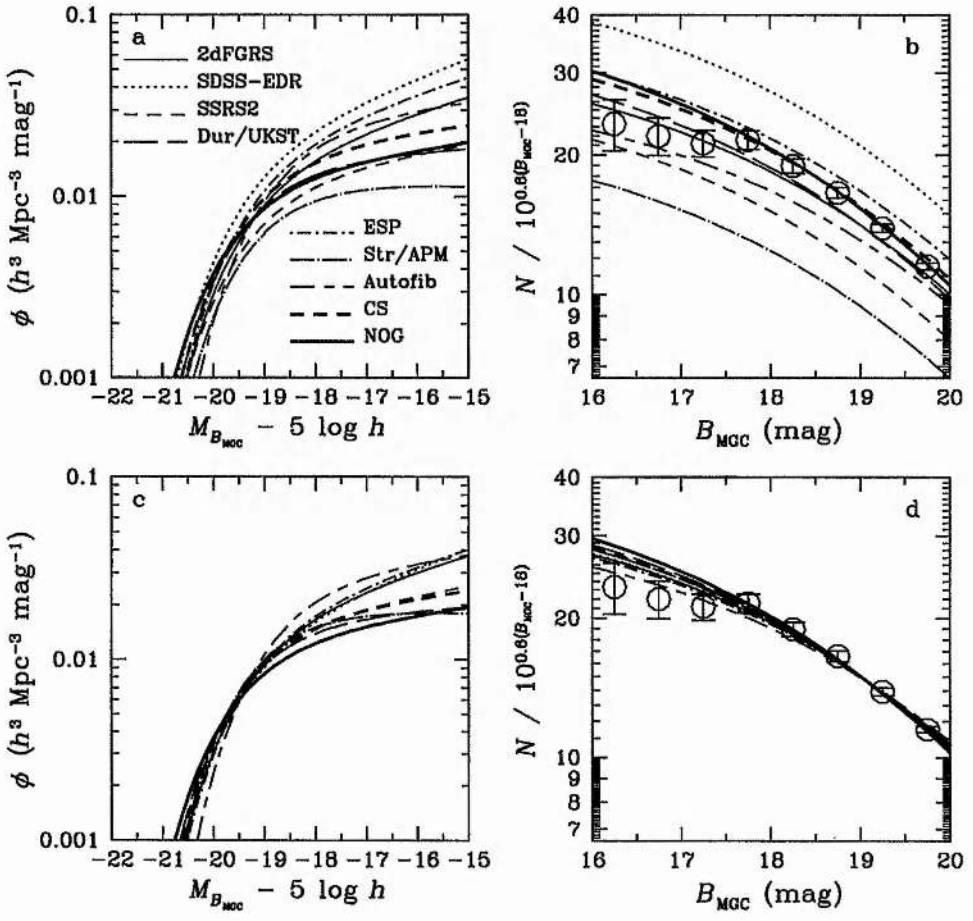

Figure 4.8: The left panels show local LFs before (upper) and after (lower) renormalisation to the MGC-BRIGHT counts. The right panels show the number count predictions of these LFs and the LSS corrected MGC-BRIGHT counts. After the recalculation of the LF normalisations, ϕ_*, we note that all LFs match the data almost equally well.

As previously mentioned LSS will clearly affect all but the very largest surveys. In § 4.2 we found that the MGC required LSS corrections of a few per cent at $B_{\rm MGC} < 19$ mag. Norberg et al. (2002) found that the 173 sq deg overlap region between the SDSS-EDR and the 2dFGRS was over-dense by 5% relative to the full 2dFGRS. They also found a 7% difference (to $b_J = 19.2$) between their 740 deg^2 NGP and 1095 sq deg SGP regions. From Fig. 4.8(b) we can see that the MGC counts at $B_{\rm MGC} < 17.5$ mag are lower than expected (by a few per cent, depending on the value of M^*) despite the LSS correction to the full 1835 sq deg of the 2dFGRS, indicating some local effect. This will bias the normalisations of shallow surveys like the SSRS2 ($b_{\rm lim} = 15.5$ mag).

We note that most fitting methods do not solve for ϕ_* directly and instead it is derived separately using a variety of methods, which also contributes to the variation in ϕ_*. For example, even though Yasuda et al. (2001) used less restrictive galaxy selection criteria than Blanton et al. (2001), they found a g^* LF normalisation 13% lower than that of Blanton et al. (2001), which must be put down to a difference in method.

4.5.3 Determining ϕ_*

Over the range $16 \leq B_{\rm MGC} < 20$ mag the MGC provides the most reliable number count data in existence and therefore provides the most reliable constraints on ϕ_*. The contours of Fig. 4.9 show the appropriate ϕ_* values for any given combination of M^* and α. These were derived from our LSS corrected MGC-BRIGHT counts over the intermediate range $16 \leq B_{\rm MGC} < 20$ mag by minimising χ^2 as a function of ϕ_*.

We derive the ϕ_* values appropriate for the LFs listed in Table 4.2. The revised values and their associated probabilities are listed in columns 2 and 3 of that Table 4.3. Figs. 4.8(c) and (d) show the resulting LFs and their predicted counts after revision. All surveys now give comparable and reasonable probabilities. However, the variation of ϕ_* among the different surveys after renormalisation is no less than before. This is due to the fact that the counts constrain the combination $\phi_* M^*$ and that the variation in M^* is comparable to that of ϕ_* before renormalisation.

4.5.4 The local luminosity density

Taking $M_{\odot_{b_J}} = +5.3$ mag and using the revised LF normalisations we calculate the luminosity density, j, using:

$$j_{b_J} = L_{*_{b_J}} \phi_* \Gamma(\alpha + 2), \tag{4.8}$$

which is derived in Appendix B.6. Note that we convert $M^*_{B_{\rm MGC}}$ to $M^*_{b_J}$. The calculated values of j_{b_J} are listed in the last column of Table 4.3. We find a mean b_J luminosity density of $\overline{j_{b_J}} = 1.88 \pm 0.03 \pm 0.07 \times 10^8 h L_\odot$ Mpc^{-3}, where the first error is due to the (Poisson) uncertainty in the counts and the second is due to the range of M^* and α values. Note that the 2dFGRS and SDSS-EDR, which must be considered the most reliable LFs, give a slightly higher value of $j_{b_J} = 1.94 \times 10^8 h L_\odot$ Mpc^{-3}.

4.5.5 The optimal Schechter parameters

We now attempt to use the shape of the counts to constrain the other two Schechter parameters. Note that this assumes that the cosmology, k and e-corrections are known.

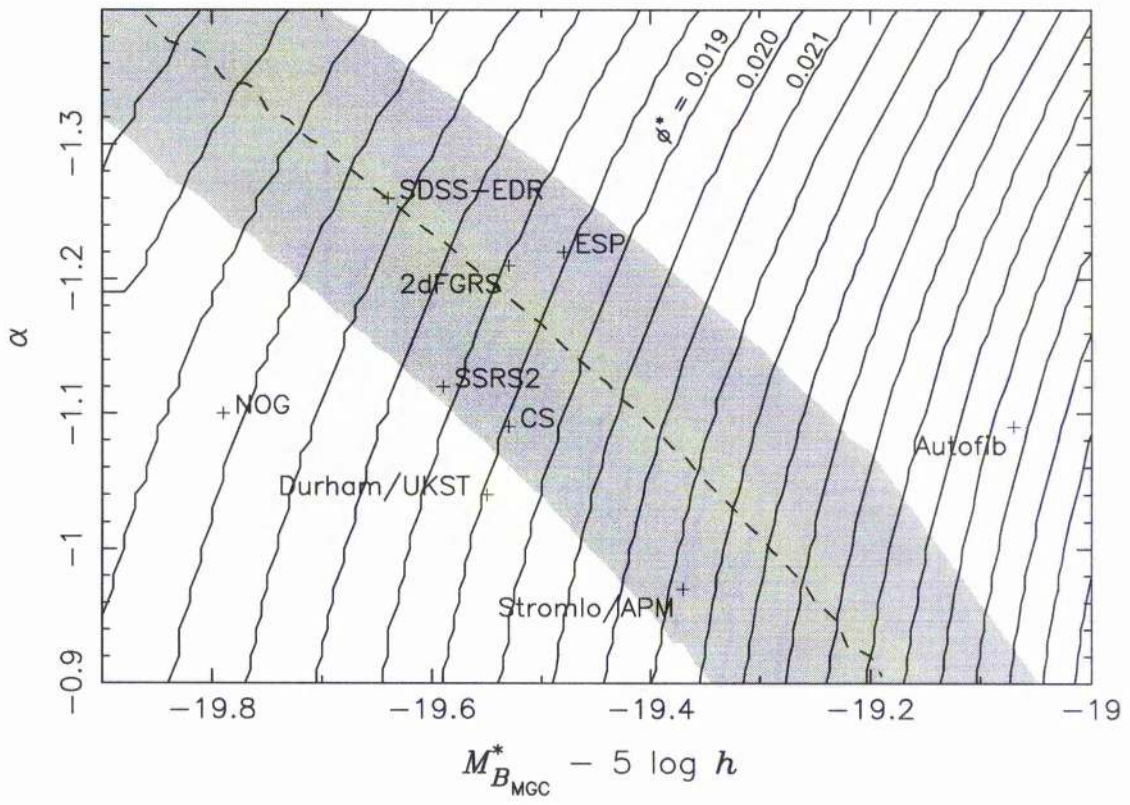

Figure 4.9: The contours show the best-fitting value of the LF normalisation, ϕ_*, for given values of M^* and α. These were derived by χ^2-minimisation over the range $16 \leq B_{\rm MGC} < 20$ mag (cf. Fig. 4.8). The ϕ_* values of the contours increase from 0.011 h^3 Mpc^{-3} on the left in steps of 0.001 to 0.033 on the right as indicated. The positions of the LFs of Table 4.2 in the M^*-α plane are also indicated. The corresponding ϕ_* values are listed in Table 4.2. The dashed line shows the best-fitting value of α (and ϕ_*) for a given value of $M^*_{B_{\rm MGC}}$. The gray shaded region shows the 1σ error on α.

We minimise χ^2 as a function of α for each value of M^* and ϕ_*. The result is the dashed line in Fig. 4.9. The shaded region shows the $\pm 1\sigma$ error from the fit. Although none of the surveys are excluded (after renormalisation), the SDSS-EDR and 2dFGRS are in particularly good agreement with our counts.

We now fit for all three Schechter parameters simultaneously. This requires minimising χ^2 along the dashed line of Fig. 4.9. No minimum is achieved in the parameter space that we use. M^* determines the behavior of the counts at the bright end. The comparatively low MGC-BRIGHT counts in the range $16 \leq B_{\rm MGC} < 17.5$ mag require an unrealistically faint M^* and in consequence a very high ϕ_* and shallow α.

Using the MGC-BRIGHT counts alone we can determine ϕ_* and α for a given M^* or, alternatively, ϕ_* and M^* for a given α, but not all three parameters simultaneously. Taking a mean value of M^* from the 2dFGRS and SDSS-EDR we find an optimal set of Schechter function parameters of $\overline{M^*}_{B_{\rm MGC}} = -19.585 - 5\log h$, α=-1.23 and ϕ_*=$0.0158h^3$.

4.6 Summary

We have measured the galaxy number counts from the MGC-BRIGHT and FAINT catalogues. The number counts were corrected for LSS using the overlapping 2dFGRS-IC and for cosmic ray contamination in the faint end by extrapolating the bright cosmic by number counts to faint magnitudes. Our counts show that the steep rise seen in the bright APM counts is an artifact and therefore there is no need for strong local evolution.

We have used the corrected galaxy number counts to test various estimates of the galaxy luminosity function (2dFGRS, SDSS-EDR, SSRS2, Durham/UKST, ESP, Stromlo/APM, Autofib, CS & NOG) and find that many of them predict counts whose normalisations are inconsistent with our observations. These LFs are renormalised to the MGC counts by factors of 1.06, 0.71, 1.31, 1.06, 0.90, 1.59, 1.14, 0.97 and 0.98 respectively. After this renormalisation both the 2dFGRS (Norberg et al. 2002) and SDSS-EDR (Blanton et al. 2001) luminosity functions are in excellent agreement with our counts. From these revised values of ϕ_* we constrain the b_J-band luminosity density of the local universe for each of these luminosity functions. We find $\overline{j_{b_J}} = 1.88(\pm 0.03 \pm 0.07) \times 10^8 h L_\odot$ Mpc^{-3}, where the first error is due to the (Poisson) uncertainty in the counts and the second is due to the range of M^* and α values. The 2dFGRS and SDSS-EDR consistently give a slightly higher value of $j_{b_J} = 1.94 \times 10^8 h L_\odot$ Mpc^{-3}.

In addition to ϕ_* one other Schechter parameter can be reasonably constrained from the intermediate MGC counts alone. Thus the counts provide us with either a joint estimate of ϕ_* and α as a function of M^* or, alternatively, with an estimate of ϕ_* and M^* as a function of α. By constraining M^* we are able to recommend the optimal Schechter function parameters $M^*_{b_J} = -19.715 - 5\log h \pm 0.17$, $\alpha = -1.23 \pm 0.12$ and $\phi_* = 0.0158h^3 \pm 2 \times 10^{-4} h^3 Mpc^{-3}$.

CHAPTER 5

Galaxy Profile Decomposition via GIM2D

In this Chapter we address the problem of obtaining galaxy morphologies via galaxy profiles. In particular we discuss the automated classification package Galaxy Image 2D (GIM2D) developed by Luc Simard (see Simard 1998, Simard et al. 2002 and Tran 2000) and assess its applicability to derive morphological types for the MGC galaxies.

5.1 GIM2D

Galaxy Image 2D (hereafter GIM2D, Simard 1998, Simard et al. 2002 and Tran 2000) is a fully automated software package that will take an image of a galaxy and measure its various structural parameters. GIM2D is ideally suited to the MGC data set as it is designed to work from low signal-to-noise SExtracted catalogues, see §2.3. Specifically to use GIM2D we need a reduced SExtracter catalogue, an image and a segmentation map for each MGC field along with a point-spread-function for each galaxy.

5.1.1 Point-Spread-Function

To generate a Point-Spread-Function (PSF) we used the IRAF DAOPHOT routines DAOFIND, PHOT, PSF, NSTAR, SUBSTAR and ALLSTAR[1] on a preselected list of PSF stars for each CCD.

5.1.1.1 PSF Stars

In order to generate an accurate analytic PSF it is essential that a large number ($\geq$20) of PSF stars evenly distributed across the CCD are used. This is because we need to ensure that the averaged star light profile is only due to the effects of sky+telescope+CCD and not because of any stellar phenomena. A good PSF star will be isolated from all other bright sources and will not lie on, or too close to bad columns/rows/pixels. For each CCD from MGC-BRIGHT we extracted all the stars with STELLARICITY >0.8, FLAGS<1, 17< $B_{\rm MGC}$ <19.5 in good regions of the CCD. Setting a FLAG tolerance of less than 1 ensures that: the selected stars have not been deblended; there are no bright neighbours close enough to bias the KRON magnitude; and there are no saturated pixels. Fig 5.1 shows the initial number of PSF stars found on each CCD for each pointing. For those CCDs where there were less than 20 PSF stars the STELLARICITY and magnitude limits were tweaked until a minimum of 20 PSF stars covering the whole of the CCD were found.

[1]Detailed descriptions of DAOPHOT photometry routines can be found in Stetson (1987).

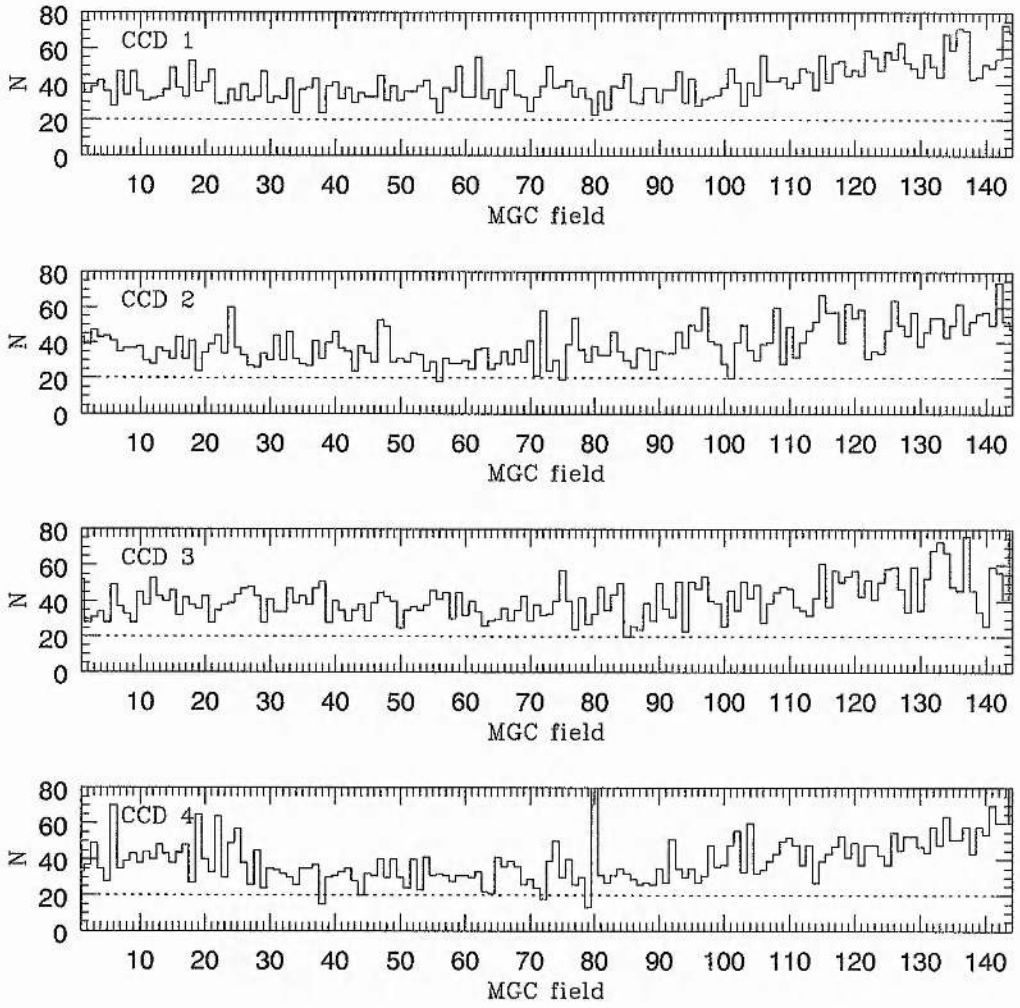

Figure 5.1: The initial number of PSF stars found on each CCD of each MGC field. The horizontal line indicates the minimum number of PSF stars required for a reasonable fit.

5.1.1.2 Generating the PSF

To generate a PSF we first use DAOFIND and DAOPHOT to identify and assign an IRAF magnitude to every object on the CCD. The PSF routine then uses the output files from DAOPHOT and DAOFIND as well as the list of PSF stars to generate an initial PSF using the PENNY2 analytic function (Davis 1994). This PSF is a combination of an elliptical Gaussian and a Lorentzian, both aligned along arbitrary and independent position angles. The PENNY2 analytic function representing the Gaussian and Lorentzian combination consists of 5 parameters and is modeled thus:

$$\text{PENNY2} = A \times \left(\frac{(1 - P_3)}{(1 + z)} + P_3 \exp^{(-0.693e)} \right) \tag{5.1}$$

where,

$$z = \frac{x^2}{P_1^2} + \frac{y^2}{P_2^2} + xyP_5 \tag{5.2}$$

and

$$e = \frac{x^2}{P_1^2} + \frac{y^2}{P_2^2} + xyP_4 \tag{5.3}$$

Here A is a normalizing factor and P_n are the fitted parameters. We define the fitting radius of the PENNY2 profile to be equal to the median seeing of each CCD, see Davis (1994). This PSF is fitted by NSTAR to a group of stars. SUBSTAR then uses this to subtract off any PSF star neighbours that could influence the PSF. The PSF routine is then run over the subtracted image. As a check on the quality of the PSF the ALLSTAR routine was used to generate a PSF and to subtract the star from the CCD image. If the PSF fit is good the PSF stars should be cleanly subtracted from the image leaving only sky noise. For the most part the PSF generated provided a good fit to the stars. However, in some cases the initial PSF star list had to be amended as some of the PSF stars lay near CCD defects. Fig 5.2 displays the mean χ^2 per degree of freedom of the PSF fits to stars on each CCD of each MGC field. The individual χ^2 values are calculated by ALLSTAR for each star and are a measure of the goodness-of-fit of the derived PSF.

Finally, a PSF at the location of each galaxy is generated by the DAOPHOT routine SEEPSF. This takes the galaxy coordinates and the derived analytic PSF form to produce a simulated PSF image at the exact location of each MGC galaxy.

5.1.2 Postage stamps

The reduced SExtracter catalogue for use by GIM2D must include the PIXEL X & Y coordinates, background (ADU counts), detection threshold above background (ADU counts) and isophotal area (PIXEL^2) of each galaxy as the first five parameters. In the MGC these correspond to columns 3, 4, 14, 15 & 16 respectively, see Table A.1. This catalogue is generated from the master catalogue for each CCD and is given the suffix .gfxt.

A segmentation image is one in which the background is set to zero and each objects pixels are set to a unique value. The segmentation image of each MGC field is a

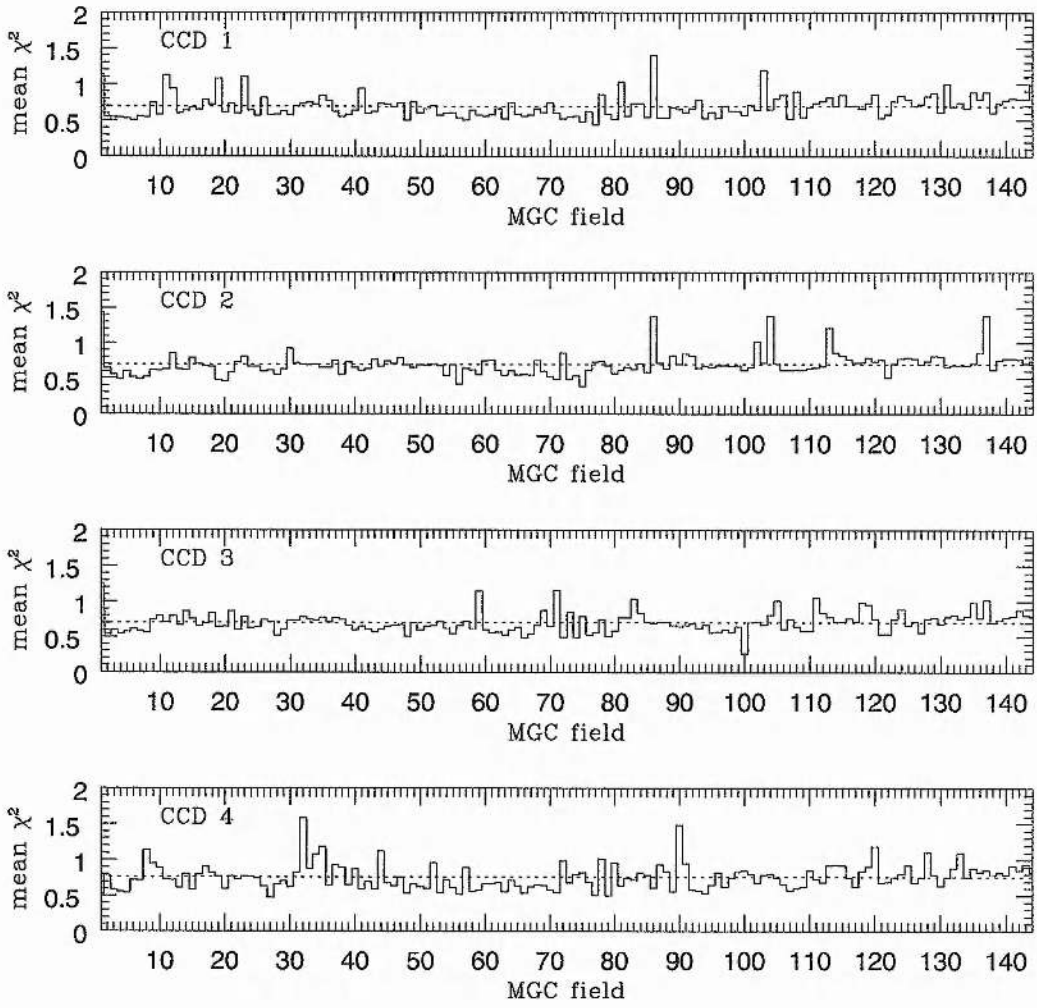

Figure 5.2: The mean χ^2 for the PSF fits to stars on each CCD of each field. The dashed line indicate the overall mean of the PSFs for each CCD.

Table 5.1: This table lists the initial GIM2D paramerers used here. We assume a de Vacouleurs bulge and exponental disk profile. To use a Sersic bulge profile the last line should read: 2.1, 2.1, 0.2, 4.0, 3.8 (see Tran 2000).

Initial value	Best value	Min	Max	Initial pertubation	Symbol	Description
300	NA	NA	NA	NA		Number of models
500.0	500.0	1.0	1000.0	1000.0	L	Total flux
0.5	0.5	0.0	1.0	1.0	(B/T)	Bulge fraction (B/T)
2.5	2.5	0.0	5.0	5.0	r_e	Bulge effective radius
0.35	0.35	0.0	0.7	0.7	e	Bulge ellipticity
90.0	90.0	-360.0	360.0	180.0	θ_b	Bulge position angle
2.5	2.5	0.0	5.0	5.0	r_d	Exponential disk scale length
45.0	45.0	0.0	85.0	85.0	i	Disk inclination
90.0	90.0	-360.0	360.0	180.0	θ_d	Disk position angle
0.0	0.0	-1.0	1.0	0.1	Δx	Subpixel x offset position
0.0	0.0	-1.0	1.0	0.1	Δy	Subpixel y offset position
0.0	0.0	0.0	0.0	0.0	I_{sky}	Background level
4.0	4.0	4.0	4.0	0.0	n	Power index ($r^{1/n}$)

natural product of SExtracter. The postage stamp version of each galaxy image and its segmentation image is produced by the GIM2D pre-processing routine called XGAL.

XGAL takes the relevent CCD image, segmentation image and .gfxt file produces a postage stamp image and postage stamp segmentation image for each galaxy. These postage stamps have their SExtractor derived backgrounds subtracted from them. The size of each postage stamp is some multiple of the isophotal area of each galaxy. We set the XGAL parameters to extract postage stamps with widths and heights with areas 15 times the isophotal area of each galaxy.

5.1.3 Profile fitting

Once we have the PSF image, object image and segmentation image for each galaxy we used the GIM2D routine GIMFIT to derive the various galaxy parameters. GIMFIT uses the *Metropolis* algorithm (Metropolis et al. 1953) to constrain the twelve galaxy parameters of the standard 2D galaxy model, see Table 5.1.

5.1.3.1 The GIM2D galaxy model

The 2D galaxy model adopted by GIMFIT has 12 parameters, see Table 5.1, and is made up of 2 distinct parts, a bulge and a disk. The first part, the bulge, takes the standard

Sersic profile, Sersic (1968):

$$I_r = I_e exp(-k[(r/r_e)^{1/n} - 1]), \tag{5.4}$$

where k is calculated numerically by Capaccioli (1989) to be

$$k = 1.9992n - 0.371, \tag{5.5}$$

I_r is the surface brightness at radius r, I_e is the surface brightness at r_e , r_e is the bulge effective radius and n is the bulge power index. The value of k given by Eqn 5.5 ensures that r_e encloses half the bulge-light for any value of n. When n=4, k reduces to the de Vaucouleurs value of k=7.6697. Here we initially assume a de Vaucoulers bulge profile.

The second (disk) component is modeled in the standard exponential form

$$I_r = I_0 exp(-r/r_d), \tag{5.6}$$

where I_0 is the central surface brightness of a face-on (i=0°) disk with a scale length r_d. Both the disk and (de Vaucouleurs) bulge profiles are derived in magnitude form in Appendix B.7. The disk inclination angle is calculated by

$$i = arccos(\sqrt{1 - e_{disk}}), \tag{5.7}$$

where e_{disk} is the apparent disk ellipticity. Eqns. 5.4 and 5.6 are for the circularly symmetric case only. For non-circularly symmetric cases the bulge and disk profiles are modified by

$$r_e = r_{e_a}\sqrt{1 - e} \tag{5.8}$$

and

$$r_d = r_{d_a}\sqrt{1 - e_{disk}} \tag{5.9}$$

where r_{e_a} and r_{d_a} are the radii of the semi-major axis (a) of the bulge and disk respectively. We make the additional assumption that all disks are optically thin and set the absorption parameter, C_{abs}, to C_{abs}=0. The total fluxes of the de Vaucouleurs bulge and exponential disk are then calculated by

$$F_{bulge} = 7.214\pi r_e^2 I_e \tag{5.10}$$

and

$$F_{disk} = 2\pi r_d^2 I_0. \tag{5.11}$$

GIM2D also calculates the half-light radius of each galaxy by integrating Eqns 5.4 and 5.6 out to infinity using the best fitting parameter set.

5.1.3.2 Metropolis algorithm

The algoritum needed to search through our 12-dimensional space must be adept at climbing out of the local minima which will be prolific throughout the complicated topology. The metropolis algorithm (here after MA) was designed for such a purpose, see Simard et al. (2002), Metropolis et al. (1953) and Silk & Wyse (1993). The MA starts from a user defined set of parameters, compares the model to the data and calculates the probability, P_0, that this is the correct parameter set. It then calculates random perturbations of the parameter set and calculates the probability, P_1, that the new set are the correct parameters. The initial parameter set used here can be seen in Table 5.1. If $P_1 > P_0$ the new parameter set is accepted and the process repeated until convergence is achieved. The size of the perturbations is determined by the "temperature" of the MA. Initially the MA is "hot" and large perturbations are used. However, if too many perturbations are accepted the MA will "cool-off" and the size of the perturbations is reduced. This process can also work in reverse allowing the MA to "heat-up". For cases where $P_1 < P_0$ then the MA will have probability, P_1/P_0, of accepting this parameter set even though it will take the MA to higher locations in the parameter space. In this way the MA attempts to jump out of any minima it finds. This unique feature also allows the MA to jump to parameter values outside the user defined range, in other words the Min & Max values of Table 5.1 are soft limits.

The MA defines convergence to be when two parameter sets are less than 3σ of the perturbation distribution apart and are separated by 100 iterations. The maximised parameter space is then Monte-Carlo sampled N times, where N>100 see Table 5.1, and the median of each parameter distribution is taken to be the final value of that parameter. The quality of the final parameter set is then assessed by a reduced χ^2 statistic calculated by GIM2D for each galaxy.

5.1.3.3 GIM2D output

Once the final 12 model parameters have been derived GIM2D writes them, as well as the parameters from the other N models, to a .log file. The final parameters are indicated by the letter "P" and are given with their 3σ errors. The half-light radius and reduced χ^2 are also shown as well as the mean and standard-deviation of the background of the input (SExtractor background subtracted) image. GIM2D also creates an image of the galaxy using the model parameters and a model-subtracted residual image. Examples of these along with mask and input images are shown in Fig. 5.3 for the three main Hubble types: Elliptical (top), Spiral (middle) and Irregular (bottom). The mask images, particularly for the Spiral, indicate the need for accurate SExtractor deblending. However, the slight contamination of the Spiral mask by the bright star does not appear to have seriously affected the profiling, as can be seen in the Spiral model image. The dark patches in the residual images indicate the presence of structure, such as spiral arms, not modeled by GIM2D. In Fig 5.4 we show examples of bulge and disk dominated galaxies (chosen by their (B/T) parameter) covering the range $16 < B_{\rm MGC} < 20$ in 1 magnitude bins. Fig. 5.5 shows how their observed/measured (azimuthally averaged) and GIM2D

profiles compare [2]. The two dotted lines in Fig. 5.5 show the individual disk and central bulge components, the dashed line is the summed (unconvolved) profile and the solid line is the azimuthally averaged profile measured from the GIM2D model image (i.e including convolution with the PSF). The number in the bottom left corner is the statistic we use to assess the goodness-of-fit of the measured model profile to the observed profile. The statistic is essentially an rms, for $\mu(r)_{obs_i}$ >26 only, calculated as

$$rms = \sqrt{\frac{\sum_{i=1}^{N}(\mu(r)_{obs_i} - \mu(r)_{m_i})^2}{N}}, \tag{5.12}$$

were $\mu(r)_{obs}$ and $\mu(r)_m$ is the measured surface brightness of the observed and model galaxy at some radius r and N is the number of data points used. We note that, with the exeption of MGC02952, all the rms vlues quoted in Fig. 5.5 indicate good profile fits, rms< 0.5. The reason for the high rms of MGC02952 can be found by looking at its postage stamp on Fig. 5.4. We notice that this object has a close bright companion, and so the difference in the model and data is down to GIM2D distinguishing between the two. Where as, the real profile is contaminated by the nearby object. This effect can also be seen, though to a much lesser extent, in MGC16751 and MGC15280.

5.2 GIM2D Credibility

Having used GIM2D to analyse all the galaxies in MGC-BRIGHT in the range 16< $B_{\rm MGC}$ <20, we now need to assess its accuracy and over what magnitude range the galaxy parameters should be believed. The first test is to compare those MGC-BRIGHT parameters which are replicated by GIM2D, these are the half-light radius, the (un-dust-corrected) galaxy magnitude and the effective surface brightness.

5.2.1 Magnitudes

The top panel of Fig. 5.6 shows how the un-dust-corrected measured MGC best magnitudes compare with the profiled GIM2D magnitudes. The mean magnitude difference is, $\overline{\Delta m}$ = − 0.126, indicating that GIM2D tends to over-estimate the galaxies magnitude. The value of $\overline{\Delta m}$ remains more-or-less constant, changing by ∼0.006 when only galaxies brighter than $B_{\rm MGC}$=17 are used. The GIM2D over-estimation of galaxy magnitudes is not surprising as GIM2D estimates the flux by integrating the light profile out to infinity whilst the MGC magnitudes are derived from within 2.5 Kron radii or within the 26 mags/sq arcsec isophote (see Chapter 2).

5.2.2 Half-light radii

The middle panel of Fig. 5.6 shows how the GIM2D and MGC half light radii (HLR) differences vary with MGC magnitude. The mean HLR difference is, $\overline{\Delta \rm HLR}$=0.093 arcsec, indicating that GIM2D also tends to over-estimate the galaxies HLR. Unlike the magnitudes the value of $\overline{\Delta \rm HLR}$ tends to increase when only galaxies brighter than $B_{\rm MGC}$=17 are used. This isn't surprising as the brighter galaxies are mostly closer and therefore

[2] All profiles where measured using the **STARLINK** Extended Surface Photometry (ESP) routine, see Grey, Taylor & Privett (2002).

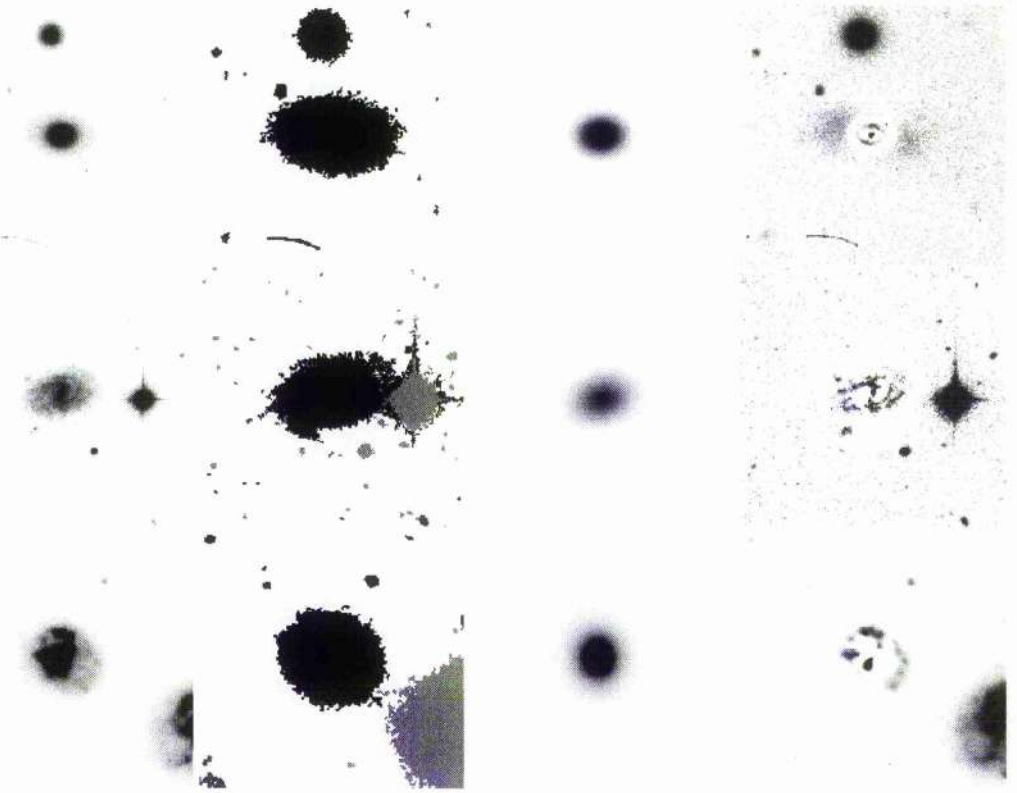

Figure 5.3: Shown here are the GIM2D input, mask, model and residual images for the main Hubble types: Elliptical (top), Spiral (middle) and irregular (bottom).

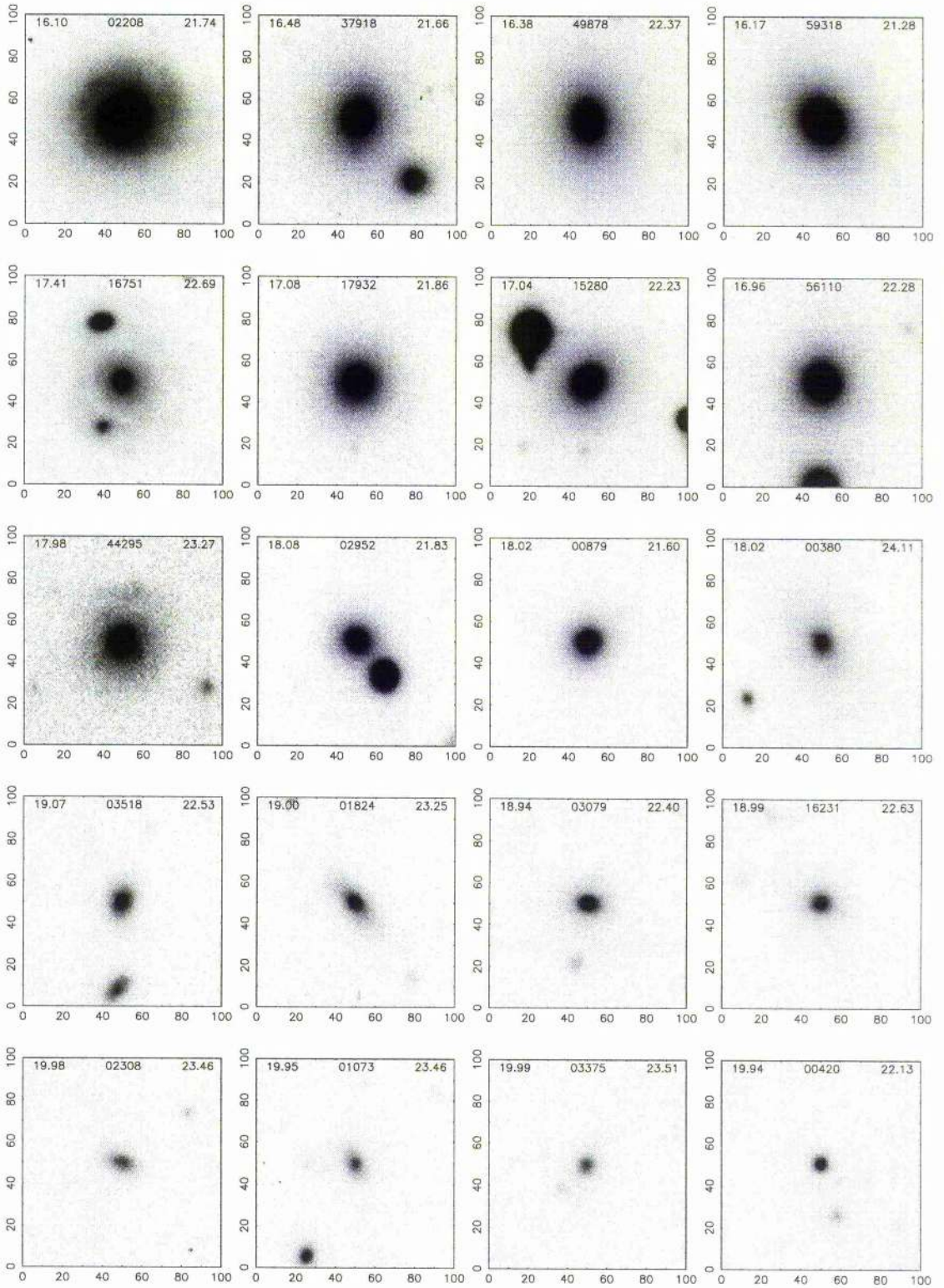

Figure 5.4: Example galaxies with (B/T)=0.2 (left), 0.4 (center left), 0.6 (center right), 0.8 (right) at B_{MGC}=16 (top), 17 (2nd), 18 (3rd), 19 (4th) and 20 (bottom). Each galaxy is displayed in a 100×100 pixel box and is centered at the pixel coordinates (50,50). The galaxies MGC magnitude, ID number, and MGC surface brightness are shown in the top-left, center and right respectively. Galaxies are displayed between background-1.5σ (white) and 21.5 mags/sq arcsec (black).

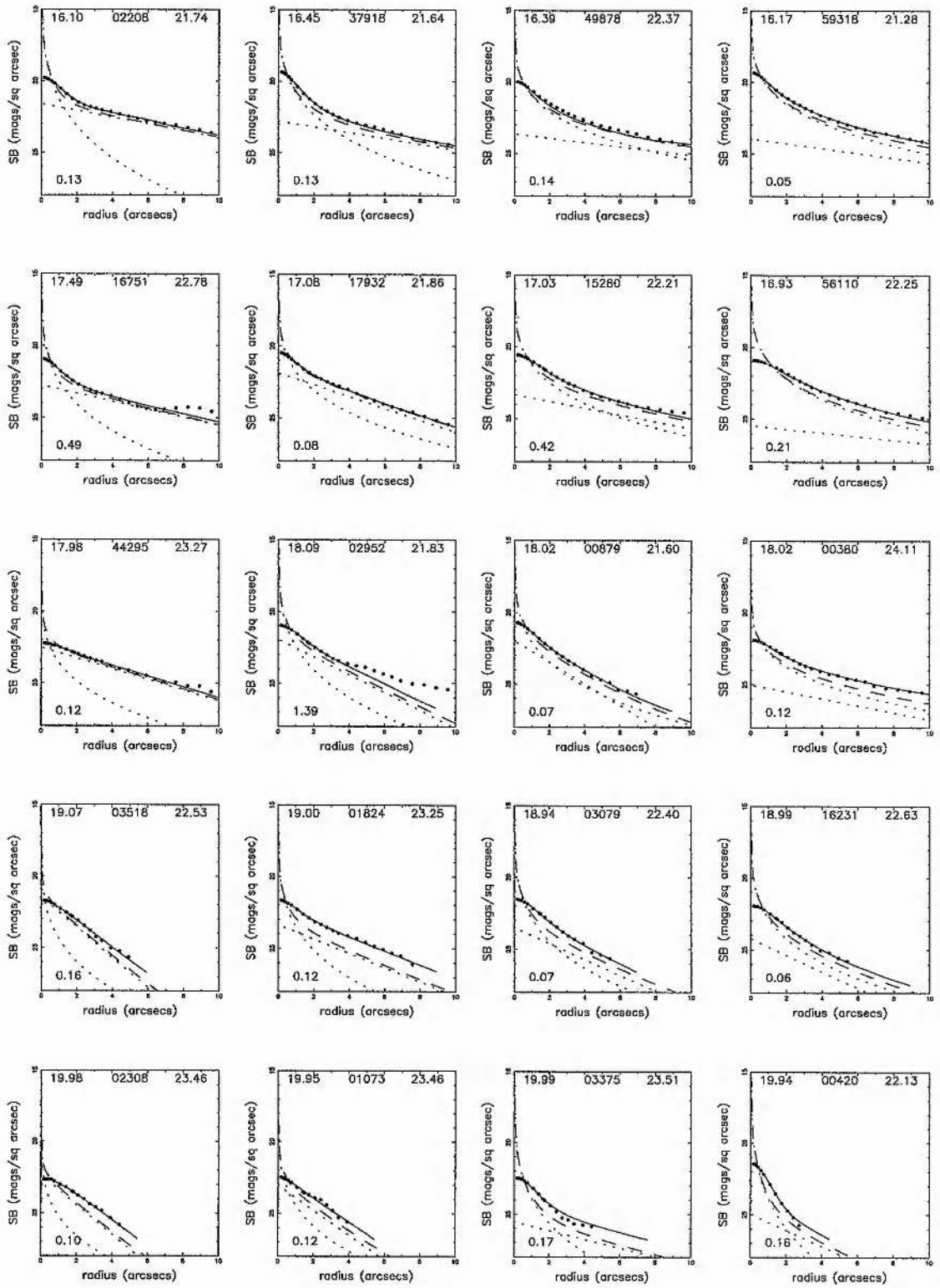

Figure 5.5: The measured and GIM2D derived profiles of the galaxies shown in Fig. 5.4. The two dotted lines show the individual disk and central bulge components, the dashed line is the combined (unconvolved) profile and the solid line is the measured model profile. The galaxies MGC magnitude and MGC surface brightness are shown in the top-left and top-right respectively and a goodness-of-fit statistic is shown in the bottom left.

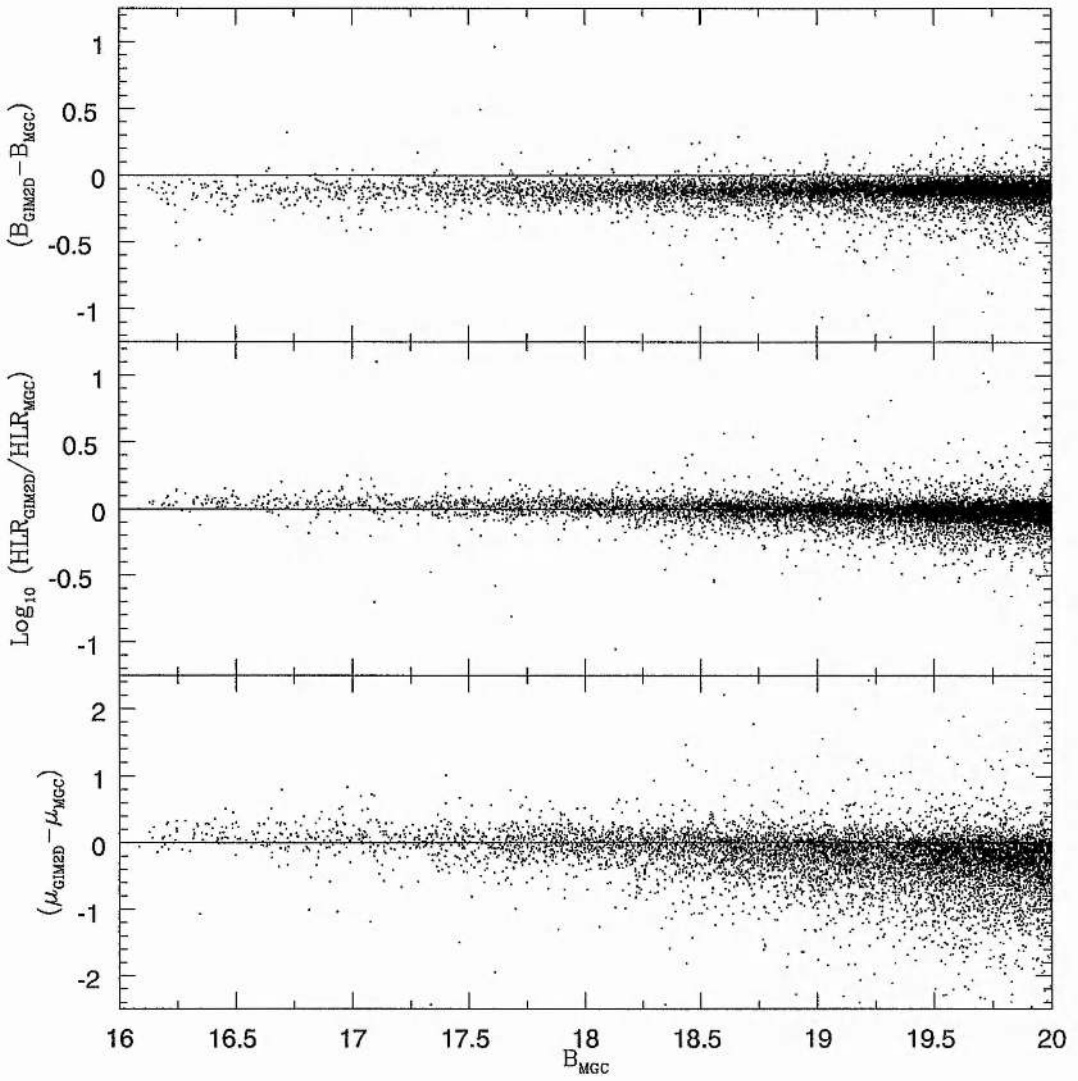

Figure 5.6: A comparison of GIM2D and MGC measured parameters: un-dust-corrected magnitude (top), half-light radii (HLR, middle) and effective surface brightness (μ_{eff}, bottom). Δm is given by $\Delta \mathrm{m}=B_{\mathrm{MGC}_{\mathrm{GIM2D}}}-B_{\mathrm{MGC}}$ and similarly for ΔHLR and $\Delta\mu_{eff}$.

appear bigger, and as GIM2D calculates a slightly brighter magnitude it is not surprising that the HLR are also slightly larger.

During this process we found that there are a small number of galaxies (31) with GIM2D HLR<1 pixel (0.333 arcsecs). These 31 galaxies indicate cases in which GIM2D has failed to correctly model the galaxies. In these cases either the bulge or disk was collapsed to a point by GIM2D and consequently all have Re=0 or Rd=0. GIM2D will collapse the bulge or disk to a point if either has a measured Re or Rd less then 0.02″. Although GIM2D has erred in measuring these galaxies HLR, for a substantial fraction of them the model profiles seem reasonable representations of the observed galaxy light distribution. However, there are three cases where GIM2D has obviously failed (MGC90054, MGC90090 and MGC90107). This we attribute to the presence of a bright star being very close to the faint, low-surface brightness galaxy. This has resulted in a deblending error and caused GIM2D to model the star+galaxy profile. Therefore the galaxy coordinates no longer represent the center of the model and hence the measured model profile (automatically measured assuming the galaxy coordinates to be the center of the light distribution) is essentially just noise. Other failures seem to be caused by problems in the outer regions of the galaxy as at no point was the inner bulge profile poorly estimated. This would seem to suggest that the problems here are due to an error in background calculation and not due to errors within GIM2D.

5.2.3 Effective surface brightness

The bottom panel of Fig. 5.6 shows how the GIM2D and MGC effective surface brightness (μ_{eff}) differences vary with MGC magnitude. We calculate the surface brightness as shown in Eqn. 2.7. The mean difference in μ_{eff} is, $\overline{\Delta\mu_{eff}}$ =-0.24 mags/sq arcsec, indicating that GIM2D over-estimates the galaxies effective surface brightness. Given the comparative size and sign in the differences in magnitude and HLR (Δm<ΔHLR) the sign and size of $\overline{\Delta\mu_{eff}}$ is not unexpected.

5.2.4 The χ^2 and rms distributions

We now look at the distribution of χ^2 statistic calculated by GIM2D for each of the profiles. The GIM2D χ^2 is a pixel-to-pixel χ^2 calculated as

$$\chi^2 = \frac{1}{\nu}\sum_i \left(\frac{O_i - M_i}{\sigma_i}\right)^2, \tag{5.13}$$

(Luc Simard priv. comm) rather than a direct comparison of the model to observed profile. Here O_i is the observed value of pixel i with expected variance σ_i. M_i is the model pixel value and ν is the number of degrees of freedom. Fig. 5.7 shows how the χ^2 varies as a function of seeing (top), apparent magnitude (middle) and surface brightness. There appears be a slight tendency for the χ^2 to favor lower values for galaxies with poor seeing. This is not unexpected because as the seeing increases, light profiles become smoothed out making it easier to model the PSFs as well as the galaxy light distribution. There is no obvious trend as to how the GIM2D χ^2 varies with magnitude and surface brightness, other than a general decrease in the mean χ^2 towards low magnitude/surface brightness. Unsurprisingly, we find that the χ^2 indicates that it is easier for GIM2D to reproduce small faint blurry objects than the large bright resolved galaxies with, for example, spiral arms and HII regions. Following this we can state that the GIM2D χ^2 is not a good estimator of the goodness-of-fit of the GIM2D model profile to the observed profile. We note here that the χ^2 statistics should ideally be calculated within some fixed isophote i.e. the MGC

detection isophote, $\sim$ 26 mags/sq arcsec. If the GIM2D χ^2 where calculated using just the pixels within the galaxy area, instead of the whole postage stamp, the degrees of freedom would be dramatically reduced for fainter objects making it more useful.

As shown in § 5.1.3.3 we calculate the root-mean-square (rms) for each measured observed and model profile. In Fig. 5.8 we show how the rms varies with seeing, apparent magnitude and surface brightness. We find that there is no indication of a significant relationship between rms and either seeing, magnitude or surface brightness. We take that the lack of an upturn in rms at faint magnitudes and/or low-surface brightness indicates that GIM2D is accurately modeling galaxy profiles to the limits of the MGC-BRIGHT sample.

5.2.5 The GIM2D parameters

We now need to add some weight to the statement that GIM2D accurately models galaxies down to the limits of the MGC-BRIGHT catalogue. To do this we first return to the HLR. Fig. 5.9 shows how the MGC and GIM2D HLR radii vary as a function of magnitude. We notice that in both cases the mean HLR never drops below the median seeing and that, as expected, only for the GIM2D HLR does the -1σ line fall below this limit. Figs. 5.9, 5.10 and 5.11 show how the distributions of the GIM2D measured parameters (B/T), bulge effective radius (Re), ellipticity (e) and position angle ϕ_{bulge} and disk exponential scale length (Rd), inclination (i) and position angle (ϕ_{disk}) relate to magnitude. Only galaxies with (B/T)>0.5 are shown in Fig. 5.10 and those with 0<(B/T)$\leq$0.5 in Fig. 5.11. For Fig. 5.9 only galaxies with (B/T)>0 are used, see below. Aside from a slight increase in ellipticity with magnitude there are no obvious unexpected relationships with $B_{\rm MGC}$ for any of the parameter distributions shown.

From Figs. 5.10 and 5.11 we see that the median Re and Rd reach the median seeing at $B_{\rm MGC}$=19.5 and 20 respectively. Even though the profiles of galaxies at $B_{\rm MGC}$=20, see Fig 5.5 bottom row, appear well modeled we fix the MGC-GIM2D reliability limit at $B_{\rm MGC}$=19.5. By doing this we ensure that the MGC-GIM2D sample is not biased against bulges at $B_{\rm MGC}$ <19.5.

5.2.6 The low (B/T) population

We now use a fine (B/T) bin size to break down the data into 1 magnitude bins, Fig. 5.12 shows this refined distribution. We see that there is a large ($\sim$ 38%) low (B/T) population that are not confined to a particular magnitude and that the vast majority have (B/T)=0. This (B/T)=0 population have GIM2D parameter distributions which appear consistent in all ways with those of the total galaxy population. Fig. 5.13 shows a random sample of these (B/T)=0 galaxies at 16 (top row), 17 (2nd row), 18 (3rd row), 19 (4th row) & 20 (bottom row) magnitudes. Note that both Spiral and Irregular galaxy types are seen here. Their measured and GIM2D derived profiles are shown in Fig 5.14. All the galaxies have measured bulge and/or disk profiles that are flatter than an exponential profile. For this reason we now refer to this (B/T)=0 population as Flat Profile Anomalies or FPAs. From Fig. 5.13 we argue that many of the FPAs have profiles perturbed by HII star-forming regions which then get smoothed out into the flattened azimuthally averaged proiles.

It is worth mentioning here that Marleau & Simard (1998) have also found this FPA population and they go on to demonstrate that the profiles of these galaxies are flatter than an exponential i.e β<1 in Eqn 1.9. This flat profile can either be a real structural feature or can be caused by merging and/or rapid star formation. Marleau & Simard (1998) show that the flat profiles from merging or star formation can be identified via a colour gradient. They demonstrate that acceptable fits to the flat galaxy profiles without a colour gradient can be obtained by running GIM2D with a pure Sersic profile giving a mean index n of $\overline{n}$=0.62. However, whilst achieving acceptable profiles any information regarding (B/T) is lost. It is interesting to note that although their data is based on

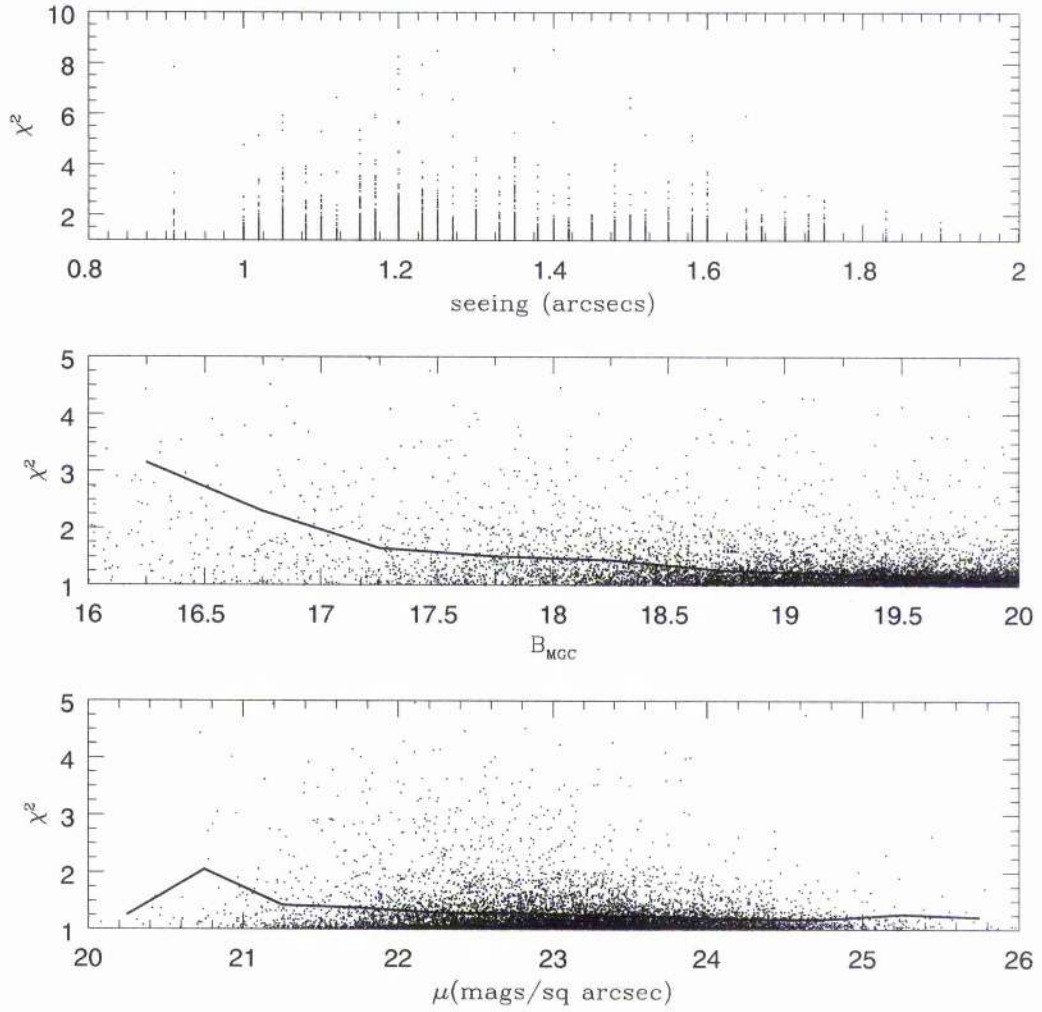

Figure 5.7: The χ^2 distributions with seeing (top), $B_{\rm MGC}$ (middle) and μ (bottom). The solid lines are the mean GIM2D χ^2 values for each 0.5 mag and 0.5 mags/sq arcsec bin.

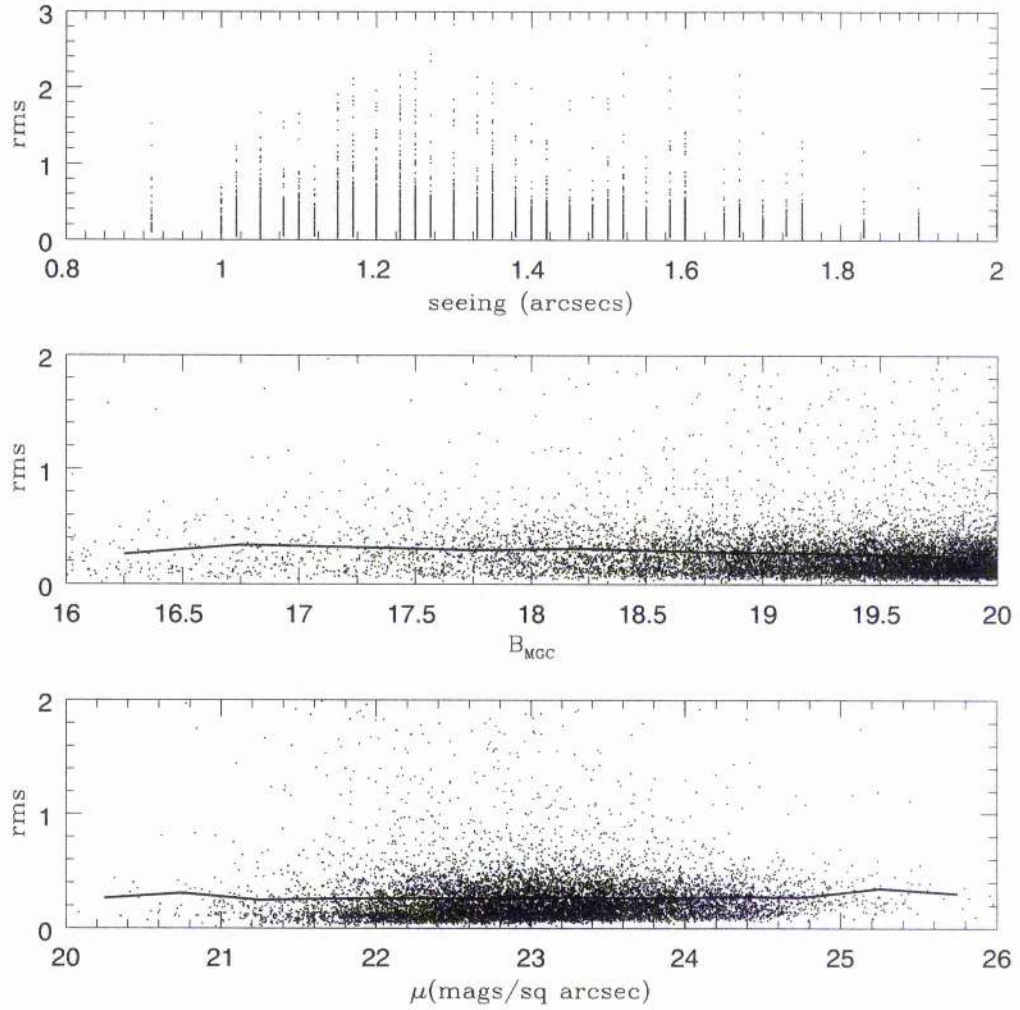

Figure 5.8: The rms distributions with seeing (top), $B_{\rm MGC}$ (middle) and μ (bottom). The solid lines are the mean rms values for each 0.5 mag and 0.5 mags/sq arcsec bin.

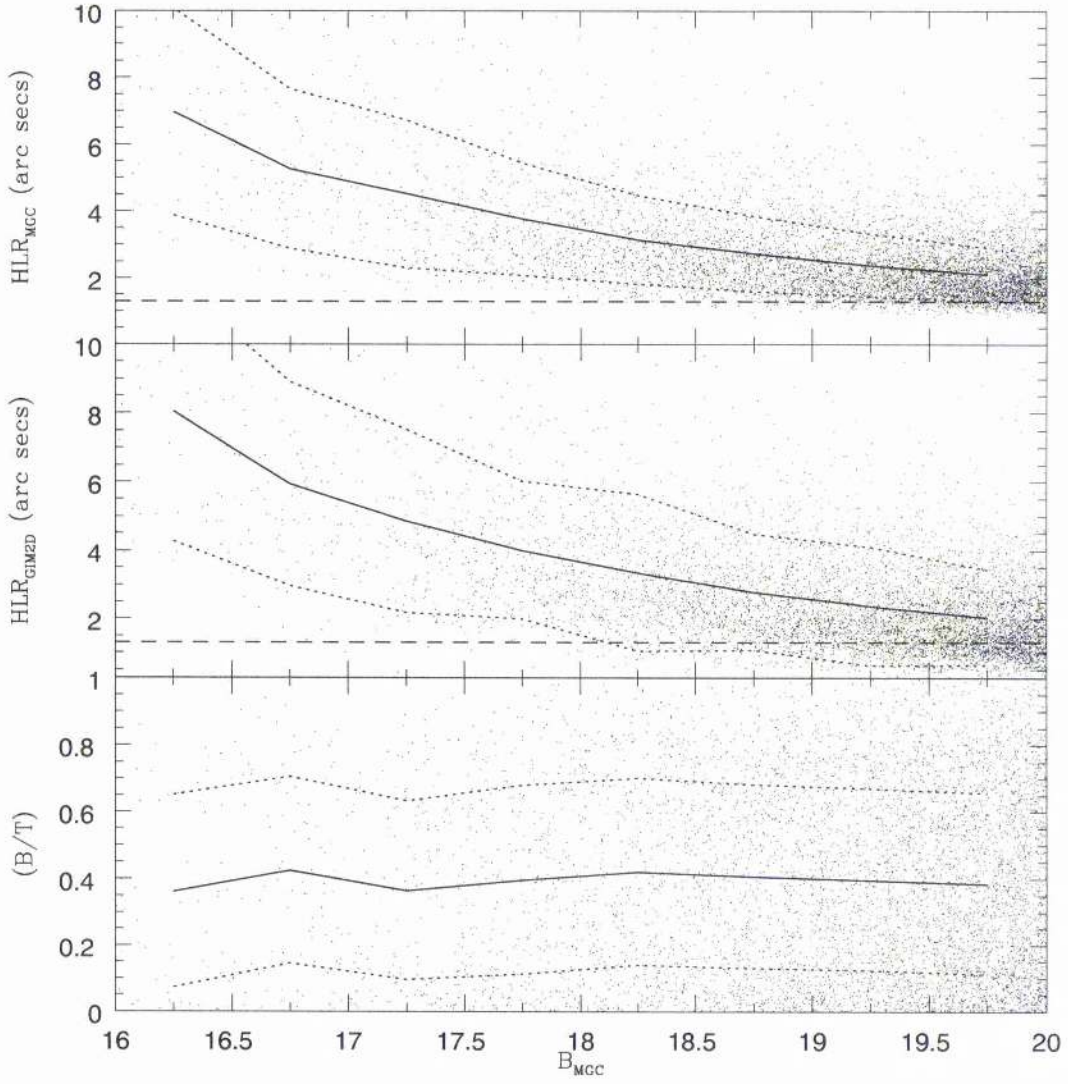

Figure 5.9: The variation with magnitude of the MGC (upper panel), GIM2D (middle panel) half-light radii (HLR) and bulge-to-total light ratio (B/T) (bottom panel). In each case the solid line represents the mean HLR or (B/T) in each 0.5 mag bin, the dotted lines are the $\pm 1\sigma$ limits and the dashed line in the top and middle panels is the $1.3''$ median MGC seeing.

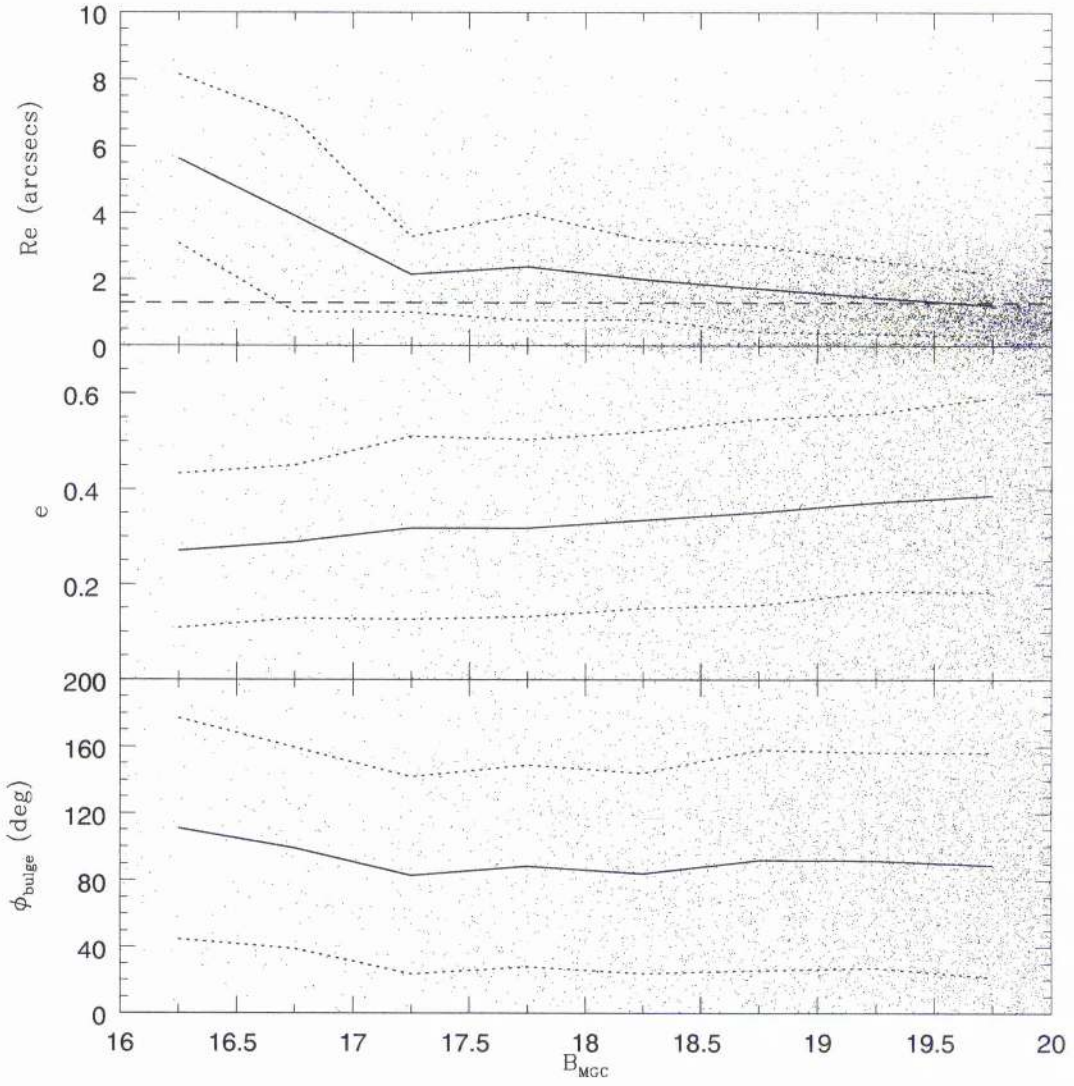

Figure 5.10: The variation of bulge effective radii (Re, top panel), bulge ellipticity (e, center panel) and bulge position angle (ϕ_{bulge}, bottom panel) with $B_{\rm MGC}$. In each case the solid line indicates the mean parameter in each 0.5 mag bin and the dotted lines are the $\pm 1\sigma$ limits. Only galaxies with (B/T)>0.5 are used here.

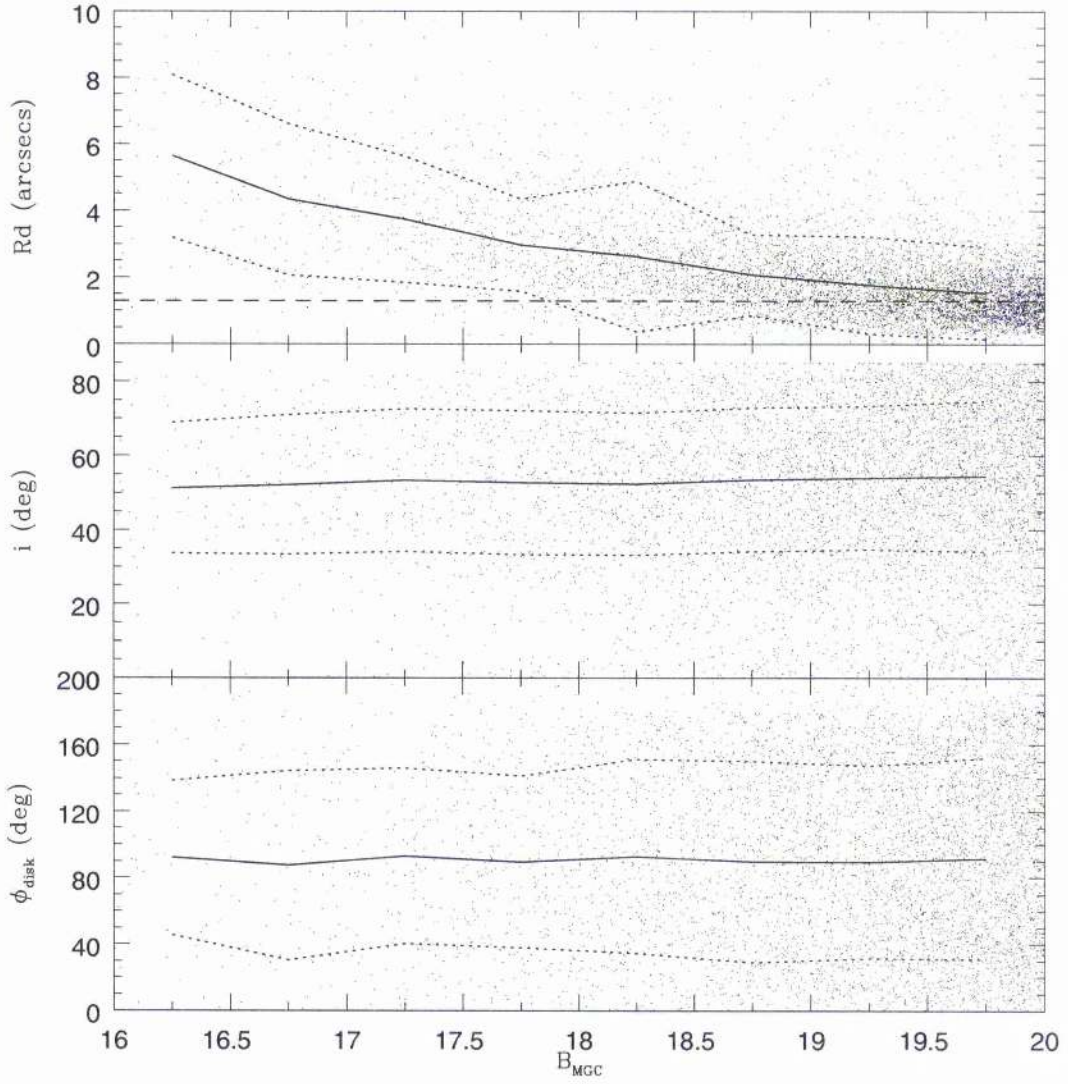

Figure 5.11: The variation of exponential disk scale length (Rd, top panel), disk inclination (i, center panel) and disk position angle (ϕ_{disk}, bottom panel) with $B_{\rm MGC}$. In each case the solid line indicates the mean parameter in each 0.5 mag bin and the dotted lines are the $\pm 1\sigma$ limits. Only galaxies with $0<(B/T)\leq 0.5$ are used here.

Table 5.2: The (B/T) ranges for each Hubble type.

Class	(B/T) range	$N_{16<B_{MGC}<19}$
E/S0	1.0<(B/T)<0.5	929
S(B)abc	0.5<(B/T)<0.1	997
S(B)d/Irr	0.1<(B/T)<0.0	444
FPA	(B/T)=0	1025
Total		3395

Hubble deep field galaxies they find a fraction of galaxies with $0 \leq (B/T) < 0.1$ that is surprisingly similar to our own low redshift data, 46% in this work and 43% in Marleau & Simard (1998).

5.3 Colours & Hubble Types

The MGC, although only imaged in a single (B-band) filter, overlaps with the Sloan Digital Sky Survey Early Data Release (SDSS-EDR, specifically run 756 strip 10, York et al. 2000). By combining MGC-BRIGHT and SDSS-EDR we are able to get colour information for a subset of our galaxies. We choose to limit our sample here to only those brighter than B_{MGC} =19 mags. Details of the matching process for MGC-SDSS-EDR, as well as MGC-2dFGRS and 2dFGRS-SDSS-EDR photometric comparisons see Cross et al. (2003).

Of the 9804 galaxies processed by GIM2D, 3395 have B_{MGC} <19 mags and 3342 have SDSS-EDR colours. The distribution of these galaxies in colour- colour space can be seen for each Hubble type, as well as the FPA population, in Fig. 5.15 [3]. To assign a Hubble type for each galaxy we make cuts in (B/T) based on data from Kent (1985), Table 5.2 shows the cuts used (see Appendix. C for a discussion of morphological classification schemes). We use the bluest colour available in order to high-light the differences between non-star-forming Ellipticals and star-forming Spiral/Irr galaxies. Note how the FPA distribution resembles that of the Sd/Irr galaxies.

Fig. 5.16 shows how the galaxies are distributed in (B/T) and colour (u^*-g^*) and the fractions of each population in each colour bin. The vast majority of the high (B/T), Ellipticals, are red in colour with the Irregulars dominating the blue end and the Spirals forming a transient population between the two extremes. Fig. 5.16 validates our choice of Hubble type (B/T) cuts. However, there are (as always) some exceptions to this. Notably some very blue, (u^*-g^*)<0.8, bulge dominated galaxies and red, (u^*-g^*)>2.2, disk dominated galaxies. From a visual inspection we note that the classifications seem reasonable.

[3]We stick with the SDSS-EDR magnitude notation of * for their, as yet, unfinilised magnitude system.

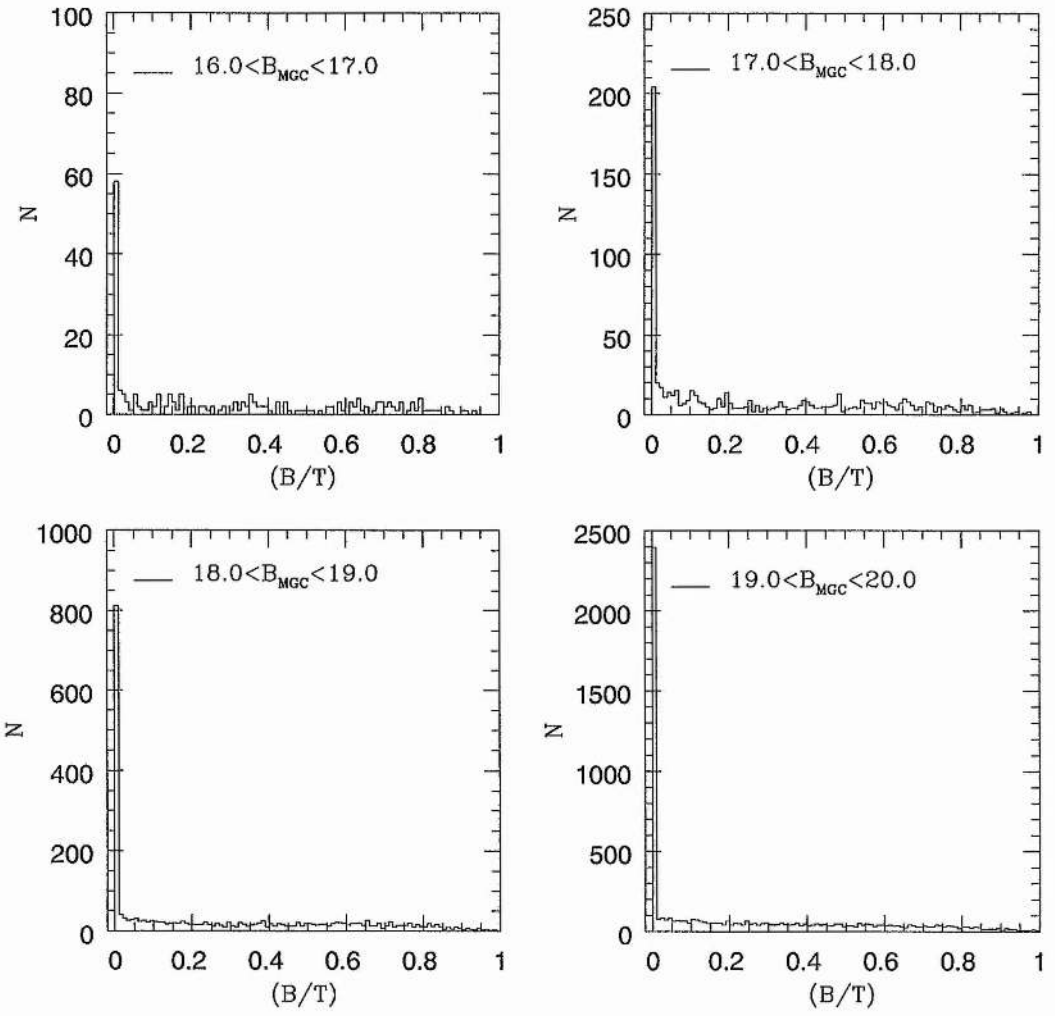

Figure 5.12: The distribution of the bulge-to-total light ratio (B/T) in 1 magnitude bins. Note that we now show the total number of galaxies in each bin.

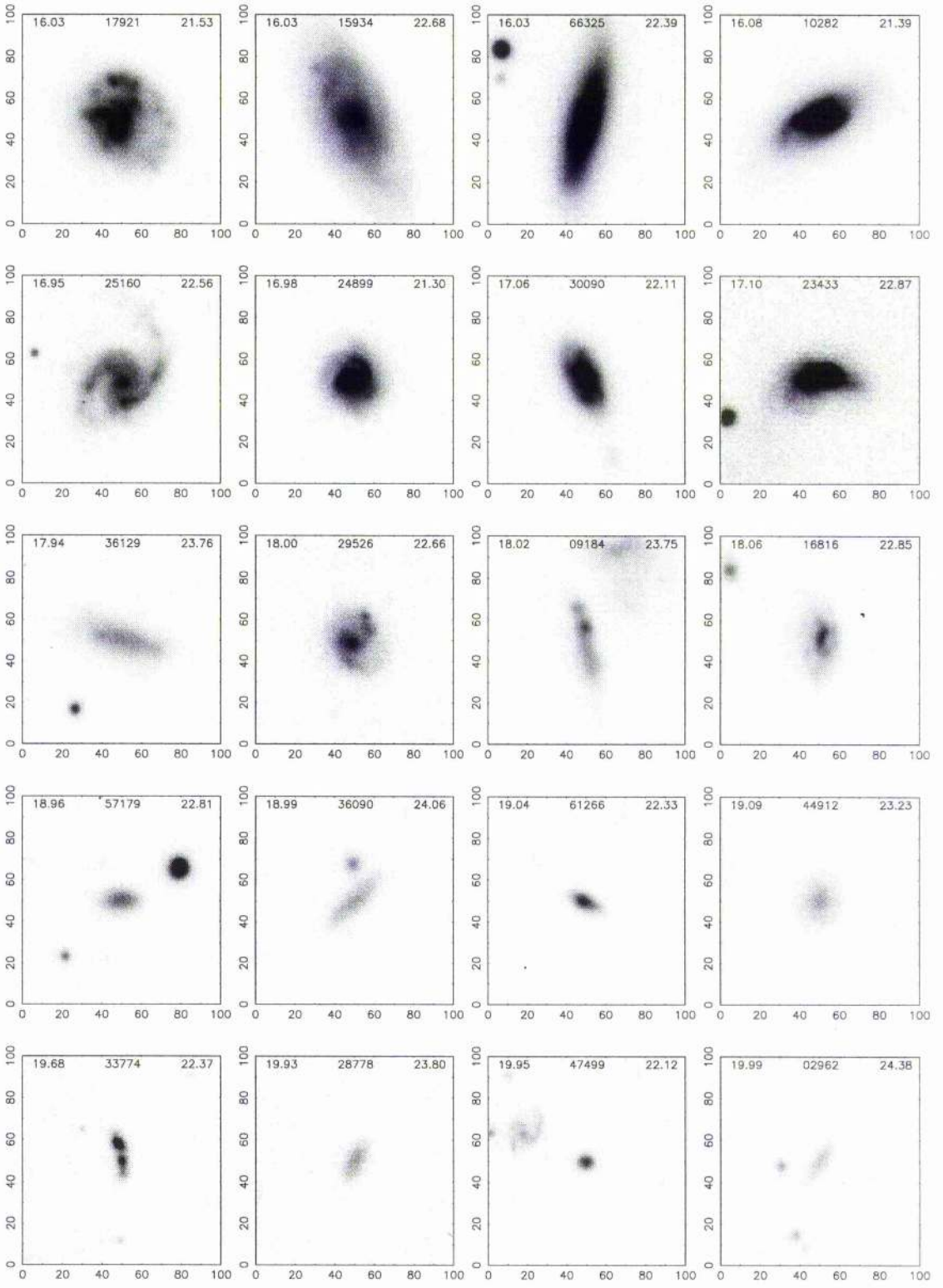

Figure 5.13: A random sample of (B/T)=0 galaxies at 16 (top), 17 (2nd), 18 (3rd), 19 (4th) & 20 (bottom) magnitudes. All galaxy types are seen here. Each galaxy is displayed in a 100×100 pixel box and is centered at the pixel coordinates (50,50). The galaxies magnitude, ID number, and surface brightness are shown in the top-left, center and right respectively. Galaxies are displayed between background-1.5σ and 21.0 mags/sq arcsec.

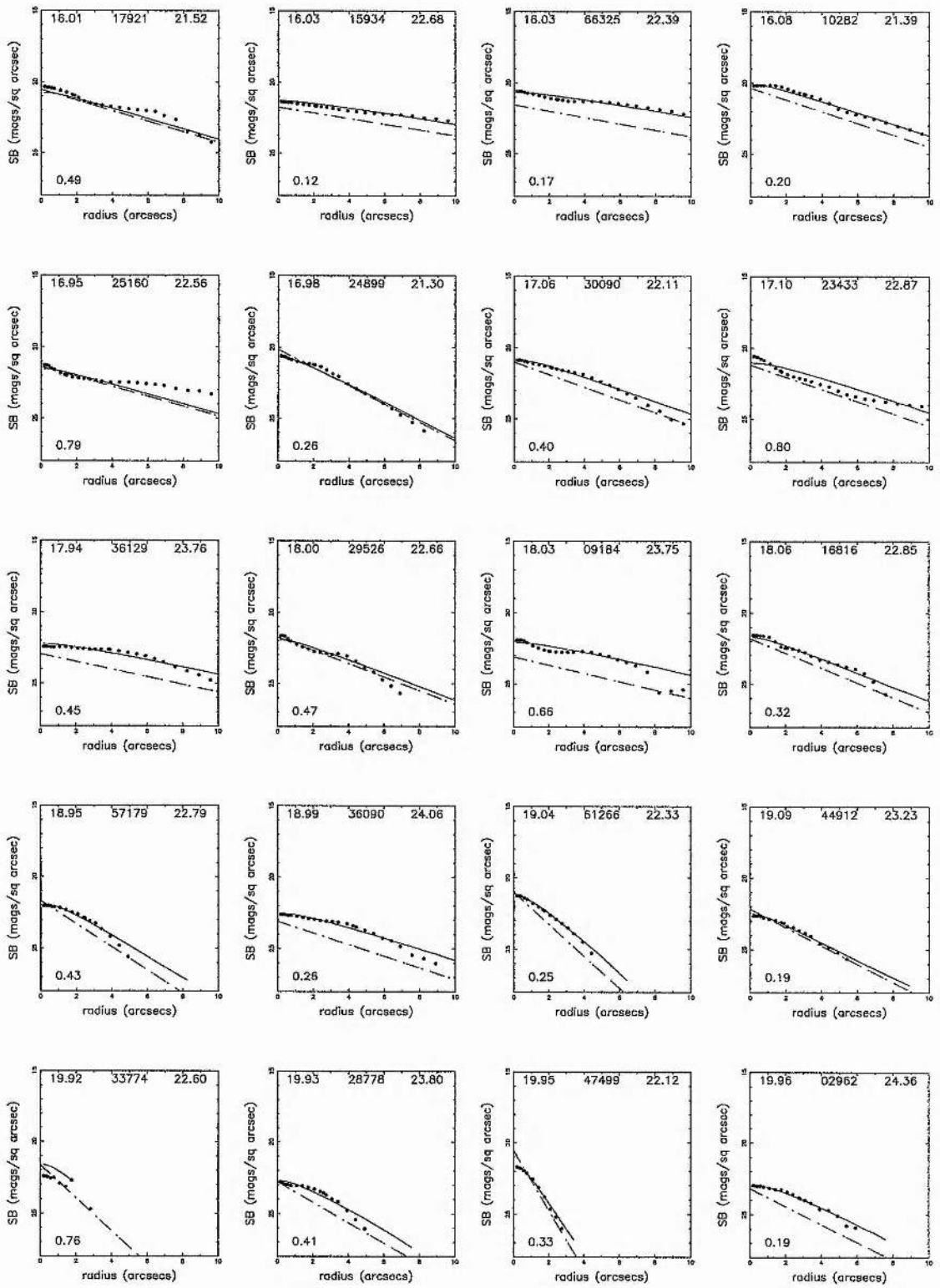

Figure 5.14: The measured and derived profiles of the (B/T)=0 galaxies shown in Fig. 5.13. The dotted lines indicate the bulge and disk GIM2D model profiles, the dashed line is the combined (unconvolved) profile and the solid line shows the measured model profile. The galaxies MGC magnitude and MGC surface brightness are shown in the top-left and top-right respectively and a goodness-of-fit statistic is shown in the bottom left.

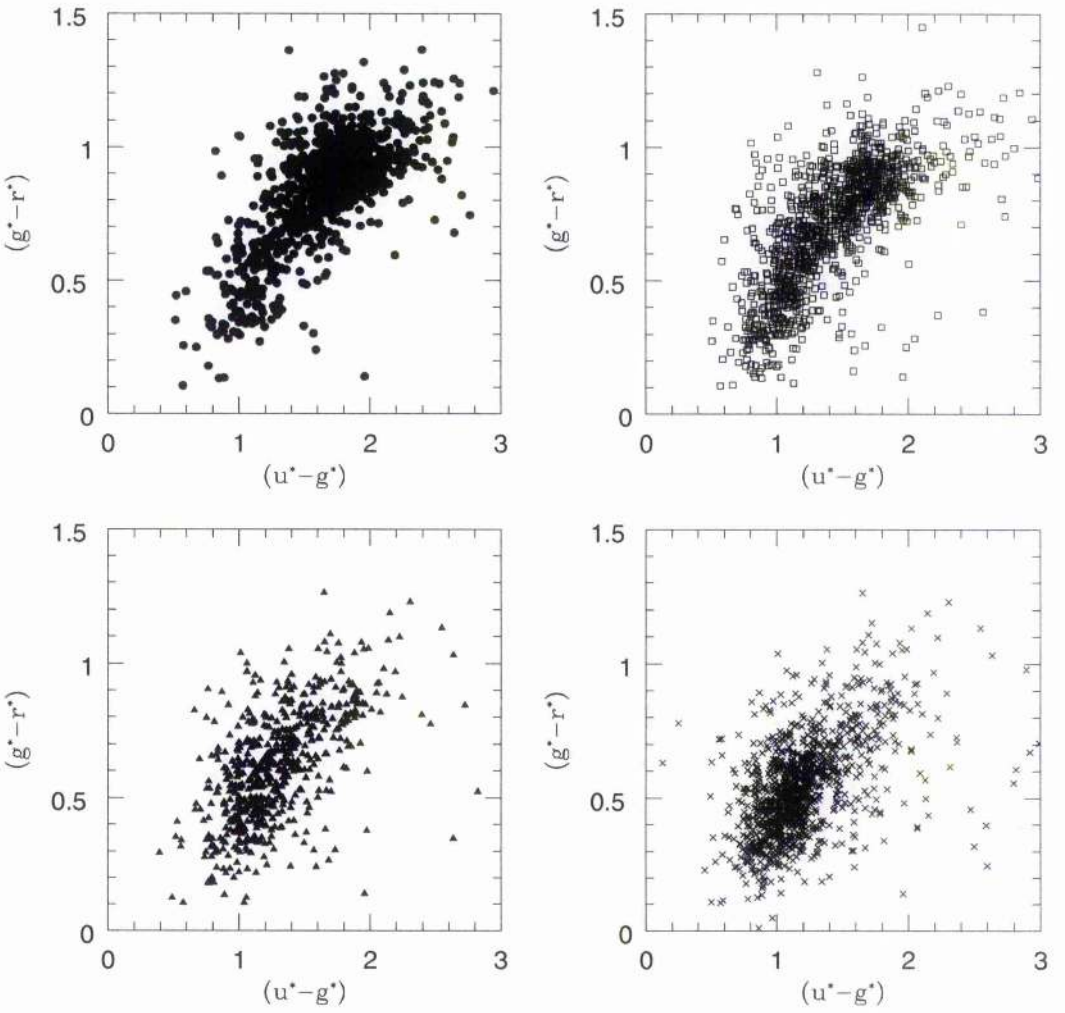

Figure 5.15: A galaxy colour-colour plot for E/S0 (filled circles, top-left), Sabd (open squares, top-right), Sd/Irr (filled triangles, bottom-left) and FPA (crosses, bottom-right). Note that the (B/T)=0 galaxies are distributed in the same way as the Sd/Irr population.

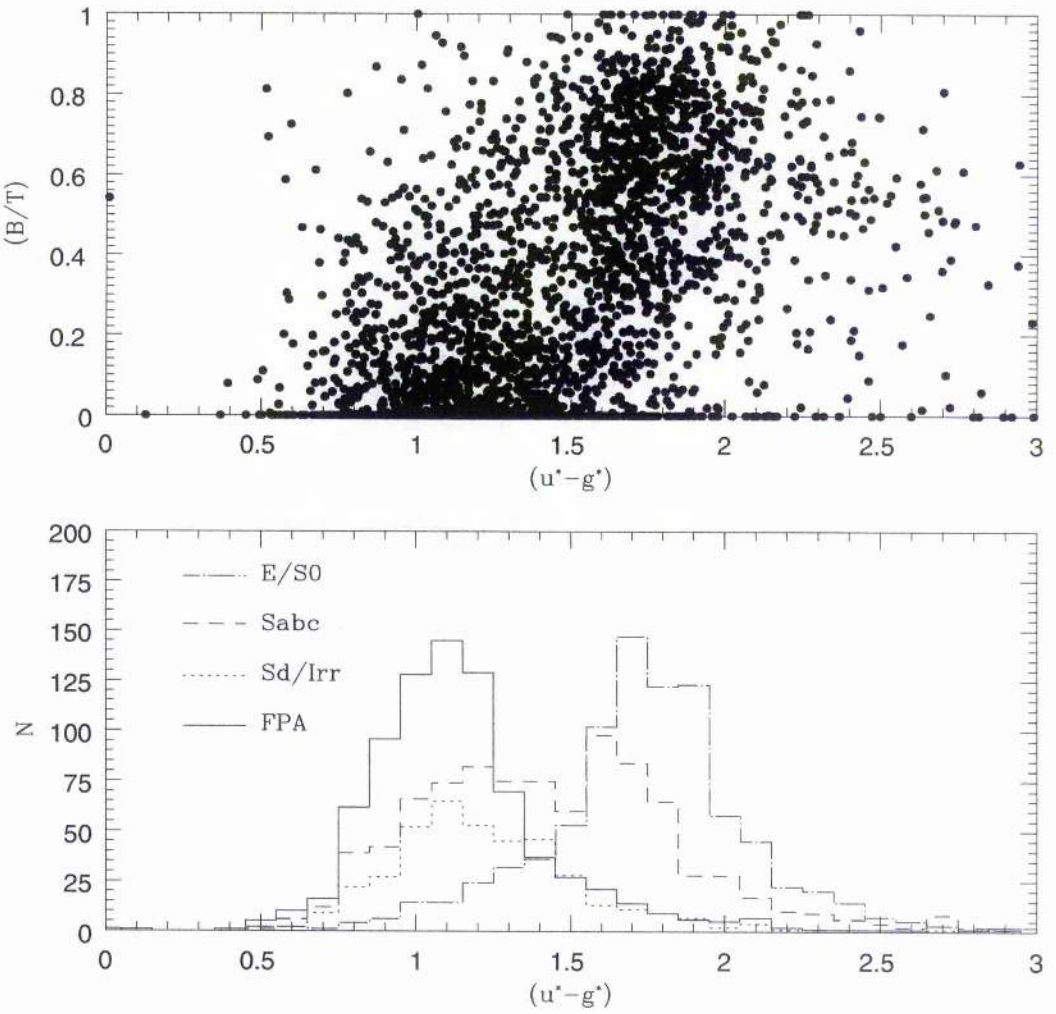

Figure 5.16: Top panel: The distribution of all the galaxies in (B/T)-(u^*-g^*) space. Note how well the Elliptical ((B/T)>0.5) and Sd/Irr ((B/T)<0.1) are separated. Lower panel: A histogram of the objects in each population in 0.1 colour bins.

5.4 FPA and red Spiral galaxies

From the colour histogram in Fig. 5.16 we have seen that the FPA population is dominated by very blue objects indicating that they appear to be undergoing intense star-formation. Figs. 5.17 & 5.18 show examples of red, (u^*-g^*)>1.8, and blue, (u^*-g^*)<1.3, FPA galaxies. The point of interest here is that the red objects are dominated by either edge-on spiral galaxies or low surface brightness galaxies, whilst the blue objects appear to be an adhoc selection of Spiral and Irregular objects. Once again the Sabc galaxy distributions appear to be bi-modal in colour, with a division of ($u^* - g^*$) ~1.5. From visual inspection both the red and blue spiral galaxy samples appear to be definite spirals with no obvious, other than colour, distinction between the two populations. We further discuss the red and blue Spirals in terms of their redshift distribution in Chapter 6.

5.5 Sersic profiles

As noted previously, the FPA profiles are poorly fitted by a de Vaucouleurs plus exponential profile due to there flatness. To try to get some more meaningful structural parameters we re-ran GIM2D over a sample of FPA galaxies using a pure Sersic profile. The FPA sample is taken from a restricted catalogue defined in Chapter 6. Whilst a pure Sersic profile may enable us to achieve a better fit to the galaxy profile, any morphological information in the (B/T) parameter that we could use to separate the FPA-Spirals and FPA-Irregulars is lost. Fig. 5.19 shows how changing to a pure Sersic model changes the GIM2D χ^2 statistic and how this change varies with magnitude, surface brightness and colour. In most cases, ~88%, the Sersic χ^2 is lower than the de Vaucouleurs χ^2. The difference in χ^2 is not affected by either magnitude, surface brightness or colour. Figs. 5.20 and 5.21 show the a random selection of FPA galaxies and their measured and measured-model profiles respectively. In all cases using a pure Sersic model has provided reasonable fits to the FPA galaxy profiles across the magnitude and surface brightness range.

Having established that a pure Sersic model accurately profiles the FPA galaxies we now look at the properties of the FPA population. Fig 5.22 shows the distribution of the Sersic index, n. The median of the distribution is 0.64 with a standard deviation of σ=0.2. Despite the difference in redshift these numbers are strikingly similar to those found for a sample HDF objects in Marleau & Simard (1998) (median n=0.62, σ=0.18). This is apparent similarity may indicate that the FPA population has had no net evolution i.e that over time/redshift the number of galaxies evolving into the FPA state is the same as the number evolving out of the FPA state. Or alternatively, that a Sersic index of around n=0.62 is an intrinsic property of the FPA galaxy population. Figs. 5.23 and 5.24 show examples of FPA galaxies with Sersic indicies of n=0.5 and n=1.0 respectively. There is no apparent difference between the types of galaxy in each in each sample indicating that the Sersic index cannot be used to discriminate between FPA-Spirals and FPA-Irregulars. Further confirmation of this may me gained by noticing that Fig. 5.22 is not bi-modal. If the Sersic index could be used to distinguish between the two FPA types one might expect each type to be congregated around different Sersic indicies. Figs. 5.25 and 5.26 show how the Sersic index n varies with apparent magnitude & surface brightness and redshift, absolute magnitude & colour respectively. There are no obvious relationships between the Sersic index and any of the galaxy parameters shown here.

5.6 Classifying the FPA galaxies

We have already seen that the FPA galaxies are a mixture of Spiral and Irregular galaxies. We know that whilst accurately modeling the FPA profiles the Sersic index cannot be used to discriminate between the two FPA types (Figs. 5.23 and 5.24) and likewise colour

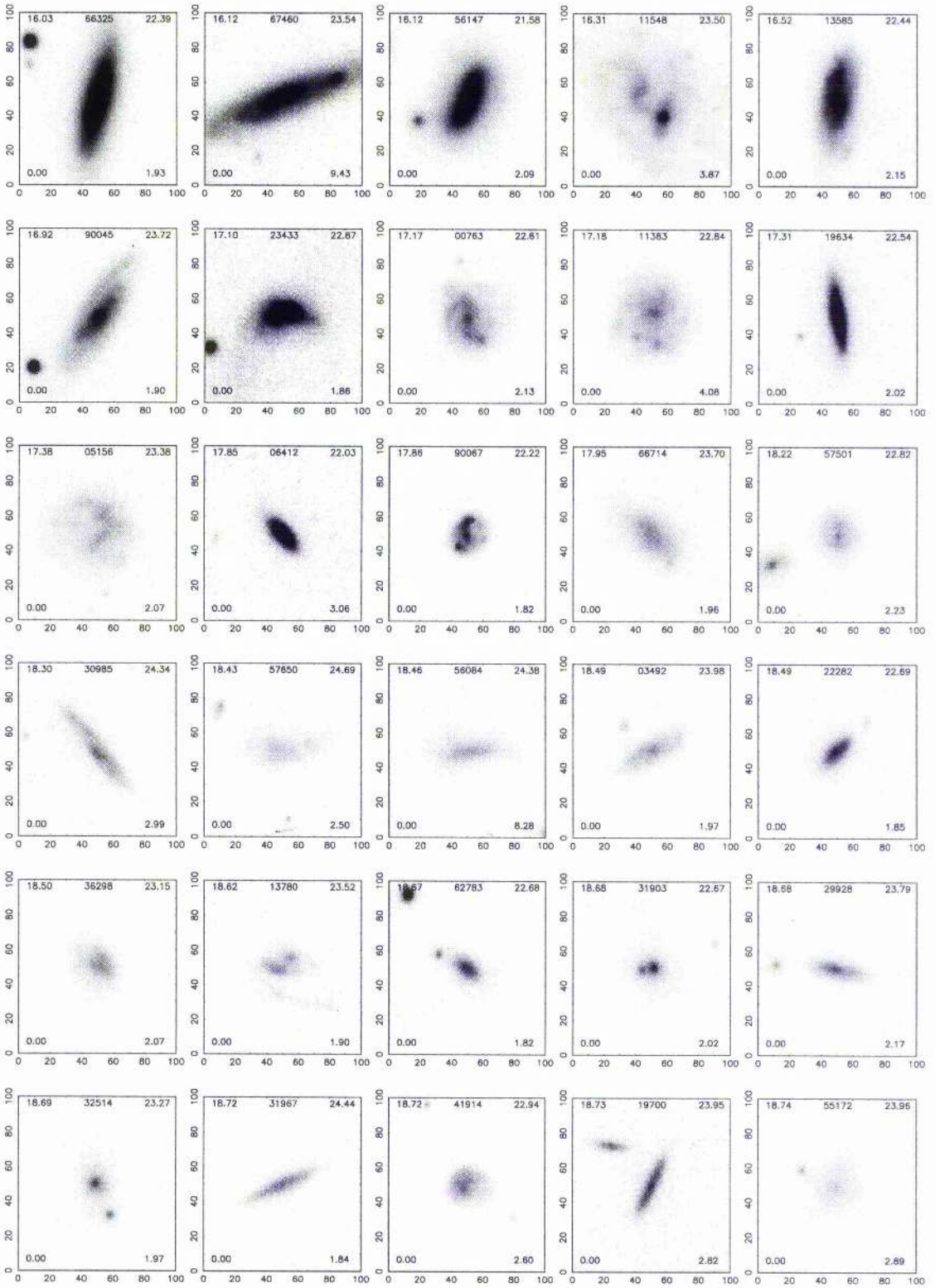

Figure 5.17: A random selection of red, (u^*-g^*)>1.8, FPA galaxies displayed from background-1.5σ to 21 mags/sq arcsec.Each galaxies magnitude (top-left), MGC ID (top-center), surface brightness (top-right), (B/T) (bottom-left) and colour (bottom-right) are shown. Galaxies are ordered in magnitude.

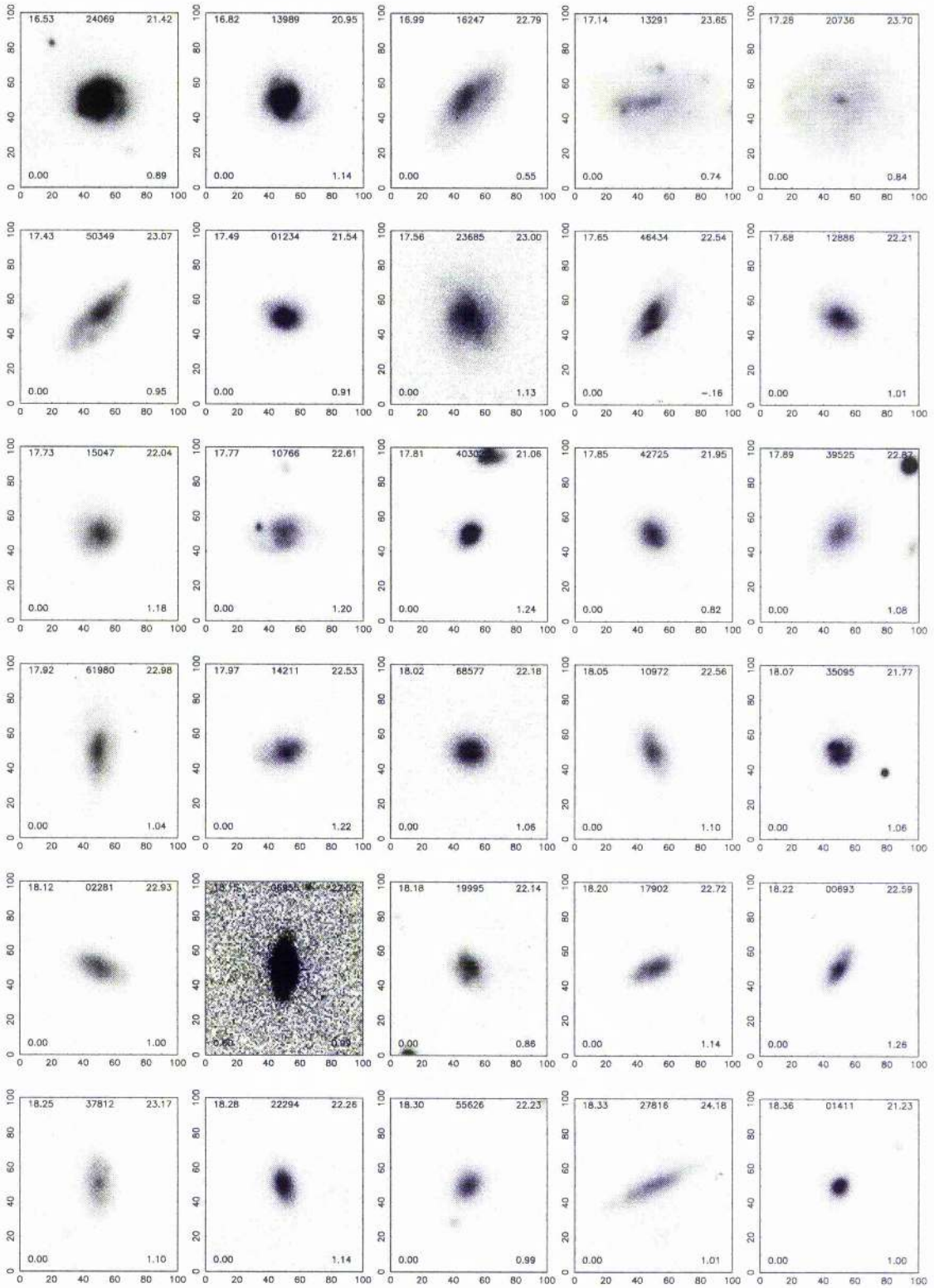

Figure 5.18: A random selection of blue, $(u^*\text{-}g^*)$<1.3, FPA galaxies displayed from background-1.5σ to 21 mags/sq arcsec.Each galaxies magnitude (top-left), MGC ID (top-center), surface brightness (top-right), (B/T) (bottom-left) and colour (bottom-right) are shown. Galaxies are ordered in magnitude.

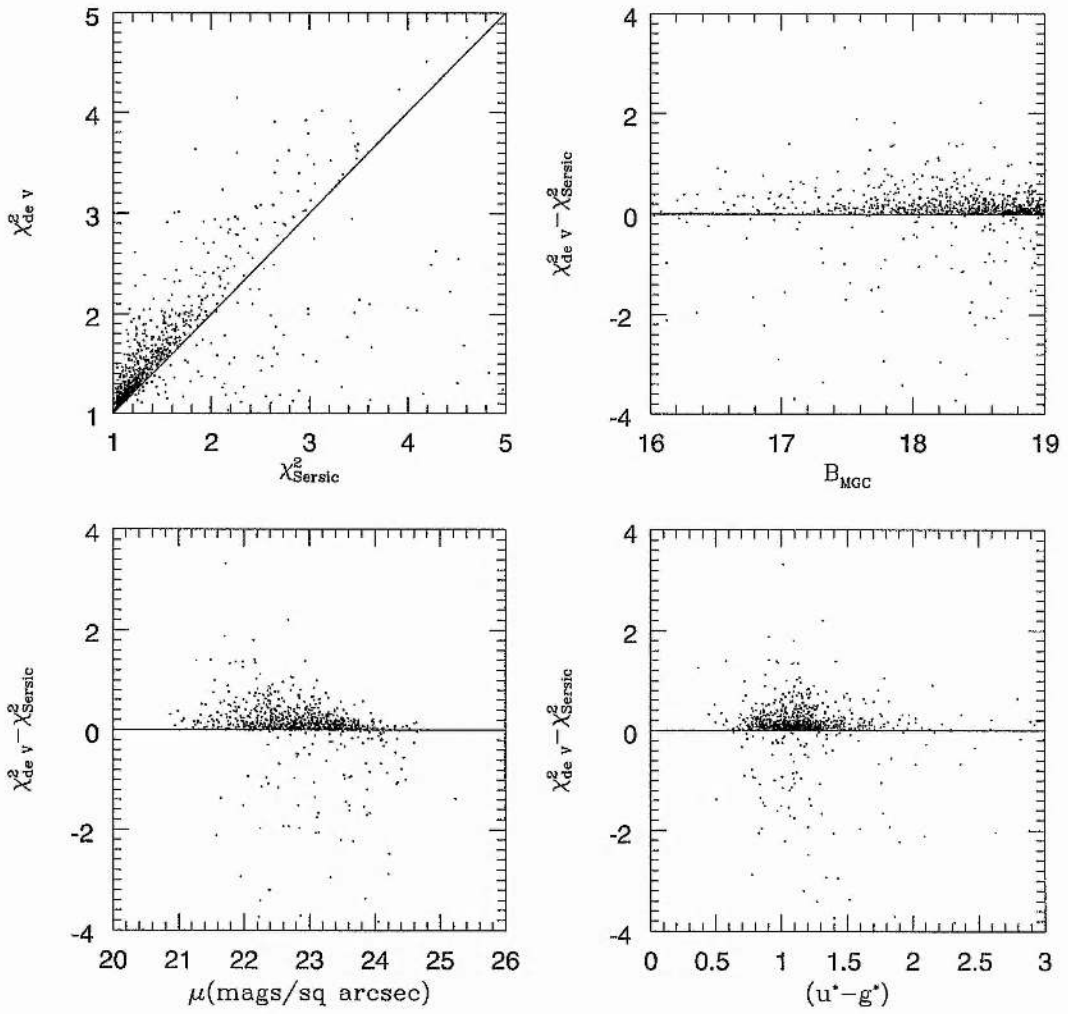

Figure 5.19: The differences in the GIM2D χ^2 (top-left) and how it is effected by magnitude (top-right), surface brightness (bottom-left) and colour (bottom-right).

Table 5.3: Breakdown of observer assigned FPA Hubble types.

Class	$N_{16<B_{\rm MGC}<19}$
FPA-E/S0	25
FPA-S(B)abc	349
FPA-S(B)d/Irr	612
FPA-unclassifiable	30
Total	1025

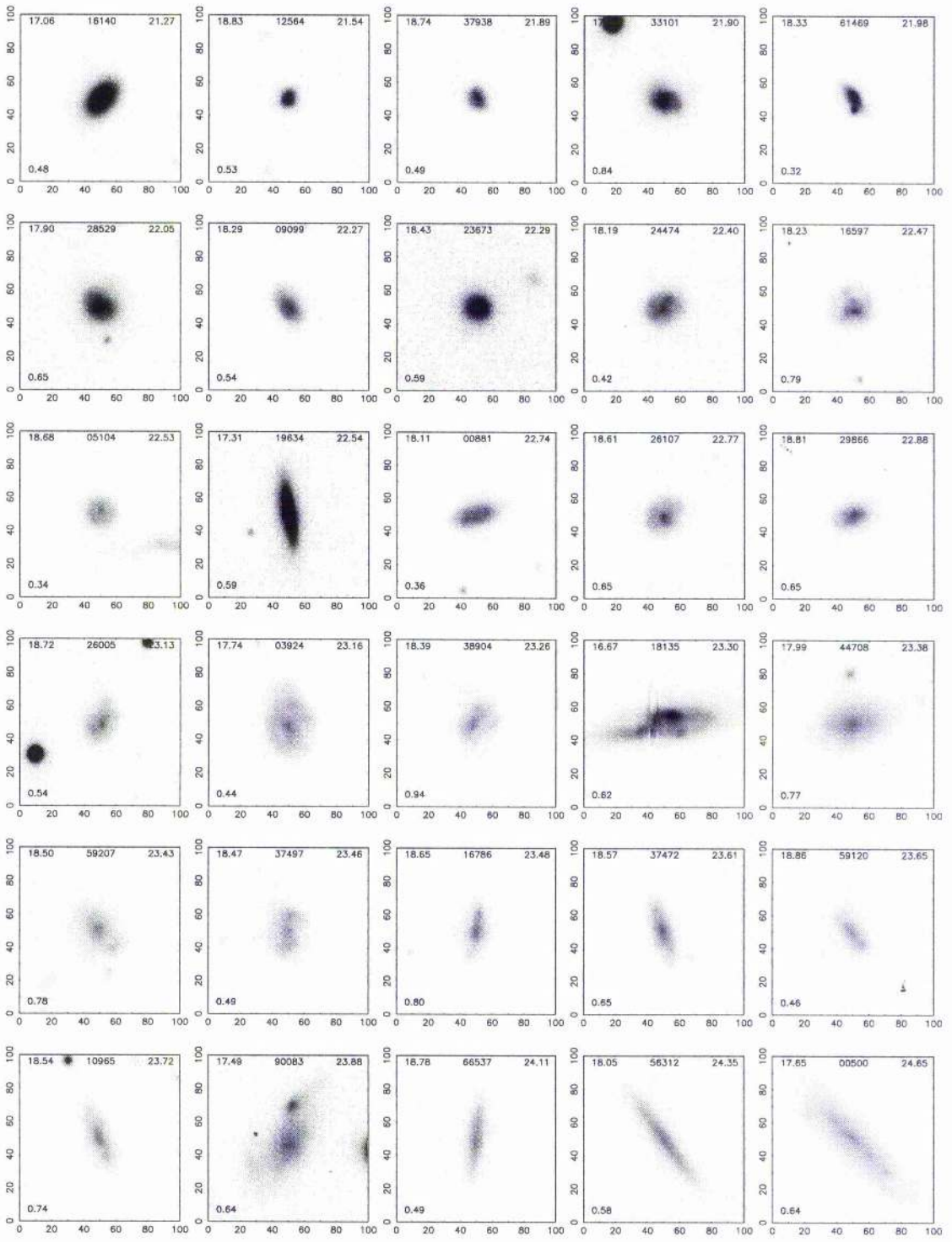

Figure 5.20: A random selection of FPA galaxies ordered in surface brightness. The numbers shown are magnitude (top-left), MGC-ID (top-center), surface brightness (top-right) and Sersic index (bottom-left).

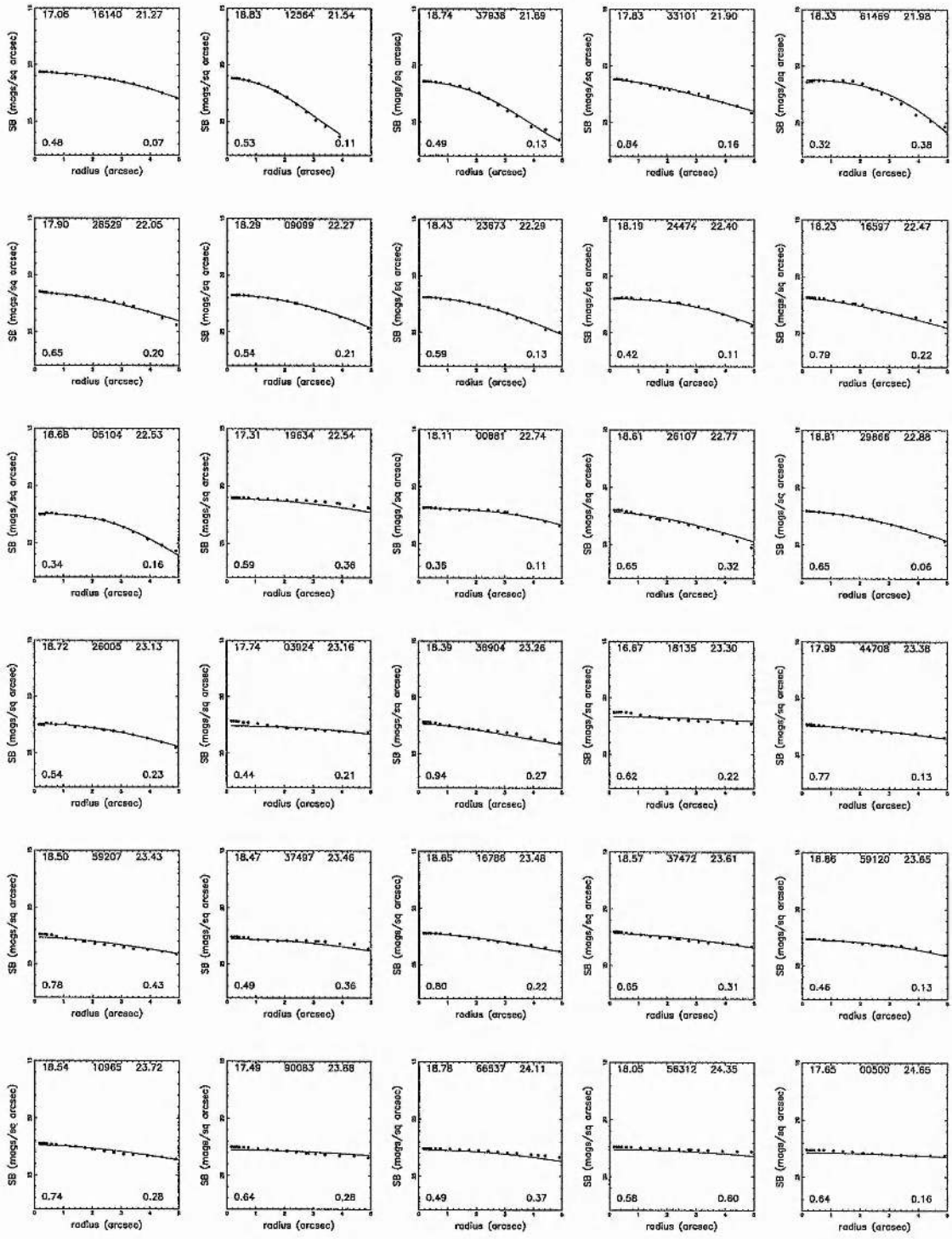

Figure 5.21: The measured profile and GIM2D pure Sersic model profiles of the FPA galaxies shown in Fig. 5.20. The numbers shown are magnitude (top-left), MGC-ID (top-center), surface brightness (top-right), Sersic index (bottom-left) and the rms goodness-of-fit statistic (bottom-right).

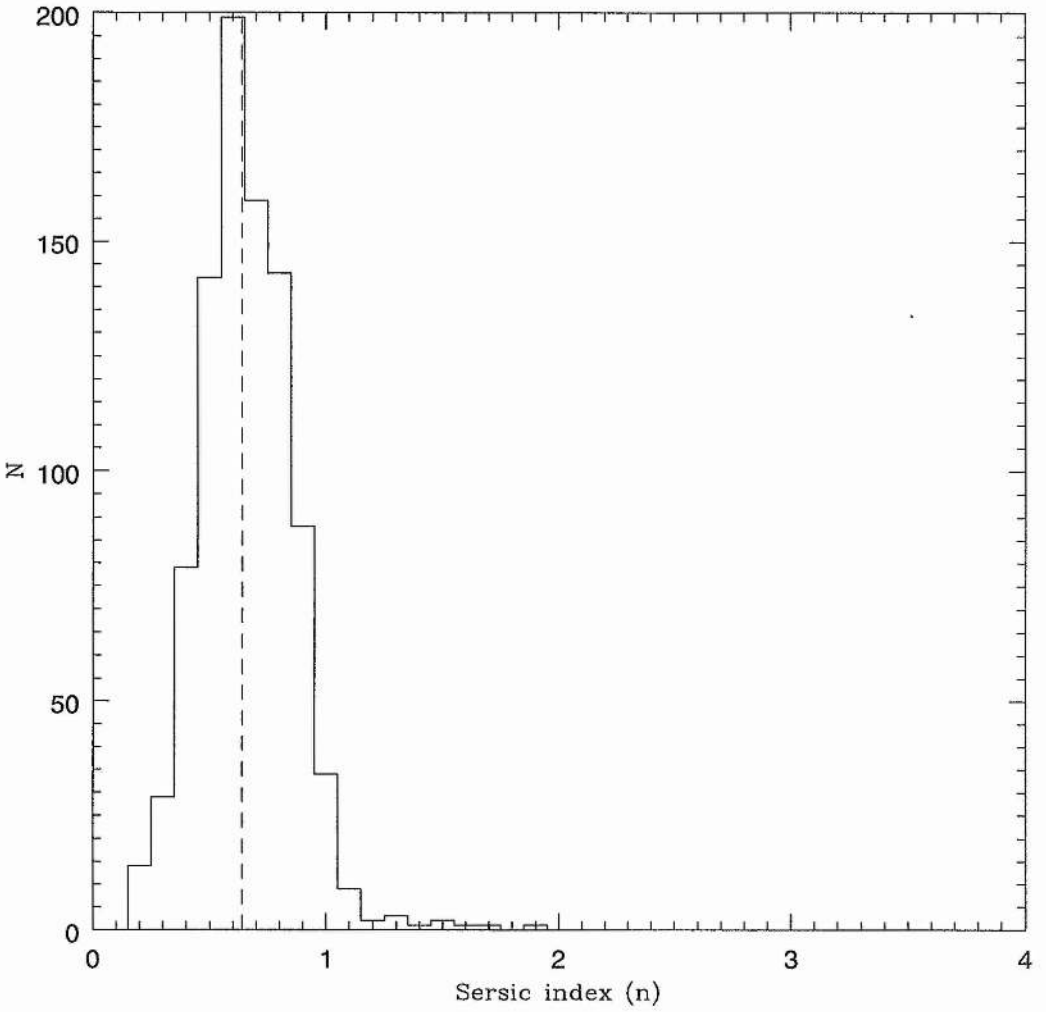

Figure 5.22: The distribution of the Sersic power index (n). The median Sersic power index is $\overline{n}$=0.64 (the dashed line) with a spread of $\pm 1\sigma$=0.2.

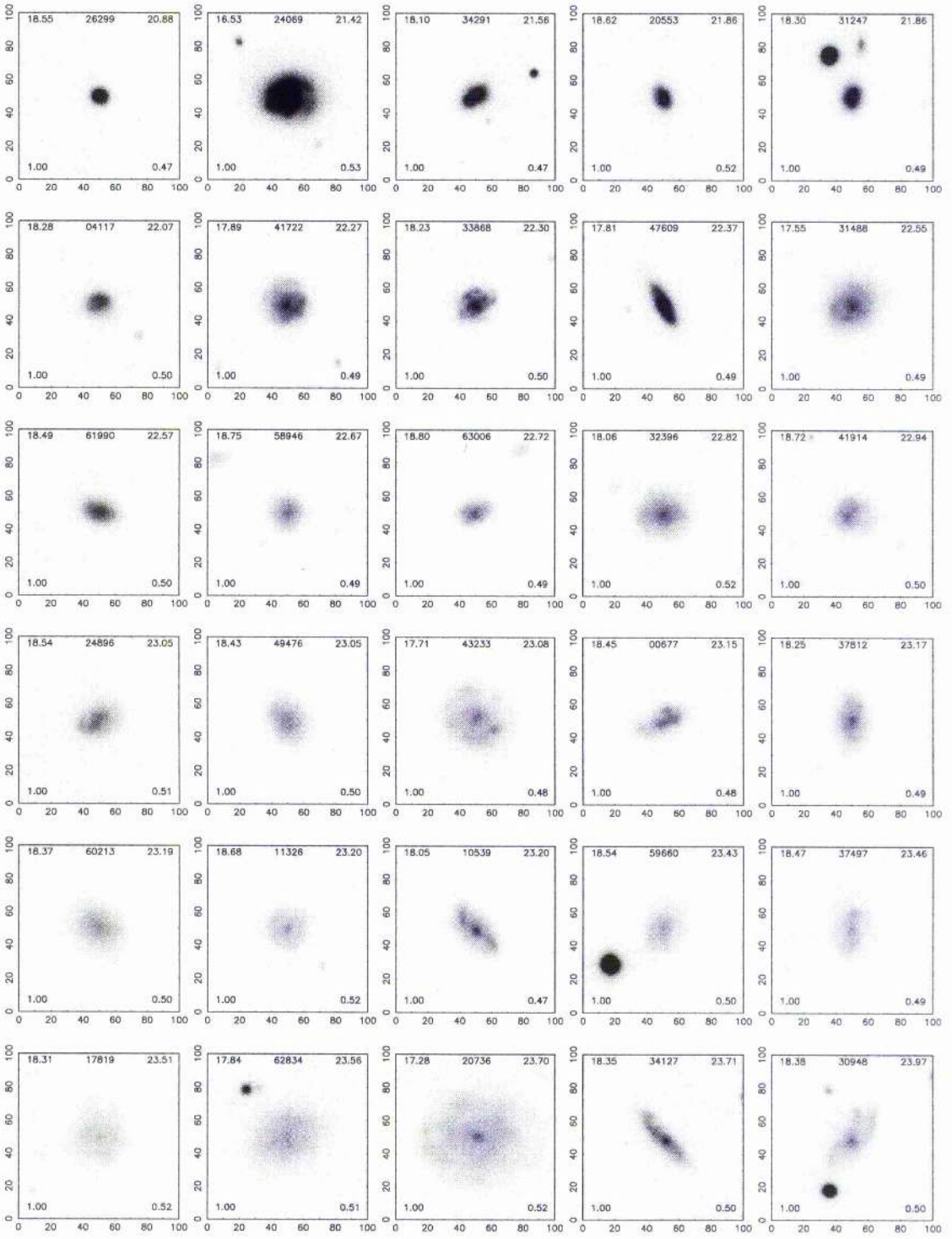

Figure 5.23: A random selection of FPA galaxies with Sersic index n=0.5.

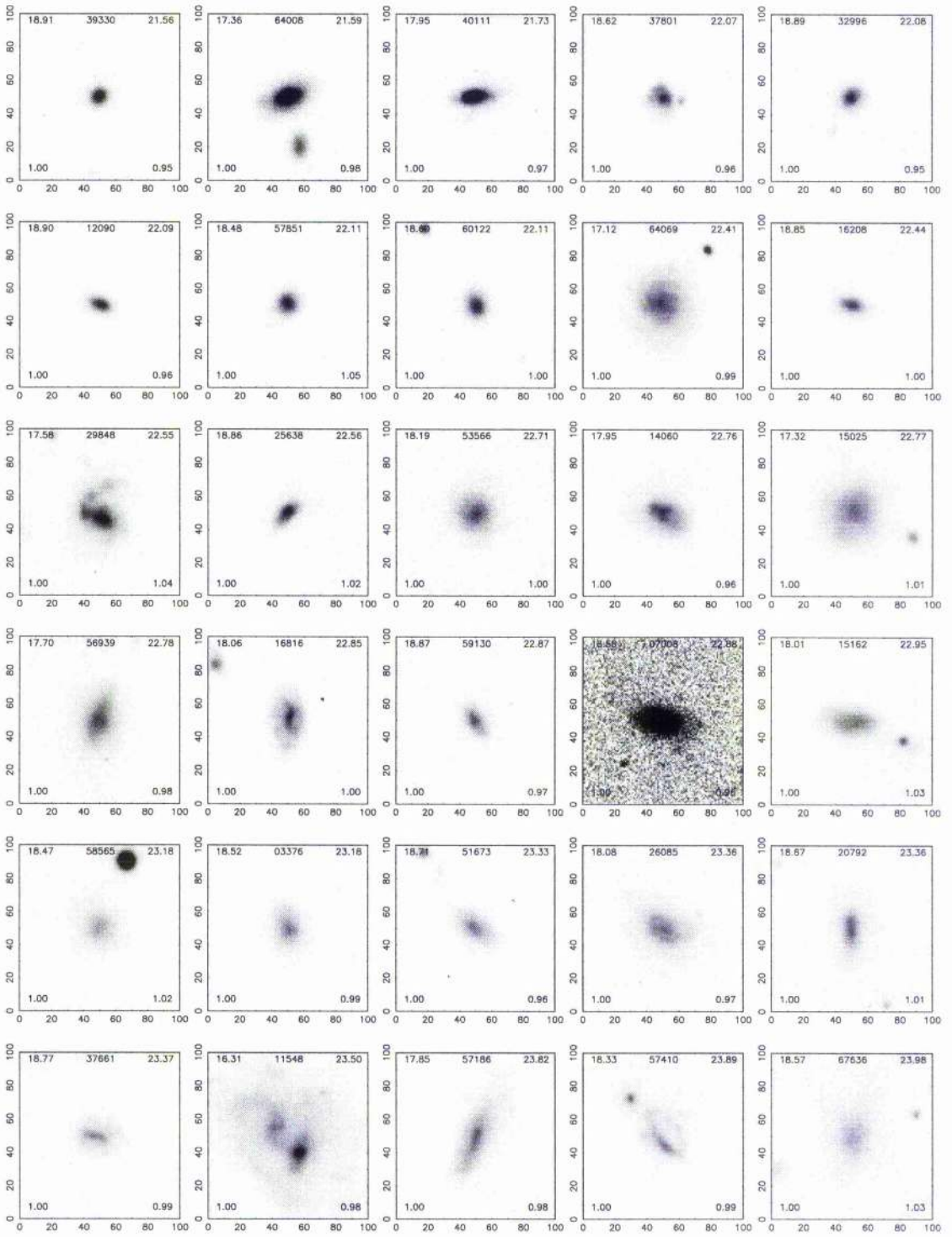

Figure 5.24: A random selection of FPA galaxies with Sersic index n=1.0.

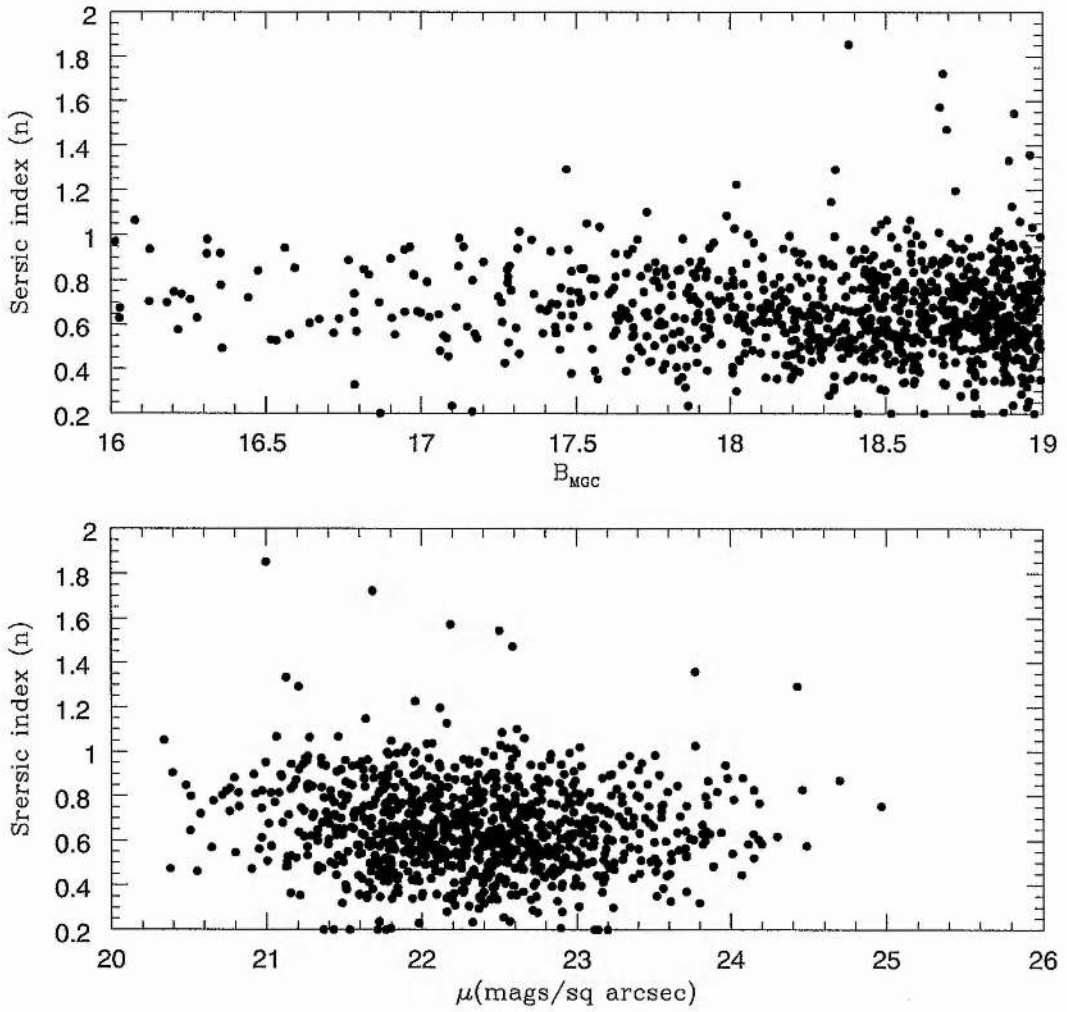

Figure 5.25: The distribution of the Sersic power index (n) with magnitude, B_{MGC}, and apparent surface brightness, μ.

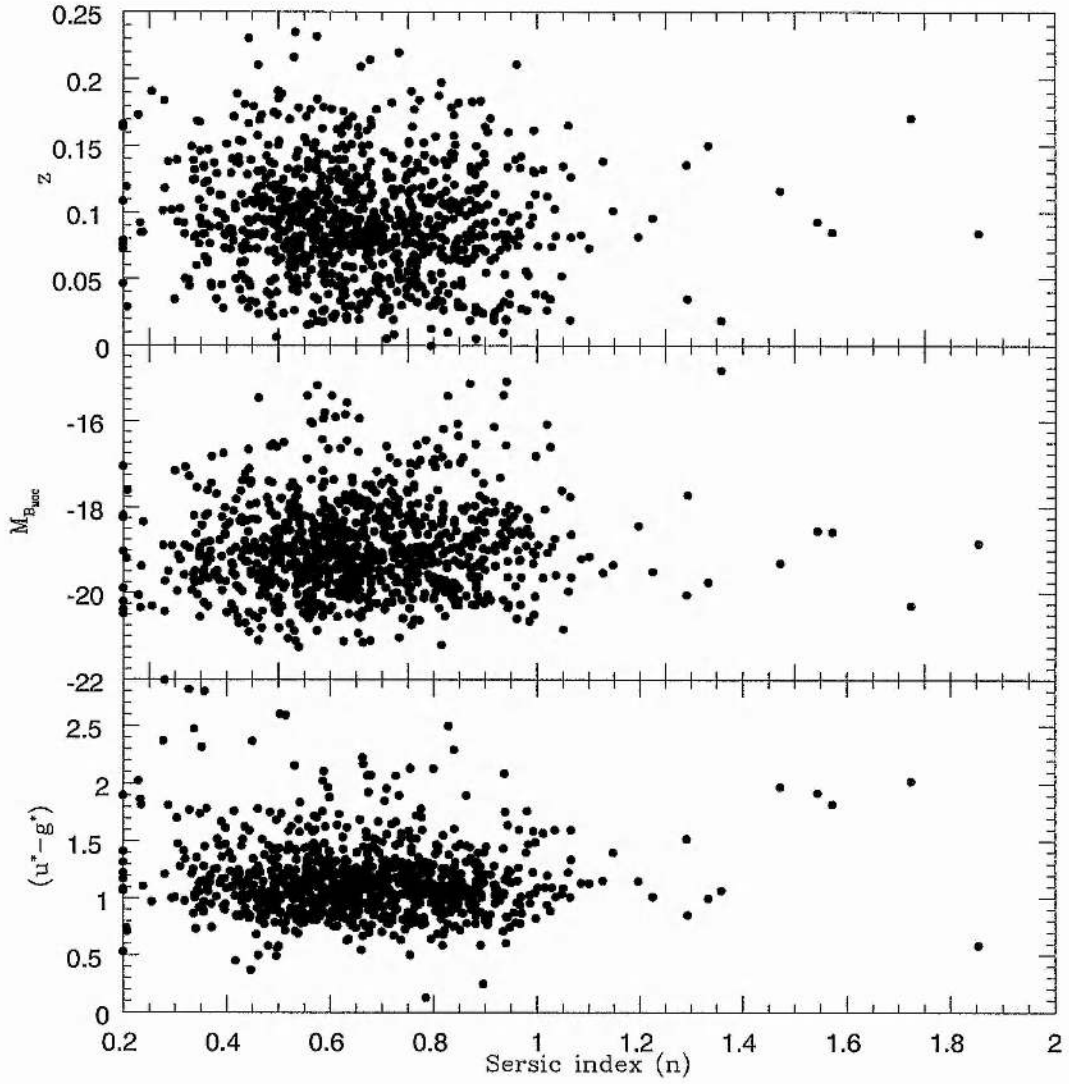

Figure 5.26: The distribution of the Sersic power index (n) with redshift (top), absolute magnitude (middle) and colour (bottom).

(Fig. 5.17 and 5.18). Fig. 5.13 and Appendix C.2 also suggest that neither magnitude or surface brightness can be used as a discriminator. We believe we have tried using cuts in every available MGC-BRIGHT-GIM2D parameter and parameter combination to accurately divide the FPA population into Sabc and Sd/Irr subsets. None have worked to our satisfaction.

Whilst we have not been able to separate out the general Spiral and Irregular galaxies, we can isolate the special case edge-on Spirals. We are able to use an, MGC measured, ellipticity cut of $e_{\rm MGC}$ >0.6 to isolate the FPA edge-on Spiral galaxies, see Fig. 5.27. Doing this we find that there are 121 FPA edge-on Spirals, reducing our FPA sample to 904 "normal" Spiral and Irregular galaxies at $B_{\rm MGC}$ <19. However, further investigation reveals that whilst this provides a clean edge-on Spiral sample it is not a complete sample. A substantial portion of thick-edge-on or very near edge-on galaxies are not isolated by this cut and to reduce the ellipticity limit would risk contamination. Henceforth, we decided to visually inspect and assign Hubble types to all the FPA galaxies, see Table. 5.3 and Fig. 5.28. We find that, as previously suspected, the FPA galaxies are dominated by Sabc and Sd/Irr galaxies. However, it should be noted that it was found that one could not, with any real confidence, assign Hubble types to galaxies at $B_{\rm MGC} \geq$18 mags. And so the numbers shown in Table. 5.3 are by no-means wholly reliable.

5.7 Morphological number counts

We now use our (B/T) and visual classifications to examine the relative numbers of each of the galaxy populations, see Table 5.2. Fig. 5.29 shows how the population fractions vary with magnitude and surface brightness. From all the 3395 classified galaxies down to $B_{\rm MGC}$=19, we find that of the total galaxy population 28.10% are E/S0 galaxies, 39.64% are Sabc galaxies, 31.37% are Sd/Irr galaxies (or alternatively 24.25% E/S0, 33.12% Sabc, 12.13% Sd/Irr and 30.52% FPA). From Fig. 5.29 we find that the Sabc fractional population increases at bright magnitudes whilst the E/S0 and Sd/Irr both vary little with magnitude. The Sabc fractions show an increase with decreasing surface brightness, and the E/S0 population show the expected decline with lowering surface brightness. The Sd/Irr population fractions initially rise with decreasing surface brightness distribution but then flatten out at around μ=23.25 mags/sq arcsec.

The argument for enhanced star-formation in the FPA population is further supported by noting that the FPAs have a brighter mean surface brightness than either the Sabc or Sd/Irr populations.

Fig. 5.30 and Table 5.4 show the MGC-BRIGHT morphological galaxy number counts. We convert our counts to the b_j band using Eqn. 4.1 with a $(B-V)$=0.94 for the total counts. For the morphological counts we take the mean (u^*-g^*) colour and combine it with Eqn. 3.1 to get a type dependent $(B-V)$. We see that in all cases the MGC counts tag-on well to the much deeper counts of Cohen et al. (2002), with the Sabc galaxies dominating, albeit slightly, the MGC counts at all magnitudes. Importantly we note that we have not attempted to renormalise either the MGC or Cohen et al. (2002) galaxy counts.

5.8 Summary

In this Chapter we have provided a description of GIM2D and how it was used to measure galaxy parameters for all galaxies in MGC-BRIGHT at $B_{\rm MGC}$ >16 mag. As well as comparing the GIM2D derived to measured galaxy profiles we have examined the GIM2D calculated χ^2 distribution and compared it to our measured RMS for each profile. The differences between those MGC-BRIGHT parameters which are reproduced by GIM2D are also examined. We believe that GIM2D has been successful in being able to accurately

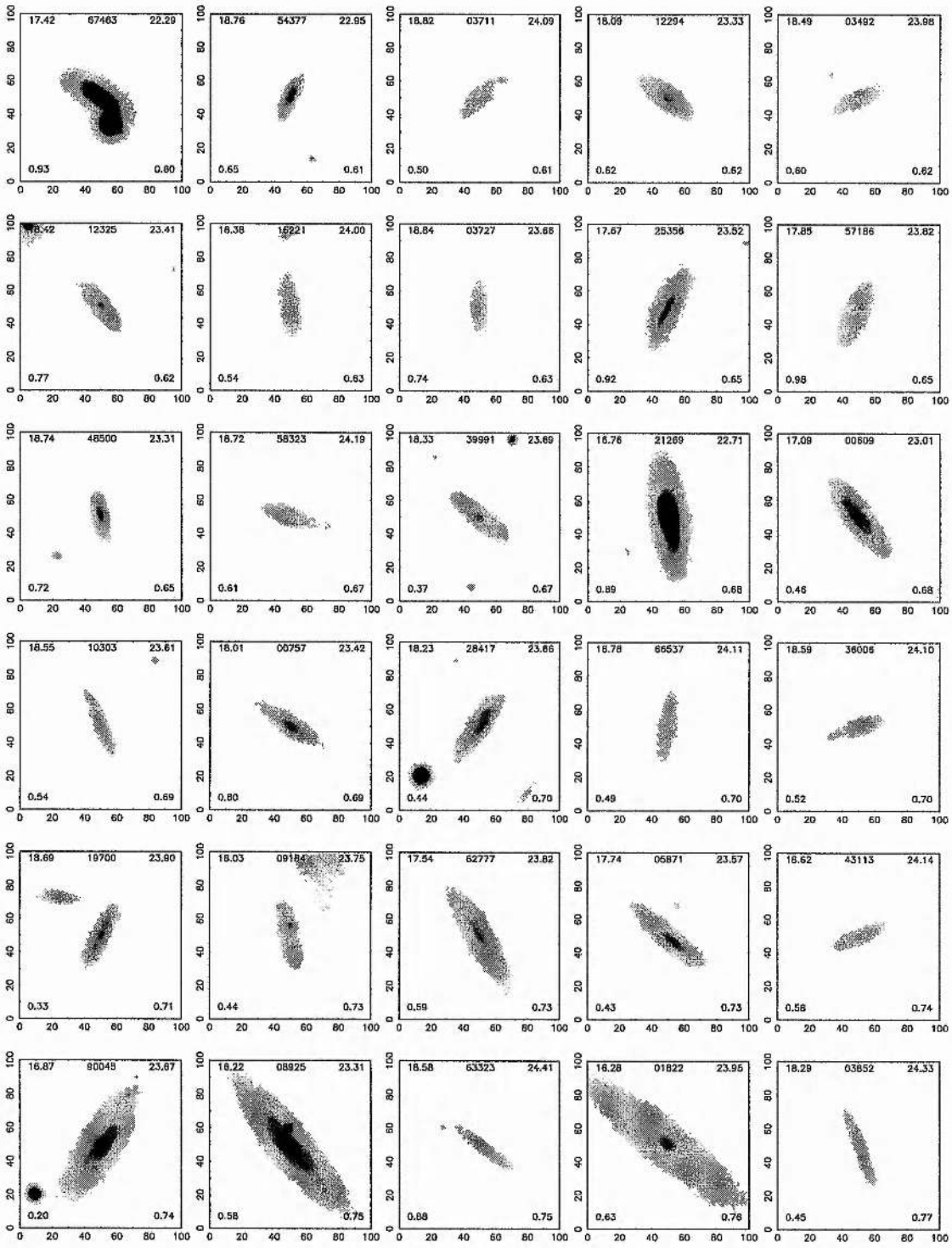

Figure 5.27: Edge-on FPA Spiral galaxies isolated using an ellipticity cut of $e_{\mathrm{MGC}} > 0.6$. The galaxies are ordered in decreasing surface brightness. The numbers shown are magnitude (top-left), MGC-ID (top-center), surface brightness (top-right), Sersic index (bottom-left) and ellipticity (bottom-right).

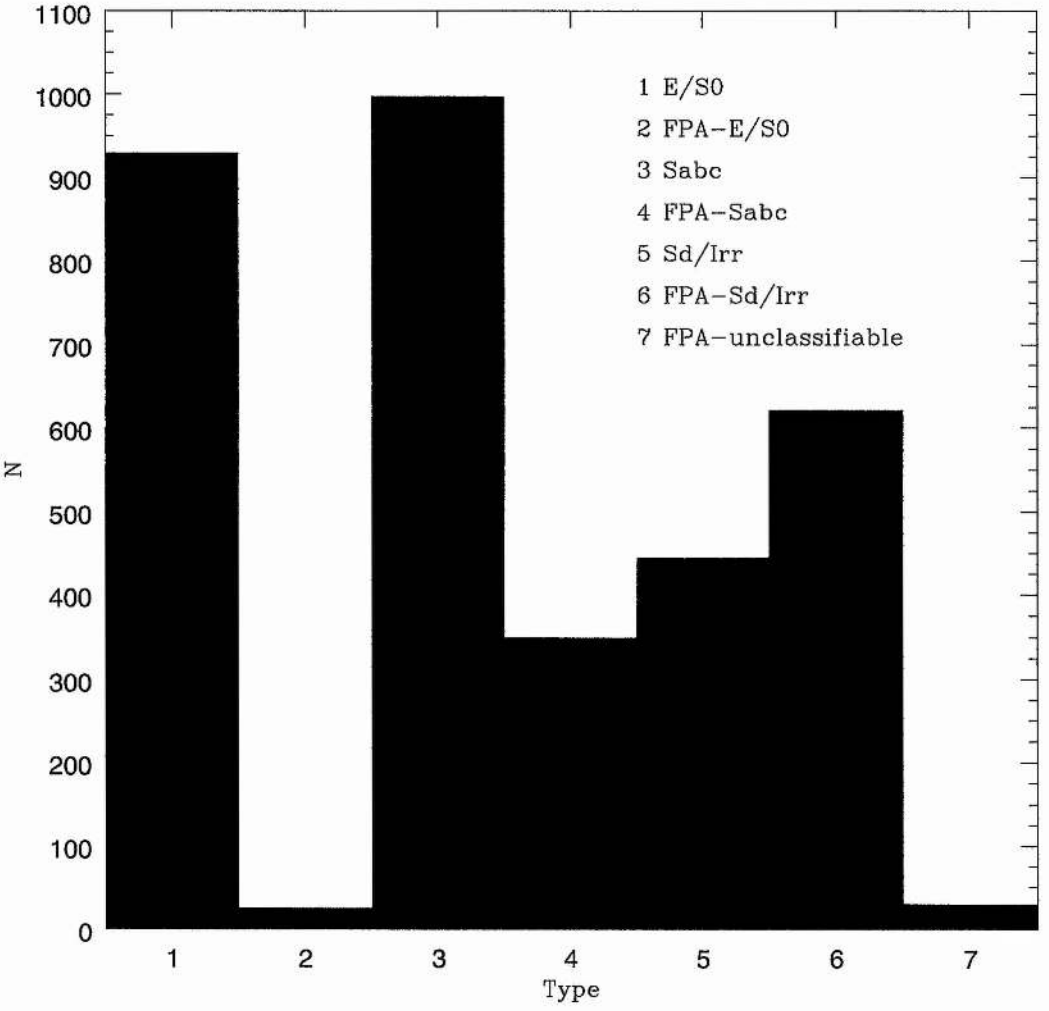

Figure 5.28: A histogram summary of the numbers of galaxies in each Hubble type.

Table 5.4: The MGC morphological galaxy counts per sq deg.

$B_{\rm MGC}$	$N_{E/S0}$	N_{Sabc}	$N_{Sd/Irr}$
16.25	0.50	0.97	0.61
16.75	1.25	1.66	0.99
17.25	2.10	2.91	2.48
17.75	4.36	6.21	4.69
18.25	7.25	11.71	9.02
18.75	12.56	18.25	15.30

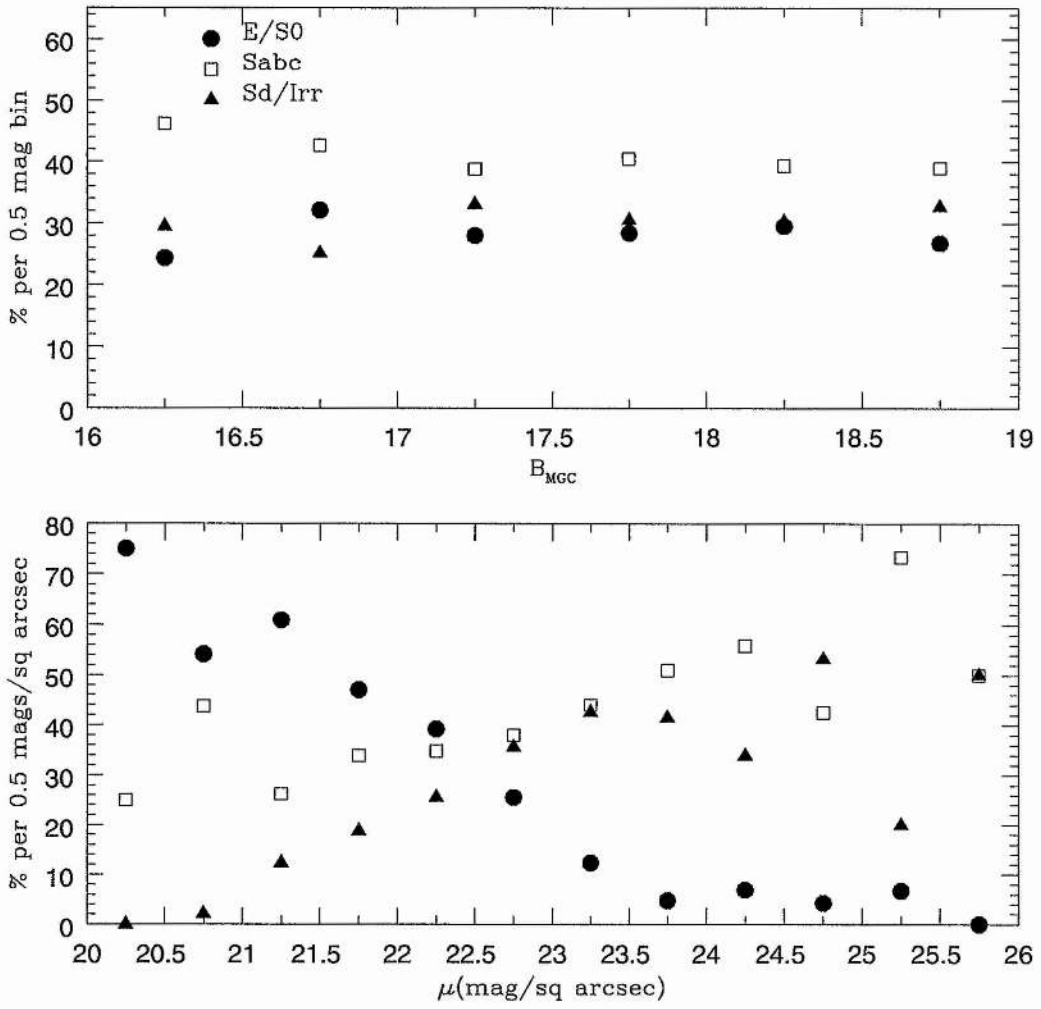

Figure 5.29: The fractions of the identified galaxy populations, after visulal classification, as a function of apparent magnitude ($B_{\rm MGC}$, top panel) and $B_{\rm MGC}$ -band surface brightness (μ, bottom pannel). The crosses indicate the FPA distributions before eyeball classificaion.

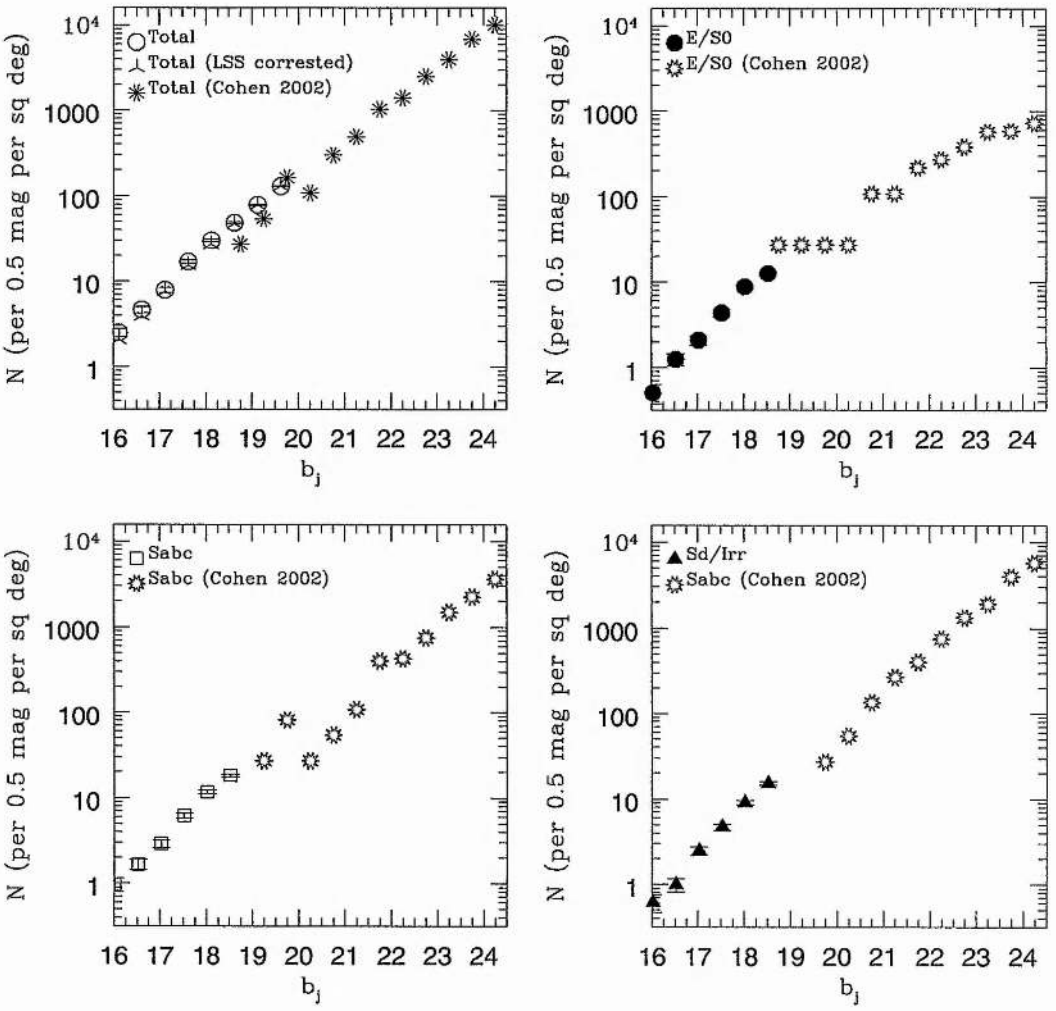

Figure 5.30: The MGC-BRIGHT morphological number counts. In all cases our counts tag on well with those of Cohen et al. (2002).

model galaxy profiles and reproduce known parameter distributions. We believe that GIM2D produces reliable model profiles down to the limits, $B_{\rm MGC}$=19.5 and μ_{app}=26 mags/sq arcsec.

We have used cuts in (B/T) to identify four distinct galaxy populations: E/S0 galaxies with (B/T)>0.5, Sabc galaxies with 0.1<(B/T)<0.5, Sd/Irr galaxies with 0<(B/T)<0.1 and a population of Flat Profile Anomalies (FPA) with (B/T)=0. We stress that, for the FPA sample, a (B/T)=0 does not indicate the absence of a bulge. Only that a burst of star-formation in the outer regions of the galaxy, triggered by a merger or some internal process, has caused a flattening of the light profile making it impossible for GIM2D to fit an $r^{\frac{1}{4}}$ bulge component.

From looking at how the galaxy parameters vary with colour and morphological type, we find that the spiral population is bi-modal in colour and that the FPA population forms a skewed distribution in (u^*-g^*). The FPA distribution is peaked at (u^*-g^*)=1.1 with an extended red tail. From looking at galaxies in the red tail and centered around the blue peak we find that the FPA sample can be broken down into two distinct groups: i) Red galaxies, (u^*-g^*)>1.5, which are a combination of edge-on spirals and low surface brightness galaxies and ii) normal blue galaxies, (u^*-g^*)<1.5. We return to the Spiral colour bi-modality in Chapter 6. The FPA galaxies appear to occupy the same parameter space as Irregulars but they contain, as well as Irregulars, blue, and therefore star-forming, Spiral galaxies.

The FPA galaxy population can only be identified from the local galaxy sample as having a (B/T) of exactly 0. We are able to extract a clean but incomplete sample of edge-on sprials from the FPA population by taking a cut in MGC measured ellipticity, e_{MGC} ($e_{\rm MGC}$ >0.6 for edge-on spiral galaxies). We have attempted to visually classify all FPA galaxies at $B_{\rm MGC}$ <19 mags but found that these classifications to be unreliable at $B_{\rm MGC}$ <18.

We have looked at the relative numbers of the different populations and produced morphological galaxy number counts. We find the E/S0, Sabc and Sd/Irr galaxies make up 28.10%, 39.64% and 31.37% of the total galaxy population. We find that whilst the fractions of E/S0 and Sd/Irr galaxies remain constant with magnitude the Sabc fractions show a slight decrease but remain the dominant population. In terms of surface brightness the E/S0 and Sabc behave as one might expect, decreasing and increasing respectively with lowering surface brightness. The Sd/Irr, however, show a peak at around 23.25 mags/sq arcsec which we suggest may be caused by otherwise faint, but now star forming (FPA) galaxies.

We have compared our total and morphological count to those of the much deeper counts provided in Cohen et al. (2002). We find that, for the total and morphological counts, there is no need to re-normalise the counts.

The apparent properties of the local galaxy population can be best understood in terms of colour, effective surface brightness and (B/T). In the next chapter we use the available redshift data to try to understand the galaxy population in terms of their redshifts and physical parameters.

CHAPTER 6

The Physical Properties of Galaxies

We now combine our GIM2D profiles with redshift and colour information gained from the two Degree Field Galaxy Redshift Survey (2dFGRS, Colless et al. 2001) and the Sloan Digital Sky Survey Early Data Release (SDSS-EDR, Stoughton et al. 2002). The 2dFGRS is a b_J-band spectroscopic survey based on an extended and revised version of the APM catalogue (Maddox et al. 1990 and Cross et al. 2003). The 2dF contains ~250,000 galaxies down to b_J=19.45 mag with a median redshift of $\overline{z}$=0.11. The survey covers two continuous strips in the North (NGP, $09^h50^m < \alpha_{1950} < 14^h50^m$ and $-7.5^o < \delta_{1950} < +2.5^o$) and South (SGP, $21^h40^m < \alpha_{1950} < 3^h40^m$ and $-37.5^o < \delta_{1950} < -22.5^o$) Galactic poles. It is the NGP strip that overlaps with the MGC (see Fig. 6.1).

The SDSS is a spectroscopic *and* imaging survey conducted in 5 photometric bands (u, g, r, i and z). The SDSS-EDR contains ~14 million objects down to g^*=22 mag, 54,008 of which have spectra. The SDSS-EDR covers a total area of 462 sq deg which is comprised of data taken in 3 regions of the sky, the celestial equator, the NGP and the SGP. The SDSS-EDR data that coincides with the MGC is contained in SDSS run 756, strip 10. Fig. 6.1 shows how the MGC 2dFGRS-NGP and SDSS-EDR overlap.

In this chapter we use the redshift information to look at the **physical** properties of galaxies and then derive morphological luminosity functions. We assume an Einstein-de Sitter cosmology with H_o=100 Km/s/Mpc.

6.1 Redshifts and Completeness

As previously noted the MGC survey region overlaps the SDSS-EDR, § 5.3, as well as the 2dFGRS-NGP, § 4.2. From matching the MGC to the 2dFGRS and SDSS-EDR surveys (see Cross et al. 2003 for matching details) and removing all low signal-to-noise objects ($B_{\rm MGC}$>19), as well as all galaxies with z <0.003 we reduce our sample to 3113 galaxies. This low-z cut was chosen because it marks the limits of the stellar distribution, see Fig 6.2, and at z=0.003, cz=900 km/s which is greater than the Galactic escape velocity (~600 km/s, Keith Horne priv. comm). The MGC-BRIGHT redshifts were taken from an MGC run on the 2dF instrument and direct MGC matching with the 2dFGRS and SDSS-EDR, and the NED database (NASA Extra-galactic Data base, http://nedwww.ipac.caltec.edu/). Table 6.1 shows how many redshifts from each source are used in the MGC-BRIGHT-GIM2D-z sub-sample.

Of these 3113 galaxies 3078 have colours gained from the MGC matching with the SDSS-EDR. All this means that, of all the GIM2D'd galaxies in the magnitude range 16< $B_{\rm MGC}$ <19, 90.7% have redshifts and SDSS-EDR colours. Table 6.2 summarises all this. Fig. 6.3 shows the completeness as a function of apparent magnitude (top), surface brightness (middle) and colour (bottom). We find that where there are sufficient galaxies (≥50) the completeness is constant with magnitude and colour, but begins to decrease

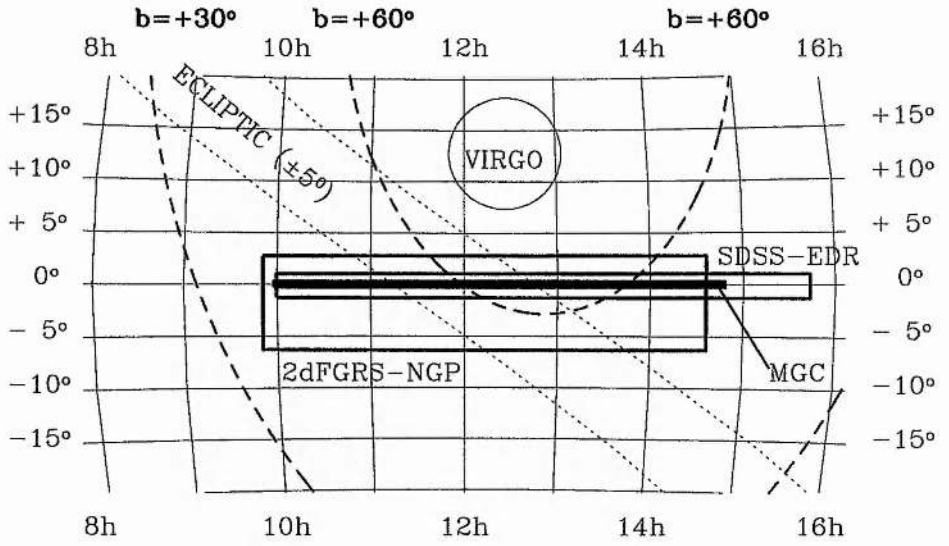

Figure 6.1: The area covered by the overlapping MGC, 2dFGRS-NGP and SDSS-EDR regions. This figure is reproduced with permission from Cross et al. (2003).

Table 6.1: The number of redshifts in MGC-GIM2D-z from each redshift source.

z source	N_{gal}
2dFGRS	2766
SDSS-EDR	270
MGC	48
NED	29
Total	3113

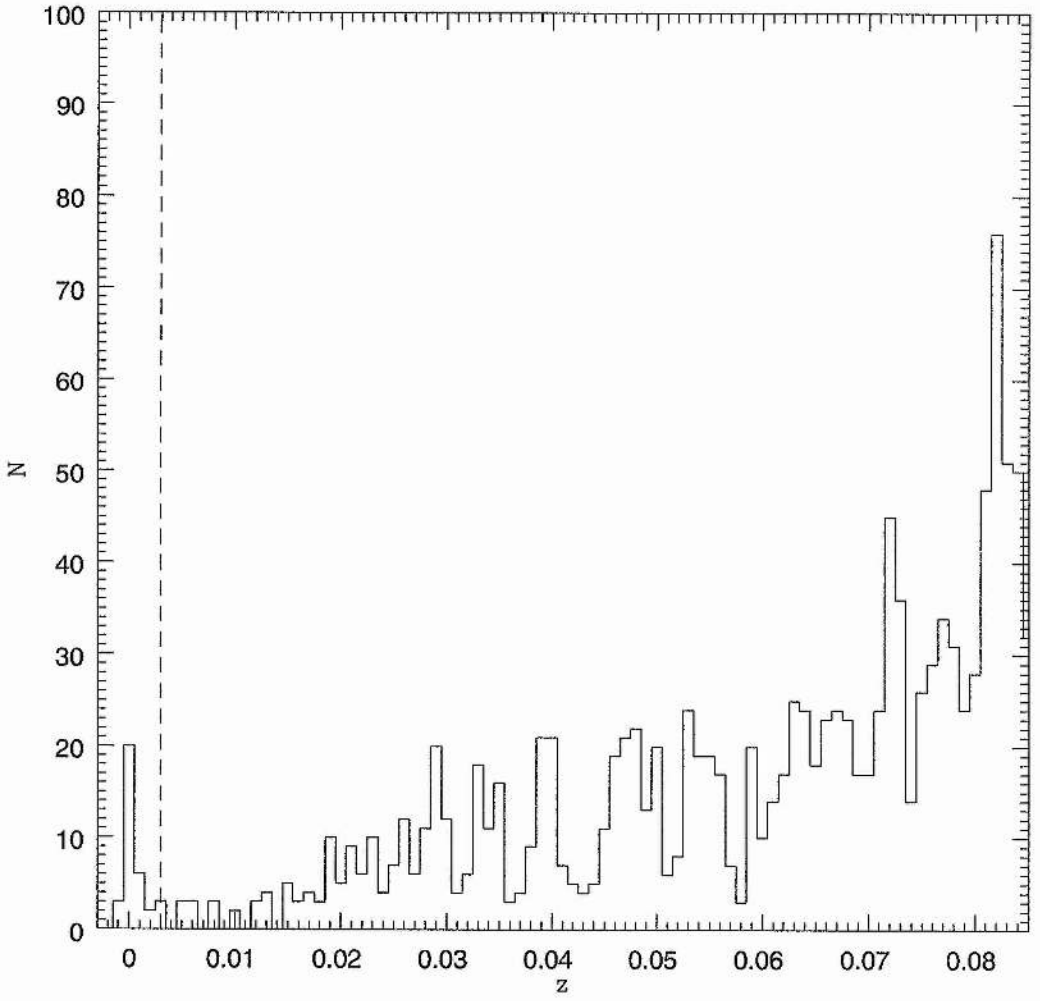

Figure 6.2: A close up of the low-z histogram. The dashed line indicates the z=0.003 redshift cut.

Table 6.2: The numbers of galaxies in each MGC-GIM2d sub-sample.

Sample	N_{gal}
16< $B_{\rm MGC}$ <19 (MGC-GIM2D)	3395
16< $B_{\rm MGC}$ <19 with z>0.003 (MGC-GIM2D-z)	3113
16< $B_{\rm MGC}$ <19 with z>0.003 and colours (MGC-GIM2D-z-COL)	3078

for dim galaxies (μ_{eff} >24.2 mags/sq arcsec). The drop in completeness cannot simply be put down to low numbers as the magnitude and colour completenesses are constant regardless of the numbers of galaxies in the bin. We suggest that the drop in completeness at high and low surface brightness is a result of a surface brightness selection effect within the 2dFGRS and SDSS-EDR catalogues shown in Cross (2002).

At the time of writing the MGC-z survey is incomplete. To make up for this we have combined redshifts from 4 different redshift surveys (see Table. 6.1) each with there own selection biases. The combination of all the different selection effects makes it impossible to do a full and proper analysis, such as that by Cross 2002, until the MGC-z survey is complete. We must therefore confine our study to the range μ_{eff} =20.2 to 24.2 mags/sq arcsec (similar to the overall 2dFGRS limits, e.g. Cross et al. 2003).

6.2 Physical Galaxy parameters

In order to get the physical parameters of each galaxy we require the proper distance, d_p (i.e., the actual physical separation today). The proper distance is derived in Appendix B.4. As the universe expands it affects the distribution of light as it moves through space. This has two effects, firstly to diminish the incident flux, and secondly, to stretch apart parallel light rays. To accommodate this we must define two more distances: the angular diameter distance, d_a, used to calculate the physical size of galaxies and the luminosity distance, d_l, used to calculate the galaxies absolute magnitude. d_a and d_l are related to the proper distance by Eqn. 6.1 and Eqn. 6.2 respectively.

$$d_a = \frac{\mathrm{d_p}}{(1+z)} \tag{6.1}$$

$$d_l = \mathrm{d_p}(1+z) \tag{6.2}$$

Eqn. 6.3 is used to convert the (small) angular measurements of Re_θ into the physical units of kiloparsecs, Kpc:

$$\tan(Re_\theta) \approx \frac{Re}{d_a} \tag{6.3}$$

and similarly for Rd_θ and HLR_θ. Here Re_θ, Rd_θ and HLR_θ are the apparent angular measurements of Re, Rd and the half-light radii. To get the absolute magnitude, M, we

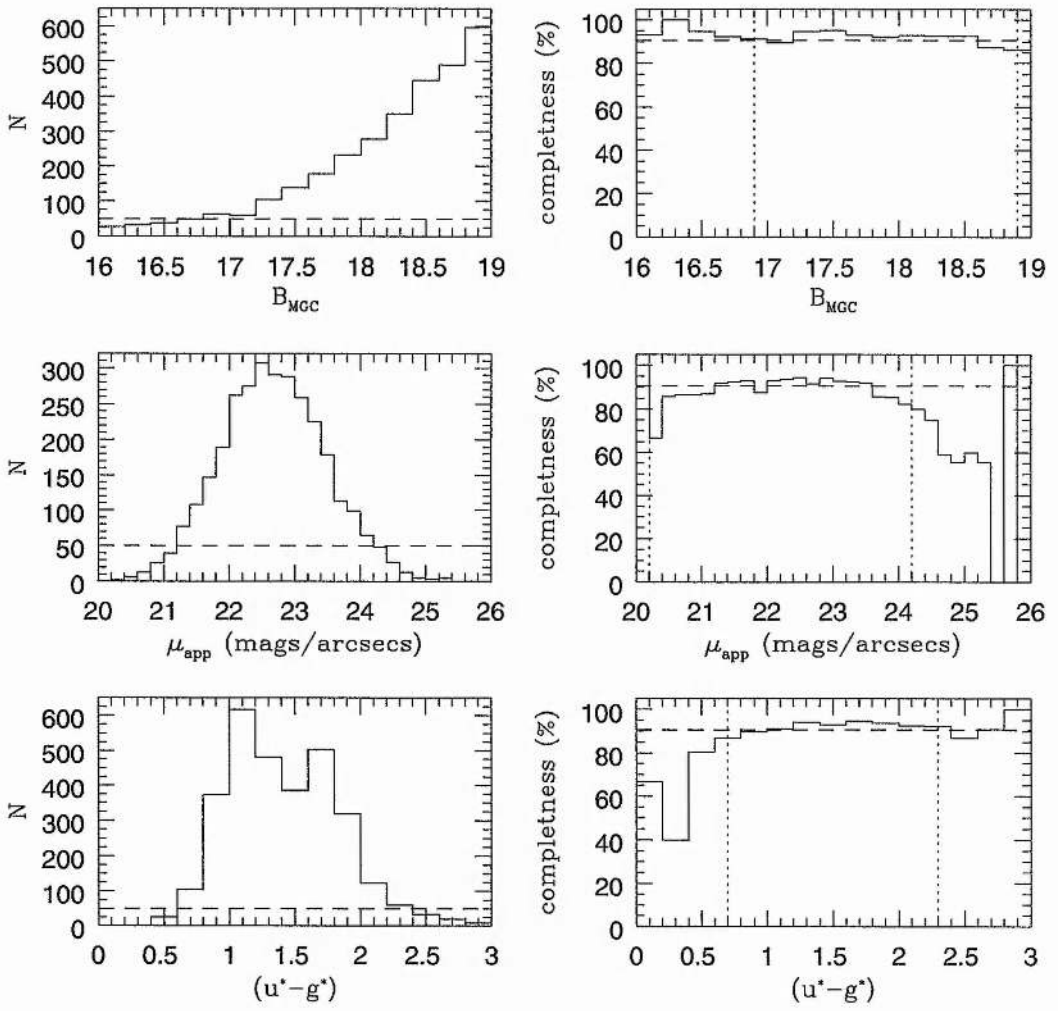

Figure 6.3: The numbers (left) and completeness (right) of the MGC-GIM2D-z-COLOUR sample as a function of $B_{\rm MGC}$ (top), μ_{app} (middle) and $(u^* - g^*)$. The dashed line in the left panels indicates the 50 galaxy limit. On the right the bins outside the dotted lines contain less than 50 galaxies and dashed line indicates the overall completeness (90.7%).

use d_l and the standard distance modulus equation as given in Eqn. 4.4 and derived in Appendix B.2, with a $k+e$ correction of:

$$k + e = 2.5z + 2.5\log((1+z)^{-0.75}) \tag{6.4}$$

6.3 Galaxy redshift distribution

Figs. 6.4 and 6.5 show this reduced sample in absolute magnitude-z and RA-z space respectively. In both Figs. galaxy clusters in the MGC strip can be seen as concentrations in z. The redshift distributions are most spikey (clustered) in the redshift range $z \sim 0.08$ to 0.11. This is most noticeable in the E/S0 distribution, indicating that as expected Elliptical galaxies are found predominantly in denser environments and therefore more clustered (i.e, the well known morphology-density relation Dressler 1980; Dressler et al. 1997).

We have seen in Chapter 5 that there appear to exist two different types of Spiral galaxies that are separated in colour only. Fig. 6.6 shows the redshift distributions of the total Spiral (top), red Spiral (middle) and blue Spiral (bottom) galaxy populations as well as their N(z) histograms. Although somewhat less apparent than in Fig. 6.5 in the total and red spiral distributions we can still identify the galaxy clusters. This weakening of the cluster signal is expected as the fragile spiral disk is easily destroyed in a cluster environment. However, the galaxy clusters all but disappear (fade into the background Spiral signal) when only blue Spirals are shown. This is in line with the findings of Lewis et al. (2002) and Balogh et al. (2002) who report a suppression in the star-formation of disk systems during cluster infall based on $H-\alpha$ equivalent widths.

Fig. 6.7 shows that the population naturally falls into two sub-groups of bulge ($(B/T) > 0.4$) and disk ($(B/T) < 0.4$) systems. We therefore elect to determine whether there is any correlation between (B/T) and magnitude/surface brightness for each sub-group. We find that there is no correlation of (B/T) with absolute magnitude below (B/T)=0.4 and only a slight one above (B/T)=0.4. We also see that, as expected, the highest surface brightness galaxies are bulge dominated with only a slight trend at $(B/T) < 0.4$. The derived scaling laws in Fig. 6.7 are, obviously, heavily biased by the FPA galaxies. It is clear, however, that there are two populations, bulges (high (B/T)) and disks (low (B/T)) and that the bulges occupy a small region extending no further than $M_{\rm MGC} \leq -17$. From the bottom panel of Fig. 6.7 we note that there is a distinct lack of bulge dominated low surface brightness galaxies. This indicates that, in the field at least, low surface brightness galaxies are intrinsically faint ($M_{\rm MGC} > -18$), and devoid of bulges.

In Fig. 6.8 we look at how the population fractions vary with absolute magnitude as well as cosmological dimming and k-corrected surface brightness (see § 6.3.2). We find that whilst there is an essentially even mix of intrinsically bright galaxies, it is the Spiral fraction that dominates, at the expense of the E/S0 galaxies, in the faint end whilst the Irregulars remain constant at all magnitudes. In terms of surface brightness we see that the trends for each galaxy population fraction remain relatively unchanged from Fig. 5.29. From Fig. 5.29 it is clear the bulge-dominated systems, i.e. Ellipticals only occur at high luminosities. They most likely occur through the process of galaxy mergers. The reason for the absence of low luminosity Ellipticals (recall Dwarf Ellipticals have exponential not de Vaucouleur profiles) is unclear. In a pure hierarchical merging scenario one might expect bulges to result from non-aligned mergers (i.e., differing angular momenta planes) however this should produce low as well as high luminosity bulges/Ellipticals. One radical possibility is that while bulges may well be formed from mergers of massive disks the disks themselves are constructed via a different process (e.g. initial collapse). One further possibility is that Dwarf Ellipticals do represent this extension and the Sersic parameter evolves from n=4 to n=1 with luminosity.

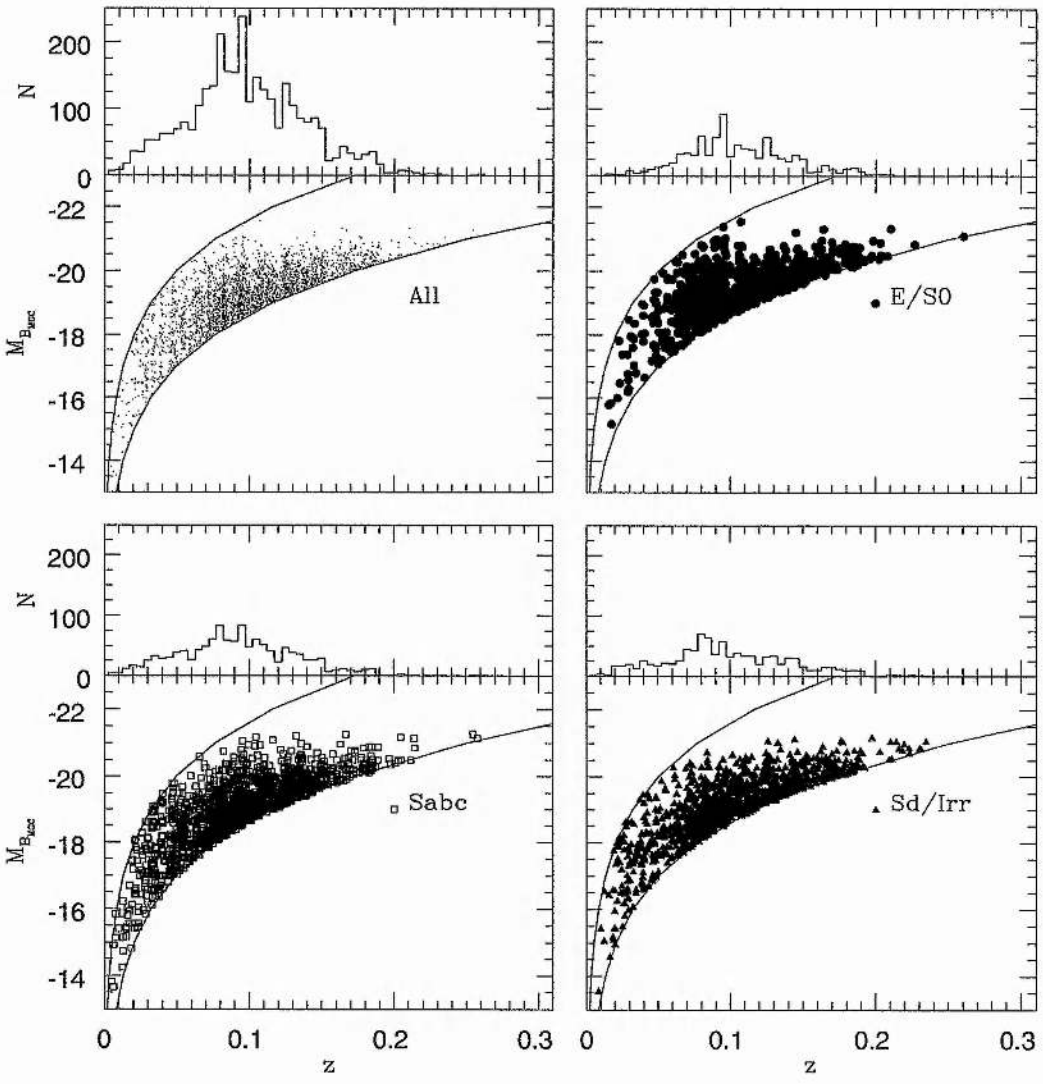

Figure 6.4: The reduced sample in $M_{B_{\mathrm{MGC}}}$-z space. The upper and lower solid lines indicate the upper (16) and lower (19) magnitude limits of the sample.

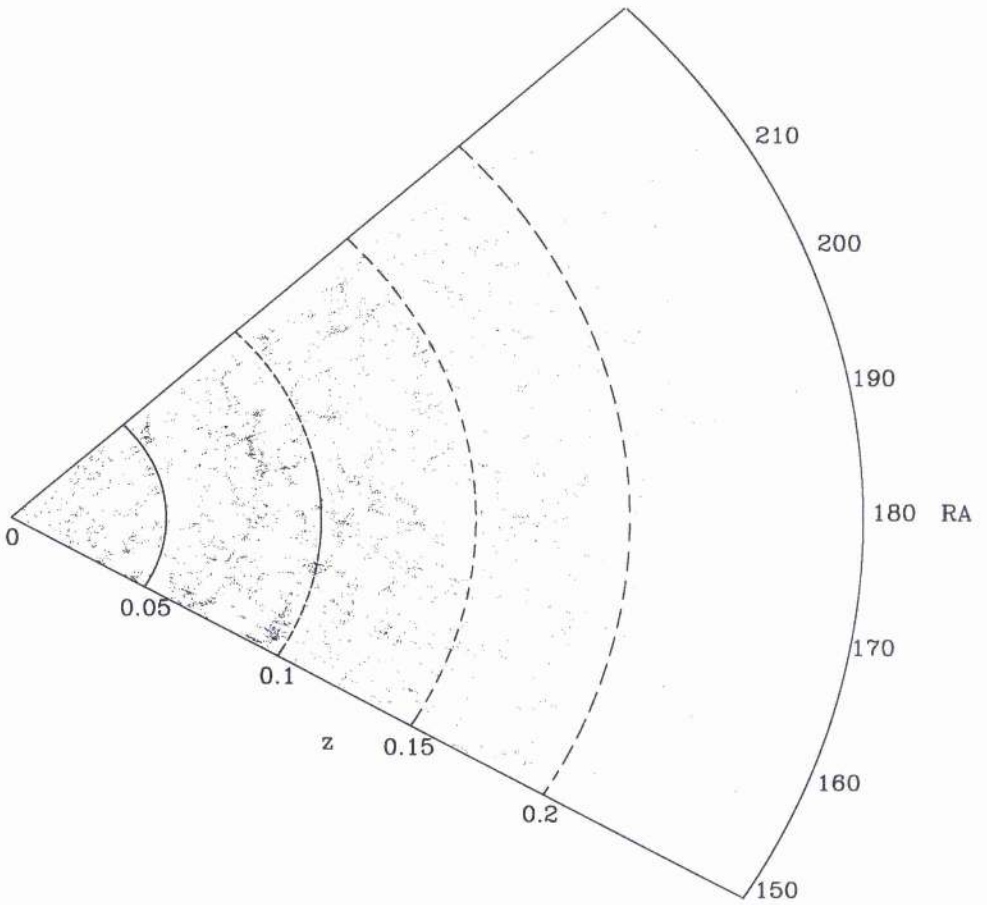

Figure 6.5: The reduced sample in RA-z space

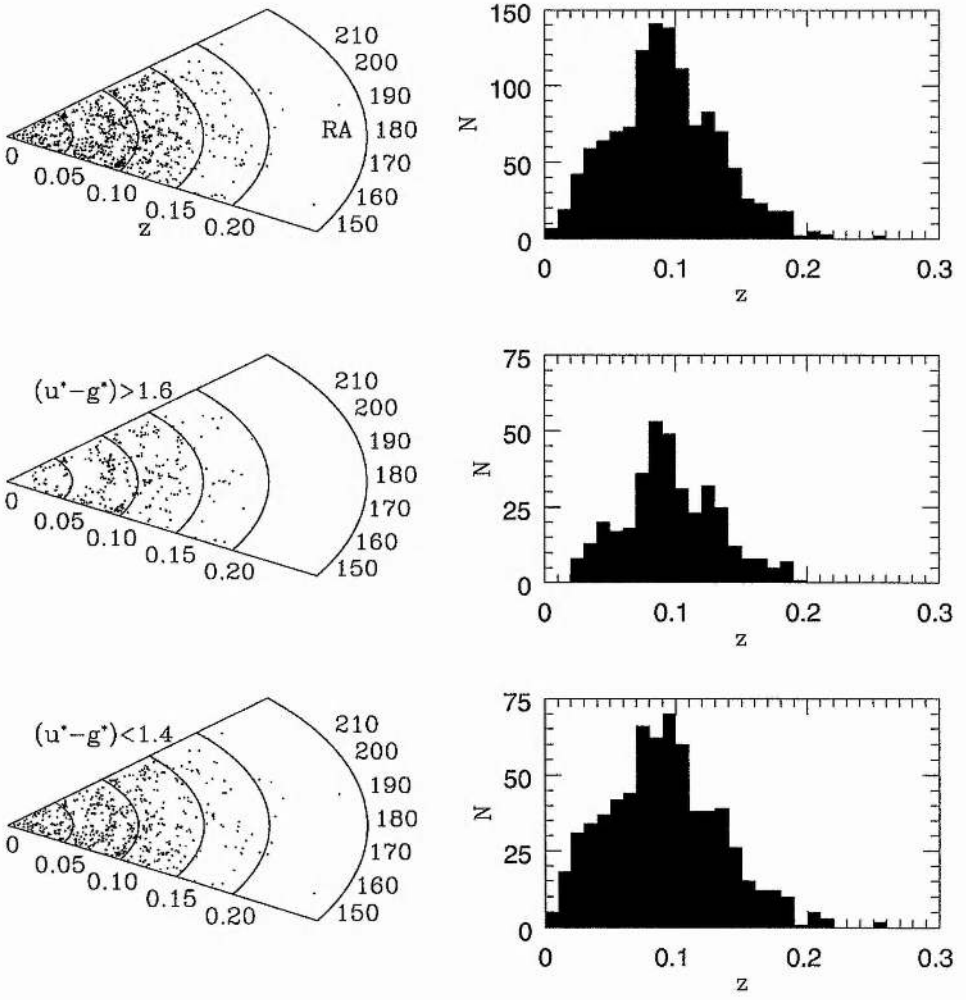

Figure 6.6: The distribution in RA-z space (left) and N(z) histograms (right) of *all* spiral galaxies (top), red spiral galaxies (middle) and blue spiral galaxies (bottom).

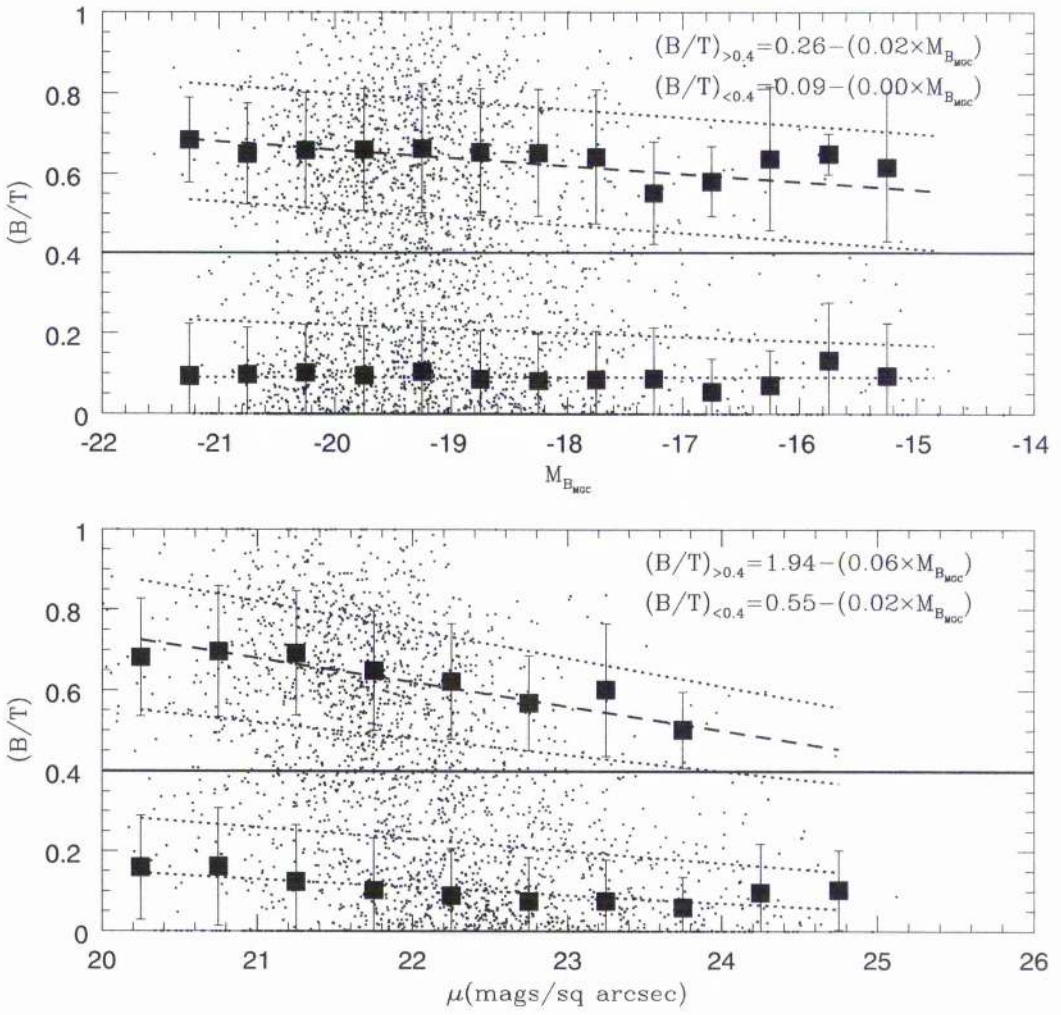

Figure 6.7: The GIM2D (B/T) parameter distributed in absolute magnitude (top) and cosmological dimming and k-corrected surface brightness (bottom). The dashed and dotted lines represent the best linear fit to the mean (B/T) per 0.5 mag/surface brightness (solid squares) and 3-σ clipped errors respectively, both above and below the dividing line at (B/T)=0.4. In each case the equation representing the best fit to the mean (B/T) is given in the panel.

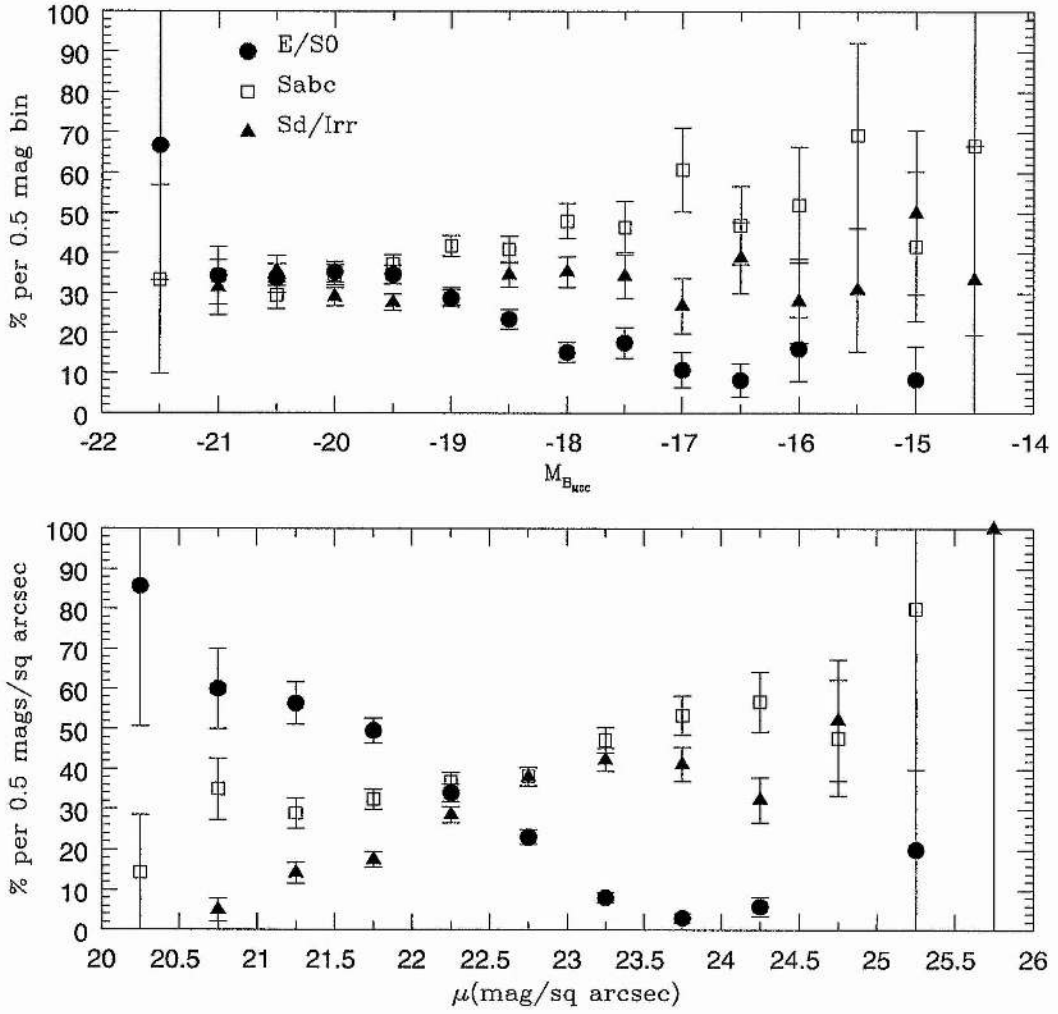

Figure 6.8: The variation of the population fractions with absolute magnitude (top) and cosmological dimming and k-corrected surface brightness (bottom).

6.3.1 Physical size

Fig. 6.9 shows how each galaxy type is distributed in half-light radius (HLR) with absolute magnitude. For each galaxy type there is, as expected, an obvious size-magnitude relation. It should be noted that here (and all subsequent similar figures) the distributions will be subject to Malmquist bias. In other words there are more galaxies at brighter magnitudes than fainter magnitudes as its easier to detect them.

We now want investigate scaling relations within the galaxy population, however because of the Malmquist bias we cannot fit directly to the data and need to minimise this bias. There are two ways to overcome this, the first is via detailed corrections as in Cross et al. (2001), the second is to minimise the selection bias by representing the data in bins with $3-\sigma$ clipped standard deviation errors. We then use a χ^2 minimisation method to fit the bin centers weighted by the standard deviations. By doing this the errors are not associated with the accuracy of the means but reflect the variance of the population within the bin (down to a certain minimum, $\sim$10) hence the fit is not biased towards bins containing larger numbers of galaxies. Although, to first order, this method eliminates the Malmquist bias it does not circumvent all possible selection biases. A detailed treatment of the selection biases is a major endeavor and can only be embarked on once the MGC-z survey is complete.

Other than a greater degree of scatter in the Sabc galaxies, there is no real difference in the distributions of the Sabc and Sd/Irr galaxy types indicated by the similarity in the HLR-$M_{\rm MGC}$ scaling law. The E/S0 galaxies follow a different scaling law that is inconsistent with the Kormendy relation (Kormendy 1977 and Kormendy & Bender 1996). In general we find that E/S0 galaxies are smaller than later types at any given absolute magnitude and that, as expected, intrinsically faint galaxies are smaller than bright galaxies. This has implications that any survey with a high surface brightness threshold will be primarily biased against Spirals plus Irregular galaxies. This should not be the case for the MGC-BRIGHT as the obvious gap between the Spiral and Irregular galaxies and the surface brightness limit, see Fig. 2.21, indicates that MGC-BRIGHT is complete down to its isophotal surface brightness limit of 26 mags/sq arcsec. However the redshift surveys are based on predominantly 2dFGRS data at this stage which have significantly brighter surface brightness limit of around 24 mags/sq arcsec (see Cross et al. 2003).

6.3.2 Absolute surface brightness

To get the absolute surface brightness, μ_{abs}, we correct the apparent surface brightness, μ_{app}, for k and e as well as surface brightness dimming from the expansion of the universe:

$$\mu_{abs} = \mu_{app} + 10\log(1+z) - k - e, \tag{6.5}$$

where $k+e$ is given in Eqn. 6.4.

In Fig. 6.10 we show the galaxies distributed in absolute magnitude and absolute surface brightness, otherwise known as a bi-variate brightness distribution (BBD, see Driver 1999; de Jong & Lacey 2000; Cross & Driver 2002). We see that the galaxies are not randomly distributed and that the faintest galaxies tend to have the lowest surface brightness. We note that only the E/S0 galaxies lie in a relatively distinct region from the main population. Although the Sabc and Sd/Irr galaxies follow different scaling laws the scatter is too great to be able to identify morphologically dependent relations. Cross & Driver (2002) convert the gradient of the de Jong & Lacey (2000) (dJL) late type luminosity-size relation in terms of magnitude to be $\beta_{dJL} = 0.49 \pm 0.04$ (where $\frac{\mu}{M} \propto \beta$). This is significantly steeper than we find for either the Sabc or Sd/Irr galaxies, $\beta_{MGC-Sabc}$=0.19, $\beta_{MGC-Sd/Irr}$=0.30, see Fig. 6.10 bottom left and right. This sizable difference is not entirely surprising as β_{dJL} was calculated from much redder I-band data. Cross & Driver

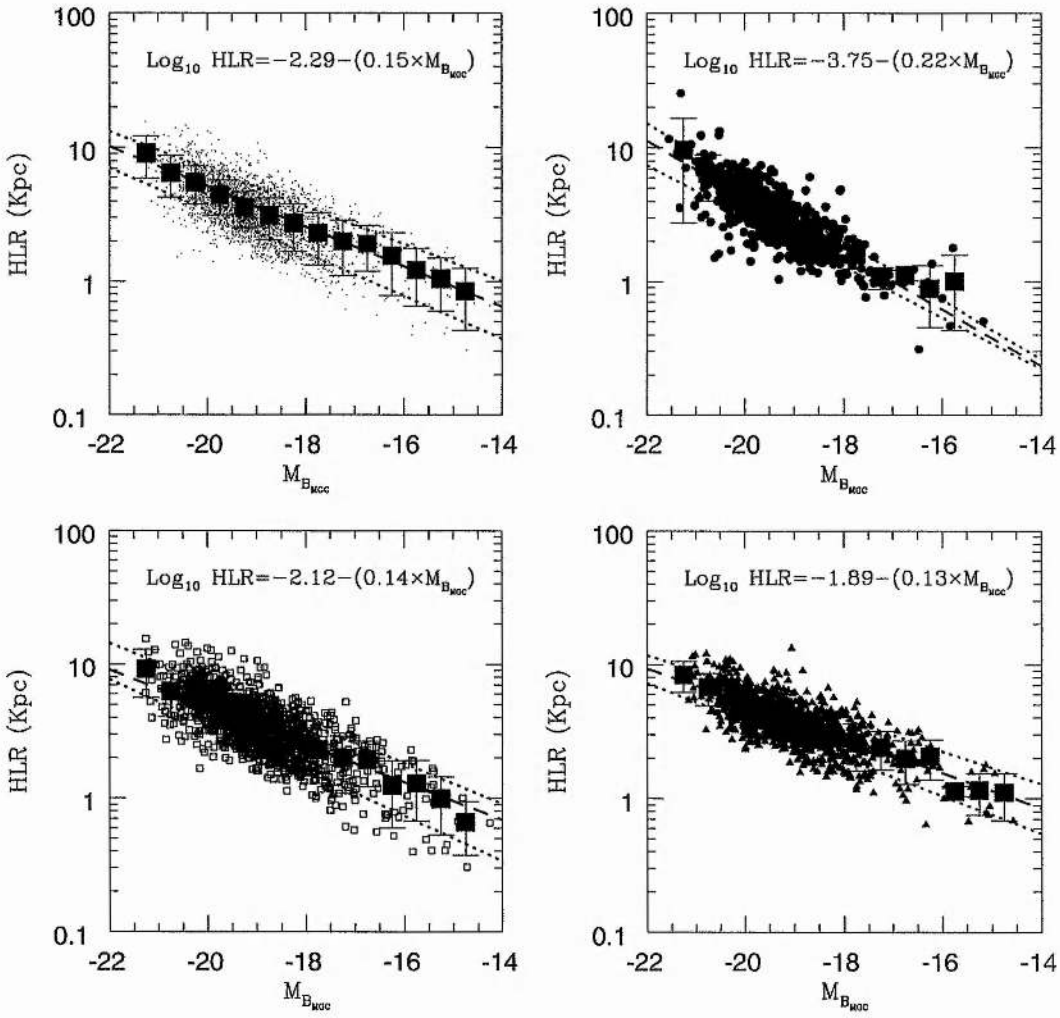

Figure 6.9: The variation of half-light radii, HLR, with absolute magnitude, $M_{B_{\rm MGC}}$ for all (top-left), E/S0 (top-right), Sabc (bottom-left) and Sd/Irr galaxies (bottom-right). The solid squares mark the mean HLR in each 0.5 mag bin, the errors are the 3-σ clipped standard deviation. The dashed and dotted line are the best linear fits to the mean and standard deviations respectively. The best fit equation for the mean HLR is given in each panel. The solid line is the magnitude-size relation for a pure disk with central surface brightness μ_o=26 mags/sq arcsec.

(2002) argue that a luminosity-surface brightness relation should appear steeper in redder colours, should there exist a (b_j-I) colour magnitude relation similar to that found in Blanton et al. (2001) for the (g^*-r^*) colour.

We now compare the overall BBD (Fig. 6.10, top left) to that found for an HDF sample by Driver (1999) and the 2dFGRS by Cross & Driver (2002). Whilst we find a much shallower gradient than the $z \approx 0.4$ HDF sample the 2dFGRS magnitude-surface brightness relation is similar to our own ($\beta_{\rm HDF}$=0.67, $\beta_{\rm 2dFGRS}$=0.28, $\beta_{\rm MGC}$ = 0.25). All this indicates that the overall magnitude-surface brightness relation found in Cross et al. (2001) appears real, with the caveat that the MGC z's are at present predominantly based on the 2dFGRS dataset. However, due to the similarity of the Sabc and Sd/Irr distributions the BBD may not be a useful tool for determining specific Hubble types or even galaxy morphology in general beyond a bulge-dominated or disk dominated classification scheme, see Appendix C.2 for a further discussion of this point.

6.3.3 Colour-Magnitude diagram

In Fig. 6.11 we show the un-k-corrected colours and note that the E/S0 galaxies occupy a distinct red region and that there are different scaling laws for each type. As there are two Spiral populations, red ($(u^* - g^*)$ >1.5) and blue ($(u^* - g^*)$ <1.5) spirals, we derive a separate scaling law for each population. We find that both the red and blue Spirals follow the same scaling law, further confirming that the red Spirals are Spirals, and that the Sabc scaling law is noticeably similar to that of the Sd/Irr galaxies. This similarity indicates that colour cannot be confidently be used to discriminate between the Sabc and Sd/Irr galaxies.

From the colour-absolute magnitude distribution (CMD) we note that there appears to be a trend for the brighter E/S0 galaxies to have redder colours. This trend would appear to contradict the hierarchical formation scenario, in which the intrinsically bright (massive) galaxies should be blue due to star-formation from merging. However, large galaxies will typically acrete *relatively* smaller objects with little global change. So a big red galaxy may retain its red colour after a merger event. The Sabc and Sd/Irr galaxy CMD are both blue and relatively flat indicative of recent universal star-formation. The fact that redder (E/S0) galaxies have a steeper slope than the bluer (Sabc and Sd/Irr) galaxies hints that if one does indeed consider just red objects, or the same objects viewed through a redder filter, then the colour-magnitude relation will steepen. This can also be seen by noting that the $+1\sigma$ fit for the Spiral galaxies (Fig. 6.11, bottom left), which passes through the redder galaxies only , is significantly steeper than the fit to the mean $(u^* - g^*)$ points.

The substantial overlap between all the classes in all the parameter spaces shown prevents us from being too specific. However, we can say that generally the brightest galaxies are large, red and on the most part elliptical, with the highest surface brightness. Whilst the less luminous are smaller, more diskey, blue and have a lower surface brightness. Having said that, it should be noted that the very reddest galaxies are due to extinction in edge-on Sabc types. All this is echoed in the work of Blanton et al. (2002).

6.4 Bulges and disks

We now want to investigate the properties of the bulges and disks of galaxies, i.e. we want to see if the bulges of Spirals are the same as Ellipticals and whether the Spiral disk is the similar to an Irregular. To do this we use the (B/T) parameter to split the galaxy sample into four populations: pure bulge (high (B/T)), embedded bulge (intermediate (B/T)), surrounding spiral (intermediate (B/T)) and pure spiral (low (B/T)). We note here that the FPA galaxies are not used in this study as their bulge and disk

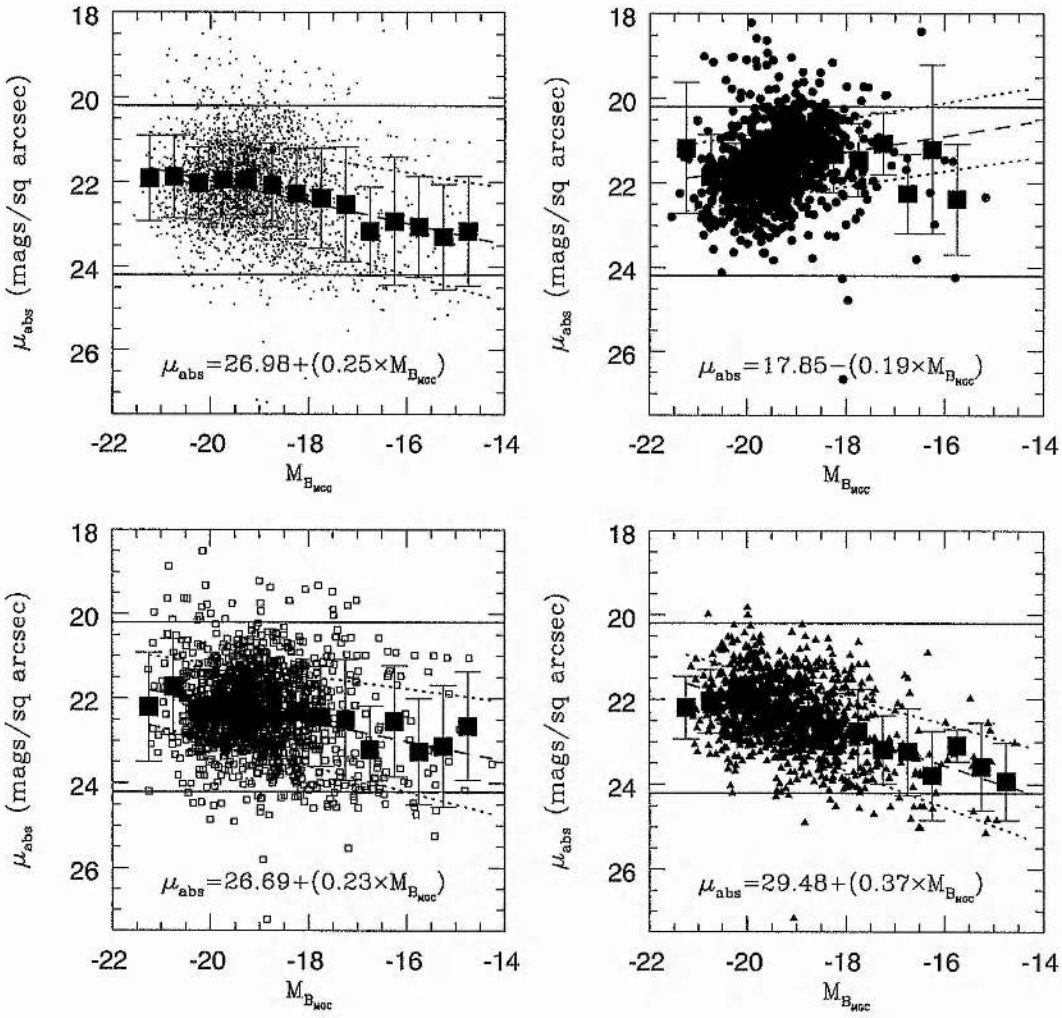

Figure 6.10: The variation of absolute surface brightness, μ_{abs} with absolute magnitude, $M_{B_{\rm MGC}}$ for all (top-left), E/S0 (top-right), Sabc (bottom-left) and Sd/Irr galaxies (bottom right). The solid lines indicate the surface brightness selection limits. The solid squares mark the mean surface brightness in each 0.5 mag bin, the errors are the 3-σ clipped standard deviation. The dashed and dotted line are the best linear fits to the mean and standard deviations respectively. The best fit equation for the mean surface brightness is given in each panel.

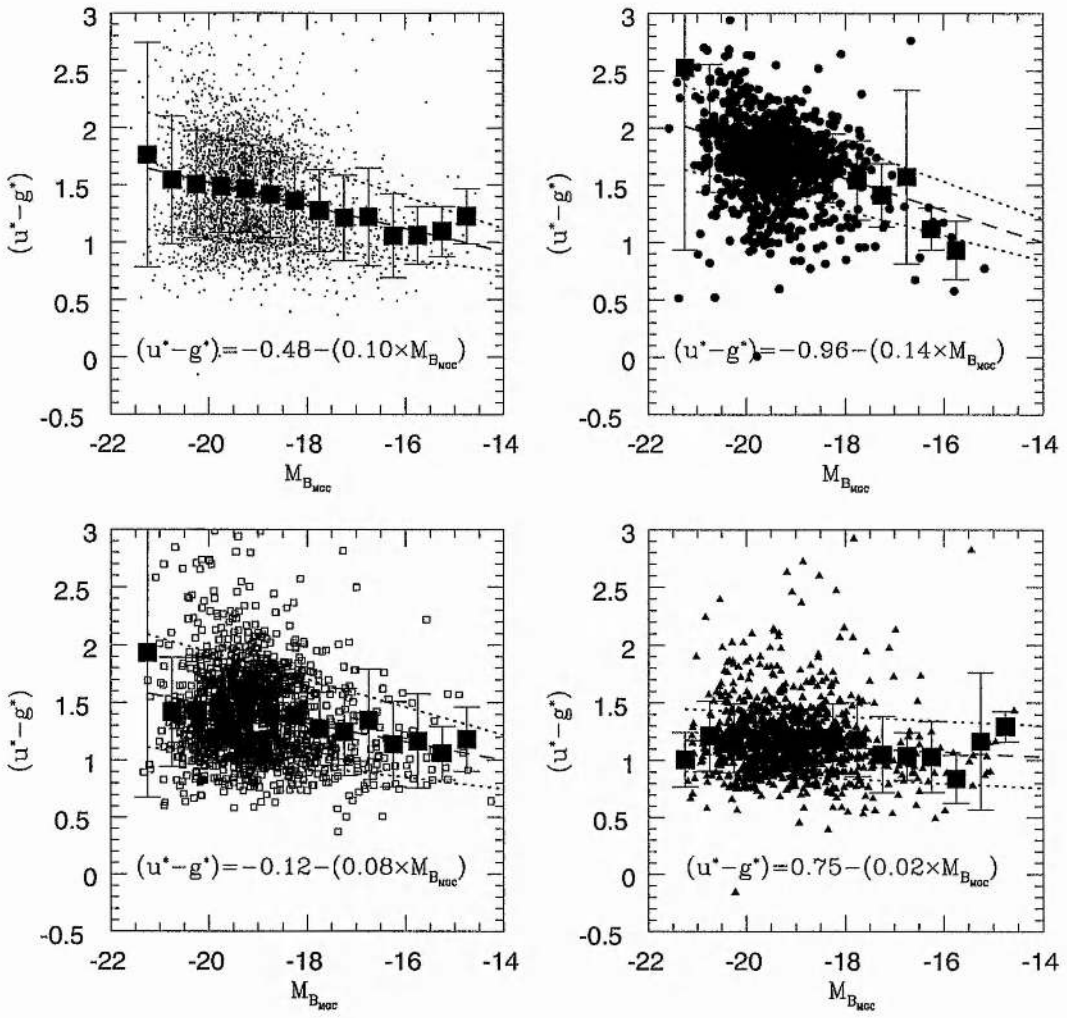

Figure 6.11: The variation of $B_{\rm MGC}$-band absolute magnitude with apparent colour for all (top-left), E/S0 (top-right), Sabc (bottom-left) and Sd/Irr galaxies (bottom right). The solid line separates the red, $(u^* - g^*) > 1.5$, and blue, $(u^* - g^*) < 1.5$, Spiral galaxies. The solid squares mark the mean colour in each 0.5 mag bin, the errors are the 3-σ clipped standard deviation. The dashed and dotted line are the best linear fits to the mean and standard deviations respectively. The best fit equation for the mean colour is given in each panel.

parameters are unreliable. For the pure bulge and disk we recalculate the galaxies magnitude and surface brightness using the Re & L_{Bulge} and Rd & L_{Disk} values respectively. The embedded bulge and surrounding disk populations consist of the same galaxies with the only difference being that for embedded bulges the bulge parameters are used and similarly for the surrounding disks. Fig. 6.12 shows how these four populations are distributed in $M_{B_{\rm MGC}}$ and z, not the similarity between the pure bulge and E/S0 as well as the pure disk and Sd/Irr distributions of Fig. 6.4. It is not surprising that the embedded bulges and surrounding disk distributions scatter over the lower M-z limit as neither the bulge or disk only magnitudes are representative of theses mid-range (B/T) galaxies. Figs. 6.13 & 6.14 show how the bulge and disk size and surface brightness vary with absolute magnitude. We see from the pure bulges (Fig. 6.13, top left) that the scaling law now follows to the Kormendy relation (Kormendy 1977) as measured by Djorgovski & Davis (1987) ($\frac{\mu}{M}_{DD}$ =-0.71, $\frac{\mu}{M}_{BULGE}$ =-0.55). The Djorgovski & Davis (1987) measurement of the size-luminosity relation was measured from a survey of ~260 early-type galaxies. The galaxy selection and completeness of their sample is described in detail in Djorgovski (1985). Our pure bulge sample is of comparable size, containing 209 galaxies at $(B/T) > 0.8$, and extends over a similar magnitude range. However, our sample does extend to a lower surface brightness than Djorgovski (1985). Given this, and the fact a pure bulge system is essentially an isolated Elliptical, the similarity between the two derived surface brightness-absolute magnitude relations is not unexpected, but does add confirmation that the GIM2D bulge parameters are accurate. In each case the pure and embedded bulges follow completely different scaling laws, whilst the pure and surrounding disks follow more similar distributions. Once again comparing these two with the scaling laws of de Jong & Lacey (2000) and Cross & Driver (2002), we see that whilst the surrounding disks are essentially invariant with magnitude there is a good agreement with the 2dFGRS and the pure disks (Irregulars). There is still a discrepancy of a factor of ~2 between our relation for pure disks and that de Jong & Lacey (2000) for late type galaxies. Again we put this down to a colour-magnitude relation in (b_j-I), see Section 6.3.2, and/or the N(z) incompleteness.

Looking again at the embedded bulges it appears that there may be two discernible trends. In Fig. 6.15 we look at how the bulge absolute magnitude and surface brightness relation varies with (B/T). In the top left panel we clearly see the well known Kormendy relation for Elliptical galaxies (Kormendy 1977). However we find that as (B/T) decreases we get the introduction of a population of bulges that look less like Ellipticals (i.e do not follow the Kormendy relation), but note that even in the lowest (B/T) range there still exist some Elliptical like bulges. We see that the trend still persists, even when we exclude galaxies with bulge magnitudes $B_{\rm MGC} < 19$ mags, which indicates that it is real and not due to noise. Figs. 6.16 shows a similar trend for the disk component, that they become less disk like as (B/T) rises. We suggest that the non-Elliptical bulges are due to the presence of bars in Spiral galaxies or an evolution of the Sersic parameter from $n = 4$ at high (B/T) to $n < 4$ at low (B/T).

To summarise all this, we find that whilst pure bulges follow the Kormendy relation, embedded bulges follow this relation only at $(B/T) > 0.6$, after which the relationship breaks down with some bulges following it whilst others do not. In all cases pure and surrounding disks appear inseparable and exhibit a flatter luminosity-surface brightness relation that previous work suggests.

6.5 Morphological LFs

Having visually classified all our FPA galaxies we are able to use the morphological galaxy counts, shown in Fig. 5.30 and tabulated in Table. 5.4, to examine the galaxy LF as a function of type. In Table. 6.3 we show the E/S0, Sabc and Sd/Irr Schechter function parameters of the 2dFGRS (Madgwick et al. 2002), SDSS-EDR (Nakamura et al. 2002), ESP (Zucca et al. 1997), Stromlo/APM (Loveday et al. 1992), Autofib (Heyl et al. 1997), SSRS2 (Marzke et al. 1998), NOG (Marinoni et al. 1999) and CS (Brown et al. 2001) surveys. The morphological LFs are displayed in Fig. 6.17. From SDSS-EDR we use their

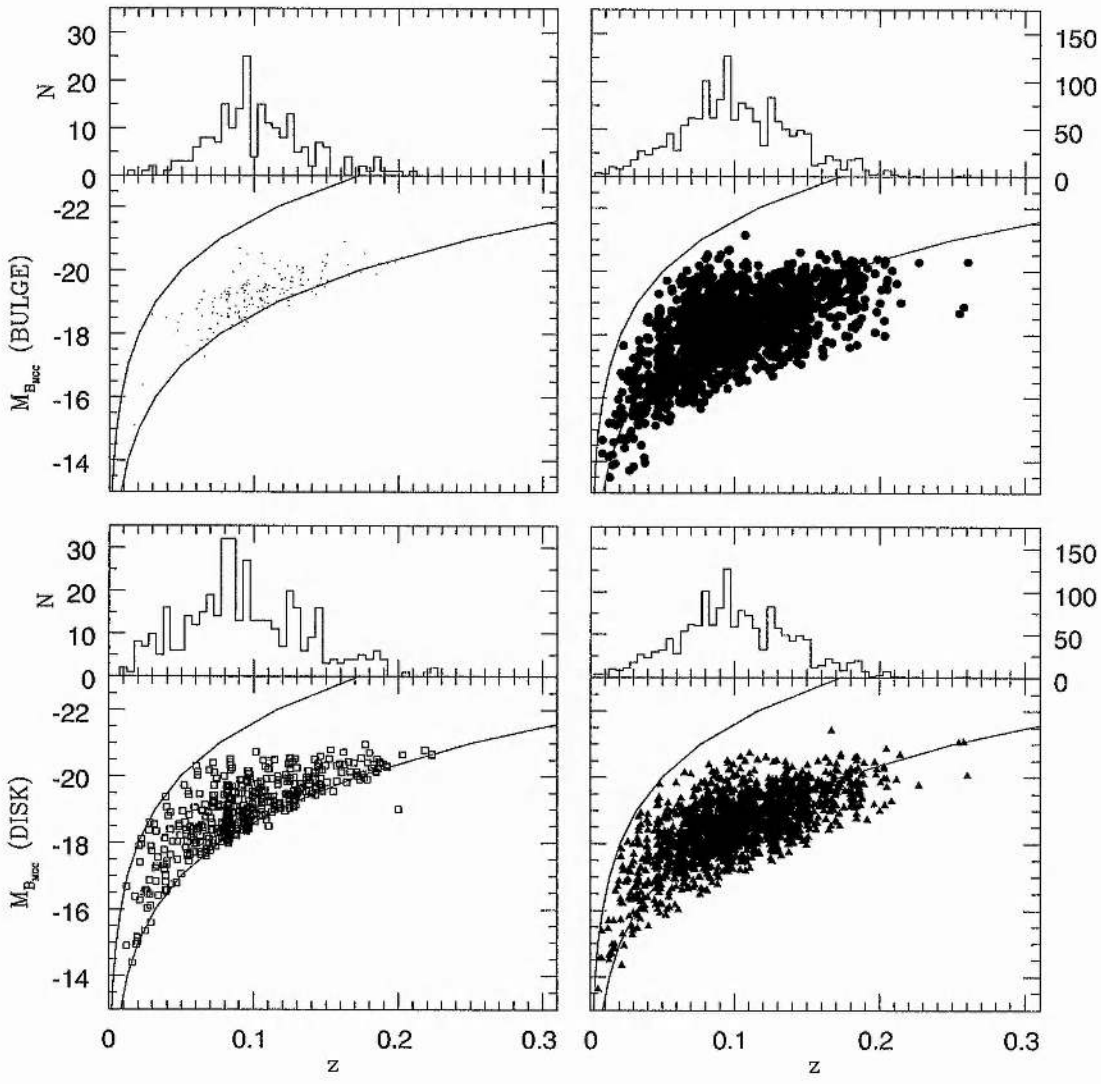

Figure 6.12: As Fig. 6.4 but for pure bulges (top-left), embedded bulges (top-right), pure disks (bottom-left) and surrounding disks (bottom right).

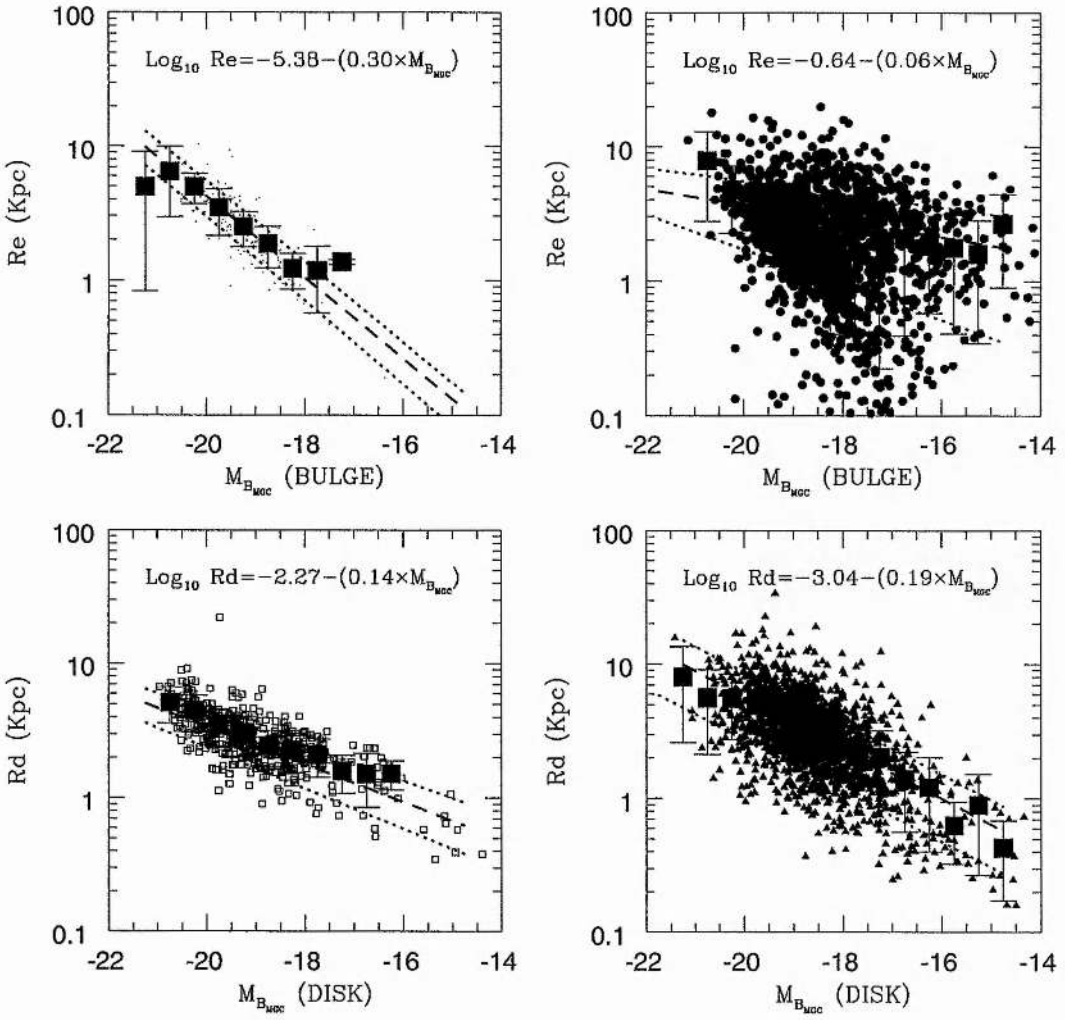

Figure 6.13: The variation of bulge and disk size with $B_{\rm MGC}$-band absolute magnitude for pure bulges (top-left), embedded bulges (top-right), pure disks (bottom-left) and surrounding disks (bottom right). The solid squares mark the mean bulge/disk size in each 0.5 mag bin, the errors are the 3-σ clipped standard deviation. The dashed and dotted line are the best linear fits to the mean and standard deviations respectively. The best fit equation for the mean bulge/disk size is given in each panel.

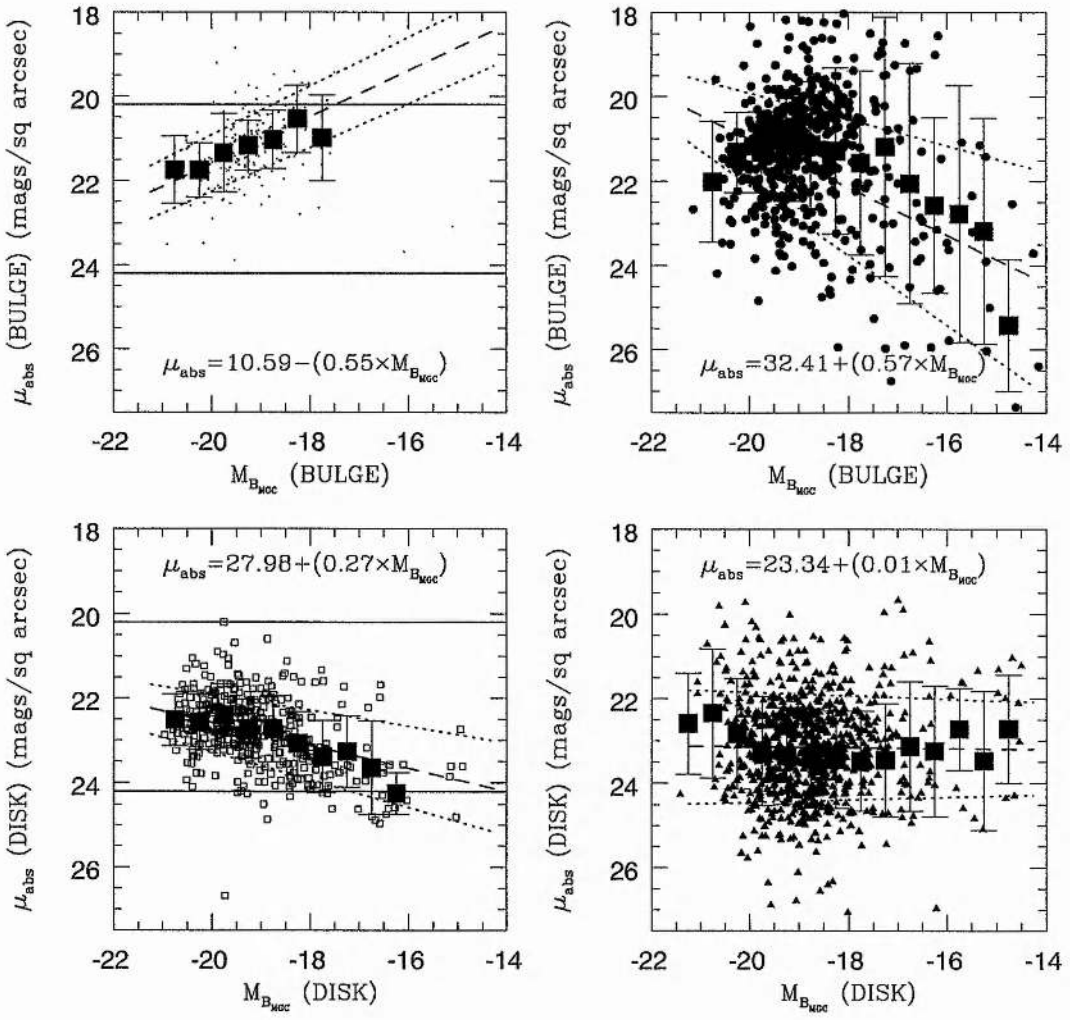

Figure 6.14: The variation of bulge and disk corrected surface brightness, μ_{abs}, with $B_{\rm MGC}$-band absolute magnitude for pure bulges (top-left), embedded bulges (top-right), pure disks (bottom-left) and surrounding disks (bottom right) with $B_{\rm MGC} < 19$ bulge and disk components. The solid lines mark the surface brightness selection limits. The solid squares mark the mean bulge/disk μ_{abs} in each 0.5 mag bin, the errors are the 3-σ clipped standard deviation. The dashed and dotted line are the best linear fits to the mean and standard deviations respectively. The best fit equation for the mean bulge/disk μ_{abs} is given in each panel.

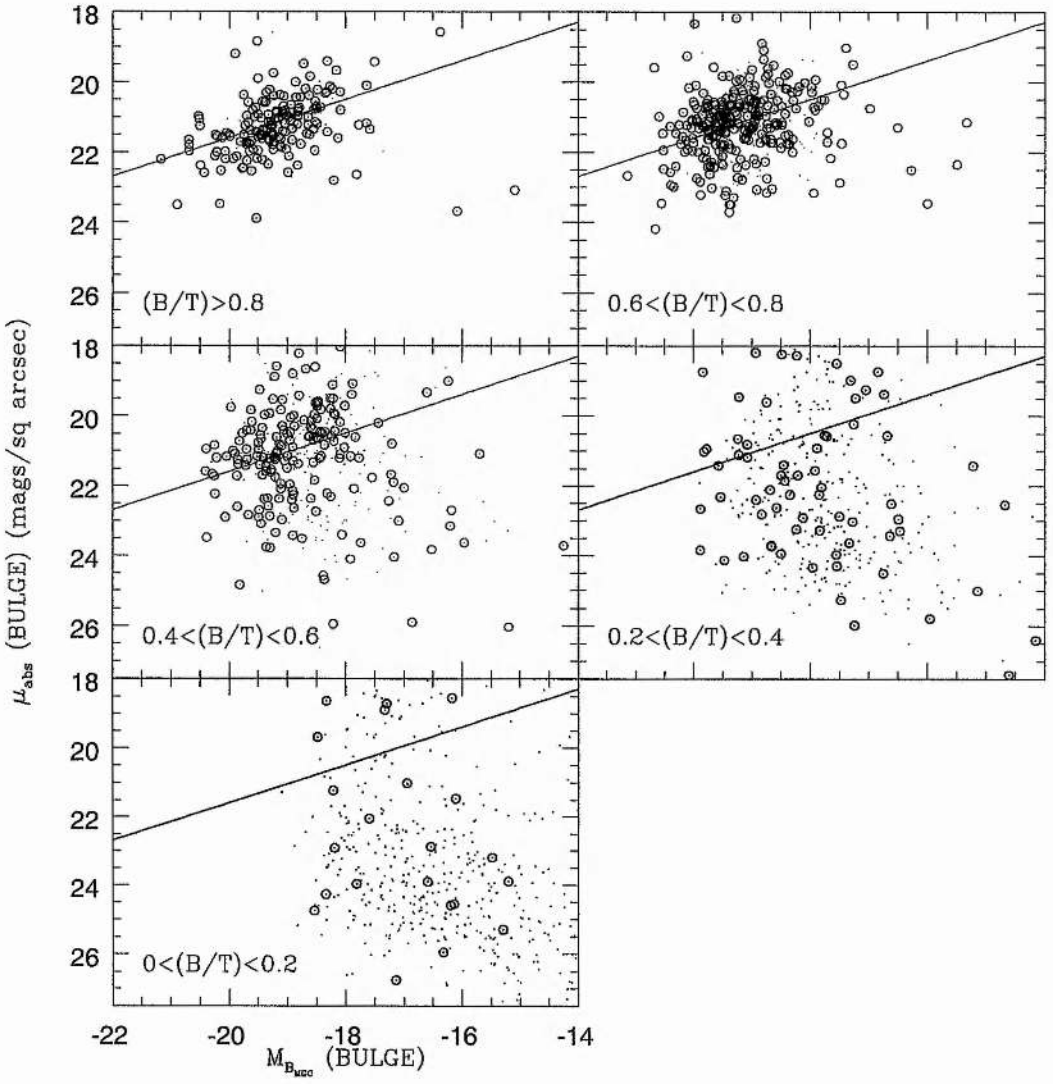

Figure 6.15: The variation of bulge surface brightness μ_{abs} with $B_{\rm MGC}$-band absolute magnitude and (B/T). The solid line represents the surface brightness-magnitude relation for pure bulges shown in Fig. 6.14. The open circles mark the points with bulge magnitudes $B_{\rm MGC} < 19$ mags. Note the introduction of a population of bulges that look less like Ellipticals as (B/T) decreases.

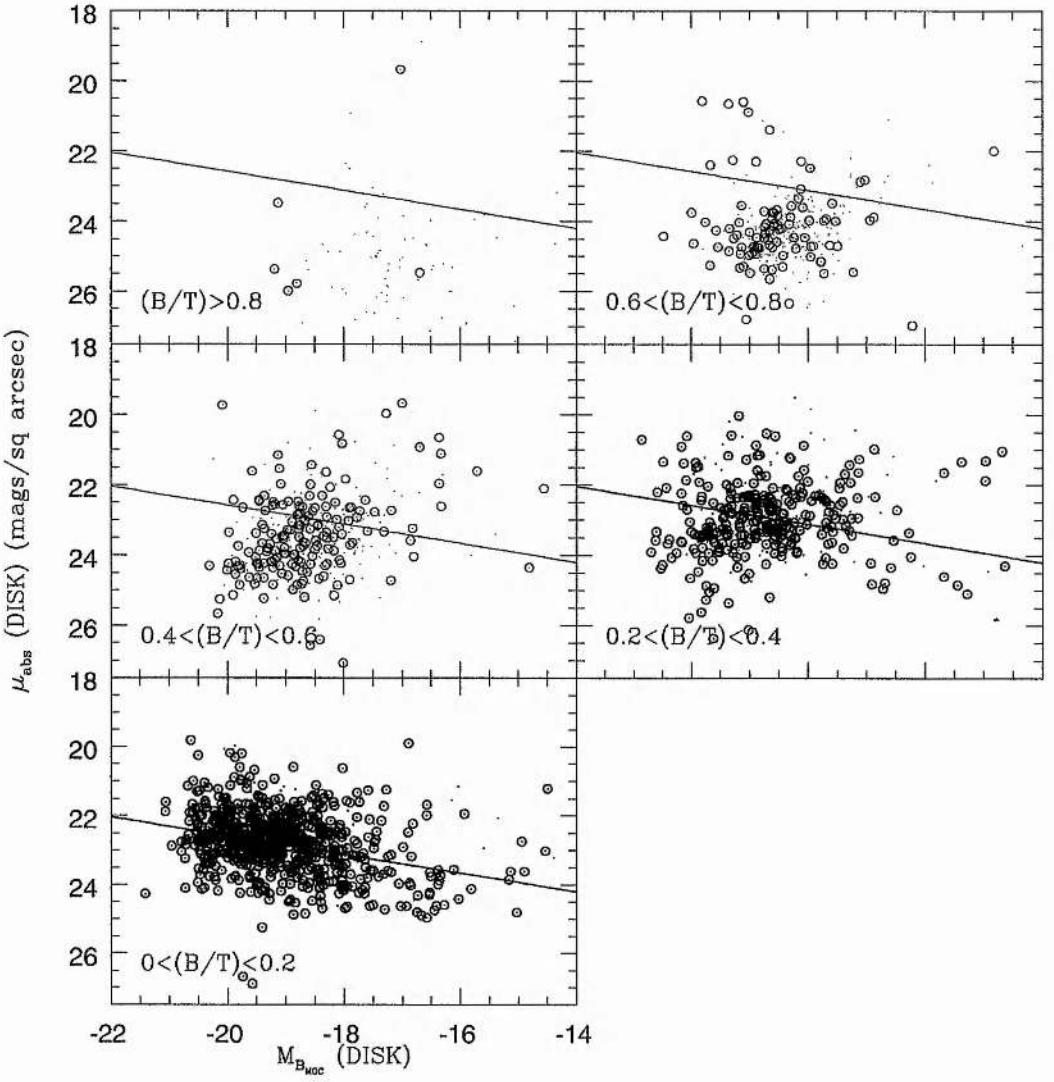

Figure 6.16: As Fig. 6.15 but for disk magnitudes and surface brightness. The solid line represents the surface brightness-magnitude relation for pure disks shown in Fig. 6.14. The open circles mark the points with disk magnitudes $B_{\rm MGC} < 19$ mags.

early Spirals and Im LF parameters to represent our Sabc and Sd/Irr galaxies respectively. As suggested in Nakamura et al. (2002) we have multiplied their ϕ^* values by a factor of 1.29 in order to compensate for the underdensity of bright galaxies r^* <16 in the SDSS-EDR northern stripe. For the 2dFGRS we take the η-types=1, 2 & 4 to be representative of the E/S0, Sabc and Sd/Irr galaxies respectively. ESP give LF parameters for galaxies with and without spectroscopic emission lines which we take to be Sabc and E/S0 galaxies respectively. The APM LFs are only given for early and late types which we take to be representative of our E/S0 and Sabc galaxies. For the APM there is no ϕ_* given for each morphological type and so here we use half the value given in Table. 4.2 for both E/S0 and Sabc types. From Autofib we use their red E LF parameters as equivalent to our E/S0, their Sab for our Sabc and their Scd for our Sd/Irr galaxies. The SDSS-EDR, ESP and Autofib retrieve their LFs via the STY or a modified STY (SSTY) estimators. Both these estimators are variants of the SWML estimator (see below) and are discussed in detail in Sadage, Tamman & Yahil (1979) and Willmer (1997) (STY) and Heyl et al. (1997) (SSTY). Whilst NOG give Schechter function parameters for E/S0 galaxies they use a much finer classification for the later types. We take the NOG Sa-Sb and Sm-Im parameters to be representative of our broad Sabc and Sd/Irr classes. It should be noted the NOG Sm-Im should be treated with caution as the 1σ errors on α and M^* are $\sim\pm0.6$ and ±1 respectively (Marinoni et al. 1999). Also according to Willmer (1997) "The Turner method is extremely sensitive to the number of objects as well as bin width..." and the Sm-Im was calculated from a total of only 619 galaxies. The CS survey does not give LFs as a function of morphological type but for the $\frac{1}{3}$ reddest and bluest galaxies. We take these to be representative of our E/S0 and Sabc types respectively.

To summarise all this, the noticeable discrepancy between the LF parameters of the same type is mainly due to the different morphological classification techniques used by different authors. The essential result here is that we see a general trend whereby E/S0s have $\alpha < -1$, Sabc $\alpha = -1$ and Sd/Irr $\alpha > -1$.

To estimate the MGC morphological LFs we use the Stepwise Maximum Likelihood technique (hereafter SWML) developed in Efstathiou, Ellis & Peterson (1988), Willmer (1997) and extended for a BBD in Cross (2002). Basically the LF is broken into N_P steps (magnitude bins). For each step, k, the galaxy number density ϕ_k is given using the equation derived in Willmer (1997) and Cross (2002):

$$\phi_k = \frac{\sum_i W_{ik}}{\sum_i^N \left(H_{ik} / \sum_j^{N_P} \phi_j H_{ij} \right)} \tag{6.6}$$

where N is the total number of galaxies in the sample and

$$W(x) = \begin{cases} 1 & \text{if } -\Delta M/2 \leq x \leq \Delta M/2 \\ 0 & \text{otherwise} \end{cases} \tag{6.7}$$

and

$$H(x) = \begin{cases} 0 & \text{if } x \geq \Delta M/2 \\ \frac{1}{2} - \frac{x}{\Delta M} & \text{if } -\Delta M/2 \leq x \leq \Delta M/2 \\ 1 & \text{if } x \leq -\Delta M/2 \end{cases} \tag{6.8}$$

Equ. 6.6 is derived by maximising the likelihood equation

Table 6.3: LF parameters for E/S0, Sabc, Sd/Irr galaxies.

LF	$M^*_{B_{\rm MGC}} - 5\log h$	α	ϕ^* (h^3/Mpc^3)	j_{b_j} ($10^8 h L_\odot$/Mpc^3)	Estimator	Ω_M, Ω_Λ
	E/S0					
2dFGRS	-19.45	-0.54	0.0099	0.785	SWML	0.3, 0.7
SDSS-EDR	-19.21	-0.83	0.0061	0.176	STY	0.3, 0.7
ESP	-19.49	-0.98	0.0110	1.010	STY	1.0, 0.0
Stromlo/APM	-19.58	0.20	0.0070	1.551	SWML	1.0, 0.0
Autofib	-20.57	-1.05	0.0016	0.414	SSTY	1.0, 0.0
SSRS2	-19.53	-1.00	0.0010	0.096	SWML	0.4, 0.0
NOG	-19.23	-0.97	0.0024	0.293	Turner (1979)	1.0, 0.0
CS	-19.74	-0.13	0.0070	0.485	SWML	0.3, 0.7
	Sabc					
2dFGRS	-19.40	-0.99	0.0072	0.612	SWML	0.3, 0.7
SDSS-EDR	-19.06	-1.15	0.0122	0.397	STY	0.3, 0.7
ESP	-19.34	-1.40	0.0100	1.205	STY	1.0, 0.0
Stromlo/APM	-19.27	-0.80	0.0070	0.971	SWML	1.0, 0.0
Autofib	-19.87	-0.99	0.0022	0.288	SSTY	1.0, 0.0
SSRS2	-19.59	-1.11	0.0080	0.874	SWML	0.4, 0.0
NOG	-19.12	-0.62	0.0052	0.496	Turner (1979)	1.0, 0.0
CS	-19.80	-1.43	0.0080	0.961	SWML	0.3, 0.7
	Sd/Irr					
2dFGRS	-19.02	-1.50	0.0024	0.256	SWML	0.3, 0.7
SDSS-EDR	-18.92	-1.90	0.0005	0.137	STY	0.3, 0.7
Autofib	-19.07	-1.37	0.0030	0.269	SSTY	1.0, 0.0
SSRS2	-19.94	-1.81	0.0002	0.136	SWML	0.4, 0.0
NOG	-19.72	-2.41	0.0002	0.136	Turner (1979)	0.3, 0.7

$$L = \prod_i p_i \tag{6.9}$$

where p_i is the probability that a galaxy with absolute magnitude M_i and redshift z_i will be found in a magnitude limited catalogue (the MGC). p_i is found by Willmer (1997) and Cross (2002) to be

$$p_i \propto \frac{\phi(M_i)}{\int_{-\infty}^{M_{max(z_i)}} \phi(M)dM} = \frac{\sum_k W_{ik}\phi_k}{\sum_j^{N_p} H_{ij}\phi_j \Delta M} \tag{6.10}$$

The values of ϕ_k from Eqn. 6.6 can be used to estimate M^*, α by fitting them to a Schechter function and then normailising it with the MGC counts to get ϕ^*. Fig. 6.18 shows as histograms the un-normalised SWML LFs for all the galaxies and for each morphological type. To correct for incompleteness we multiplied the ϕ values of each magnitude bin by the overall incompleteness. This method is only valid if the completeness is consistent with magnitude, surface brightness and colour. From looking at Fig. 6.3, where there are sufficient galaxies to get an accurate completeness measurement, we find that the completeness is more-or- less consistent with magnitude, surface brightness and colour. We used a χ^2 minimisation technique to fit a Schechter function to the SWML data. Only data at $M_{B_{\rm MGC}}$ <-16 was used as at fainter magnitudes the numbers of galaxies in each mag bin is only a few, see Fig 6.4. Fig. 6.19 show the M^*-α 1, 2 and 3σ error ellipses. In order to compare our un-normalised LFs to the 2dFGRS LFs we have regenerated their LFs, keeping the quoted M^* and α's (see Table. 6.3), but substituting their ϕ_*'s with the values quoted in each panel. In all cases our Schechter functions provide better fits to the data. We note that, although it appears that the E/S0 LF is not flat but has a distinct turn over consistent with the 2dFGRS E/S0 LF, however, this is just the result of a poor fit at faint mags (see Fig. 6.18). The faint end of the total LF is dominated by what appears to be an even mix of Sabc and Sd/Irr galaxies contrary to most studies in which the faint end is overwhelmingly dominated by Irregular galaxies, see Fig. 6.17. To normalise the MGC SWML LFs we use a χ^2 technique to find, for each morphological type, the Schechter function that best predicts the galaxy number counts. The ϕ_* of SWML fitted Schechter function is then continuously adjusted until the χ^2 between the two LFs is minimised. In Fig. 6.20 we show the normalised SWML LFs (top) and the predicted and measured galaxy number counts for each morphological type. Comparing the SWML LF for the full galaxy sample with that found in Chapter 4 we see that main difference is a 11% rise in α. To arrive at a ϕ^* for the SWML LF we have used the MGC counts and in generating the SWML LF the same k and e corrections where used as in Chapter 4. Therefore we can put any discrepancies here down to the effects of combining a number of redshift surveys with different limits.

6.6 Bulge and Disk LFs

Figs. 6.21 and 6.22 show the SWML and LFs and errors for the various bulge and disk classes. Again we see a turnover in the LF for the pure and embedded bulges as well as the surrounding disks brought on by a poor fit at faint magnitudes. Whilst the pure bulge and pure disk LFs are substantially different, we see a noticeable similarity between the embedded bulge and surrounding disk LFs. This makes the LF an inappropriate tool to discriminate between the embedded bulge and surrounding disks. By looking at bulge and disk BBDs we are able to see that whilst embedded bulges appear to be the same as pure bulges, as its size in relation to the rest of the galaxy decreases ((B/T) drops) some will deviate away from their pure bulge state. We see a similar thing for the surrounding disks,

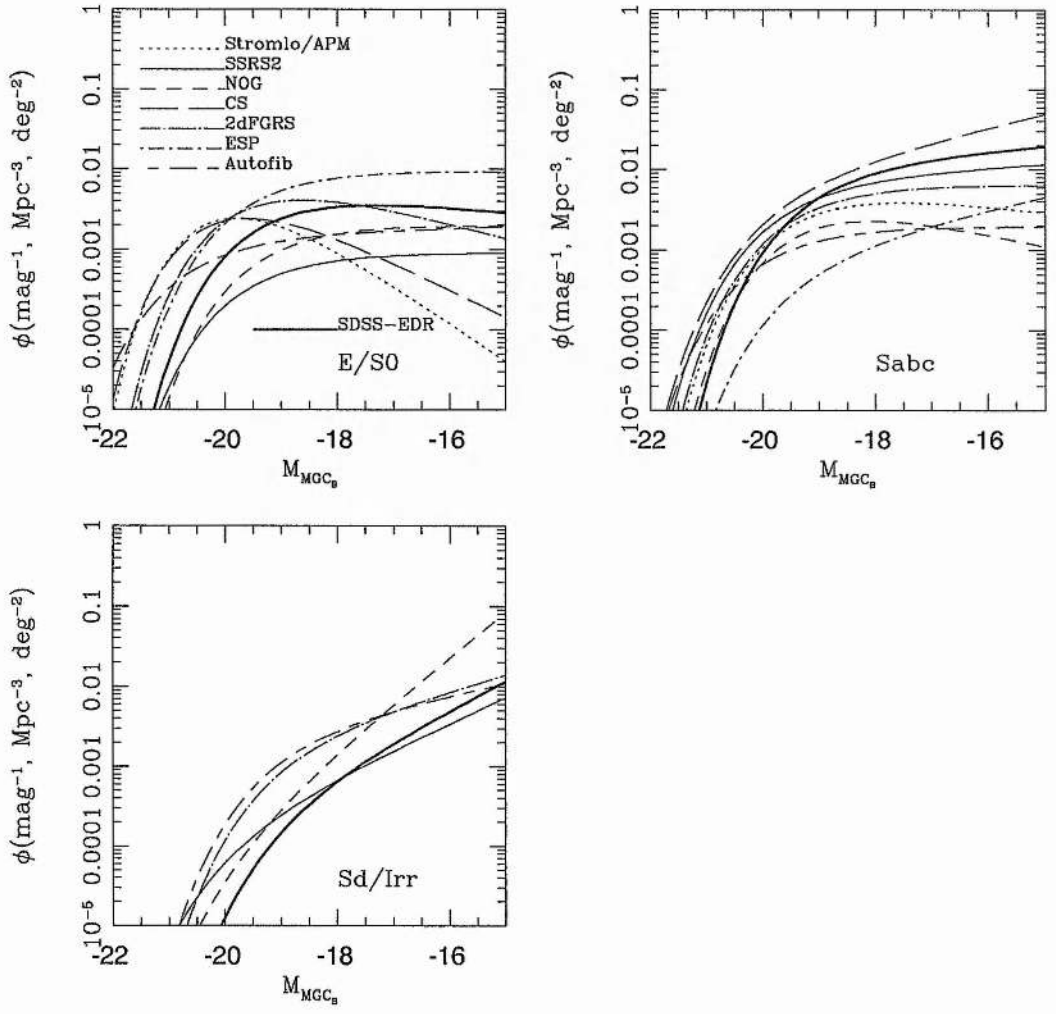

Figure 6.17: Sample LFs for E/S0 (top-left), Sabc (top-right) and Sd/Irr galaxies (bottom-left). The ample scatter between all the LFs of the same type is mainly due to different techniques in morphological classification.

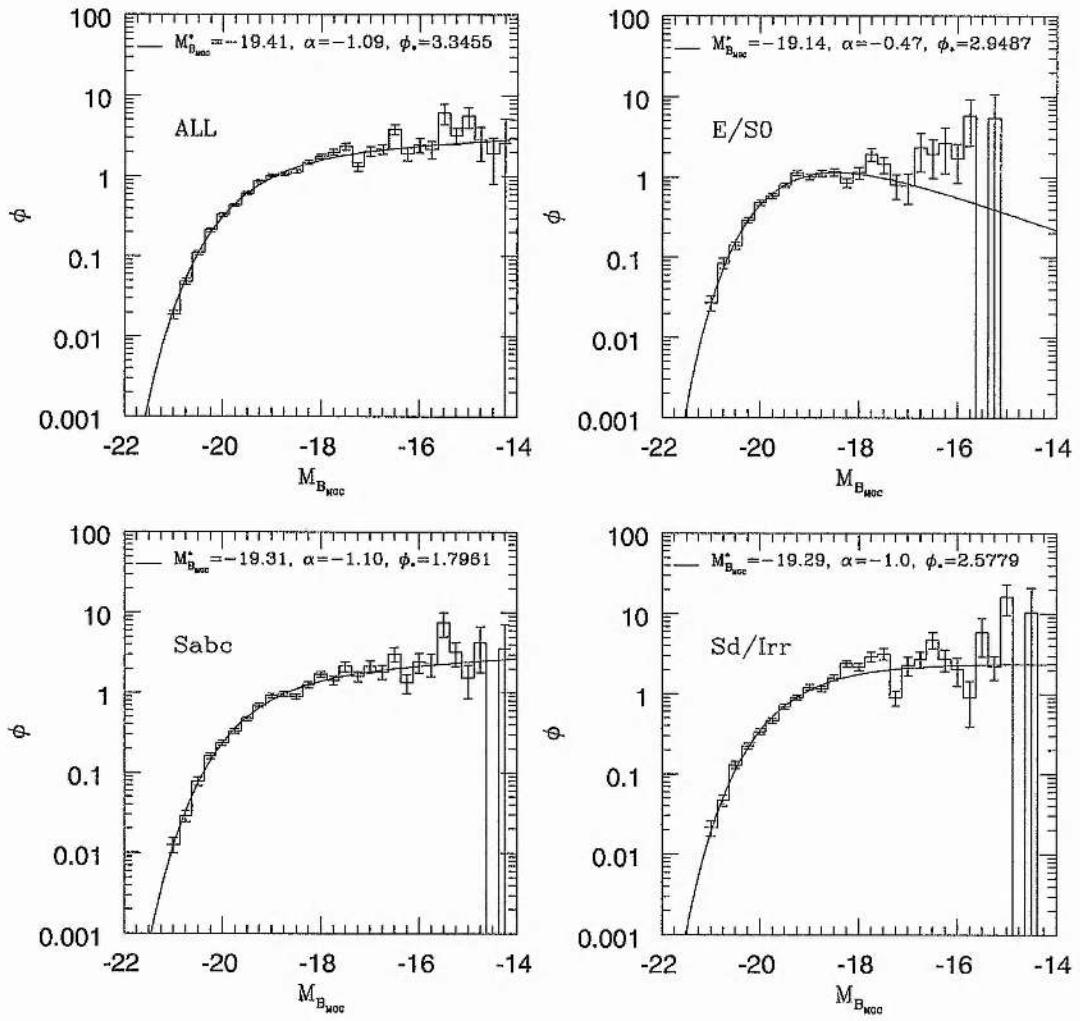

Figure 6.18: SWML LFs (histogram) for all galaxies (top-left), E/S0 (top-right), Sabc (bottom-left) and Sd/Irr galaxies (bottom-right). The solid lines show the best fit Schechter function.

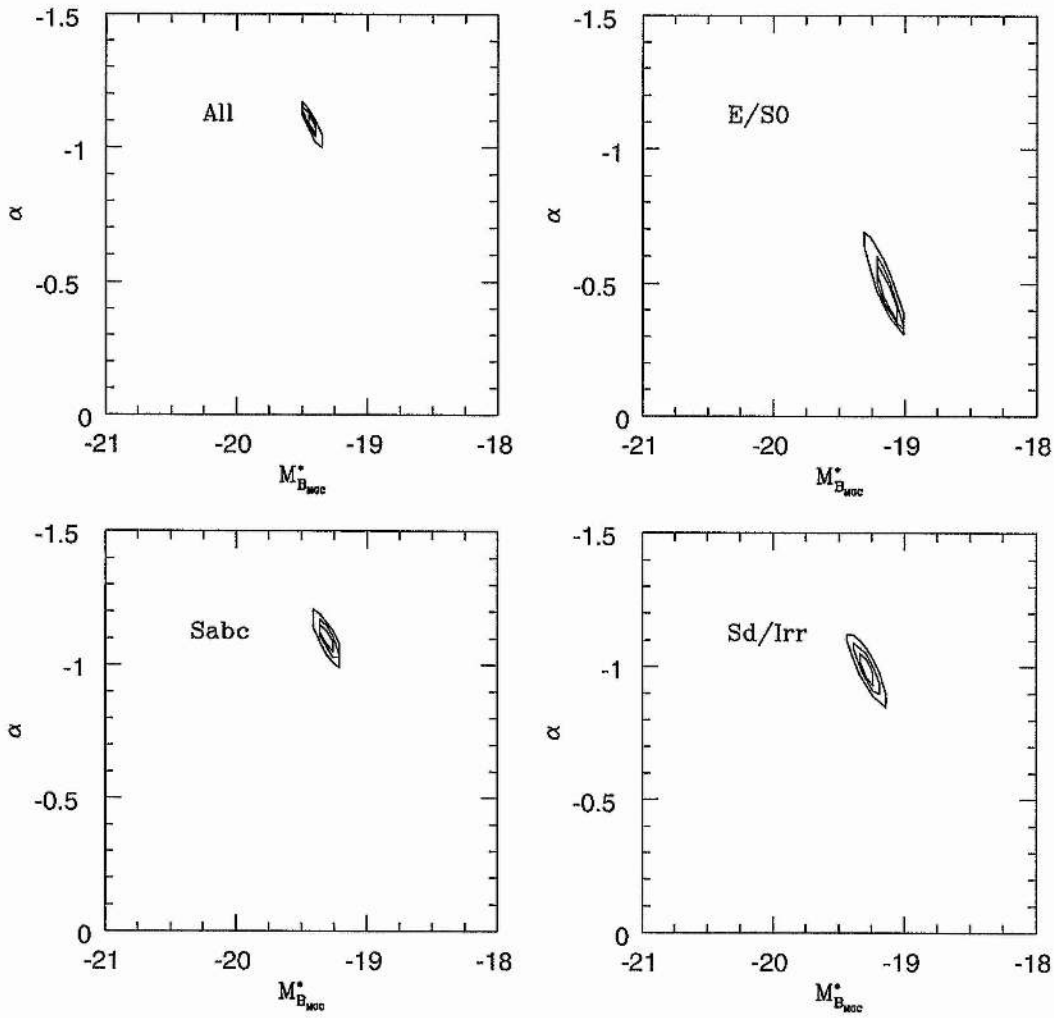

Figure 6.19: SWML M^* and α error ellipses.

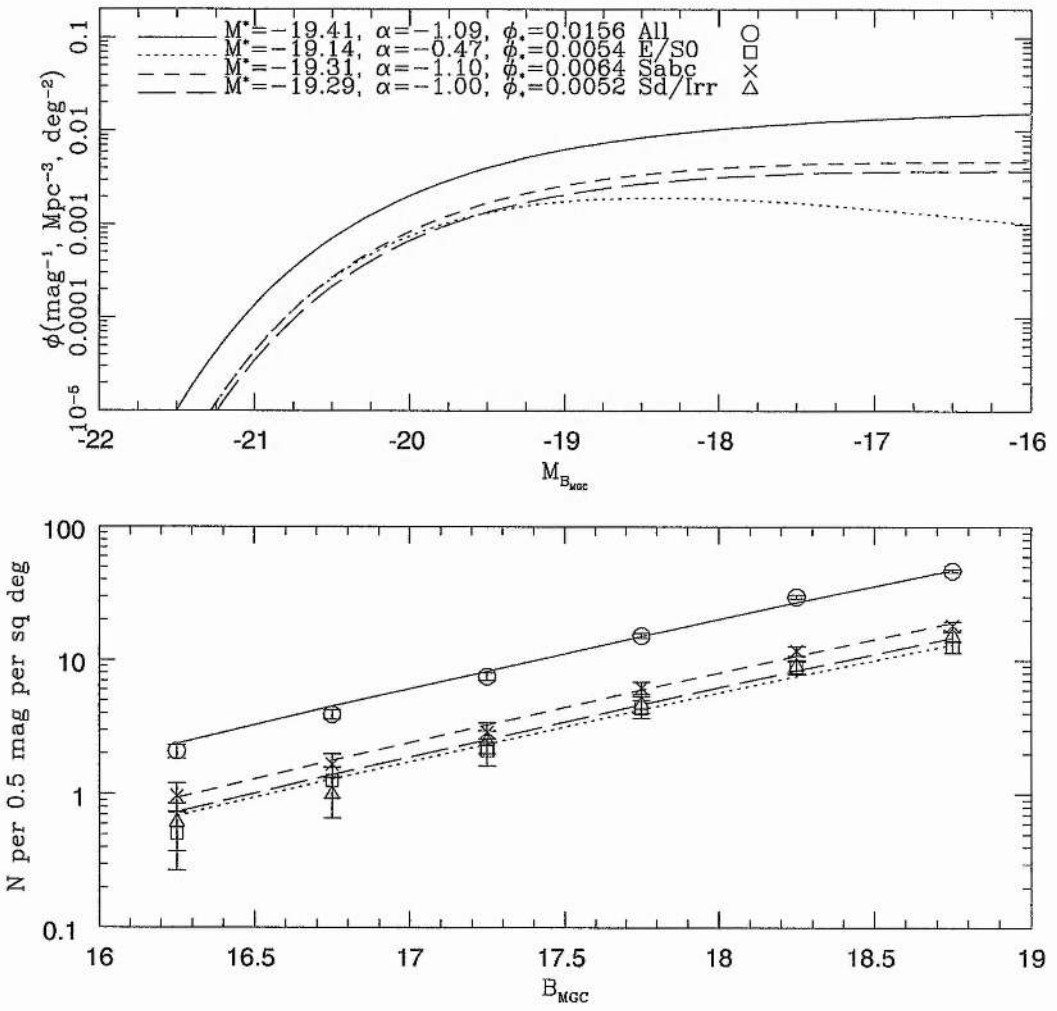

Figure 6.20: Top panel: The MGC normalised SWML LFs. Bottom panel: The predicted and measured galaxy number counts.

that their surface brightness-magnitude scaling law moves away from that of pure disks as (B/T) increases. Interestingly, whilst some bulges seems to evolve towards a pure disk scaling law the disk never approaches anything like the Kormendy law. This suggests that as (B/T) decreases it is, in some cases, the bulge that is being fundamentally altered. It may be possible that by adding a bar to a small bulge it may well force it into a parameter space normally occupied by disks.

6.7 Summary

In an attempt to better understand our sample of galaxies we restricted our study to only those galaxies in the range $16< B_{\rm MGC} <19$ and with 2dFGRS or SDSS-EDR redshifts and colours. By doing this we remove all low signal-to-noise objects ($B_{\rm MGC} \geq 19$) and are able to work with physical galaxy parameters such as HLR in Kpc and absolute magnitudes. This reduced sample consists of 3078 galaxies, of which 903 have visual classifications (i.e., FPAs). As an added check against any possible stellar contamination there is a low redshift cut of $z_{\rm min}$=0.003.

From investigating the RA-z Spiral distribution we attribute the bi-modality in colour of the Spiral population, found in Chapter 5, to the differences between field and cluster Spirals. With the excess red Spiral galaxies being due to suppressed star-formation in in-falling galaxies.

We have noted in Chapter 5 that there is substantial overlap between all the galaxy classes in any apparent parameter space. We now find that this is true for intrinsic parameters HLR, in Kpc, and $M_{B_{\rm MGC}}$ as well as absolute effective surface brightness. We find that the overall surface brightness-absolute magnitude relation found here is similar to that found in the 2dFGRS by Cross & Driver (2002) and significantly shallower than that found in the HDF by Driver (1999). We also note that the Sabc and Sd/Irr scaling laws are both shallower than that found for Spiral galaxies by de Jong & Lacey (2000) and that this, as suggested by Cross & Driver (2002), may be due to the effects of different colour-magnitude relations for data taken in different filters.

In general we can say that from the scaling laws, the most intrinsically bright galaxies are also the most elliptical, are the smallest at a given magnitude, and consequently have the highest surface brightness at a given magnitude and are also the reddest. The only exceptions to this final point are some very red edge-on Spirals.

We have used the SWML technique to derive morphological LFs, which where then normalised using MGC galaxy counts. We find that the Sabc and Sd/Irr LFs are surprisingly similar but have an excess of bright Sd/Irr and faint Sabc galaxies when compared to what is found by other authors. The faint end of the overall galaxy LF is found to be comprised of a mix of Sabc and Sd/Irr galaxies with the Spirals having a slight dominance. We find that for all intrinsic magnitudes the Spirals are the dominant population.

Our morphological scaling laws confirm what we found in Chapter 5, that it is not possible to reliably distinguish between Sabc and Sd/Irr types. We can therefore only separate out the E/S0 types from the more diskey galaxies. With this in mind we have also compared scaling laws of bulges and disks of spiral galaxies to pure bulge (E/S0) and pure disk (Sd/Irr) galaxies. We find that whilst pure bulges follow the Kormendy relation, as the galaxy becomes more diskey the bulge evolves away from the relation. This implies we are either seeing evolution of the Sersic parameter to lower values at low (B/T) and/or that the bars of Spiral galaxies distort the intrinsic Elliptical nature of bulges.

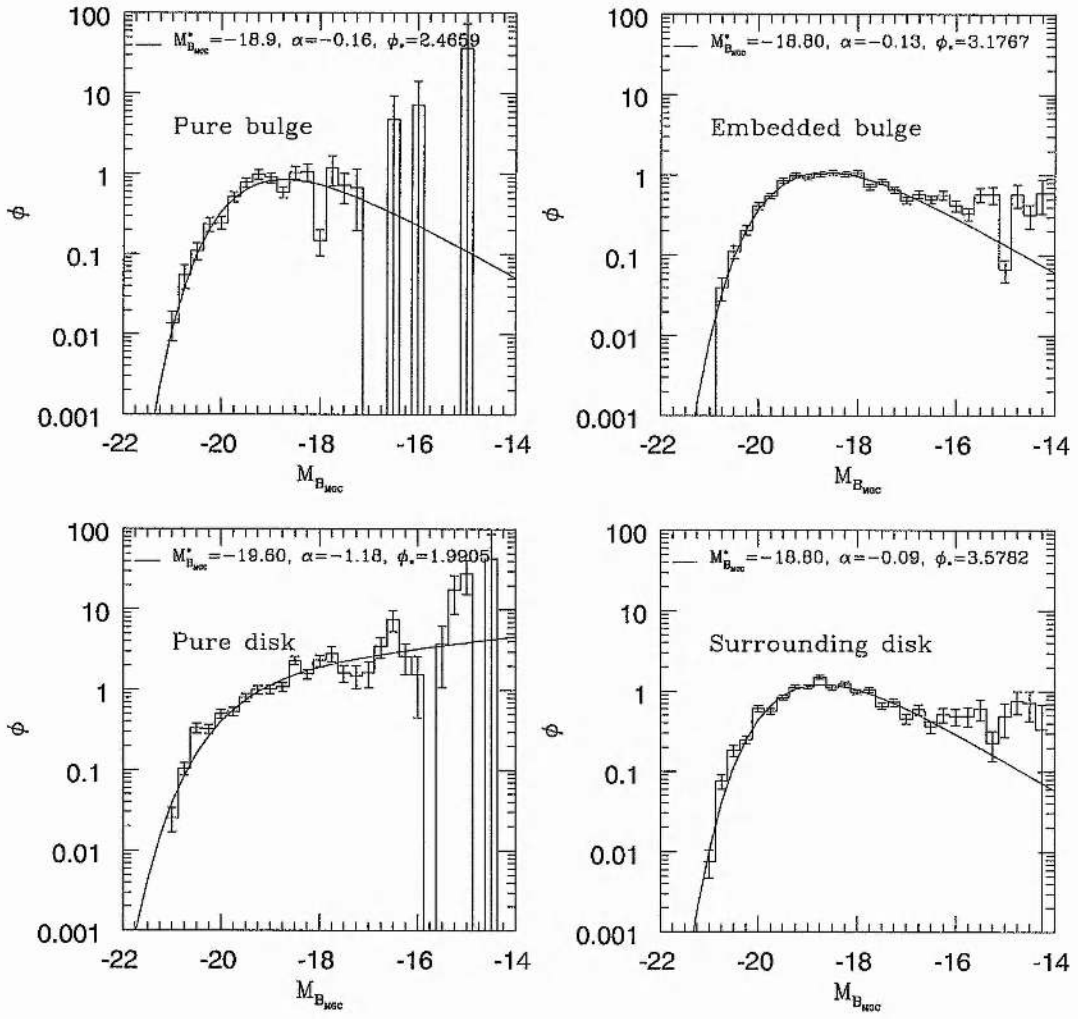

Figure 6.21: SWML LFs (histogram) for pure bulge galaxies (top-left), embedded bulge (top-right), pure disk (bottom-left) and surrounding disks (bottom-right). The solid lines show the best fit Schechter function.

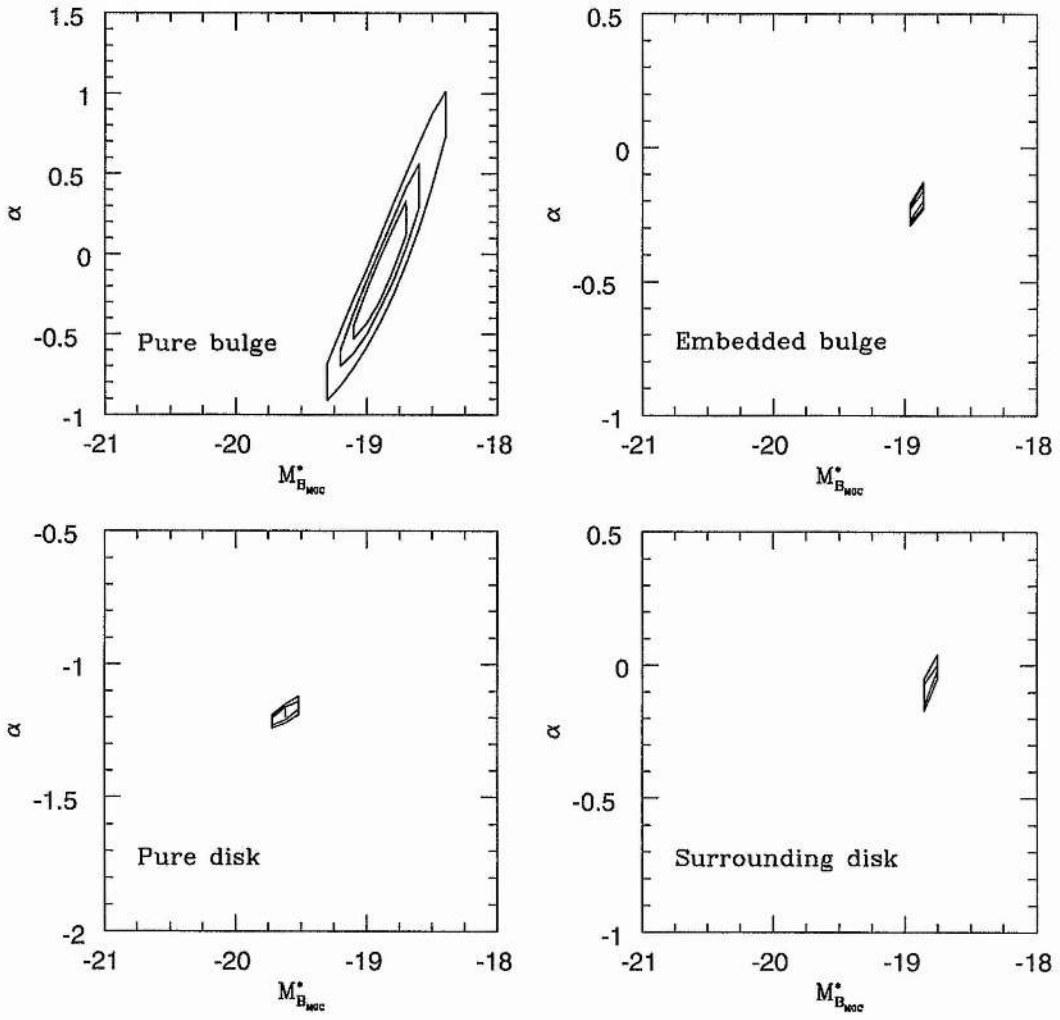

Figure 6.22: SWML M^* and α error ellipses.

CHAPTER 7

Conclusions

In this thesis we have constructed a galaxy catalogue called the Millennium Galaxy Catalogue (MGC). Our aim is to use the MGC to provide a better understanding of the local galaxy population in terms of their apparent and physical parameters and their morphologies. To achieve this the MGC needed to cover a sufficiently wide angle on the sky and go deep enough to be able to sample a representative number of galaxies in terms of galaxy distribution, magnitude and surface brightness.

7.1 The MGC

The MGC is a B-band wide angle CCD based survey comprising of 144 pointings with exposure times of 750s from the Issac Newton Telescope (INT) Wide Field Camera (WFC). It covers a total continuous area of 36 sq deg in a strip in the North Galactic Pole over an RA range of $10^{\rm h}00^{\rm m}$ to $14^{\rm h}48^{\rm m}$ (J2000). All 144 pointings are at DEC $= 00^{o}00'00''$ (J2000) and overlap with adjacent fields (see Fig. 2.2). The MGC covers a magnitude range of $16 < B_{\rm MGC} < 24$ and appears complete down to its detection isophote of 26 mags/sq arcsec (Section. 2.4 and Fig. 2.21). The whole MGC overlaps with the two-degree Field Galaxy Redshift Survey (2dFGRS) and the Sloan Digital Sky Survey Early Data Release (SDSS-EDR, see Fig. 6.1) from which we get both redshifts and colours for objects with $B_{\rm MGC} < 19.5$.

The overlap between MGC fields are used to asses the accuracy of the MGC astrometry by looking at the RA and DEC differences between objects in the overlap regions. We demonstrate the MGC to be positionally accurate to $\pm 0.08''$ in both RA and DEC (Fig. 2.5).

Photometric calibration (Section. 2.2) was done by calculating an initial zero point for each field. This initial zero point was based on a zero point-air mass relation derived using ~ 100 standard stars from 4 Landolt fields observed over a wide range of RA and air mass. We then use the differences in magnitude between objects observed in the overlap regions to tweak the zero points until a minimum χ^2 is achieved. In doing this we are able to arrive at an internal photometric accuracy of ± 0.03 mags (see Fig. 2.7).

Object detection (Section. 2.3.2) is performed using the multi-thresholding algorithm of SEXTRACTOR with a minimum object size of 10 pixels above the 26 mags/sq arcsec isophote. Once an object is detected and deblended we then use the Schlegel & Finkbeiner (1998) dust maps to correct the magnitude for internal Galactic extinction. The STELLARICITY parameter given for each object is then used in its classification. At $B_{\rm MGC} < 20$ mags all obvious stars are classified by their STELLARICITY parameter (STELLARICITY >0.9 for $15< B_{\rm MGC} <20$ and >0.65 for $B_{\rm MGC} <15$, see Fig. 2.17). All other objects were visually inspected and classed as either star, galaxy, asteroid, cosmic ray, CCD defect, diffraction spike or noise. Any poorly deblended objects were fixed by hand

(Table. 2.1). At $B_{\rm MGC} > 20$, star-galaxy classification was performed in a statistical way such that the bright star count gradient remained constant at fainter magnitudes (Section. 2.3.7). However, cosmic rays where identified as having a semi-major axis of $0.7 < \rm b < 1$ pixel at $B_{\rm MGC} < 22.5$ and a FWHM$< 0.9 \times$ *seeing* at $B_{\rm MGC} > 22.5$. As a result of the different star-galaxy classifications the MGC is split into two sub-catalogues. MGC-BRIGHT contains all object at $B_{\rm MGC} \leq 20$ mags and MGC-FAINT all those at $B_{\rm MGC} > 20$ mags. MGC-BRIGHT was then used to define exclusion regions around CCD defects, satellite trails, etc. After removal of objects in the exclusion regions MGC-BRIGHT contains 10,097 galaxies over an area of 31.39 deg^2 whilst MGC-FAINT covers 27.68 deg^2 with 769,965 galaxies.

With the exception of the SDSS, the MGC covers a wider area than other CCD surveys, (see Fig. 1.9) and is of much higher image quality than previous photographic surveys and the SDSS. Although of a smaller area than the SDSS the MGC extends to a much deeper isophoptal limit making it the state-of-the art high-precision photometric survey. The MGC is the principal product of this thesis which has now been publicly released (Liske et al. 2003) and provides the highest quality insight into the local universe ($16 < B_{\rm MGC} < 20$). The full scientific exploitation, of which the subsequent chapters are the first phase, will continue for many years.

7.2 The Galactic Halo

In Chapter 3 we put the MGC to its first use by using the stellar distribution to investigate the structure, specifically the flattening, of the stellar halo surrounding the galaxy. To do this we look at how the stellar distribution changes across the survey (with RA) and compare it to predicted distributions from a galaxy model. The model we use is the 3 component Gilmore (1984) model, comprising of a stellar halo and a thin and thick disk, and is well tested and described in the literature (and Section. 3.2). All variables in the model are held fixed, except the halo flattening, axial ratio (c/a), which was allowed to vary in the range $0.4 \leq (c/a) \leq 0.8$ in increments of 0.01.

Initially, using the full stellar sample, we find the halo signal to be strongest in the range $17 < B_{\rm MGC} < 19$ with an axial ratio of (c/a)=0.54 giving a best fit to the star counts (Table. 3.1). Using the colours from the SDSS-EDR we are able to construct a colour-magnitude diagram (CMD) of our stellar sample (Section. 3.3.2 and Fig. 3.3). From examining the CMD we find the purest halo signal to exist in the F-star region at $B_{\rm MGC} > 18$ mags.

It has been noted in the literature that the process of Hierarchical merging, and in particular any recent mergers, should lead to sub-structure in the halo (as the infalling galaxy is drawn into long tidal threads) (see Section. 3.3.3). Simulations predict that the Galaxy formed from the merging of smaller systems, and that the current satellite galaxies are the surviving remnants of such systems. It is thought that this process is still going on in the outer halo. The signature of clustering in coordinate space, although at fainter magnitudes than used here, has previously been detected in the form of tidal streams from the Sagittarius dwarf spheroidal galaxy in F-star samples. To try to asses the amount of clustering in our stellar sample we employ a variety of different statistical methods: counts-in-cells (Section. 3.3.3.1), angular correlation function (Section. 3.3.3.2) and the Lee 2d test (Section. 3.3.3.3). None of the tests report any solid detection of clustering in either the full or F-star samples. As an aside, we note that for the full stellar sample we find a very flat angular correlation function (Fig. 3.13). This is particularly encouraging as it is what is expected, thus providing independent confirmation that our star galaxy separation (at least at $B_{\rm MGC} < 20$) is accurate (Gilmore, Reid & Hewett 1985).

Although there appears to be no clustering present, we refit the models using only data at $B_{\rm MGC} > 18$ mags and at high Galactic latitude ($b > 0.45°$) to avoid contamination from the thin/thick disks and/or low Galactic latitude ($l < 340°$) to reduce unwanted bulge contributions (Section. 3.3.4). This way we are ensuring we get the purest halo signal

possible. We find that we get the optimum result using all the F-stars at $B_{\rm MGC} > 18$ mags with both the b and l cuts giving an axial ratio of (c/a)=0.56±0.01 (Fig. 3.21).

This study is the first to examine in detail the structural and clustering properties of the Galactic Halo at bright magnitudes. We have been able to derive the halo flattening to within smaller errors than previous authors but failed to detect any substructure as might be predicted by Hierarchical merging. This suggests that any major phase of Hierarchical merging occurred in the early life of the Galaxy.

7.3 The MGC Luminosity function

Before we could arrive at a definitive MGC luminosity function (LF) we first had to derive the galaxy number counts by making a statistical correction for large scale structure (LSS) (Section. 4.2). To do this, the counts from the 2dFGRS within the same area as the MGC were calculated. The number of MGC galaxies in each magnitude bin was then multiplied by the ratio of the 2dFGRS to the 2dFGRS-MGC counts in each bin (Fig. 4.3). This method is not affected by completeness or photometric issues as long as they affect the 2dFGRS-MGC region in the same way as the whole 2dFGRS survey. The down side to this method is that due to the lower magnitude limit of the 2dFGRS no LSS correction can be done at $B_{\rm MGC} > 19.6$ mags. However, as the LSS scaling factor inversely correlates with magnitude and that in the $B_{\rm MGC} = 19.25$ bin it is less than the error bars no LSS correction should be needed. The counts are also corrected for a small (1 to 2%) incompleteness in the cosmic ray counts at $B_{\rm MGC} > 22.5$ mags (see Section. 4.3). At all magnitudes the MGC galaxy counts are fully consistent with those of other authors (Table. 4.1 and Fig. 4.6). As the MGC counts cover the range $16 < B_{\rm MGC} < 24$ they provide a definite connection between the photographic and CCD counts. In the bright region the MGC counts are consistently higher than the APM, ruling out the need for strong local evolution as previously advocated.

We have used the MGC counts to renormalise the predicted counts (and hence ϕ_*) from the LFs of other authors (Tables. 4.2 and 4.3). We use the favoured $\Omega_m = 0.3$, $\Omega_\Lambda = 0.7$ cosmology as well as appropriate k and e corrections. Once renormalised we find that the predicted counts of the 2dFGRS and SDSS-EDR provide the best fits when renormalised by factors of 1.06 and 0.71 respectively. Using all the renormalised LF's we find a mean luminosity density of $\overline{j_{b_J}} = 1.88 \times 10^8 h L_\odot$ Mpc^{-3}. Finally, by taking M^* to be the mean of the 2dFGRS and SDSS-EDR, we are able to use the MGC counts alone constrain both ϕ^* and α (Section. 4.5.5). We find the optimal MGC LF parameters to be $\overline{M^*}_{B_{\rm bJ}} = -19.715 + 5\log h$, $\alpha = -1.23$ and ϕ_*=0.0158h^3.

As the MGC represents the prime galaxy survey to-date, providing the definitive link between photographic and CCD data, the counts and Schechter function parameters presented here supersede those from all previous data for the local universe. We have also firmly established that there is no need invoke strong local evolution and/or local voids (in the NGP).

7.4 Galaxy morphologies

The software package GIM2D has been implemented in order to obtain structural parameters to all MGC-BRIGHT galaxies in the range $16 < B_{\rm MGC} < 20$. GIM2D uses 3 postage stamps: a galaxy image, a mask (or segmentation) image of the galaxy and a PSF image at the galaxy coordinates to derive various structural parameters such as bulge-to-total light ratio, exponential disk scale length, bulge effective radii and half-light radii etc. The mask image is produced as a byproduct of SEXTRACTOR and the PSF from DAOFIND and

DAOPHOT IRAF routines. To derive these parameters we have, in the first instance, constrained the GIM2D metropolis algorithm to fit a de Vaucouleurs bulge and exponential disk profile (Section. 5.1).

We find that GIM2D is able to accurately reproduce galaxy profiles down to $B_{\rm MGC} = 19.5$ mags and $\mu_{app} = 26$ mags/sq arcsec (Section. 5.2, Figs. 5.9, 5.10 and 5.11). However, we have found that for a substantial fraction ($\sim 38\%$) of the galaxies, GIM2D has profiled them as pure disks with a (B/T) of *exactly* zero (Section. 5.2.6 and Fig. 5.12). This population of galaxies have profiles that are substantially flatter than pure exponential, so in order to achieve the best possible fit GIM2D was forced to remove the bulge component from the model, hence (B/T)=0 (Fig 5.14). It is for this reason we that call this population of galaxies Flat Profile Anomalies (FPA).

By using cuts in (B/T) we are able to assign broad Hubble types to the galaxies, whilst initially keeping the FPAs as a separate population. By restricting ourselves to galaxies at $B_{\rm MGC}$ <19 and combining MGC-BRIGHT with SDSS-EDR we are able to get colours for 3342 galaxies (Section. 5.3, Table. 5.2). We find that, as expected, E/S0 galaxies are red and Sd/Irr galaxies are blue. However, the Sabc galaxies are bi-modal with both blue and red peaks and the FPAs are dominated by very blue galaxies (Fig. 5.16).

Investigating the FPA population (Section. 5.4) we find that they are distributed across the magnitude range and are a mixture of Spiral and Irregular galaxies. This, together with their blue colour, leads us to believe that the FPAs are Spiral and Irregular galaxies that are under-going rapid star formation. This has caused an increase in the azimuthally averaged disk profile, thereby flattening the overall profile. We note here that it may be worthwhile re-imaging these galaxies in near-IR photometric bands as they should be more robust to star-formation. However, to try to further understand the FPA galaxy population we re-ran GIM2D over a sample of FPA galaxies with redshifts (see below) using a Sersic only profile (GIM2D does not allow for two separate Sersic profiles to be fitted to the bulge and disk). We find that in most cases this substantially improves the fit to the galaxies profile (Fig. 5.21) and that the galaxies are clustered about a median Sersic index of $n = 0.62$ with a standard deviation of $\sigma = 0.2$ (Fig. 5.22). This is surprisingly similar to that found for a sample FPA galaxies found in the Hubble Deep Field and may therefore be an intrinsic property of star-forming (FPA) galaxies. We find that there is no relation between the Sersic index and either apparent magnitude, surface brightness, redshift, absolute magnitude or colour and that it cannot be used to discriminate between FPA-Spiral and FPA-Irregulars.

Having visually redistributed the FPA galaxies (Table. 5.3 and Fig 5.28), we find that the local universe to $B_{\rm MGC} < 19$ is made up of 28.10% E/S0 galaxies, 39.64% Sabc galaxies and 31.37% Sd/Irr galaxies. We find that the Sabc fractional population increases at bright magnitudes whilst the E/S0 and Sd/Irr both vary little with apparent magnitude. The Sabc fractions show an increase with decreasing surface brightness, and the E/S0 population show the expected decline with lowering surface brightness. The Sd/Irr population fractions initially rise with decreasing surface brightness distribution but then flatten out at around μ_{app}=23.25 mags/sq arcsec (Fig. 5.29). We have derived morphological number counts (Table. 5.4 and Fig. 5.30) and found that once again one does not need to renormalise either the E/S0, Sabc or Sd/Irr counts for them to match with deeper counts.

By combining the MGC with GIM2D (currently the best software available for obtaining structural parameters) we have provided its first proper test for large samples of local galaxies. As such the population fractions and morphological number counts presented here, we deem to be the most accurate available to the community for use within cosmological models. We have clearly established that the traditional exponential+de Vaucouleurs profile is insufficient to describe a substantial fraction of the galaxy population and that one really needs to consider a double Sersic profile.

7.5 Intrinsic galaxy parameters

After matching the MGC-BRIGHT GIM2D'd galaxies to the 2dFGRS and SDSS-EDR we find that we have a sample of 3078 galaxies with photometric and structural parameters, as well as colours and redshifts (Table. 6.2). This sample is 90.7% complete in the magnitude range $16 < B_{\rm MGC} < 19$ and this completeness is constant with both magnitude and colour but drops off at both low and high surface brightness (Fig. 6.3). The drop-off in completeness with surface brightness we attribute to surface brightness selection effects in the 2dFGRS and SDSS-EDR.

Looking at how the galaxies are distributed in redshift we find that red Spiral galaxies are more clustered than blue Spirals (Fig. 6.6). From this we suggest that the red Spiral population is the result of suppressed star formation in galaxies infalling into cluster environments.

Using the redshifts, and for simplicity an Einstein de Sitter cosmology, we are able to convert apparent magnitudes into absolute magnitudes, correct surface brightness for cosmological dimming and convert angular sizes into physical units of Kpc. Looking at how (B/T) is distributed, we find that both bulge and disk dominated galaxies vary little with absolute magnitude, but that both the bulge and disk dominated galaxies tend to lower values of (B/T) with decreasing surface brightness, albeit at different rates (Fig. 6.7).

The size-absolute magnitude scaling laws (Section. 6.3.1 and Fig. 6.9) of the Sabc and Sd/Irr galaxies are very similar whilst the E/S0 galaxies follow a much steeper relation. In constructing a BBD (Section. 6.3.2 and Fig. 6.10) we find an overall surface brightness-magnitude relation that is consistent with that found in the 2dFGRS. We find that the E/S0 population occupy a distinct region from the rest of the galaxy population and that the surface brightness-magnitude relation is distinct from that of the Sabc and Sd/Irr galaxies which show too much scatter to be able to reliably discern separate scaling laws. We find that the Sabc and Sd/Irr galaxies follow similar colour-absolute magnitude scaling laws and that in all cases the colour-absolute magnitude distributions are consistent with a hierarchical formation scenario (Section. 6.3.3 and Fig. 6.11).

Given that we cannot reliably separate the Sabc and Sd/Irr galaxies, in Section. 6.4 we investigate the individual bulge and disk components of galaxies, ignoring the FPAs due to their unreliable bulge and disk parameters. We find that pure bulge and disk galaxies follow distinctly different scaling laws, with the pure bulges following the Kormendy size-magnitude relation of Elliptical galaxies. However, as (B/T) decreases the size-magnitude scaling law moves away from the Kormendy relation to a much flatter relation (Fig. 6.15). Essentially the bulges of galaxies cease to look like Ellipticals as the galaxy becomes more disky. We suggest that this is the result of an evolution of the Sersic index from $n = 4$ at high (B/T) to $n < 4$ at lower (B/T) possibly, in some cases, caused by the introduction of bars to the bulges of Spiral galaxies. Further progress is hampered until software capable of double-Sersic profile fitting is developed.

7.5.1 Morphological LFs

We have used a StepWise Maximum Likelihood (SWML) technique to estimate total and morphological LFs. These are then normalised using the MGC total and morphological counts (Section. 6.5). The total LF is similar, in M^* and ϕ_*, to that derived in the traditional way in Chapter 4 (Fig. 6.20). The inconsistency in α we attribute to the effects of combining a number of redshift surveys with differing limits. It is therefore of the up-most importance to complete the MGC-z survey. We find that the Sabc and Sd/Irr are similar but with the Spirals having higher normalisation. The SWML technique is also used to derive LFs for bulges and disks (Section. 6.6). Whilst the pure bulges and pure disks have substantially different LFs, there is a definite similarity between the LFs of embedded bulges and surrounding disks (Fig. 6.21).

To summarise, we have found that E/S0 galaxies can be identified using magnitude,

surface brightness and colour, and that Sabc and Sd/Irr galaxies are inseparable. Looking at the bulges and disks of galaxies we find that whilst bulges initially follow a Kormendy relation, as (B/T) decreases some move away to a flatter relation similar to that of pure disks. From this we conclude that we are either seeing evolution of the Sersic parameter to lower values at low (B/T) and/or that the bars of Spiral galaxies distort the intrinsic Elliptical nature of bulges.

From adding redshift and colour information to our structural parameters we construct the most detailed and deepest local galaxy catalogue currently available. As a result of this we have established that the currently favoured Hubble types can not be relied upon to describe galaxies with any real physical meaning, as there is no clear distinction between the later types in any intrinsic parameter space. We find for the first time that bulges of galaxies only follow the Kormendy relation whilst the bulge is the dominant feature of the galaxy, and that as the disk grows relative to the bulge they evolve towards a much flatter relation. This finding makes a strong case that in-order to understand galaxies one must be able to perform proper bulge-disk decovolution and take into account a galaxies component parts.

7.6 Future work

There is still no satisfactory way to discriminate between Sabc and Sd/Irr galaxies. Furtherer investigation into this will be carried out by re-profiling some (the FPA) or all of the galaxies using two separate Sersic profiles to model the bulge and disk separately. By doing this we will achieve accurate profiles and retain the (B/T) parameter. Another possible solution lies with colours. If, as we believe, the profile flatness in the Spirals is a result of rapid star formation, then colour gradients with a blue rise in the outer disk should be observable for the FPA-Spirals, whilst the FPA-Irregular colour gradients will be flat.

It would also be worthwhile re-imaging some or all of the MGC in the near-IR (H-band). This would be advantageous as the H-band is more robust to star-formation and free from problems of dust and inclination. Because of this near-IR images of galaxies are much smoother than their B-band counterparts, see Fig. 7.1, which makes them easier to deconvolve into their bulge and disk components. Unlike the B-band, which is dominated by the short lived giant O and B stars, the H-band provides a good tracer of a galaxies dynamical mass. Gavazzi, Pierini & Boselli (1996) have demonstrated that for late type galaxies the best connection between luminosity and dynamical mass is in the H-band. This, they argue, is because the H-band observes the peak of the black-body emission from the main stellar population as opposed to focusing on the transient star-burst population of the B-band. Therefore the H-band traces both the dynamical mass as well as the shape of the potential well.

One other morphological method we have yet to test is the use of ANNs. Whilst the ANN is sure to be able to provide fairly consistent ($\sim \pm 1$ T-type) morphologies, they offer no real scientific advancement. As ANNs are essentially a speeded up human-eye we gain no quantitative information on the physical properties of the different groups of galaxies. However, because ANNs are trained on a set of visually classified galaxies the T-types (for the FPAs at least) may not be reliable. This is especially true for faint and/or low surface brightness galaxies, as we have found it extremely difficult to confidently visually classify galaxies at $B_{\rm MGC} > 18$ mags.

Further analysis of galaxy bulge and disk parameters should also be carried out in order to investigate the apparent evolution of the bulge away from the Kormendy relation. This may lead to a bulge classification scheme akin to that of the one proposed by Kormendy & Bender (1996) for Elliptical galaxies, which could be used to distinguish between the late type galaxy classes.

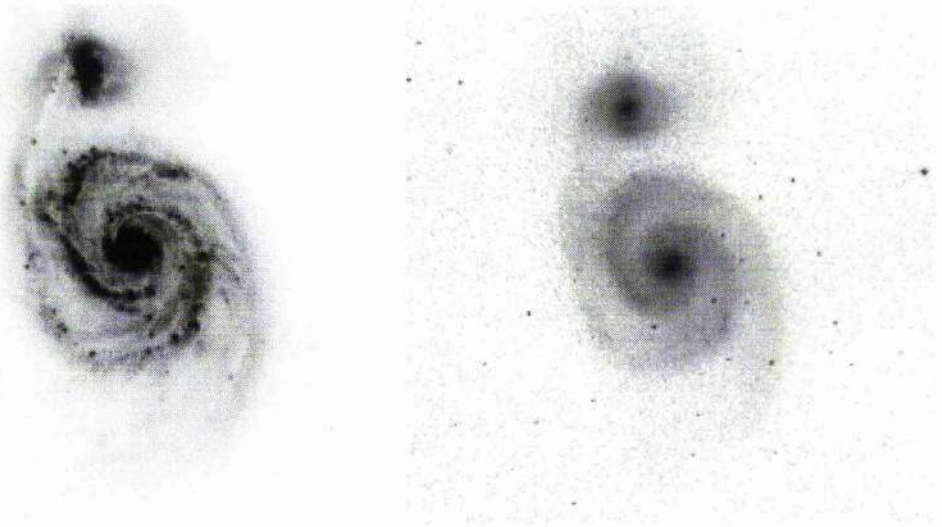

Figure 7.1: The galaxy M51 observed in the B (left) and H (right) bands. Imaged reproduced from the NASA/IPAC Extragalactic Database (NED, http://nedwww.ipac.caltech.edu/).

REFERENCES

Abraham R., Valdes F., Yee H., van den Bergh S., 1994, ApJ, 432, 75

Abraham R., Tanvir N., Santiago B., Ellis R., Glazebrook K., van den Bergh S., 1996, MNRAS, 279, 47

Alonso M. V., da Costa L. N., Latham D., P.S. P., Milone A., 1994, AJ, 108, 1987

Arnouts S., de Lapparent V., Mathez G., Mazure A., Mellier Y., Bertin E., Kruszewski A., 1997, A&AS, 124, 163

Arnouts S., D'Odorico S., Cristiani S., Zaggia S., Fontana A., 1999, A&A, 341, 641

Babul A., Rees M., 1992, MNRAS, 255, 246

Bachall J., Soneira S., 1981, ApJS, 47, 353

Bachall J., Soneira S., 1984, ApJS, 55, 67

Bahcall J., 1986, ARA&A, 24, 577

Balogh M., Couch W., Smail I., Bower R., Glazebrook K., 2002, MNRAS, 335, 10

Bertin E., Arnouts S., 1996, A&AS, 117, 393

Bertin E., Dennefield M., 1997, A&A, 317, 43

Bertin E. SExtractor users guide v2.0. 2002

Binggeli B., 1993, in Meylan G., Prugniel P., eds, ESO/OHP Workshop on Dwarf Galaxies. p. 13

Blair M., Gilmore G., 1982, PASP, 94, 742

Blanton M. et al., 2001, AJ, 121, 2358

Blanton M. et al., 2002, submitted

Broadhurst T., Ellis R., Shanks T., 1988, MNRAS, 235, 827

Brown W., Geller M., Fabricant D., Kurtz M., 2001, AJ, 122, 714

Bruzual A., Charlot S., 1993, ApJ, 405, 538

Cabanac R., de Lapparent V., Hickson P., 200, A&A, 364, 349

Capaccioli M., 1989, in Corwin H., Bottinelli L., eds, The World of Galaxies. Springer-verlag, Berlin, p. 208

Chen B. et al., 2001, ApJ, 553, 184

Cohen S., Windhorst R., Odewahn S., Chiarenza C., Driver S., 2002, submitted

Cole S., Lacey C., Baugh C., Frenk C., 2000, MNRAS, 319, 168

Colless M. et al., 2001, MNRAS, 328, 1039

Collins C., Heydon-Dumbelton N., MacGillivray H., 1989, MNRAS, 238, 379

Corwin H., de Vaucouleurs A., de Vaucouleurs G., 1985, Southern Galaxy Catalogue. University of Texas, Austin

Couch W., Jurcevic J., Boyle B., 1993, MNRAS, 264, 241

Crone M., Evrard A., Richstone D., 1996, ApJ, 467, 486

Cross N., Driver S., 2002, MNRAS, 329, 87

Cross N. et al., 2001, MNRAS, 324, 825

Cross N., Driver S., Liske J., D.J. L., 2003, in preperation

Cross N., 2002, PhD thesis, University of St Andrews, St Andrews, Scotland

Davis L. A Reference Guide to the IRAF/DAOPHOT Package. IRAF Programming Group, National Optical Astronomy Observatories, 1994

de Jong L., Lacey, 2000, ApJ, 545, 781

de Vaucouleurs G., de Vaucouleurs A., Corwin J., 1976, The Second Reference Catalogue of Bright Galaxies. (Austin: University of Texas Press)

de Vaucouleurs G., de Vaucouleurs A., Corwin H., Buta R., G. P., Fonque P., 1991, The Third Reference Catalogue of Bright Galaxies. Springer, Berlin

de Vaucouleurs G., 1959, Handbuch der Physik, 53, 311

Disney M., 1976, Nat, 263, 573

Djorgovski S., Davis M., 1987, ApJ, 313, 59

Djorgovski S., 1985, PhD thesis, University of California, Berkeley

Doinidis S., Beers T., 1989, ApJ, 340, 57

Dressler A. et al., 1997, ApJ, 490, 577

Dressler A., 1980, ApJ, 236, 351

Drinkwater M., Phillips S., Gregg M., Parker Q., Smith R., Davies J., Jones J., E.M. S., 1999, ApJ, 511, 97

Driver S., Cross N., 2000, in Kraan-Korteweg R., Henning P., Andernach H., eds, Mapping the Hidden Universe. p. 319

Driver S., Phillipps S., 1996, ApJ, 469, 529

Driver S., Phillipps S., Davies J., Morgan I., Disney M., 1994, MNRAS, 266, 155

Driver S., Windhorst R., Griffiths R., 1995, ApJ, 453, 48

Driver S., 1999, ApJ, 526, 69

Efstathiou G., Ellis R., Peterson B., 1988, MNRAS, 232, 431

Ellis R., Colless M., Broadhurst T., Heyl J., Glazebrook K., 1996, MNRAS, 280, 235

Ferguson H., Babul A., 1998, MNRAS, 296, 585

Fitchett M., Webster R., 1987, ApJ, 317, 653

Fitchett M., 1988, MNRAS, 230, 161

Freeman K., 1970, ApJ, 160, 811

Fukugita M., Ichikawa T., Gunn J., Doi M., Shimasaku k., Schnider D., 1996, AJ, 111, 1748

Gardner J., Sharples R., Carrasco B., Frenk C., 1996, MNRAS, 282, 1

Gavazzi G., Pierini D., Boselli A., 1996, A&A, 312, 397

Gilmore G., Reid I., 1983, MNRAS, 202, 1025

Gilmore G., Wyse R., 1985, AJ, 90, 10

Gilmore G., Reid I., Hewett P., 1985, MNRAS, 213, 257

Gilmore G., Wyse R., Jones J., 1995, AJ, 109, 1095

Gilmore G., Wyse R., Kuijken K., 1989, ARA&A, 27, 55

Gilmore G., Wyse R., Norris J., 2002, ApJ, 574, L39

Gilmore G., 1984, MNRAS, 207, 223

Grey N., Taylor M., Privett G. ESP - Extended Surface Photometry, V0.10-8, Users manual. Starlink, Rutherford Appleton Laboratory, 2002

Groth E., Peebles P., 1977, ApJ, 217, 385

Gunn J. et al., 1998, AJ, 116, 3040

Hambly N., Irwin M., MacGillivray H., 2001, MNRAS, 326, 1279

Hartwick F., 1987, in Gilmore G., Carswell B., eds, The Galaxy. Reidel, Dordrecht, p. 281

Helmi A., White S., 1999, MNRAS, 307, 495

Helmi A., White S., de Zeeuw P., Zhao H.-S., 1999, Nat, 402, 53

Hewett P., 1983, PhD thesis, University of Edinburgh, Edinburgh, Scotland

Heydon-Dumbleton N., Collins C., MacGillivary H., 1989, MNRAS, 238, 379

Heyl J., Colless M., Ellis R., Broadhurst T., 1997, MNRAS, 285, 613

Huang J.-S. et al., 2001, A&A, 368, 787

Hubble E., 1925, ApJ, 62, 409

Hubble E., 1926a, ApJ, 63, 236

Hubble E., 1926b, ApJ, 64, 321

Hubble E., 1929, ApJ, 69, 103

Hubble E., 1934, ApJ, 79, 8

Hubble E., 1936a, ApJ, 84, 270

Hubble E., 1936b, ApJ, 84, 517

Hubble E., 1939, The Realm of the Nebulae. (New Haven: Yale University Press)

Ibata R., Gilmore G., Irwin M., 1994, Nat, 370, 194

Ibata R., Irwin M., Cambresy L., 2002, MNRAS, 332, 921

Ibata R., Wyse R., Gilmore G., Irwin M., Suntzeff N., 1997, AJ, 113, 634

Ibata R., Irwin M., Lewis G., Stolte A., 2001, ApJ, 547, 133

Impey C., Bothun G., 1997, ARA&A, 35, 2671

Infante L., Pritchet H., Quintana H., 1986, AJ, 91, 2

Irwin M., Lewis J., 2001, New Astronomy Review, 45, 105

Johnston K., Hernquist L., Bolte M., 1996, ApJ, 465, 278

Johnston K., Majewski S., Siegel M., Reid N., Kunkel W., 1999, AJ, 118, 1719

Jones L., Fong R., Shanks T., Ellis R., Peterson B., 1991, MNRAS, 249, 481

Kent S., 1985, ApJ, 59, 115

Kirshner R., Oemler A., Schechter P., 1978, AJ, 83, 1549

Koo D., Kron R., 1992, ARA&A, 30, 613

Koo D., 1986, ApJ, 311, 651

Kormendy J., Bender R., 1996, ApJ, 464, 119

Kormendy J., 1977, ApJ, 218, 333

Kron R., 1980, ApJS, 43, 305

Kummel M., Wagner S., 2000, A&A, 353, 867

Kummel M., Wagner S., 2001, A&A, 370, 384

Landolt A., 1992, AJ, 104, 340

Lauberts A., Valentijn E., 1989, The surface photometry of the ESO-Uppsala galaxies. Garching: European Southern Observatory(ESO)

Lauberts A., 1982, ESO/Uppsala survey of the ESO(B) atlas. Garching: European Southern Observatory(ESO)

Lee K., 1979, J. Am. statist, Ass, 74, No. 367, 708

Lewis I. et al., 2002, MNRAS, 334, 673

Lilly S., Tresse L., Hammer F., Crampton D., Le Ferve O., 1995, ApJ, 455, 108

Liske J., Lemon D., Driver S., Cross N., Couch W., 2003, submitted

Loveday J., Peterson B., Efstathiou G., Maddox S., 1992, MNRAS, 390, 338

Lupton R. et al., 2002, in prepertion

Maddox S., Efstathiou G., Sutherland W., 1996, MNRAS, 283, 1227

Maddox S., Sutherland W., Efstathiou G., Loveday J., Peterson B., 1990b, MNRAS, 247, 1

Maddox S., Efastathiou G., Sutherland W., Loveday J., 1990, MNRAS, 243, 692

Madgwick D. et al., 2002, MNRAS, 333, 133

Marinoni C., Monaco P., Giuricin G., Costantini B., 1999, ApJ, 521, 50

Marleau F., Simard L., 1998, ApJ, 507, 10

Marzke R., Da Costa L., 1997, ApJ, 113, 185

Marzke R., Geller M., Huchra J., Corwin Jr H., 1994, ApJ, 108, 437

Marzke R., Da Costa L., Pellegrini P., Willmer N., M.J. G., 1998, ApJ, 503, 617

Mateo M., 1998, ARA&A, 36, 435

Mattig W., 1958, *Astron. Nachr*, 284, 109

Metcalfe N., Fong R., Shanks T., 1995, MNRAS, 274, 769

Metcalfe N., Shanks T., Fong R., Jones R., 1991, MNRAS, 249, 498

Metcalfe N., Fong R., Shanks T., Fong R., Roche N., 1995, MNRAS, 273, 257

Metcalfe N., Fong R., Shanks T., Campos A., McCracken H., Fong R., 2001, MNRAS, 323, 795

Metropolis N., Rosenbluth A., Rosenbluth M., Teller A., Teller E., 1953, Journal of Chemical Physics, 21, 1087

Morrison H., 1993, AJ, 106, 578

Naim A. et al., 1995a, MNRAS, 274, 1107

Naim A., Lahav O., Sodre Jr L., Storrie-Lombardi M., 1995b, MNRAS, 275, 567

Nakamura O., Fukugita M., Yasuda N., Loveday J., Brinkmann J., Schneider D., Shimasaku K., Subbarao M., 2002, submitted

Newberg H. et al., 2002, ApJ, 569, 245

Nilson P., 1973, Acta Universitatis Upsaliensis. Nova Acta Regiae Societatis Scientiarum

Upsaliensis, Uppsala Astronomiska Observatoriums Annaler, Uppsala: Astronomiska Observatorium

Norberg P. et al., 2002, MNRAS, 336, 907

Norris J., Ryan S., 1991, ApJ, 340, 403

Odewahn S., Stockwell E., Pennington R., Humphreys R., Zumach W., 1992, AJ, 103, 318

Odewahn S., Humphreys R., Aldering G., Thurmes P., 1995, PASP, 105, 1354

Odewahn S., Windhorst R., Driver S., Keel W., 1996, ApJ, 472, 13

Paradoni I. et al., 1999, A&A, 345, 448

Paturel G., Fouque P., Bottinelli L., Gouguenheim L., 1989, A&AS, 80, 299

Peacock J., 1999, Cosmological Physics. Cambridge University Press.

Pearce F., Jenkins A., Frenk C., White S., Thomas P., Couchman H., Peacock J., Efstathiou G., 2001, MNRAS, 326, 649

Peebles P., 1969, ApJ, 221, 1039

Peterson B., Ellis R., Efstathiou G., Shanks T., Bean A., Fong R., Zen-Long., 1986, MNRAS, 221, 233

Phillipps S., Jenkins C., Dopita M., Sadler E., Binette E., 1996, AJ, 91, 1062

Phillips S., Driver S., 1995, MNRAS, 274, 832

Pimbblet K., Smail I., Edge A., Couch W., O'Hely E., 2001, MNRAS, 327, 588

Ratcliffe A., Shanks T., Parker Q., Broadbent A., Watson F., Oates A., Collins C., Fong R., 1998, MNRAS, 300, 417

Reid A., Majewski S., 1993, ApJ, 409, 635

Reyle C., Robin A., 2001, A&A, 373, 886

Rhee G., van Haarlem M., Katgert P., 1991, A&A, 246, 301

Sadage A., Tamman G., Yahil A., 1979, ApJ, 232, 252

Sandage A., 1961, The Hubble Atlas of Galaxies. (Washington, DC: Carnegie Inst. Washington)

Sandage A., 1998, in Livio M., Fall S., Madau P., eds, The Hubble Deep Field. p. 1

Schechter P., 1976, ApJ, 203, 297

Schlegel D., Finkbeiner D., 1998, ApJ, 500, 525

Seares F., Kapteyn J.C & Van Rhijn P., 1930, The Mount Wilson Catalogue of Photometric Magnituds in Selected Areas 1-139. Carnegie Inst. Washington, Pub. No.402.

Searl L., Zinn R., 1978, ApJ, 225, 3575

Sersic J., 1968, Atlas de Galaxies Australes (Cordoba: Observatoro Astronomica)

Shanks T., Fong R., Ellis R., MacGillivray H., 1980, MNRAS, 192, 209

Shanks T., Stevenson P., Fong R., MacGillivray H., 1984, MNRAS, 206, 767

Silk J., Wyse R., 1993, Phys. Rep, 231, 295

Simard L. et al., 2002, ApJ, 142, 1

Simard L., 1998, in Albrecht R., Hook R., Bushouse H., eds, Astronomical Data Analysis Software Systems. p. 108

Sprayberry D., Impey C., Irwin M., Bothun G., 1997, ApJ, 482, 104

Stetson P., 1987, PASP, 99, 191

Stoughton C. et al., 2002, ApJ, 123, 485

Strauss M. et al., 2002, in press, astro-ph/0206225

Tran K.-V. GIM2D V2.2.0 Cookbook. 2000,
http://nenuphar.as.arizona.edu/simard/gim2d/gim2d.html

Tully R., Fisher J., 1977, A&A, 54, 661

Turner E., 1979, ApJ, 231, 645

Tyson J., 1988, AJ, 96, 1

Unavane M., Wyse R., Gilmore G., 1996, MNRAS, 278, 727

van den Bergh S., 1976, ApJ, 206, 883

Vivas A. et al., 2001, ApJ, 554, 33

Vorontsov-Vel'Yaminov B., Arkhipova V., 1962 to 1974, Morphological catalogue of galaxies. Vol. 1-5. State University Moscow

West M., Oemler Jr A., Dekel A., 1998, ApJ, 327, 1

White S., Frenk C., 1991, ApJ, 379, 52

White S., 1985, ApJ, 294, L99

White S., 1996, in Schaeffer R.and Silk J., Spiro M., Zinn-Justin J., eds, Cosmology and Large Scale Structure. Les Houches Session LX. Elsevire, Amsterdam, p. 349

Wielen R., 1974, Highlights of Astronomy. Vol. 3. Dordrecht: D. Reidel

Williams R. et al., 1996, AJ, 122, 1335

Willmer C., 1997, AJ, 114, 3

Wyse R., Gilmore G., 1989, in G.Contopoulous, ed, Comments on Astronomy, Vol3. p. 31:3, 135

Yanny B. et al., 2000, AJ, 540, 825

Yasuda N. et al., 2001, AJ, 122, 1104

York D. et al., 2000, AJ, 120, 1579

Zhang B., Wyse R., Stiavelli M., Silk J., 2002, MNRAS, 332, 647

Zhao H.-S., Johnston K., Hernquist L., Spergel D., 1999, A&A, 348, 49

Zucca E. et al., 1997, A&A, 326, 477

Zwicky F., Wild P., Karpowicz M., Kowal C., 1961 to 1968, Catalogue of Galaxies and of Clusters of Galaxies. Vol. 1-6. Pasadena: California Institute of Technology

APPENDIX A

MGC Parameters

Table A.1: A description of the basic MGC catalogue parameters. The parameters are listed in the order they appear for each object. Note that the parameters QUALITY and HLRADIUS are not included in MGC-FAINT.

Parameter Name	Description	Unit
OBJECT	Object ID number	
MGC	MGC field number	
X_IMAGE	Object position along x axis	pixel
Y_IMAGE	Object position along y axis	pixel
MAG_ISO	Isophotal magnitude	mag
MAG_ISO_DC	Dust corrected isophotal magnitude	mag
MAG_ISOCOR	Corrected isophotal magnitude	mag
MAG_ISOCOR_DC	Dust corrected corrected isophotal magnitude	mag
MAG_AUTO	Kron-like elliptical aperture magnitude	mag
MAG_AUTO_DC	Dust corrected Kron-like aperture magnitude	mag
MAG_BEST	Best of MAG_AUTO and MAG_ISOCOR	mag
MAG_BEST_DC	Dust corrected best MAG_BEST	mag
MAGERR_BEST	RMS error for MAG_BEST	mag
BACKGROUND	Background at centroid position	count
THRESHOLD	Detection threshold above background	count
ISOAREA_IMAGE	Isophotal area above analysis threshold	$pixel^2$
ALPHA_J2000	Right ascension of barycenter (J2000)	deg

continued on next page

continued from previous page

Parameter Name	Description	Unit
DELTA_J2000	Declination of barycenter (J2000)	deg
ALPHA_B1950	Right ascension of barycenter (B1950)	deg
DELTA_B1950	Declination of barycenter (B1950)	deg
A_IMAGE	Profile RMS along major axis	pixel
B_IMAGE	Profile RMS along minor axis	pixel
THETA_IMAGE	Position angle	deg
ERRA_IMAGE	RMS position error along major axis	pixel
ERRB_IMAGE	RMS position error along minor axis	pixel
ISOAREA_WORLD	Isophotal area above analysis threshold	deg^2
FLAGS	Extraction flags	
FWHM_IMAGE	FWHM assuming a Gaussian core	pixel
ELLIPTICITY	1 - B_IMAGE/A_IMAGE	
CLASS_STAR	Stellaricity	
CCD	CCD number	
MGC_CLASS	Classification parameter	
QUALITY	Quality/reliability parameter	
HLRADIUS	Major axis of the half-light ellipse	pixel

APPENDIX B

Derivations

B.1 Schechter function in magnitudes

We now convert the Schechter function, Eqn B.1, into its more useful magnitude form.

$$\Phi(L)dL = \phi_*(L/L_*)^{\alpha} exp(-L/L_*)dL, \tag{B.1}$$

Starting from the relationship

$$L\alpha 10^{-0.4M} \tag{B.2}$$

we can say that

$$\frac{L}{L_*} = 10^{-0.4(M-M_*)}, \tag{B.3}$$

which, differentiating w.r.t absolute magnitude, gives us

$$\frac{dL}{dM} = \frac{\delta\left(10^{-0.4}(M-M_*)\right)}{\delta M} \tag{B.4}$$

and can be rewritten as

$$\frac{dL}{dM} = \frac{\delta\left(e^{\ln\left[10^{0.4(M_*-M)}\right]}\right)}{\delta M}. \tag{B.5}$$

We now note that as

$$\log X = \frac{\ln X}{\ln 10}, \tag{B.6}$$

Eqn. B.5 becomes

$$\frac{dL}{dM} = \frac{\delta\left(e^{0.4(M_*-M)\ln 10}\right)}{\delta M}. \tag{B.7}$$

Completing the differentiation we get

$$\frac{dL}{dM} = 0.4 \ln 10 e^{0.4(M_*-M)\ln 10} \tag{B.8}$$

which can be rearranged to give

$$dL = 0.4 \ln 10 \left(10^{0.4(M_*-M)}\right) dM. \tag{B.9}$$

Substituting Eqn. B.3 and Eqn. B.9 into Eqn. B.1 we get

$$\Phi(M)(dM) = \phi_* 10^{0.4(M_*-M)\alpha} e^{-10^{0.4(M_*-M)}} 0.4 \ln 10 \; 10^{0.4(M_*-M)} dM, \tag{B.10}$$

which simplifies into its final form

$$\Phi(M)(dM) = 0.4 \ln 10 \; \phi_* 10^{0.4(M_*-M)(\alpha+1)} e^{-10^{M_*-M}} dM. \tag{B.11}$$

B.2 Distance modulus

We now derive the distance modulus equation. Starting with the relationship between apparent magnitude, m, and flux, f:

$$f \; \alpha \; 10^{-0.4m}, \tag{B.12}$$

and as we know that flux obeys the inverse square law

$$f \; \alpha \; \frac{1}{d^2}, \tag{B.13}$$

we now have that Eqn. B.12 becomes

$$10^{-0.4m} \alpha\, d^{-2}. \tag{B.14}$$

As M is defined to be the apparent magnitude of an object at a distance of 10pc, we can say that

$$10^{-0.4M} \alpha 10^{-2}, \tag{B.15}$$

and we therefore get

$$\frac{10^{-0.4M}}{10^{-0.4m}} = \frac{d^2}{10^2}. \tag{B.16}$$

Rearranging we find that Eqn. B.16 becomes

$$10^{0.4(m-M)} = \left(\frac{d}{10}\right)^2, \tag{B.17}$$

and from taking logs we have,

$$m - M = 2\left(\frac{2.5}{0.4}\right) \log\left(\frac{d}{10}\right), \tag{B.18}$$

which can be rewritten as

$$m - M = 5 \log\left(\frac{d}{10}\right), \tag{B.19}$$

and then

$$m - M = 5 \log d - 5 \tag{B.20}$$

where d is in pc, or

$$m - M = 5 \log d + 25, \tag{B.21}$$

where d is in Mpc.

B.3 Euclidean number counts

We Begin with the volume (V) distance (d) and luminosity (L) distance relations

$$V \alpha d^3, \tag{B.22}$$

$$L \alpha \frac{1}{d^2}, \tag{B.23}$$

respectively. Combining these two we get

$$V^{2/3} \alpha \frac{1}{L}. \tag{B.24}$$

and as $N \alpha V$ this becomes

$$N^{2/3} \alpha \frac{1}{L}. \tag{B.25}$$

which then becomes

$$\frac{2}{3} N \alpha -\log L. \tag{B.26}$$

Using the luminosity magnitude relation we get

$$\frac{1}{L} \alpha 10^{\frac{2}{5}m} \tag{B.27}$$

and after taking logs we have

$$-\log L \alpha \frac{2}{5} m. \tag{B.28}$$

Substituting Eqn. B.28 into Eqn. B.26 and rearranging we are left with

$$\log N \alpha \frac{3}{2}\frac{2}{5} m \tag{B.29}$$

and we therefore find that,

$$\log N \alpha 0.6m. \tag{B.30}$$

B.4 Proper distance

Here we derive the proper distance, dp, in the flat and matter dominated Einstein-de Sitter (Eds) universe. For a more general solution the reader is referred to Mattig (1958).

Starting from the Robertson-Walker (RW) metric:

$$c^2 d\tau^2 = c^2 dt^2 - R^2(t)\left(\frac{dr^2}{1-kr^2} + r^2 d\psi^2\right), \tag{B.31}$$

which describes the path of an observer through an isotropic, homogeneous and expanding universe. Here c is the speed of light, $d\tau$ is the observers measured time interval between two points, dt is the global time element, $R(t)$ is the scale factor of the universe with curvature, k, r is a time-independent radial co-moving coordinate and $d\psi$ is angular part of the observers motion. If we now use the RW metric to describe the path of a photon, $cd\tau$=0, which travels in a straight line, $d\psi$=0, in a flat universe, k=0, we find that Eqn. B.31 reduces to

$$cdt = R(t)dr, \tag{B.32}$$

or alternatively

$$r = \int \frac{cdt}{R(t)}. \tag{B.33}$$

We note the for a photon emitted at time t_1 and observed at time t_2 the changes in time *cannot* effect the integral in Eqn. B.33 as r is a co-moving parameter. We therefore have that

$$\frac{dt_0}{dt_t} = \frac{R(t_0)}{R(t_2)}. \tag{B.34}$$

As redshift, z, is defined it terms of a photons frequency, ν, as:

$$\frac{\nu_{emit}}{\nu_{obs}} \equiv (1+z), \tag{B.35}$$

and as frequency is related to time (c=νt) we get

$$\frac{\nu_{emit}}{\nu_{obs}} \equiv (1+z) = \frac{R(t_1)}{R(t_2)}, \tag{B.36}$$

and therefore

$$\frac{R_0}{R(t)} = (1 + z). \tag{B.37}$$

We now state the Friedman equation for the matter dominated flat universe:

$$\left(\frac{dR}{dt}\right)^2 = \frac{8\pi G\rho(t)R(t)^2}{3}. \tag{B.38}$$

Starting from $E = mc^2$ and differentiating w.r.t energy an mass we have

$$d\left(Mc^2\right) = -PdV, \tag{B.39}$$

where we have used the relation from thermodynamics $dE = -pdV$. As $M = \rho V$ Eqn. B.39 becomes

$$d\left(\rho_M V c^2\right) = -PdV. \tag{B.40}$$

Noting that $V\ \alpha\ r^3\ \alpha R^3$ and differentiating w.r.t time Eqn. B.40 becomes

$$\frac{d}{dt}\left(\rho_M R^3\right) = -\frac{P}{c}\frac{dR^3}{dt}, \tag{B.41}$$

which can be rearranged to its more familiar form,

$$\frac{d}{dt}\left(\rho_M R^3\right) + \frac{P}{c}\frac{dR^3}{dt} = 0. \tag{B.42}$$

In the matter dominated universe the pressure (2^{nd}) term goes to 0 and we are left with

$$\frac{d}{dt}\left(\rho_M R^3\right) = 0. \tag{B.43}$$

From this we get the relation $\rho\ \alpha\ R^{-3}$, which gives us

$$\frac{\rho(t)}{\rho_0} = \left(\frac{R_0}{R(t)}\right)^3 \tag{B.44}$$

By substituting Eqn. B.44 into Equ. B.38 we get

$$\left(\frac{dR}{dt}\right)^2 = \frac{8\pi G\rho_0 R_0^3}{3}\frac{1}{R}. \tag{B.45}$$

Eqn. B.38 gives us the relation $t^2 \alpha \frac{1}{\rho}$ and we know from Eqn. B.44 that $\frac{1}{\rho} \alpha R(t)^3$, so combining these two we have

$$\frac{R}{R_0} = \left(\frac{t}{t_0}\right)^{2/3}, \tag{B.46}$$

which can be differentiated to give

$$\frac{dR}{dt} = \frac{2R_0}{3t_0^{2/3}t^{1/3}}. \tag{B.47}$$

Combining this with Eqn. B.46 and knowing that

$$\mathrm{H} = \frac{dR}{dt}\frac{1}{R} \tag{B.48}$$

we find that the age of an Eds universe is given by

$$t_0 = \frac{2}{3\mathrm{H}_0}. \tag{B.49}$$

Substituting Eqn. B.46 into Eqn. B.33 we get

$$R_0 r = ct^{2/3}\int_{t_1}^{t_0}\frac{1}{t^{2/3}}dt. \tag{B.50}$$

Setting $\mathrm{dp} = R_0 r$ and performing the integration we arrive at

$$\mathrm{dp} = 3ct_0^{2/3}\left[t_0^{1/3} - t_1^{1/3}\right], \tag{B.51}$$

which simplifies to

$$\mathrm{dp} = ct_0\left[1 - \left(\frac{t_1}{t_0}\right)^{1/3}\right]. \tag{B.52}$$

Combining Eqn. B.37 with Eqn. B.46 we get

$$\left(\frac{t_1}{t_0}\right)^{2/3} = \frac{1}{(1+z)} \tag{B.53}$$

Inserting this and Eqn. B.49 into Eqn. B.52 we arrive at the proper distance:

$$\mathrm{dp} = \frac{2\mathrm{c}}{\mathrm{H}_0}\left(1 - \frac{1}{(1+\mathrm{z})^{1/2}}\right) \tag{B.54}$$

B.5 Volume element

We now derive the volume element for Eds universe. Starting from the volume of a sphere $V = \frac{4}{3}\pi r^3$, which differentiates to give

$$\frac{dV}{dr} = 4\pi r^2, \tag{B.55}$$

Here $r = da$ and dr is the distance traveled by a photon in time interval dt, $dr = \mathrm{c}dt$ and so Eqn B.55 becomes

$$dV = 4\pi \mathrm{c} da^2 dt \tag{B.56}$$

which can be re-written as

$$dV = 4\pi \mathrm{c} da^2 \frac{dt}{dz} dz. \tag{B.57}$$

From Eqn. B.53 we get

$$t = \frac{t_0}{(1+\mathrm{z})^{3/2}}, \tag{B.58}$$

and by substituting t_0 with Eqn. B.49 we have that

$$t = \frac{2}{3\mathrm{H}_0} \frac{1}{(1+\mathrm{z})^{3/2}} \tag{B.59}$$

which is differentiated to give

$$\frac{dt}{dz} = \frac{1}{\mathrm{H_0}(1+\mathrm{z})^{3/2}}. \tag{B.60}$$

Substituting Eqn. B.60 into Eqn. B.57 we find that the volume element at the time of emmission is given by

$$\frac{dV}{dz} = \frac{4\pi \mathrm{c} da^2}{\mathrm{H_0}} \frac{1}{(1+\mathrm{z})^{3/2}}. \tag{B.61}$$

However, as we require the co-moving volume we need to multiply Eqn. B.61 by a factor of $(1+\mathrm{z})^3$ so that we now have,

$$\frac{dV}{dz} = \frac{4\pi \mathrm{c} da^2}{\mathrm{H_0}} \frac{(1+z^3)}{(1+\mathrm{z})^{3/2}}, \tag{B.62}$$

which then becomes

$$\frac{dV}{dz} = \frac{4\pi \mathrm{c} da^2}{\mathrm{H_0}} (1+\mathrm{z})^{1/2}, \tag{B.63}$$

which is the co-moving volume velement in an Eds universe.

B.6 Luminosity density

The lumonosity density, j, is defined to be the luminosity, L, multiplied by the space density of galaxies at L, $\Phi(L)dL$, intrgeated over all L,

$$j = \int L\Phi(L)dL, \tag{B.64}$$

or

$$j = L_* \int \frac{L}{L_*}\Phi(L)dL. \tag{B.65}$$

Using Eqn. B.1 to substitute for $\Phi(L)dL$ we have

$$j = L_* \int \frac{L}{L_*}\phi_* \left(\frac{L}{L_*}\right)^{\alpha} e^{-\frac{L}{L_*}} dL, \tag{B.66}$$

which then becomes

$$j = \phi_* L_* \int_0^\infty \left(\frac{L}{L_*}\right)^{(\alpha+1)} e^{-\frac{L}{L_*}} dL. \tag{B.67}$$

The integration part of Eqn. B.67 is Euler's integral which has the gamma function solution

$$\Gamma(\alpha+1+1) = \int_0^\infty x^{\alpha+1} e^{-x} dx. \tag{B.68}$$

and so Eqn. B.67 becomes

$$j = \phi_* L_* \Gamma(\alpha+2). \tag{B.69}$$

B.7 Profiles in magnitude form

The general profile of galactic light is given as

$$I_r = I_0 exp\left(-\frac{r}{\alpha}\right)^{1/\beta}, \tag{B.70}$$

where β=1 for the exponential disk and 4 for a de Vaucouleurs bulge. α is the disk/bulge scale length, the point at which

$$I_r = I_0 e^{-1} = 0.3777 I_0 \tag{B.71}$$

Before we derive the individual bulge and disk profiles we must first obtain an expression for the central surface brightness, I_0, for both components in terms of magnitudes.

By definition the luminosity, L, of a galaxy must be equal to the integral of I_r out to infinity and over all surface angles, θ:

$$L = \int_0^{2\pi} \int_0^\infty I_r r d\theta dr. \tag{B.72}$$

Performing the integration over θ and substituting for I_r we get

$$L = 2\pi I_0 \int_0^\infty r e^{\left(-\frac{r}{\alpha}\right)^{1/\beta}} dr. \tag{B.73}$$

By introducing the variable, x, and defining it to be

$$x = \left(\frac{r}{\alpha}\right)^{1/\beta}, \tag{B.74}$$

or alternatively

$$r = \alpha x^{\beta} \tag{B.75}$$

which differentiates to become,

$$dr = \beta\alpha x^{(\beta-1)}dx, \tag{B.76}$$

Eqn. B.73 can be rewritten as

$$L = 2\pi I_0 \alpha^2 \beta \int_0^{\infty} x^{\beta} x^{(\beta-1)} e^{x} dx \tag{B.77}$$

which then simplifies to

$$L = 2\pi I_0 \alpha^2 \beta \int_0^{\infty} x^{(2\beta-1)} e^{x} dx. \tag{B.78}$$

Eqn. B.78 is in-fact Euler's integral which has the gamma function solution

$$\Gamma(2\beta - 1 + 1) = \int_0^{\infty} x^{2\beta-1} e^{-x} dx. \tag{B.79}$$

Using this Eqn. B.78 now becomes

$$L = \pi I_0 \alpha^2 2\beta\Gamma(2\beta). \tag{B.80}$$

As for either an exponential disk or de Vaucoulers bulge β will be an integer and as for integers $\Gamma(A) = (A-1)!$ we can now write

$$L = \pi I_0 \alpha^2 2\beta(2\beta - 1)!, \tag{B.81}$$

which then simplifies to become

$$L = (2\beta)!\pi I_0 \alpha^2. \tag{B.82}$$

Using the relationships $L \; \alpha \; 10^{-0.4m}$ and $I \; \alpha \; 10^{-0.4\mu}$, Eqn. B.82 becomes

$$10^{-0.4m} = (2\beta)!\pi 10^{-0.4\mu_0} \alpha^2, \tag{B.83}$$

and after taking logs we get

$$-0.4m = \log(2\beta)!\pi + 2\log\alpha - 0.4\mu_0. \tag{B.84}$$

This can now be rearranged to give an expression for the central surface brightness of a de Vacoulers (β=4) bulge or an exponential (β=1) disk:

$$\mu_0 = m + 5\log\alpha + 2.5\log\left((2\beta)!\pi\right) \tag{B.85}$$

We now use this to derive the exponential disk and de Vaucouleurs bulge profile in magnitude form.

B.7.1 Disk profile

Starting from the profile in units of intensity

$$I_r = I_0 exp\left(-\frac{r}{\alpha}\right). \tag{B.86}$$

Rewriting this as

$$I_r = I_0 exp\left(-\frac{r\ln 10}{\alpha \ln 10}\right). \tag{B.87}$$

and knowing that

$$10^{-X} = e^{\ln 10^{-X}} = e^{-X\ln 10} \tag{B.88}$$

where, in this case $X = -\frac{r}{\ln 10}$, we can say that

$$I_r = I_0 10^{(-\frac{r}{\alpha \ln 10})}. \tag{B.89}$$

Using the knowledge that $I \; \alpha \; 10^{-0.4\mu}$, Eqn. B.89 becomes

$$10^{-0.4\mu_r} = 10^{-0.4\mu_0} 10^{-(\frac{r}{\alpha \ln 10})}. \tag{B.90}$$

Taking logs and rearranging we get

$$\mu_r = \mu_0 + \frac{2.5}{\ln 10} \left(\frac{r}{\alpha}\right), \tag{B.91}$$

which can be combined with Eqn. B.85 to describe the disk-light profile.

B.7.2 Bulge profile

For a de Vaucouleurs bulge the generalised profile becomes

$$I_r = I_0 exp \left(-\frac{r}{\alpha}\right)^{1/4}. \tag{B.92}$$

However, as the bulge scale length is substantially smaller than the seeing we need to redefine the profile turn-over to a more measurable parameter that is also related to the bulge α. We use the bulge effective radius (half-light radii), r_e which is related to α via:

$$r_e = \alpha k^4 \tag{B.93}$$

where k is calculated from the recipe, $k = 1.9992\beta - 0.371$, derived numerically by Capaccioli (1989). We also need to redefine I_0 to be the surface brightness at r_e. By combining Eqn. B.92 with Eqn. B.93 we arrive at

$$I_e = I_0 e^{-k} \tag{B.94}$$

which, by making use of Equ. B.88, becomes

$$I_e = I_0 e^{-\frac{k}{\ln 10}}. \tag{B.95}$$

For the de Vaucouleurs bulge k=7.6697. Using Eqn. B.88 and Eqn. B.95, Eqn. B.92 can be written as

$$I_r = I_e \frac{10^{-3.33\left(\frac{r}{r_e}\right)^{1/4}}}{10^{-3.33}}, \tag{B.96}$$

which then simplifies to

$$I_r = I_e 10^{-3.33\left(\left(\frac{r}{r_e}\right)^{1/4}-1\right)}, \tag{B.97}$$

or

$$I_r = I_e exp\left(-7.6697\left(\left(\frac{r}{r_e}\right)^{1/4}-1\right)\right), \tag{B.98}$$

which is the de Vaucouleurs $r^{1/4}$ law.

Now going back to the relation in Eqn. B.95, we rewrite the de Vauclours law as

$$I_r = I_0 10^{-3.33} exp\left(-7.6697\left(\left(\frac{r}{r_e}\right)^{1/4}-1\right)\right). \tag{B.99}$$

and from using the relation $I\ \alpha\ 10^{-0.4\mu}$ we get

$$10^{-0.4\mu_r} = 10^{-0.4\mu_0}\ 10^{-3.33}\ exp\left(-7.6697\left(\left(\frac{r}{r_e}\right)^{1/4}-1\right)\right), \tag{B.100}$$

By implementing Eqn. B.88, we get

$$10^{-0.4\mu_r} = 10^{-0.4\mu_0}\ 10^{-3.33}\ 10^{\frac{\left(-7.6697\left(\left(\frac{r}{r_e}\right)^{1/4}-1\right)\right)}{\ln 10}}, \tag{B.101}$$

which can be re-written as

$$10^{-0.4\mu_r} = 10^{-0.4\mu_0+(-3.33)+\frac{\left(-7.6697\left(\left(\frac{r}{r_e}\right)^{1/4}-1\right)\right)}{\ln 10}}. \tag{B.102}$$

By taking logs we arrive at

$$-0.4\mu_r = -0.4\mu_0 + (-3.33) + \frac{\left(-7.6697\left(\left(\frac{r}{r_e}\right)^{1/4} - 1\right)\right)}{\ln 10}, \tag{B.103}$$

which finally gives us

$$\mu_r = \mu_0 + (2.5 \times 3.33) + \frac{2.5}{\ln 10}\left(7.6697\left(\left(\frac{r}{r_e}\right)^{1/4} - 1\right)\right). \tag{B.104}$$

Eqn. B.104 is used with Eqn. B.85 to describe a galaxies bulge-light profile.

APPENDIX C

Comparative morphopogies

Here we look at different methods of getting galaxy morphology. We use our broad classifications, gained from cuts in (B/T), to test the usefulness of the C-A system (Abraham et al. 1994 and Abraham et al. 1996) and the Bivariate Brightness Distribution (BBD, first discussed in Binggeli 1993) as morphological tools. We also compare our classifications to the eyeball classifications of a reduced sample to be used as an ANN training set.

C.1 Concentration Index

As well as calculating the light profile parameters GIM2D also produces the concentration index (C). GIM2D calculates this in the exact same way as described in Abraham et al. (1994) and Abraham et al. (1996), see Eqn. 1.2. Four different values of C are given by GIM2D, with each one calculated for α=0.1, 0.2, 0.3, & 0.4. The asymmetry index (A) of the residual images is also calculated and is done so in the way prescribed by Abraham et al. (1994) and Abraham et al. (1996), see Eqn. 1.3. In Fig C.1 we reproduce the C-A plot of Abraham et al. (1996) for each of the four concentration indices's. The solid lines indicate the boundaries between different Hubble types, see Fig. 1.6. The dashed line indicates the theoretical parameter space in which non-evolving galaxies lie (Abraham et al. 1996). We find that an α=0.2 (top right) gives the best results, in that most of the galaxies lie within the dashed line region. From here on in we only consider the α=0.2 concentration index. In Fig. C.2 we show the C-A diagram for each individual, (B/T) classified, Hubble type. From Fig. C.2 we see that only the E/S0 population are confined to there specified region whilst the Sabc and Sa/Irr are evenly scattered across the Sabc and E/S0 boundary. Note that none of the galaxies classified as Sd/Irr in (B/T) lie in the Sd/Irr region of the C-A plot. The FPA galaxies are essentially indistinguishable from the Sd/Irr, Sabc or even the E/S0 classes in C-A space. Fig C.3 shows the distribution of objects in C (top panel) and A (bottom panel) for each (B/T) classified Hubble type. In both C and A it is clear that only the E/S0 galaxies are separable from the general galaxy population. Once again the FPA population looks like a combination of the Sabc and Sd/Irr galaxy distribution.

We now look at the distributions of C and A in absolute magnitude & surface brightness, Fig. C.4, and seeing, Fig. C.5. Contrary to Abraham et al. (1994) there appears to be no way to separate Hubble types in C-μ space. From C.5 we see that, as expected, there is no variation with seeing for the asymmetry index whilst objects get less concentrated (low C) as the seeing increases. It should be noted that everything, as regards C & A, presented so-far relies on the assumption that C should correlate with (B/T) as indicated in Kent (1985). Fig. C.6 shows that a weak relationship does between C and (B/T) does exist. As C correlates with (B/T) and we know that from Fig. 5.16 (B/T) is related to colour, hence it follows that C should also be linked to colour, Fig C.7 demonstrates this relationship. Note how the Sabc, Sd/Irr & FPA populations occupy

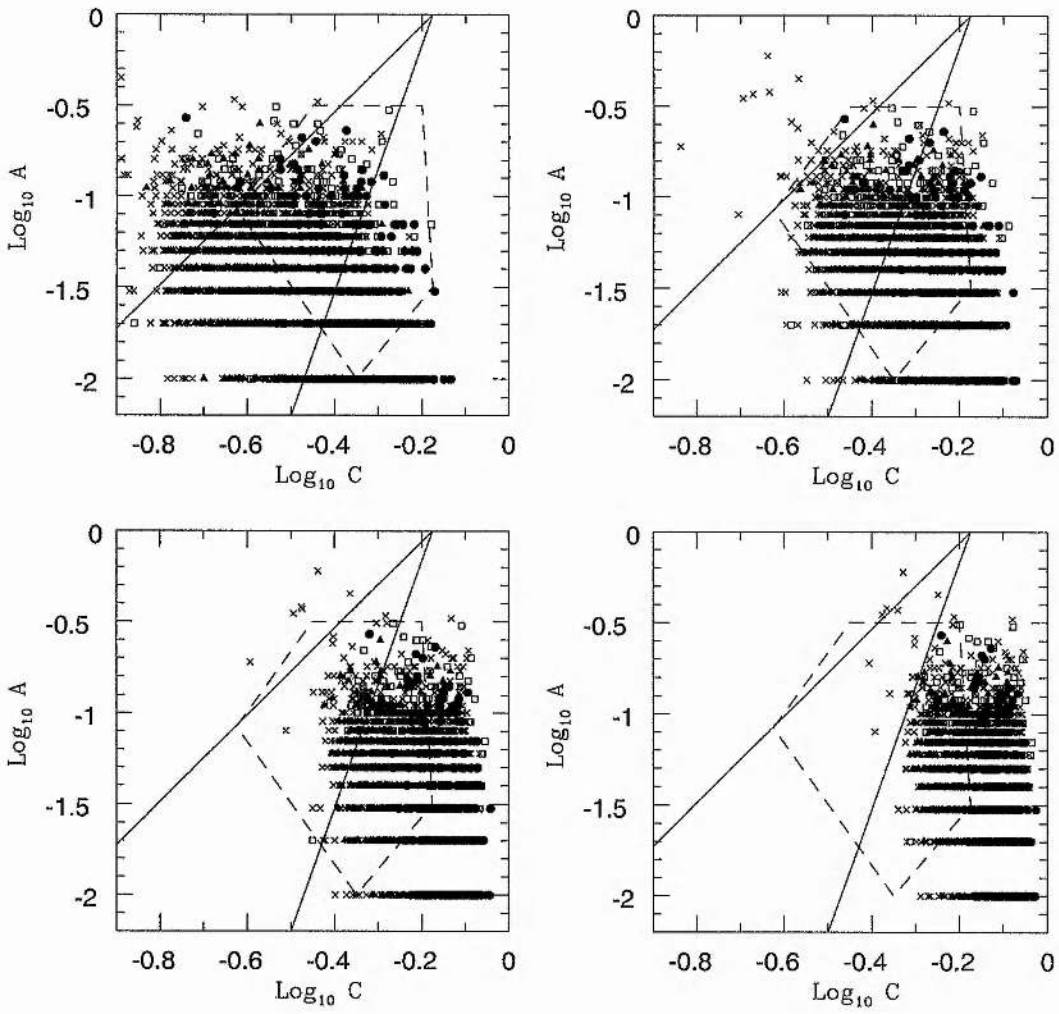

Figure C.1: The C-A plot for C with α=0.1 (top left), 0.2 (top right), 0.3 (bottom left) & 0.4 (bottom right). The solid lies indicate the boundaries between different Hubble types, see Fig. 1.6. The dashed line indicates the theoretical parameter space in which non-evolving galaxies lie (see Abraham et al. 1996). The different points indicate different Hubble types, E/S0 are filled circles, Sabc are open squares, Sd/Irr are filled triangles and FPA are crosses.

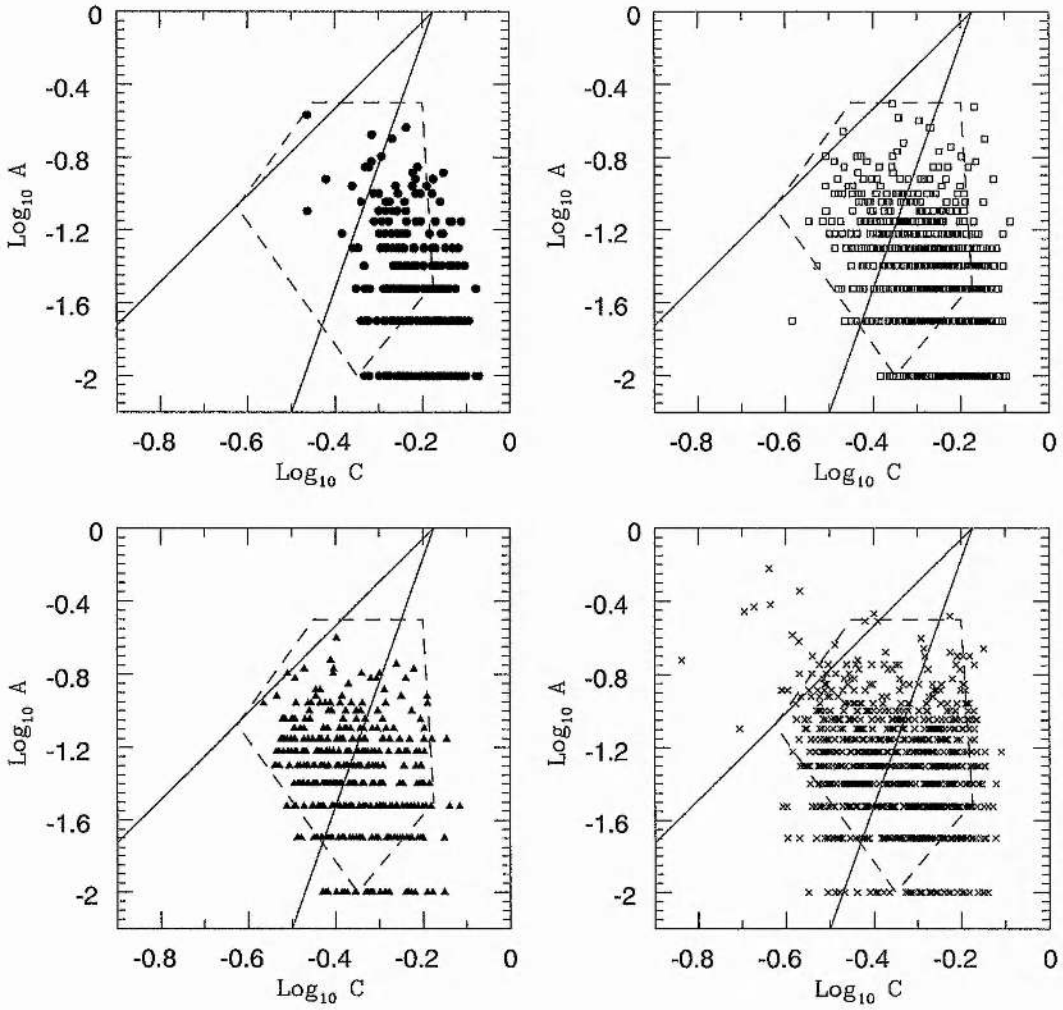

Figure C.2: The C-A plot for the Hubble types E/S0 (top left), Sabc (top right) and Sd/Irr (bottom left). The FPA population is also shown (bottom right)

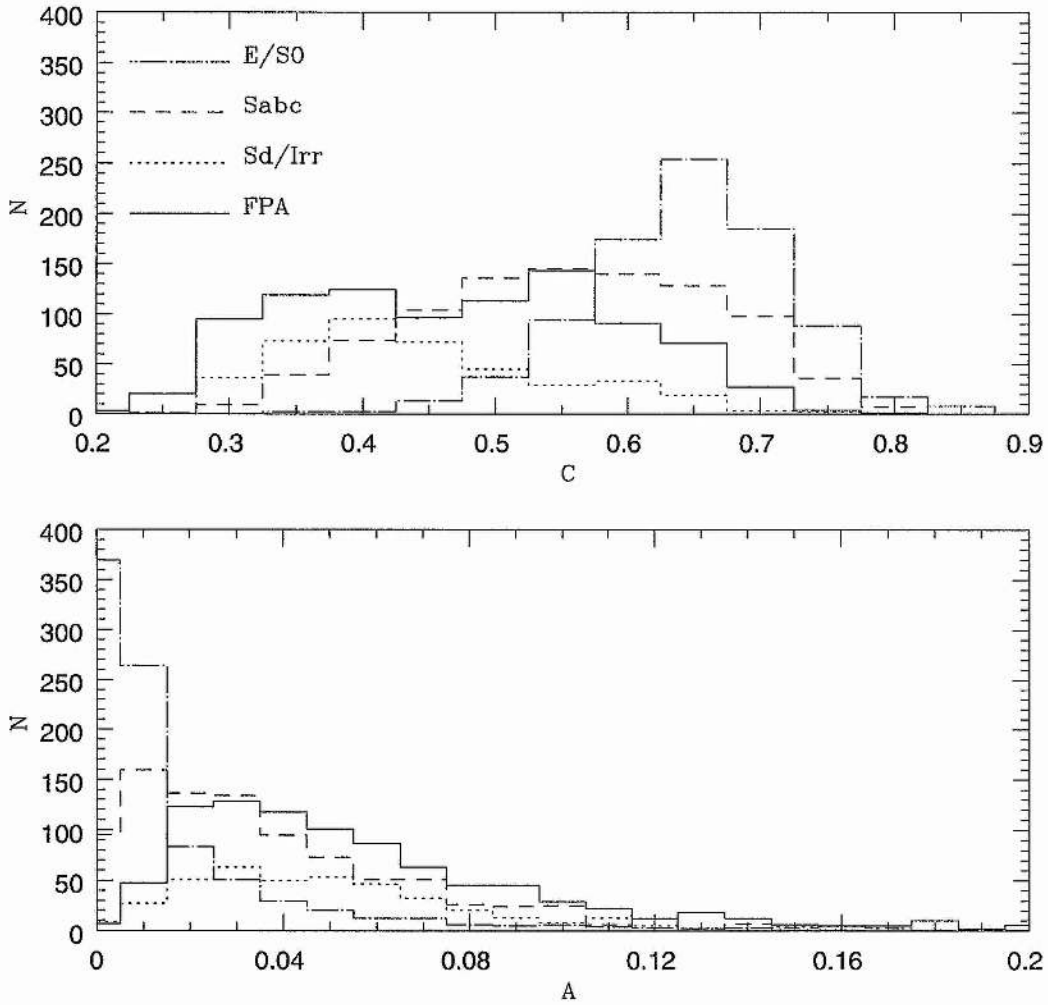

Figure C.3: The galaxy distributions in C (top panel) and A (bottom panel) for each (B/T) classified Hubble type.

exactly the same parameter space and that the Ellipticals are only separated from the whole galaxy population by the colour axis. It might be argued that the weak relationships shown in Figs. C.6 and Fig. C.7 may altogether disappear if more data points where added. If so, one would not expect to be able to use the C-A system to confirm Hubble types found by (B/T) cuts. However, if we examine the C-A diagram for galaxies at different redshifts, Fig. C.8, we find that the C-A is in-fact redshift dependent, in that at higher redshift the galaxies appear to become more concentrated. Also the agreement between the (B/T) and C-A morphologies is far from constant over the redshift range. This means that the boundaries between classes are essentially arbitrary, they need to be redefined for each redshift slice, and that the C-A is unreliable.

C.2 Bivariate Brightness Distribution

We now turn our attention to the Bivariate Brightness Distribution (BBD) as a method of determining Hubble types. As shown in Fig 1.7, we should be able to determine a galaxies morphology via its position on the BBD. Fig. C.9 shows the BBD for the full colour-redshift MGC sample. As we are using objects with redshifts we can use absolute magnitudes $M_{\rm MGC}$ and surface brightness μ_{abs}. Once again it seems as if only the E/S0 galaxies are confined to a particular region of the BBD. With the Sabc, Sd/Irr and FPA populations scattered across the parameter space available to galaxies. This scatter makes it impossible to use the BBD as it stands to get at Hubble types. We know from above colour correlates (after a fashion) with (B/T). We now add a third axis, $(u^* - g^*)$, to the BBD and define a colour-BBD, (C-BBD), Fig C.10. Although the bulk of the E/S0 galaxies are now distinguishable as sphere "floating" above the "squashed sausage" of the remainder of the galaxy population, it is still hard to see if there is any distinction between the other Hubble types. In Fig. C.11 we show the C-BBD for each of the (B/T) classified Hubble types, E/S0 (top left), Sabc (top right), Sd/Irr (bottom left) and FPA (bottom right). Here we find that the Sabd, Sd/Irr & FPA galaxies all occupy the same area in the C-BBD. Figs. C.12 to C.15 show this behavior persists even when only galaxies at z=0.05 and 0.08 are used.

Although, unlike the C-A system, there is no redshift dependency with the BBD, even when a third (colour) axis is added there is noway to reliably extract galaxies of a particular Hubble type. This includes the E/S0 galaxies as, even though they contain themselves to a particular parameter space, they are contaminated by scatter from the Sabc galaxies.

C.3 Visual comparison

We now compare our classifications to a reduced sample that has been classified by eye by an experienced observer (Odewahn Priv. comm.) to be used as and ANN training set. The training set comprises of 1952 galaxies down to an un-dust-corrected kron-like magnitude (column 9 the catalogue, see Appendix. A) of $B_{\rm MGC_{auto}}$=19. Of these 1952 galaxies 1653 have redshifts and SDSS-EDR colours. The Odewhan classifications are given mostly on the standard Hubble revised/T-type system (see Table. 1.1). However, in cases where a T-type could not be accurately assigned they where given a default T-type of 12. As well as eyeball T-types Odewhan also provides an independent measure of the un-dust-corrected kron-like magnitude, half-light radius (HLR) and concentration parameter (C). From Fig. C.16 we find that whilst Odewahn sees the galaxies as fainter, with smaller HLR, and therefore, more compact than both GIM2D and MGC, there is a correlation of T-type with (B/T). However, there is substantial overspill from the Sa (T-type=1) into what we define as the E/S0 region ((B/T)>0.5) and there is no natural division between the Sabc and Sd/Irr classes. From matching with the 2dFGRS we have acsess to the 2dFGRS classification parameter η. The details of how a galaxy is assigned an η-type are given in Madgwick et al. (2002), but basically is is the result of peforming

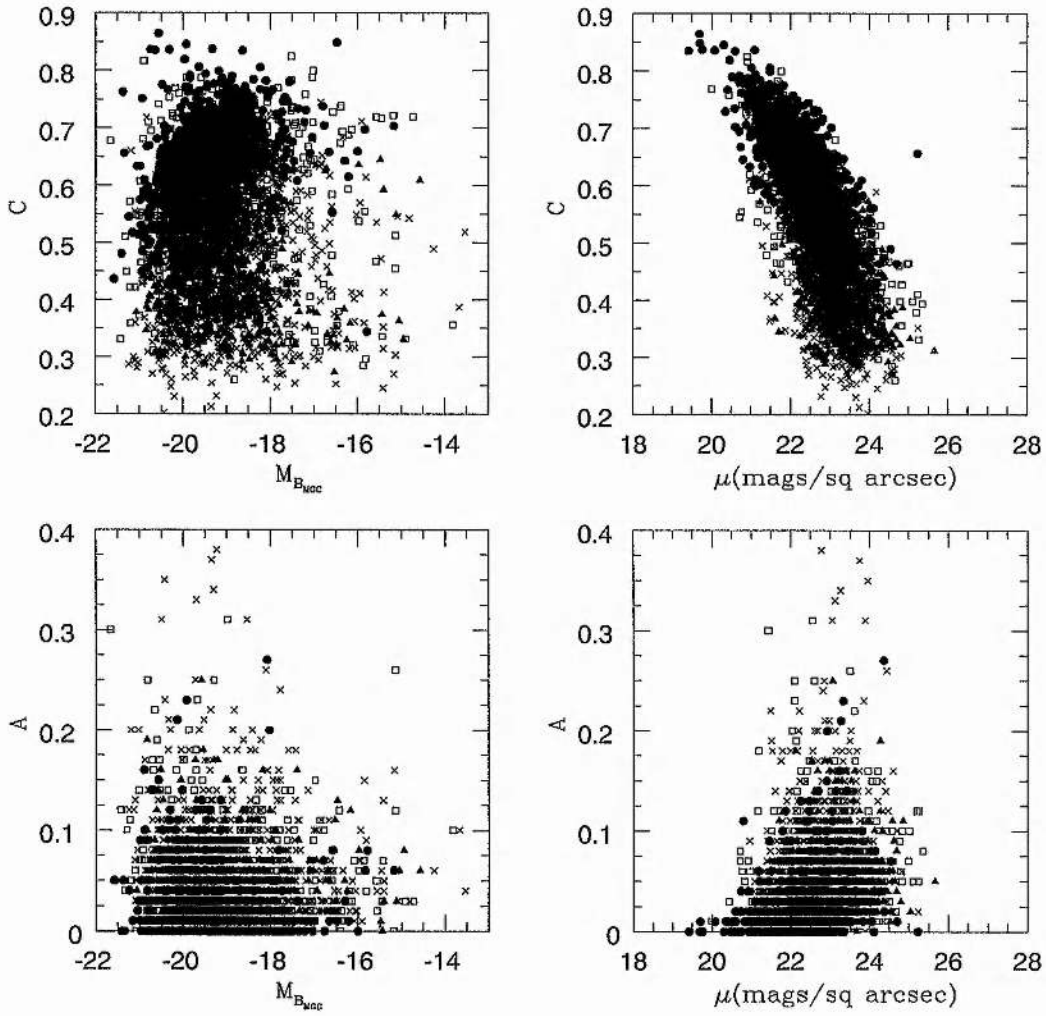

Figure C.4: The C and A distributions in absolute magnitude $M_{B_{\mathrm{MGC}}}$ and surface brightness μ.

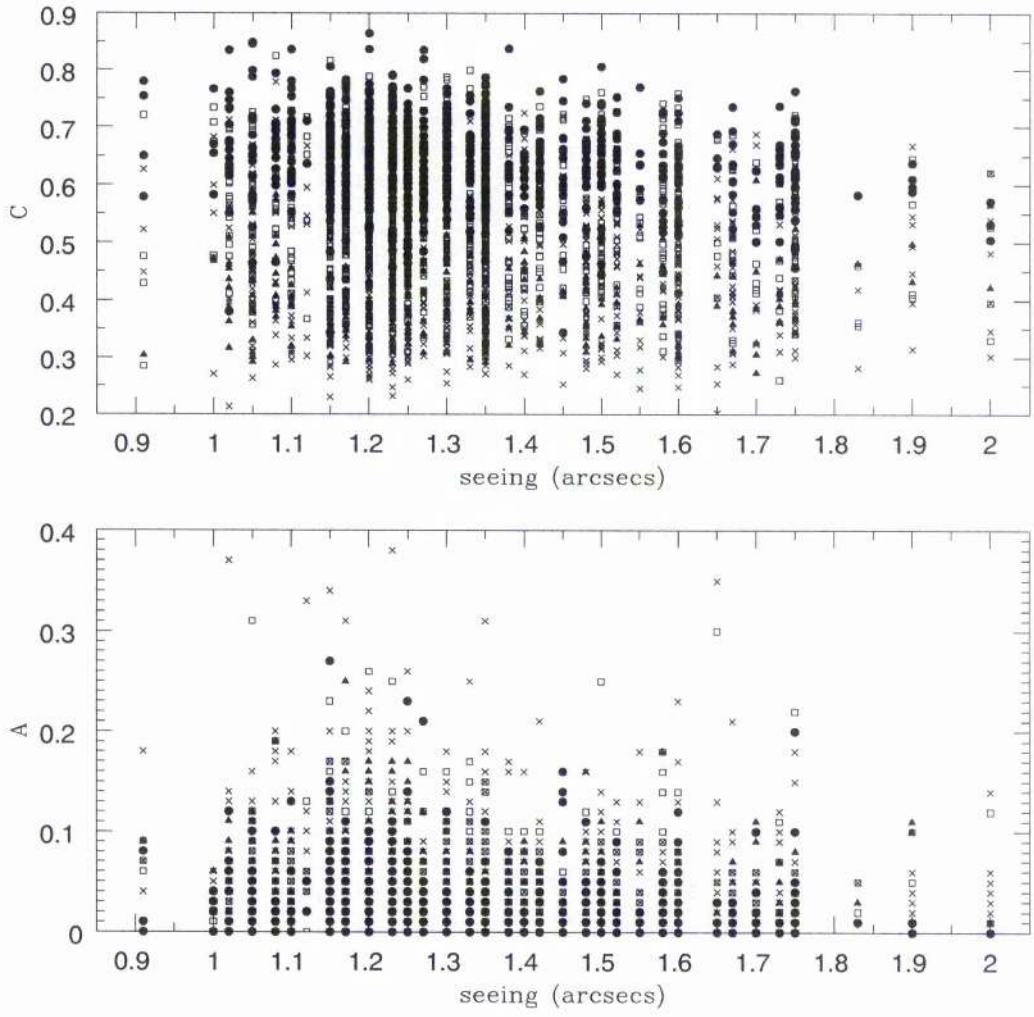

Figure C.5: Here we show how the C (top panel) and A (bottom panel) change with increasing seeing. The different points indicate different Hubble types, see Fig 5.15 and Table. 5.2.

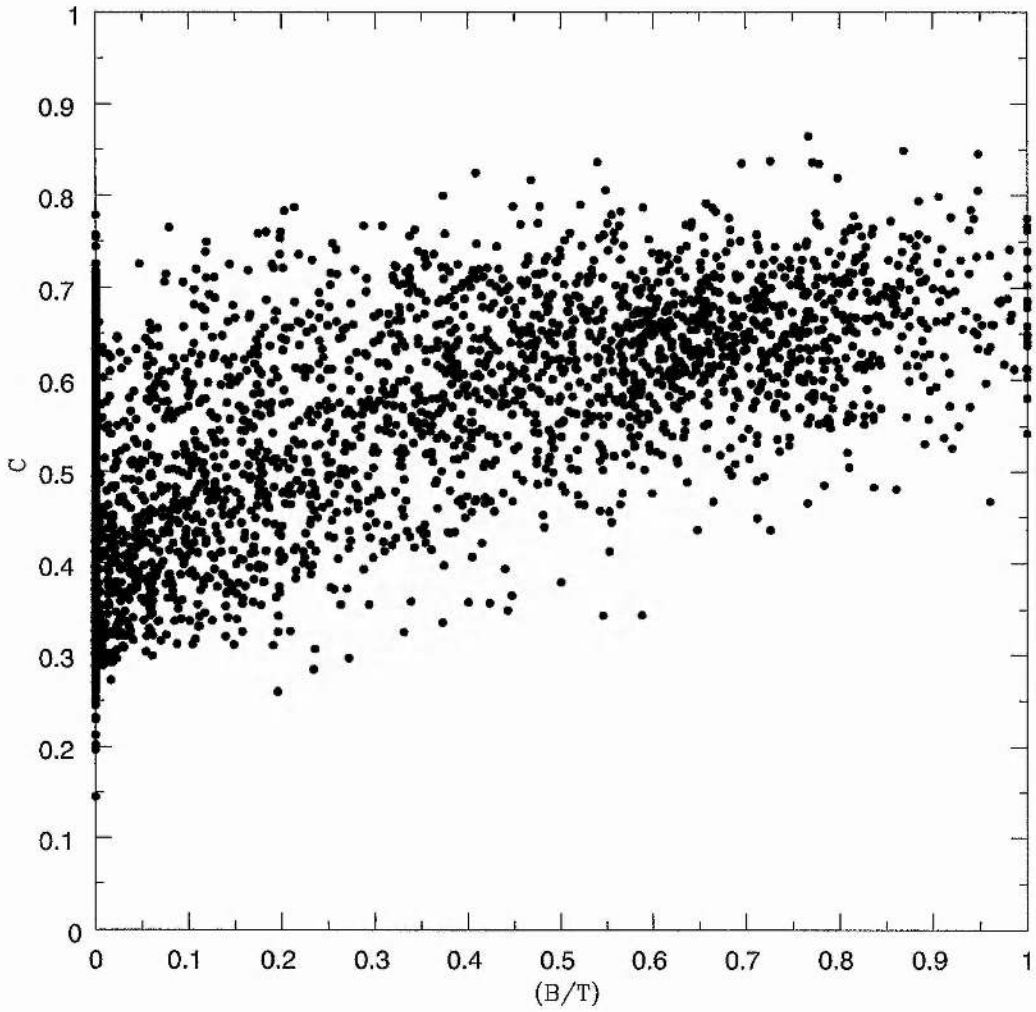

Figure C.6: The correlation between C and (B/T).

Table C.1: Here we show how we redistributed the Odewhan unclassified galaxies.

Description	T-type	N
Merger	10	91
Peculiar	10	31
Crowded	12	27
Bulge-dominated	-4	306
Disk-dominated	7	242
Bilge+Disk	2	71
Total		768

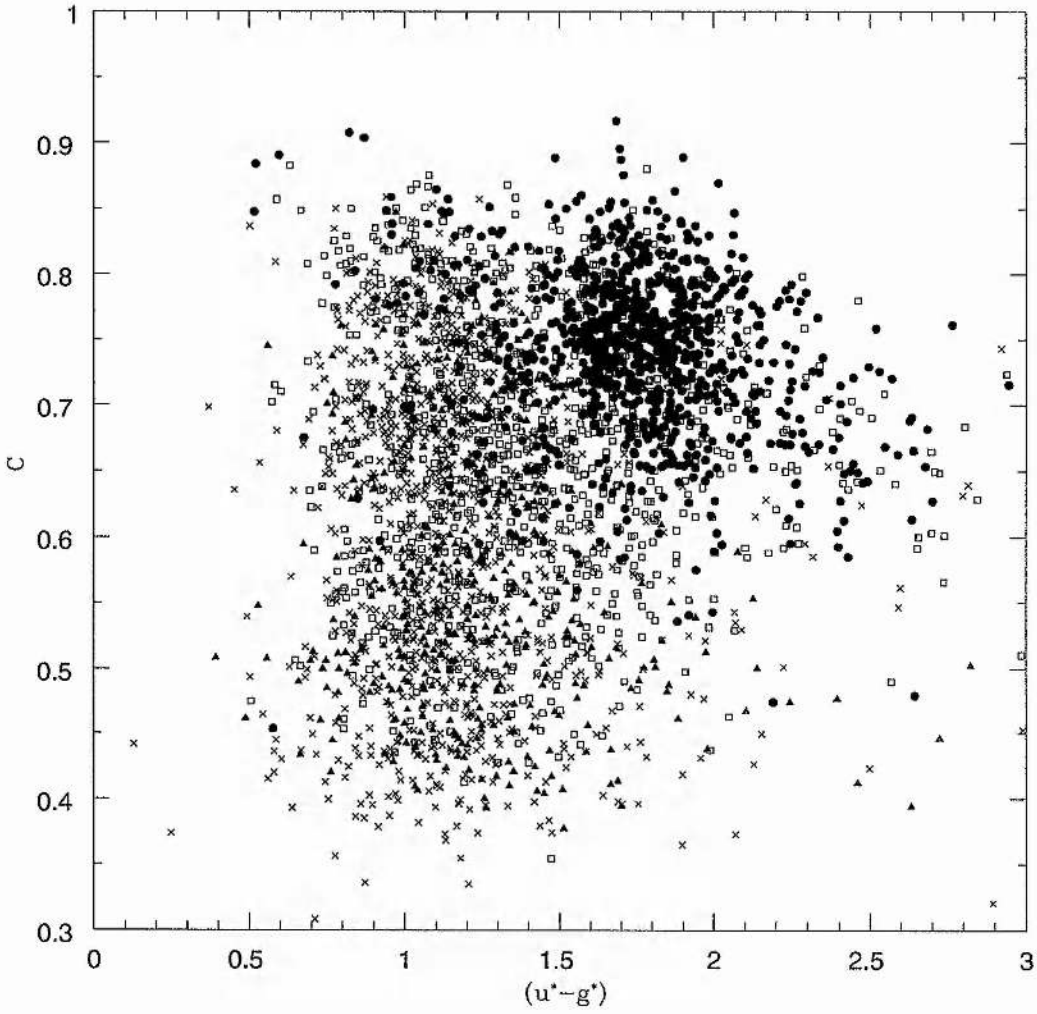

Figure C.7: The correlation between C and colour.The different points indicate different Hubble types, see Fig 5.15 and Table. 5.2.

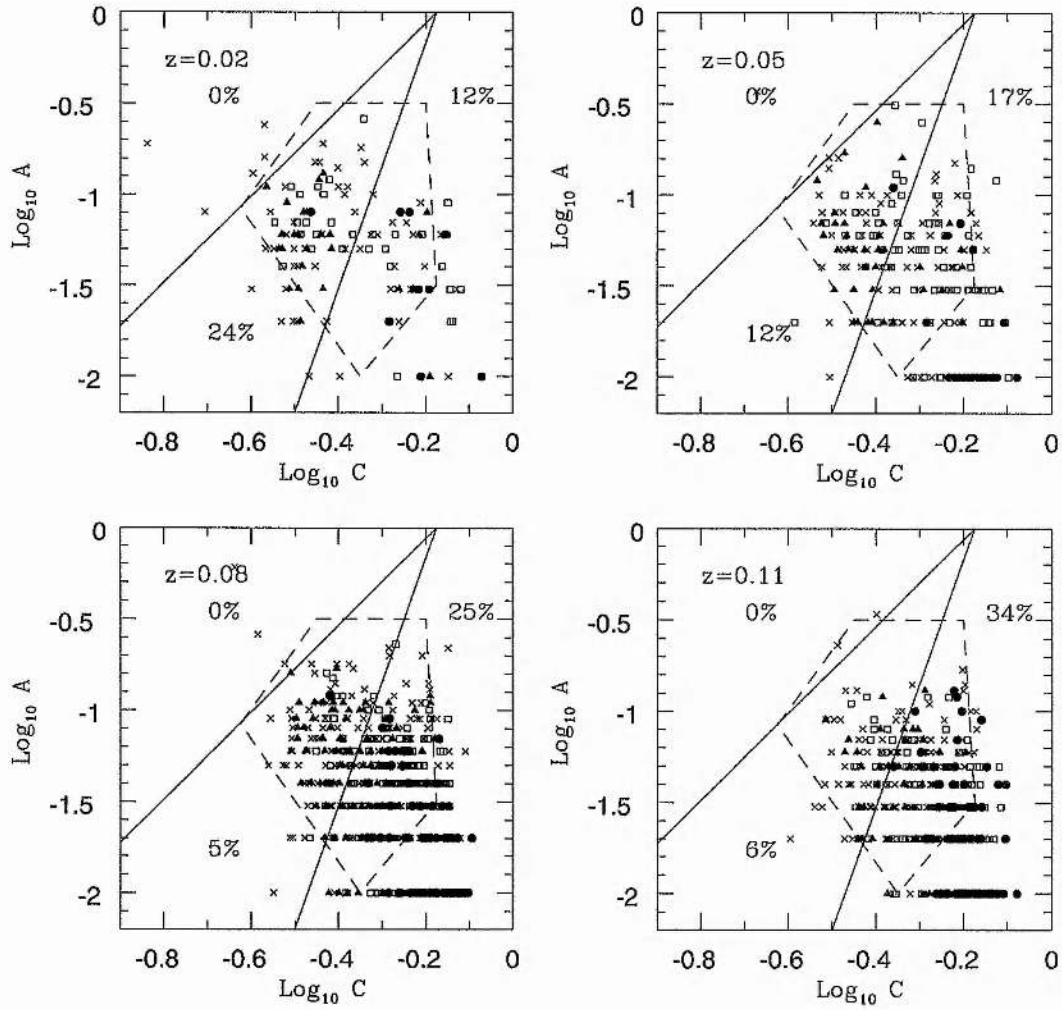

Figure C.8: The C-A diagram for different redshift slices, z=0.02, 0.05, 0.08, 0.11. The percentages in each plot indicate the amount of agreement between (B/T) morphologies and C-A morphologies for each Hubble type.

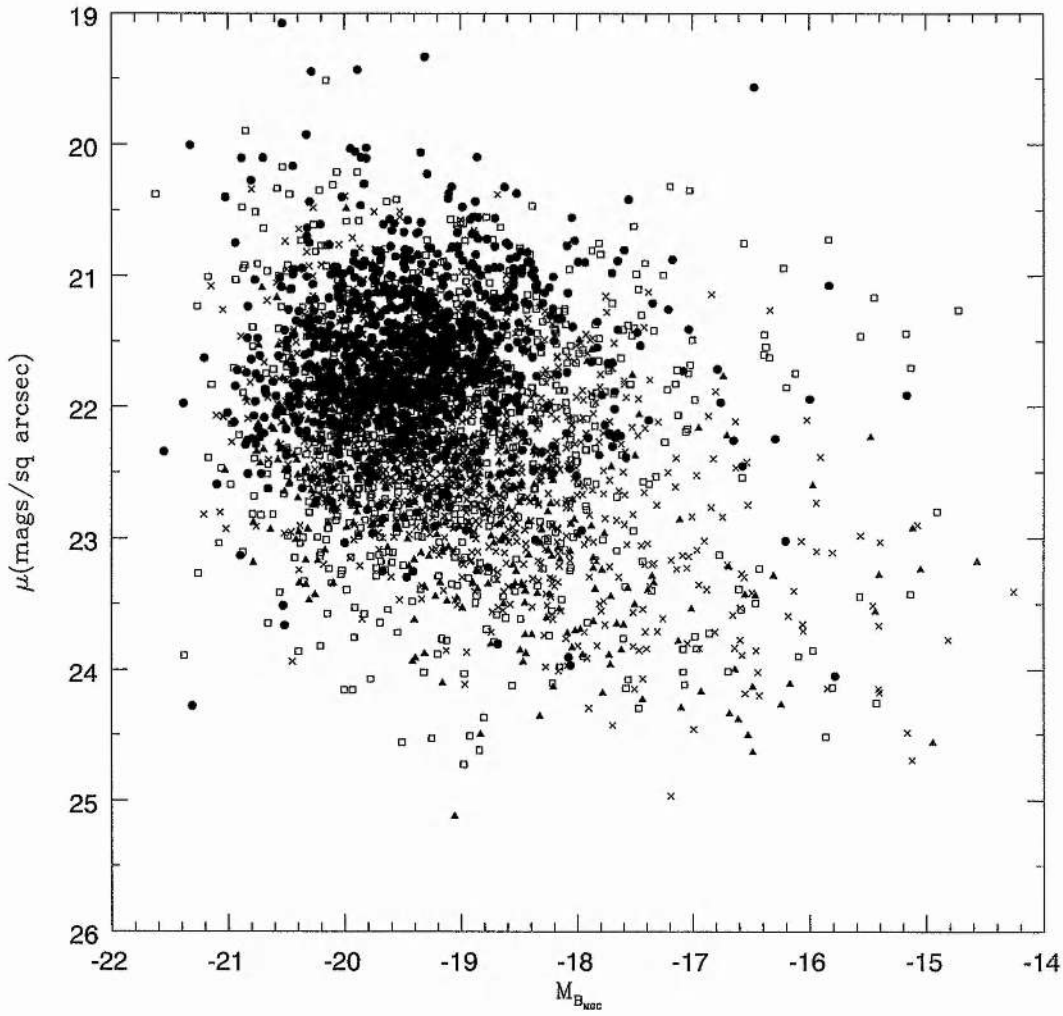

Figure C.9: The BBD for MGC galaxies with red shifts and colours. The different points indicate different Hubble types, see Fig 5.15 and Table. 5.2.

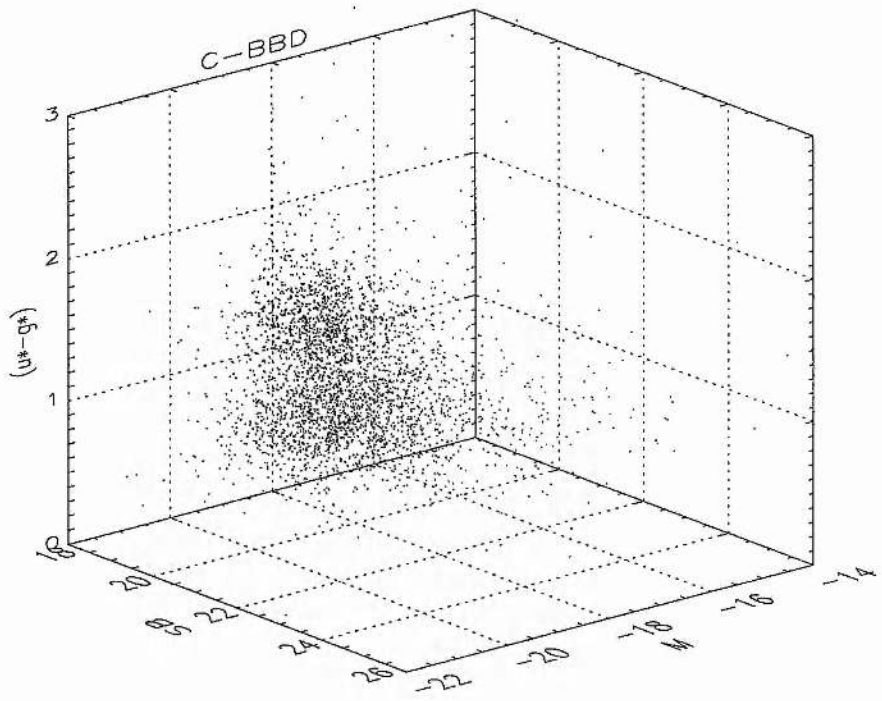

Figure C.10: The C-BBD

principal component analysis (PCA) and a galaxies spectra. There are 4 η-types: η=1 absorption line systems (E/S0), η=2 minimal emmission line system (Sab), η=3 moderate emmission lines (Scd), η=4 strong emmission lines (Irr). Fig. C.17 compares the 2dFGRS η-types to both the T-types and the MGC types. We find that, in bothe cases, whilst there is some correntaion for the Elliptical galaxies this soon dissapears for later η-types where there is no natural division between the classes. In Fig. C.18 we now compare the Odewhan T-types to our numerical classifications (see Fig. 5.28). Here we have re-assigned the class 12 galaxies according to there description provided by Odewhan (Priv. comm.), see Table. C.1. In order to distinguish the individual points we have added a random number to each galaxies T-type and MGC type. Each random number is smaller than the bin width and lies in the range -0.5< n <0.5. We find that although there appears to be some correlation between the classes, it is only the Sd/Irr galaxies that provide a comparable population fraction for this subset. The Odewhan eyeball classes over and under-estimate the E/S0 and Sabc fractions by 11% and 13% respectivly. As this subset is to be used as a training set for an ANN these results indicate the final outcome of ANN T-types. We note that our visually classed FPA Spiral and Irregular galaxies are generally given a range of T-types across the Sabc and Sd/Irr regions.

C.4 Summary

Here we have looked at the C-A system developed Abraham et al. (1994) & Abraham et al. (1996) and the BBD as a morphological tool. We find that not only is C only weakly related to (B/T) and colour but that the C-A system itself redshift dependent. For the BBD, although there is no redshift dependency, there is substantial scatter between the Sabc, Sd/Irr and FPA galaxies. The E/S0 galaxies can only really be distinguished from the rest by adding a colour axis to the BBD and even then there is still mild contamination

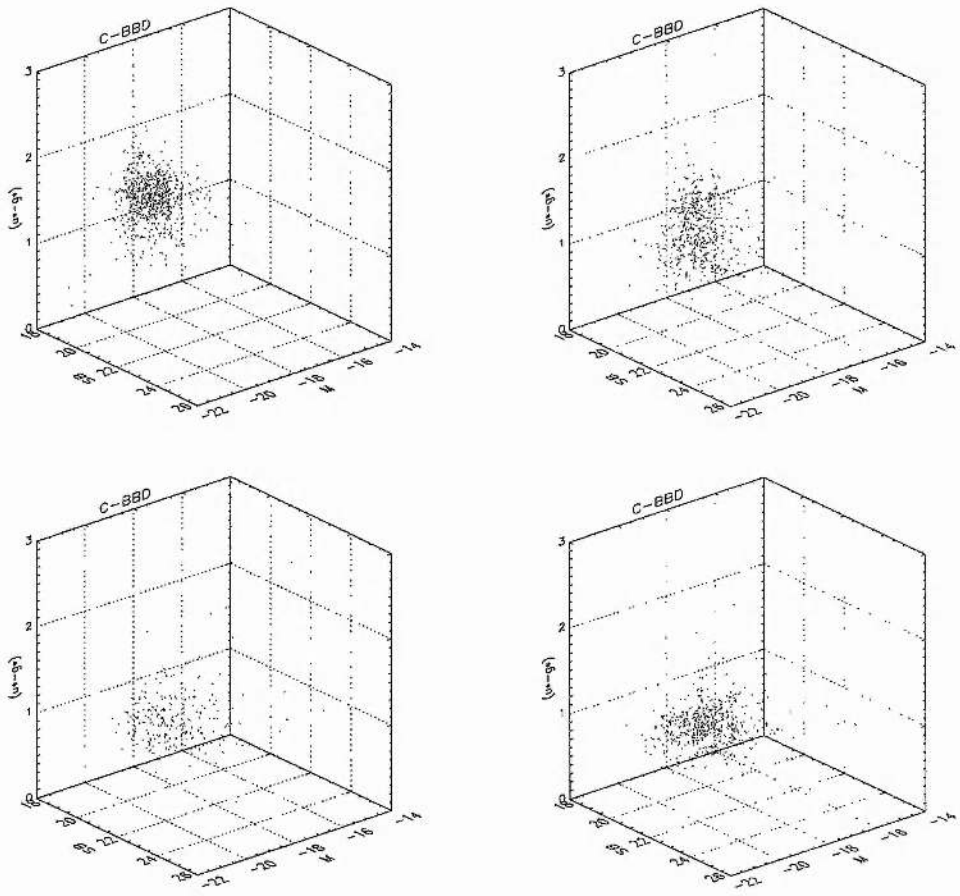

Figure C.11: The C-BBD for each of the three main bubble types, (B/T) classified Hubble types, E/S0 (top left), Sabc (top right), Sd/Irr (bottom left) and FPA (bottom right).

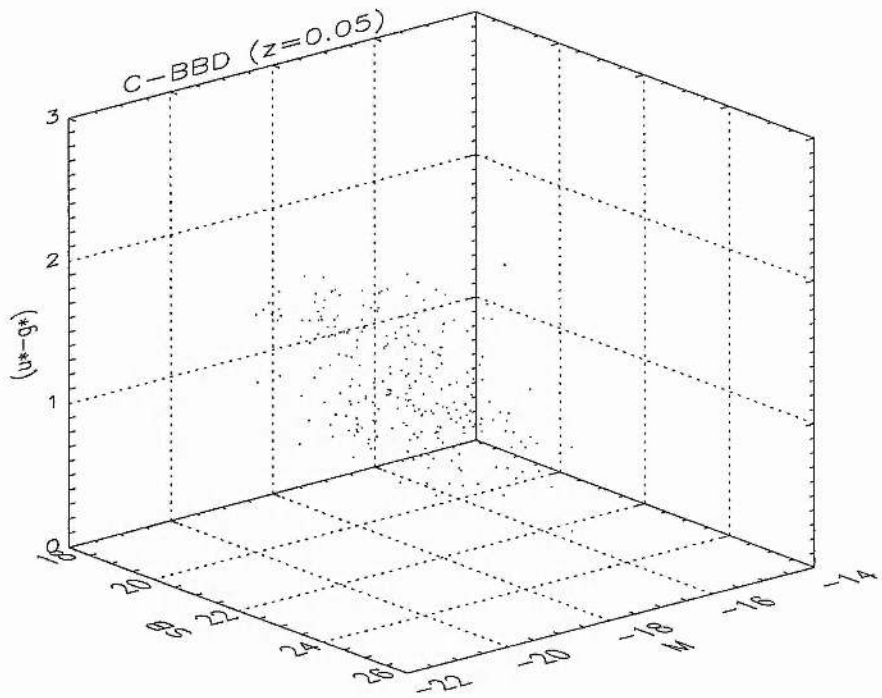

Figure C.12: The C-BBD for galaxies at z=0.05

from the Sabc population. Considering all this we believe both the C-A system and the BBD to be unreliable methods of determining a galaxies Hubble type.

We have compared our (B/T) classifications to a visually classified subset that will be used to train an ANN as well as 2dFGRS η-type classifications. We find that both the MGC and T-types only weakly correlate with η-types in the E/S0 region. For later types there is too much scatter to across the η-type boundaries for it to be of any use. We find that our visually classified FPAs are distributed across the Sabc and Sd/Irr T-type region and the fractions of E/S0 and Sabc galaxies are over and underestimated. This inconsistency with the (B/T) classifications indicates potential problems with the final ANN derived T-types.

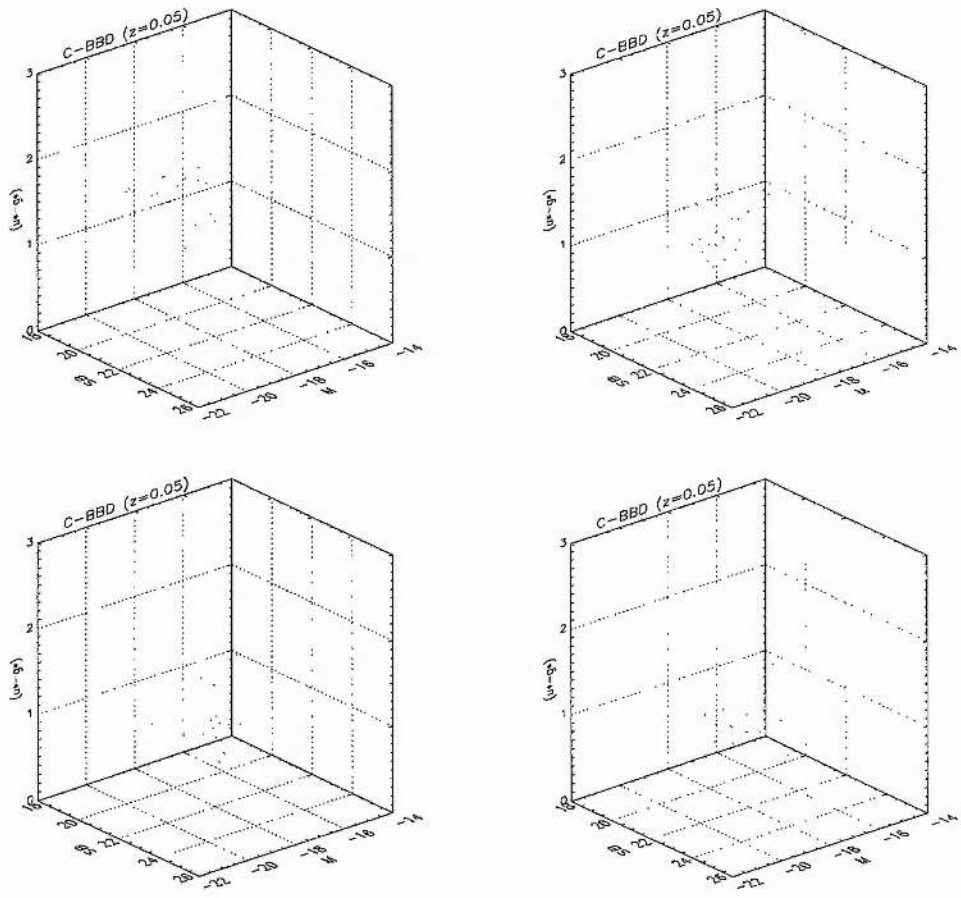

Figure C.13: The C-BBD for each of the three main bubble types, (B/T) classified Hubble types, E/S0 (top left), Sabc (top right), Sd/Irr (bottom left) and FPA (bottom right).

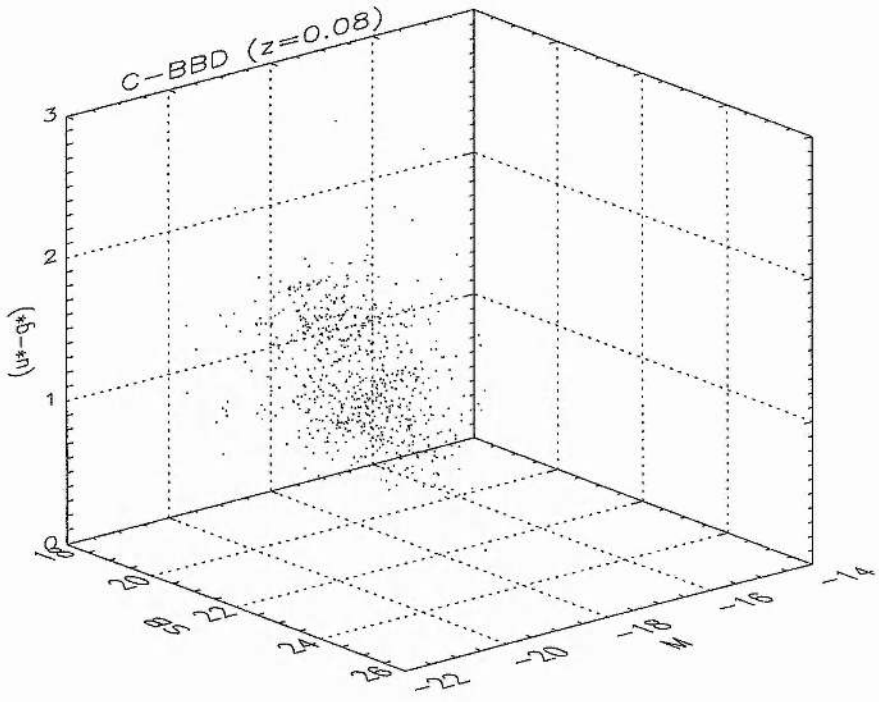

Figure C.14: The C-BBD for galaxies at z=0.08

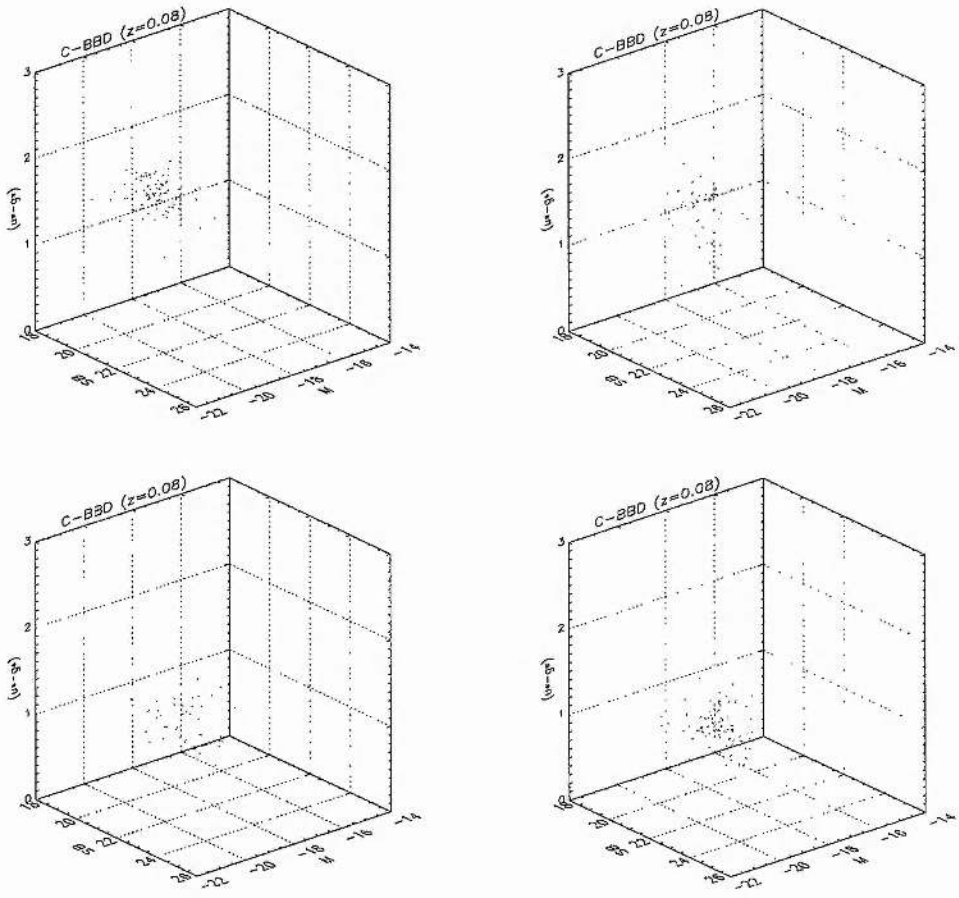

Figure C.15: The C-BBD for each of the three main bubble types, (B/T) classified Hubble types, E/S0 (top left), Sabc (top right), Sd/Irr (bottom left) and FPA (bottom right).

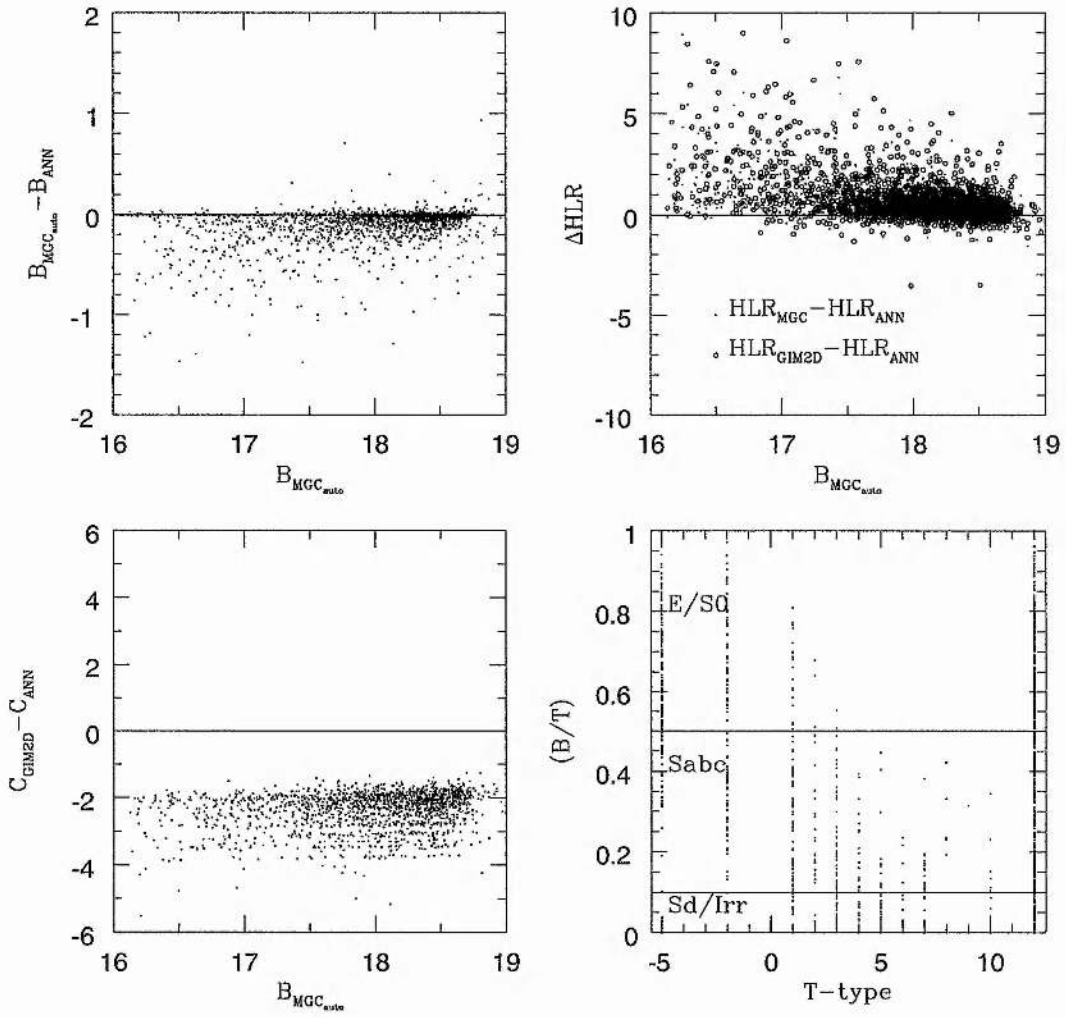

Figure C.16: The a comparison of the independently measured and classified galaxies with GIM2D/MGC properties. Top left: $B_{\mathrm{MGC_{auto}}}$ and B_{Ode}. Top right: HLR_{MGC} and HLR_{Ode} & HLR_{GIM2D} and HLR_{Ode}. Bottom left: C_{GIM2D} and C_{Ode}. Bottom right: Odewhan T-types and (B/T).

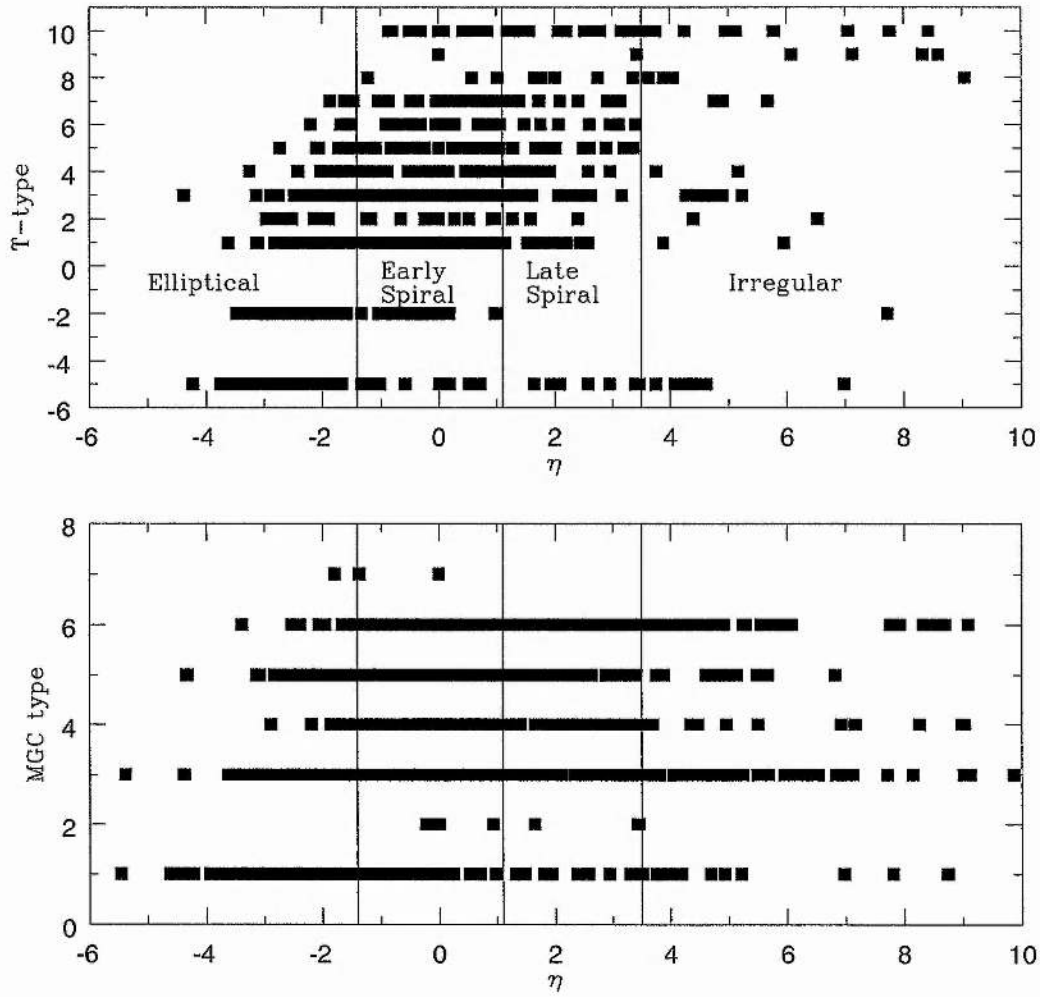

Figure C.17: A comparison of the 2dFGRS η-types with T-types (top) and MGC types (bottom).

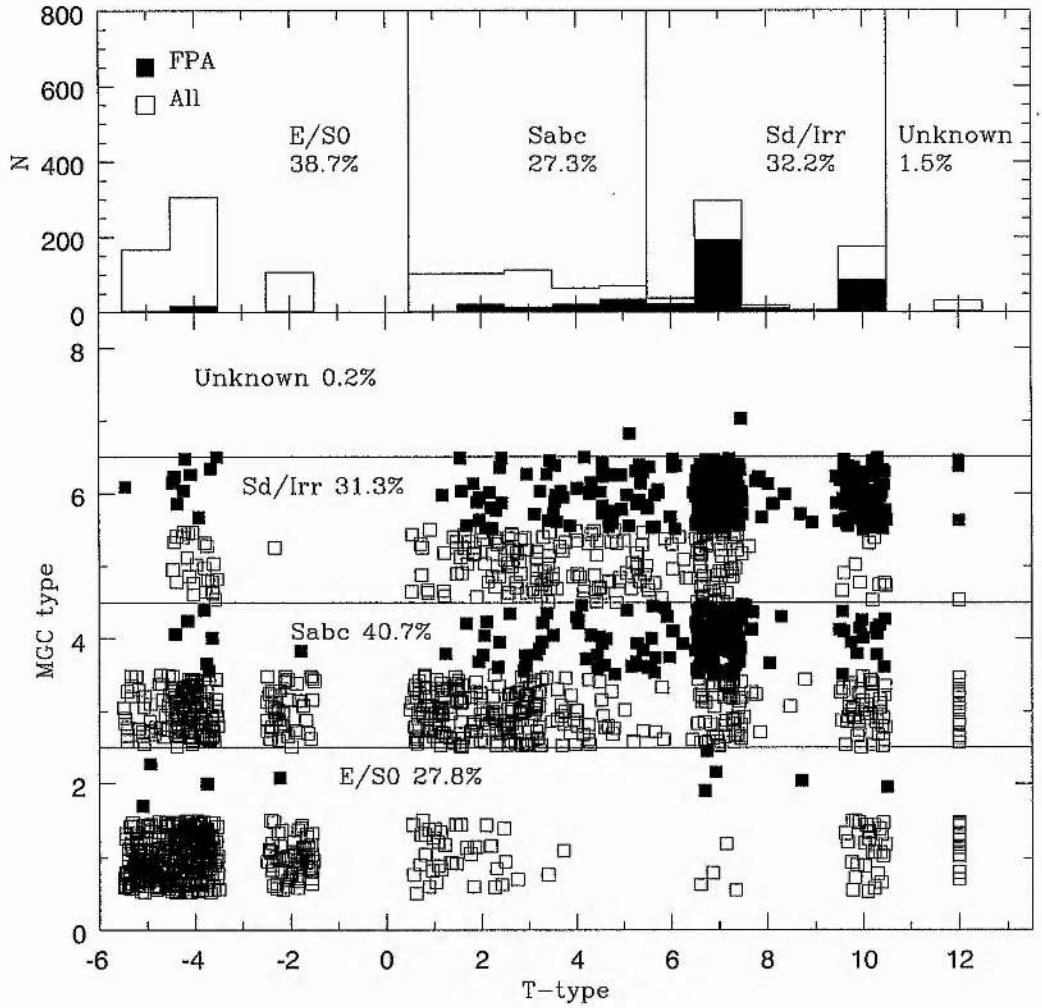

Figure C.18: Top: A histogram of the T-type distribution of the training set. Bottom: A comparison of the MGC types and Odewhan T-types. In both cases the solid squares and solid histogram represent the distribution of the FPA galaxies. The solid lines mark the division between our broad classes in the T-types top and MGC numerical classes bottom.